CCFE

CULHAM CENTRE FOR FUSION ENERGY

CCFE–R(12)17

T N Todd, R Clarke,
H Kalsi, M Kovari,
A Martin, A Muir,
Z Vizvary

THE KEY IMPACTS OF PULSED OPERATION ON THE ENGINEERING OF DEMO

THE KEY IMPACTS OF PULSED OPERATION ON THE ENGINEERING OF DEMO

T N Todd, R Clarke, H Kalsi, M Kovari, A Martin, A Muir,
Z Vizvary

EURATOM-CCFE Fusion Association, Culham Science Centre, Abingdon, Oxfordshire OX14 3DB

THE KEY IMPACTS OF PULSED OPERATION ON THE ENGINEERING OF DEMO

T N Todd, R Clarke, H Kalsi, M Kovari, Andrew Martin, A Muir, Z Vizvary
January 2010

1. Overview

1.1. Introduction

This report summarises the first year of results of analyses and literature reviews undertaken by a team new to fusion reactor studies, guided by existing Culham experts in DEMO and CTF studies via regular progress meetings. The principal aim of the study as a whole was to move towards quantifying the impact on the costs of DEMO if it were designed to operate as a pulsed tokamak, rather than steady state.

The team was developed to address a key selection of a range of pertinent issues previously identified by the experts, leaving several for assessment in future years if so desired. Appendix 9.1 shows a slide derived from one used at the study group kick-off meeting, listing the topical areas suggested by discussion between the lead author of the Milestone Report and the Culham experts, together with an indication of which ones we have been able to consider for this report. The number with crosses or delta signs represents an evident starting point for consideration of further work, but as will be seen, each of the main sections of this report notes outstanding issues for further work as well. Accordingly this Programme Area offers a considerable number of opportunities for the future and it will be up to management to prioritise these and determine the way forward.

1.2. Historical Studies

This summarises the key engineering and physics assumptions of a selection of papers from earlier years, going back to the mid-1980's. These assumptions divide naturally into premises that research in the intervening years has shown to be untenable, and others where the reviewer (who is not a reactor studies expert) is not aware of any technological or physics reason for their abandonment. These latter have therefore been classified as apparently having become "unfashionable", now requiring some kind of validity check for retention or rejection. Both types are brought out as bulleted lists at the end of the section, with far more of the type seeming to need reconsideration than those where relegation to obscurity appears to be well justified.

This section also suggests reviewing carefully the relative investment and payback finances for the pulsed versus the steady state machines, given the colossal power demand of the current drive system (which must lead to higher tokamak costs to generate compensating fusion power and/or greatly reduced electrical sales revenue). Finally there is of course an implied additional action for the future, namely checking back through the reference lists of the relevant recent literature to identify other significant articles from the past on pulsed fusion reactors.

1.3. The First Wall

Here finite element analyses of a representative model of a first wall element are summarised, both in the simplest possible individual model (a square U bar of rectangular cross-section incorporating two parallel channels for coolant flowing in opposite directions) and a monolithic stack of five of these, to check for any adverse trends as the mechanical stiffness is increased. The main aim was to determine how much thicker and heavier the first wall modules would have to be in order to achieve sufficiently low stresses for a pulsed version to survive the required number of cycles in the plant

lifetime. In the analyses carried out for this report, the wall material was EUROFER 97 (low activation steel) and the coolant was pressurised water at 10 MPa.

Literature searches turned up a variety of fatigue curves for EUROFER 97, permitting a trend curve to be inferred for the allowable strain which provides a suitable margin between the anticipated strain levels and those at which fatigue failure is probable. One of the references asserted that thermomechanical strain was about twice as damaging as simple mechanical strain (for reasons unclear), resulting in the more conservative approach of doubling the strain resulting from the analysis before considering the associated fatigue life. Wider coolant channels and thinner wall thickness between the coolant and the surface thermally loaded at a heat flux of 0.5 MW/m^2 (with and without bulk neutron heating at $25MW/m^3$) were considered as design variants intended to explore (reduce) the cyclic strain. Having checked that the temperature settling times were only around one minute at the beginning or end of the burn, pulses of 30 minutes duration were used in the analyses, typically revealing peak front surface temperatures ~350°C when starting from (and recovering to during the dwell) 200°C. These in turn created strain ranges in the order of 0.4%, largely unidirectional. However in the absence of fatigue data with a standing strain for this alloy, simply reading the projected life off the allowable strain curve results in the unacceptably small number of cycles to failure of ~500. Either of the two design modifications was found to reduce the strain to around 0.3%, at which the probable lifetime would be ~1200 cycles, much better but still way below the design target which is of the order of five thousand cycles as the blanket (First Wall) will be changed periodically. It is to be hoped that finding data or developing a model for the fatigue behaviour with finite standing strain will ameliorate this problem considerably.

1.4. The Divertor

The section on the divertor considers the three near-term concepts for the EU Power Plant Conceptual Studies (PPCS) programme, namely PPCS-A, -B, and –AB. Type A is water cooled and types B and AB are helium cooled. All the pertinent sub-assembly and materials development testing to date appears to have been aimed at establishing thermomechanical fatigue behaviour using pulsed heat fluxes intended to alternate quickly between the thermal equilibria with and without the heat flux applied. This is instructive for pulsed reactor design considerations but does not provide an experimental basis for evaluating the disbenefits of moving from a continuous to a pulsed reactor concept. Usually also the question of creep at sustained high temperature and stress is not addressed in such tests but one very relevant test series was identified which emphasises the very considerable loss of fatigue life when the stress hold-time is increased to merely around twenty minutes (remembering that we are looking for pulse lengths more like eight hours). Generally "creep fatigue" is worse than constant-stress creep or multi-cycle fatigue alone, so this detriment is certainly to be expected when moving from steady state to pulsed. However, given the apparent paucity of information on this subject for fusion materials, this section of the report is obliged to concentrate on a description of the principle blanket modules currently in mind in the EU for DEMO and necessarily has to leave the issue of the cost penalties of moving to a pulsed DEMO for future consideration.

The section begins with a reminder of Carnot efficiency, and hints at water as a preferred cooling medium since the pumping power becomes daunting for the gaseous coolants needed to operate at manageable pressures if temperatures above ~500°C are desired. (This section is concerned only with the divertor but the same could be said for the blanket, where the helium pumping power is variously estimated at ~130-400MW, to be compared with ~7MW for the water pumping of a 3.8GW PWR.) The thermodynamic efficiency becomes offset by the pumping losses and the fraction of the total fusion power exhausted to the divertor is unlikely to exceed ~15%, making any productive use of it debatable. It is also noted that there are significant materials selection issues if

coolant channels and associated heat transfer structures are to be made to run at temperatures much above this range. The PPCS-A divertor design variants restrict the coolant temperature to ~170°C if the CuCrZr coolant tubulation is used, interfaced to the W-monoblock tile with copper, rising to ~325°C if the tube is changed to EUROFER and the interface to Papyex (soft graphite). Even at the higher temperature, the Carnot efficiency of extracting the power to the divertor is only ~50% while at 170°C it would be nearer to 30%.

As described later in this section of the report, PPCS-AB and –B feature helium cooling, but with caveats noted about the pumping power (developed in detail in an appendix 9.3). Advanced reactor designs are described from other studies, extending the helium inlet temperature to 600°C at 10MPa, and the outlet towards 800°C, with a power flux capability ~10MW/m^2. Thus high thermodynamic efficiency of conversion of the heat output of the reactor is possible in principle but of course awaits demonstration of adequate operational life of the intended assemblies. The preferred design (HEMJ) comprises arrays of tungsten "thimbles" with the caps facing the plasma and the interiors cooled by an axially incident, radially exhausting jet of helium. Tests of prototypes with various surface finishes developed on the tungsten achieved up to ~1000 pulses at the required power flux (with an electron beam) which is promising but there is still some way to go before a workable solution can be claimed, especially for a pulsed reactor.

This section also reviews materials development, mentioning nano-structured ODS ferritic steels, and providing much interesting data on the effects of neutron irradiation on EUROFER, with and without ODS. These effects include hardening, raising of the ductile-brittle transition temperature and (arguably consistent with these two effects), reduction of fatigue life at large strains and increasing of it at low strains. Caveats regarding the need for further extensive materials and prototype assembly testing to determine the creep fatigue behaviour of tungsten, EUROFER etc with relevant heat fluxes, pulse lengths and levels of neutron radiation damage are emphasised.

The developmental concept for a "Super-eXpanded Divertor", a prototype of which is to be part of the MAST Upgrade is described. This offers the attraction of greatly reduced heat fluxes onto the divertor tiles but as described here, appears to be much better suited to spherical tokamak geometry than a tokamak with a conventional aspect ratio (as assumed here for DEMO), unless the advantages of a simpler divertor outweigh the penalties of a significantly enlarged vacuum vessel and toroidal field coil set.

Another awkward design performance compromise is to achieve an acceptably low front surface temperature (with a tile thick enough to tolerate the anticipated erosion between replacement intervals) without requiring undue pumping power to circulate the helium coolant, as reported from a different design study. Potential problems are noted with blocking of the fine coolant channels (~0.1-1mm) favoured for the helium coolant option (to improve its heat transfer coefficient), due to geometry changes or accumulating debris.

1.5. Coil Stresses and Fatigue

Section 4 describes progress towards achieving the not inconsiderable aim of up-dating the parts of the PROCESS code that deal with switching the design assumption from continuous to pulsed operation, in particular how the code makes allowance for the much greater number of stress cycles in the coils when "pulsed". In this initial approach, the toroidal field (TF) coil stresses alone (due to self-field and fields from the poloidal field (PF) coils, central solenoid (CS) and plasma) were considered and by reference to the ITER 98 design (ie "big ITER", which had similar parameters to a typical DEMO), a necessarily very simplified finite element (FE) model was developed to allow

basic trends to be elucidated. While the TF coil currents are expected to remain constant, the poloidal fields swing considerably, imposing out-of-plane forces on the TF superconductor and its support structure (here taken to be a double shell essentially between the TF coils and therefore outside the vacuum vessel). Large mid-plane apertures for ports for plasma heating systems etc were incorporated into the shell model, found to be important as local stress-raisers in some cases, eg the End-of-Burn situation.

Subtraction of the stress tensor components in different stages of the pulse cycle allows the alternating part of the overall stress to be deduced, which in principle can be combined with the mean stress to yield a fatigue life using one of the standard formalisms for such estimates such as Goodman or Walker. However a vital subsequent step is to parameterise fits to the FE stress results in terms of the coarse design parameters that PROCESS employs and this, with a methodology outlined in Section 4, will be a key part of the forthcoming work by the team in this area.

In order for PROCESS to estimate the fatigue life, pertinent material data is needed at the relevant temperatures, cryogenic in this case, and initial findings from other studies on a range of likely structural stainless steels are presented here. These include S-N curves for conventional fatigue life considerations, and some crack growth data which if developed would permit a more sophisticated assessment of predicted life. However, it is likely that more comprehensive data exists for crack growth measurements. Generic fatigue life curves can be calculated from the crack growth data if necessary for the intended ultimate application via some algorithm in PROCESS.

The appendix 9.4 for this section describes the present status of the stylised model, or actually "models", incorporated into PROCESS for various aspects of the TF coils. It seems that although they include reasonable details of the principal coil assemblies, these are not used consistently by the different sub-routines in the code. Accordingly future work will have to include ensuring that the code is internally consistent as well as introducing the new features accounting for fatigue in both the continuous and pulsed cases.

1.6. Fatigue of superconductors

This section considers the theme of fatigue in the superconductors themselves. Discussions early in the work for the milestone concerned the stress cycles necessarily arising in the sub-structure of the superconducting cable, where strands form electromagnetically loaded spans between contact points on their neighbours. Since the direction as well as the magnitude of the EM force changes, each span can both flex and move to change its contact points, introducing complex cyclic loads. The TARSIS facility does test strands, helping to address this issue. Test data so far, largely for ITER, is summarised and its limitations are noted, such as neglecting any deflection of the conductor support structure or testing isolated strands rather than complete cables. Whilst interesting, it reveals a considerable scatter in the response to cyclic loads of cables manufactured to the same specification, so that some degrade significantly in 1000-cycle tests of a given stress swing, and others hardly at all. Testing so far has not addressed the effect of tens of thousands of pulses creating cyclic out-of-plane stresses on the TF coil conductor, nor hold time at peak stress. Since the TF in a pulsed DEMO would be left on between maintenance interventions, say for several weeks, it has far less variation of stress than the central solenoid (CS), which of course has to experience two full bursting stress cycles per shot. The CS is therefore recognised as a more serious problem for fatigue life, but appropriate testing seems to be scant so far.

In the references considered, the degradation in superconducting performance of sample cables and test coils under electromagnetic loading is attributed to successive failure of the filaments of Nb_3Sn

within the strand, together with the known sensitivity of this superconducting material to imposed strain, here due to a combination of thermal ("wind and react"), mechanical and electromagnetic stresses. The last are tensile while the first are compressive, resulting in improvement rather than degradation at modest tensile strains. Any summary of the literature on this topic would have to conclude, "Further tests and modelling are required!"

1.7. Solenoid power supply costs

Here the question of the optimum dwell time between fusion power output pulses is addressed, simplified to just the time taken to ramp down the solenoid current from End-of-Burn to zero, and immediately to ramp it up in the opposite direction ready for current interruption to initiate the next plasma pulse. (This presumes that the plasma will be operated with only one direction of current, ie not "AC", for the reasons discussed in Section 1.) Clearly the rating of the solenoid supply rises as the dwell time decreases, while the capacity of the energy storage system falls, and *vice versa*, so that the sum of their costs has to display a minimum. A two-quadrant supply with a reversing switch was chosen rather than a four-quadrant one, since this is believed to minimise the costs.

The rating of the power supply is straightforward once the solenoid inductance and peak current (in each direction) is determined from PROCESS output, but the projected cost requires a scaling valid in the range of interest, around 100-1000MVA. Data was collected from Culham, Princeton, CERN, Cadarache and some web sites describing mains transmission links, and the result shows considerable scatter, beyond that accountable by technology trends, consideration of numbers of quadrants or possible inclusion of harmonic filters or reactive power compensation networks. This is attributed to varying market circumstances and is large enough to make any scaling more sophisticated than "about $100/kVA" essentially indefensible. The scaling for the energy storage cost is somewhat better known, and is taken from molten salt system case history, as $50/kWh.

The result of this analysis is that there is a shallow minimum in the sum of the costs of the solenoid power supply and the thermal energy store, at ~€(30 - 40)M for dwell times around 300 – 700s. Suggestions for further work include refining the dwell time model and seeking more and better data on power supply costs.

1.8. Thermal Energy Storage

The last section of this report considers present day options for energy storage, focussing on thermal energy storage and in particular the molten salt thermal energy storage systems now in good use in Spain as part of a concentrating solar power project (Andasol 1) aiming to provide power into the grid after sunset. ("Salt" here does not mean sodium chloride but more typically potassium-sodium nitrate-nitrite eutectic.)

The section opens with a summary of National Grid operating constraints and practices, eg supply demand or reduction driven by frequency drift, maximum controlled generation addition rate not to exceed 50-100MW/min (UK-EU) and the operational requirement to keep at least 1.32GW of reserve capacity available instantaneously by tolerating frequency fall (ie "spinning reserve"). (Total NG power demand is around 20 – 70GW with the worst peaks occurring in anticyclonic winter conditions, ie very cold frosty nights with little or no wind, aggravated at ~6pm by the effective coincidence of dinner cooking and lights-on timing.) This moves on to greater detail, with an emphasis on likely future trends (such as using electric car batteries as energy sources (!) to help the NG deal with short-term excess demands). It is noted that single power plants rated at over 1.32GW_e with no power output buffering capability would be an embarrassment to the NG because

sudden loss of one of them would exceed the Grid's capability to compensate automatically in the first few tens of seconds of the loss. However new nuclear plants are expected to be up to 1.6GW_e each and so this maximum single unit rating will probably be increased.

This leads naturally into the storage options, concentrating on the Andasol 1 experience. Key problems with molten salt systems include most of the loop freezing up if not kept moving or strongly trace heated, corrosion issues and various safety concerns regarding leaks. The operating temperature is ~500°C (swinging ~100°C or preferably ~30°C with the heat stored) and the thermal capacity of the eutectic named above is ~1.6J/g, about 37% of that of water, but of course circulated at essentially atmospheric pressure. Pressure drops could range over 1-10% of an equivalent helium heat transfer loop.

A sequence of spread-sheet calculations is developed, addressing the likely requirements for a thermal energy store for a pulsed DEMO, ranging from a load-following case which is particularly onerous, through to maximum tenable base-load generation (with and without 1GWe being provided to the grid in dwell periods). Presently these do not account for the benefit of the estimated ~100MW of decay heat from the blanket which would help with the dwell between fusion burns. All but the most severe set of assumptions lead to a requirement for no more than about 220,000t of salt costing about ~$140M, a very small fraction of the cost of the nuclear island. The difficult case of load-following, however, with its hypothetical requirement for the salt plant to maintain an output to the grid of a few hundred MW for nine hours overnight between high power fusion burns, leads to an unattractively large salt mass of 150,000t (or 450,000t with the more conservative temperature swing of ~30°C as used at Andasol 1). Salt storage favours short dwells and maximum reactor up-time. This also impacts favourably on the extra reactor margin required to cover the dwell time and re-energisation.

Finally some developmental concepts are also addressed, such as nickel-doped magnesium hydride thermal energy storage, capable of storing ~0.9kWh/kg of magnesium, and (in appendix 9.6) FLiBe as a combination coolant medium and tritium breeding material for the blanket is also considered.

1.9. Summary

In conclusion, it can be seen that a wide range of pertinent aspects have been addressed in this study regarding the question, "Should DEMO be pulsed or steady-state?", even if they do not fully coincide with the set of topics suggested in the kick-off meeting for the work early in 2009. A considerable number of open issues have been identified and in some areas (such as refining the power supply cost scaling or modifying PROCESS to account semi-realistically for fatigue), the status is clearly that of a work in progress. Thus there is plenty of scope for continuing this activity beyond the remit of this milestone.

2. Historical Studies

2.1. Introduction

It has long been recognised that tokamaks are, in their original and simplest manifestation, pulsed, driven by an Ohmic heating solenoid which produces and sustains the plasma current. Early in the 1980's, the Okhawa current, driven by circulating fast ions from tangential neutral beam injection (with a partially compensating back-electron current created by the fast ion drag) was recognised as having the potential to sustain the plasma current non-inductively. This provided an option to make a tokamak steady-state, much like stellarators have always been intrinsically, with the resultant attractions of much reduced cyclic fatigue and no requirement for the mains grid or a local energy storage system to cover the dwell time between fusion power "burns". Also through the 1980's, lower hybrid wave current drive and Fisch-Boozer electron cyclotron wave current drive experiments, together with a growing recognition of the theory of bootstrap current (driven by neoclassical particle loss in the presence of a radial plasma pressure gradient) consolidated an emphasis on steady-state tokamak reactors, but there have always been two widely recognised caveats: the power and cost of the non-inductive current drive system. Thus from time to time pulsed tokamak reactors have been reconsidered, in most cases with each study suggesting one or more novel features aimed at reducing the problems of fatigue and energy storage.

A brief review has been undertaken of a selection of reports summarising tokamak fusion reactor studies where the pulsed option was either the only one considered, or was compared in some detail with steady-state equivalents (such as key engineering parameters and projected costs for a comparable net electrical power fed into the grid). These reports span the period encompassing the early concepts of the 1980's through to the very recent developments of 2009, during which time experimental work and the theory of both tokamak plasmas and materials envisaged for the plasma-facing components and structural assemblies of nuclear fusion reactors have advanced considerably [1 – 12].

So what has changed, and what has remained the same? Quite strikingly, all the reports reviewed have $R \approx 8$m, $a \approx 2$m $\kappa \approx 1.7$, $B_{\emptyset o} \approx 6$T, $I_p \approx 14$MA, $\Delta\emptyset \approx 500$Wb and $P_f \approx 3$GW (with ≈ 2MW/m^2 wall loading). But there have certainly been changes in basic thinking, as will be seen below.

2.2. The Eighties

In the earliest study considered, by Ehst et al in 1984, there was no concept of any divertor, only some kind of limiter, presumably toroidal, although the plasma facing assemblies and the materials in mind for it were much like those of the present day divertor concepts for reactors. ECRH was accepted as an option for plasma heating (and perhaps current drive) but the efficiency was expected to be only ≈20% since depressed–collector gyrotrons (which now achieve $\geq$50%) had not been proven. It seems that neutral beam heating (and current drive, already demonstrated by then) was not considered but the reasons for this were not given. The problems of energy storage during the dwell period, mechanical fatigue due to the cyclic electromagnetic forces and "thermal fatigue" due to the cyclic heat loads and temperature cycling of the limiter first wall, coolant systems and heat exchangers etc were well recognised. At that time in the USA, at least, VCrTi alloy was preferred over SS 316, because of its much greater radiation damage resistance.

One novel feature, although not unique to this study, was the option of maintaining the full plasma current at much reduced density for some minutes, to permit a non-inductive current drive system (such as lower hybrid waves) to "over-drive" the current and thus recharge the solenoid. This was demonstrated many years later in tokamaks combining bootstrap, neutral beam and lower hybrid current drive, but it is disfavoured today because of poor efficiency. Either a very low reverse loop voltage is achieved and the solenoid recharge time is unacceptably long, or the loop voltage is higher but then the "adverse synergy" of the reversed electric field makes it extremely difficult for the plasma current to be sustained. Needless to say, all the while the density is low, so is the fusion output power (essentially negligible) and the plasma pressure, and hence also the equilibrium vertical field. Thus even if the very high current drive power was acceptable, electromechanical and thermomechanical cycling effects would still be very strong and this concept, called the "internal transformer", has probably rightly been abandoned.

Ehst *et al* noted that the availability of superconducting magnets with peak fields $\geq$12T was uncertain and considered that the brittleness of Nb_3Sn made it unsuitable for pulsed applications. This led them to choose NbTi coils, running at 1.8K, rather demanding for the cryoplant. Clearly there has been much progress in this field and Nb_3Sn designs for the ITER toroidal field coils and central solenoid, with no layering, are now expected to achieve peak fields of 12–13T and a reasonable tolerance of pulsed operation. The cyclic out-of-plane forces on the TF coils due to the vertical field tracking the plasma current were recognised as a fatigue issue, loading parts of the vacuum vessel which was intended to double as the TF coil support structure. The cyclic bursting stress in the OH solenoid was to be carried by steel bands integrated into it. Somewhat oversimplified expressions were used for plasma resistivity (neglecting collisionality–dependent trapping) and beta scaling ("$\beta \leq 0.24A$", presumably a β_p scaling, since a more modern equivalent might be $\beta_t = 4l_iI/aB$ (%, MA, m T) or $\beta_t \approx 24l_i\varepsilon\kappa/q$ %, equivalent to $\beta_p \approx 0.24l_i\kappa qA$ (scalar fraction)).

Flywheel energy storage was assumed for the rather short dwell times intended (of only 100 – 200 secs), to run down the OH solenoid and vertical field coils and then recharge them appropriately for the next pulse. A cost-saving trick was to use the vertical field supply to charge the solenoid and an opening switch and commutation resistor to discharge it, leaving only the modest voltage and power of the flat-top sustainment to be met by the OH supply. A feature of this design, in common with some tokamaks constructed in that period, was to arrange the PF coil set to decouple the solenoid and vertical field windings (as in CLEO, Compass etc), which has not been considered necessary in more recent designs. Thermal energy storage was discussed, including the option of allowing high temperature pressurised water to flash into high pressure steam, a scheme capable of very rapid energy release to the turbines.

2.3. The Nineties

Next is a jump forward to 1992, the Electrowatt study, which is very heavily biased towards issues of steam plant, a topic the authors clearly understood in exhaustive detail! It also evidences an excellent knowledge of the operational characteristics (and constraints) of the National Grid, which apart from a modest rise in generating plant capability appear to have changed remarkably little since then. It is, however, totally lacking any discussion of tokamak physics or engineering and oddly, cyclic thermomechanical stresses were dismissed by asserting a uniform (gradient-free) blanket temperature. Options of decreasing and increasing the helium gas flow during the $\leq$300secs dwell period were both analysed, respectively aiming to maintain the exit temperature (with a low power transfer) and a near constant power transfer (with falling temperature). A key aim was to keep the generators connected to the grid, which apparently requires $\geq$5% of the notional maximum steam power to be available throughout the dwell. However, any strong variation of the power fed

to the grid was strongly decried "because the owners of all the other generating plant connected to the grid will see their plant lifetimes reduced by accommodating cyclic loads". This issue was not mentioned to us in our visit to National Grid last year; indeed the flexibility of the overall system was repeatedly emphasised. However the retired Didcot A Station Manager has remarked to one of the authors of this milestone report, "Cyclic duties do age a plant; they were never built for that: we had to put in thicker boiler tubes at Didcot" so the issue should be borne in mind.

Methods of sustaining the full power output to the grid during the dwell were explored by Electrowatt, unsurprisingly including large steam drums but very surprisingly recommending the inclusion of a full power gas turbine to take over the load in these intervals. In an appendix, they show that even buying the gas at the high rate of 20p/therm, the annual costs of doing so were closely balanced by the revenue achieved from the electricity thus produced; so with a more favourable gas supply contract, the reactor operators might see little benefit from ever turning the fusion reactor on! Another energy storage scheme recommended for further study was liquid metals, using their heat capacity (not the latent heat of any state or phase change). The pumping power required for the helium coolant was estimated to be ≈133MW and decay heat during the dwell was expected to be ≈124MW.

Moving on a few years, we encounter summaries in the mid-1990's of the extensive studies undertaken in the USA on the ARIES and PULSAR tokamak reactor concepts, which are thoroughly based on conventional fusion thinking of the time. "Availability, Reliability and Maintainability" were rightly recognised as necessary considerations in reactor design, especially pulsed reactors, even at this early stage in fusion reactor thinking. The discipline of ARM in design evolution is a long-standing key facet of nuclear engineering and not simply an *aide memoire* when writing articles, and indeed these summaries reveal significant consideration of these aspects. Cyclic fatigue in the TF coil support structure was said to reduce the peak field capability from 16T in a steady-state plant to 13T in the pulsed version (except for a version with an unattractively low superconductor current density), offsetting a putative gain in β_t associated with higher plasma density. A valid point rarely noted elsewhere is that when all the current sustainment is by an OH transformer, and the plasma is ignited or at least strongly dominated by alpha particle heating, neither the current nor pressure profiles can be tailored to optimise the β limit (eg to access the "Second Stability Region" of high β_t). The "Second Stability Region" has never been achieved in any long-pulse tokamak experiment, and at best only questionably in fast-pulse machines with very effective wall stabilisation, since it creates very large edge gradients of plasma pressure etc and destabilises various modes while (according to theory) stabilising ballooning modes (by creating an average magnetic well). Accordingly it is rarely mentioned today, giving way to the alternative generic mode stabilisation feature of reversed [field line pitch] shear which is seen to produce an Internal Transport Barrier. However the lack of profile control in an OH-driven, very high Q reactor could be extended in today's context to not being able to achieve sawtooth control, or sustained "internal transport barriers", popular if high confinement time factors (on the usual scaling law) are considered necessary to achieve ignition.

It was deemed vital to avoid thermal cycling in the whole heat transport system, leading the PULSAR designers to include "an innovative sensible heat storage system in the outer shield" – "sensible" here means capable of being sensed, ie specific heat, not latent heat of any kind. It was said to be capable of supporting the full thermal output power of the reactor for at least the first ≈200 seconds of the dwell period. Another somewhat novel aim was to seek a design that could run efficiently at half power, by way of load-following. This is admirable in some respects but unusual in that generally the investment costs of the plant have to be recovered by electricity sales as speedily as possible.

Silicon carbide begins to make an appearance as a blanket structure material, with helium cooling, while for the liquid metal (Li) cooled blanket option, titanium nitride coated vanadium alloy was suggested to insulate the walls of the coolant tubing, in order to reduce electromagnetic eddy current induction and associated pumping losses.

As now, a neutron multiplier (here beryllium) was considered essential in the tritium breeding blanket, also contributing usefully to the total power output.

Bootstrap currents were well recognised by this time, with typical fractions around 40% of Ip. Typically the L-mode ITER 89P confinement time scaling was used, but with high multiplying "H Factors" ≈2.5 (with no physics justification or rationale given in these summary papers). Positive attributes included the use of a fixed boundary equilibrium solver to generate consistency between the desired plasma parameters and all the coil currents, and a good account of TF ripple effects (albeit neglecting the now common idea of ferritic inserts which it was said for ITER can "save two TF coils"). However an inelegant feature was to dismiss all considerations of the divertor design, heat load problems, fatigue etc, leaving them for others to address.

Figure 1 of the Bathke reference is reproduced here, giving a clear breakdown of the projected costs of PULSAR in comparison with ARIES steady-state reactor options with similar degrees of optimism in physics and engineering. This shows that the pulsed reactor was about 25% more expensive than the steady-state equivalent, considering the tokamak load assembly, power supplies and in-shield energy store alone. (It should be recalled that these comprise only about half of the total cost of a reactor site, the cost of the other half being little affected by the choice of pulsed or steady-state.)

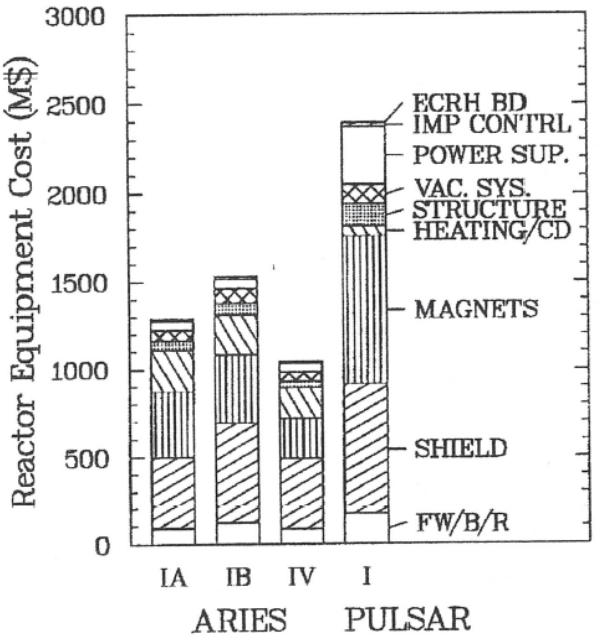

Figure 1. Reactor Equipment (RE) cost (*i.e.*, just the tokamak) for the 1-GWe PULSAR-I, updated ARIES-IA and -IB, and ARIES-IV tokamak power plants.

Moving up to 16T peak toroidal field with a low current density Nb_3Sn winding, they claimed that a 21T peak field capability could be realised in a ternary (eg NbSnTa or $(NbTa)_3Sn$) alloy "for only about 10% more cost". This may have referred only to the field and current density achievable simultaneously, since coil stresses were not mentioned. The mainstream design however was the usual ≈12T peak, with 6.7T at the nominal major radius of 9.2m (this radius being a little larger than usual in such studies).

These papers include costs comparisons with coal and fission stations, but there was then no issue of a "carbon tax" or carbon sequestration, nor were the full long-term costs of fission radwaste disposals being realistically accounted for. The papers by Wang et al, also from the mid-1990's, incorporate much the same basic engineering parameters but a few interesting differences in approach. These include a much higher bootstrap fraction (≈75%), lower hybrid current drive to

assist plasma current ramp-up and (in one of them) use of JET L-mode transport scaling (including an inward pinch velocity) to infer energy confinement time – albeit then given an H factor of up to 3.3 to permit an overnight load-following scenario with output power reduced from $2.7GW_{th}$ in the day to only $1.5GW_{th}$. The high bootstrap fraction was the result of assuming an Advanced Tokamak q profile, with $q_o \approx 2.3$, $q_{min} \approx 1.3$ and $q_a \approx 4.5$: the authors noted that this may be unstable to low-mode-number modes (such as the 3,2 or possibly the 2,1).

Somewhat curiously, the OH power supply considerations invoked no novelties to reduce the rating, asserting that 1.4GVA was necessary – but close inspection of the waveforms reveals this to be the instantaneous negative-quadrant reactive power associated with the rapid ramp-down of the precharge current to initiate the plasma, which others achieve with an opening switch and commutation resistor. There is much evidence of conventional tokamak thinking of the era, such as concerns over the achievement of an adequately small "$t_{He}*/t_E$" to assure helium exhaust, minimal helium density profile peaking, and worries over density–limit disruptions occurring in the plasma ramp-down phase when the fusion (and OH) power reduces but the density is still very high. This latter is a real problem in today's tokamaks as the auxiliary heating power turns off, but can be dealt with by suitable control of the density decay, if the torus pumping speed is high enough to facilitate that.

AC plasma current operation was seriously proposed, which usually today is disfavoured, because difficulties in aligning divertor and antenna protection tiles are most easily overcome by "ski-ramping" the adjacent tiles to suit the preferred direction of the scrape-off layer power flux, which is sensitive to the plasma current direction. Also of course if neutral beam heating is intended, the beams are all or mostly arranged to co-inject, dictating the plasma current direction.

Ripple losses were well addressed, again without mentioning the option of ferritic inserts under the TF coil limbs to reduce the ripple. The design had ripple ≈1.5%, and a scaling for the ripple losses was given ($P_{loss} \propto \delta_{ripple} (R/a)^2$) but this led to an unfulfilled need for the ripple to be $\leq$0.5%.

One of Wang's designs has a flux swing of almost 2000Wb(!), with a 10m major radius. Also very unusually, a monolithic solenoid was chosen instead of a stack of pancakes, which would sacrifice significant aspects of plasma shaping control throughout the flux-swing.

2.4. The Noughties

Moving forward to very recent years, Maisonnier's paper of 2008 would seem to typify current thinking, referencing the EU Power Plant Conceptual Studies and the use of the PROCESS code.

Most of this paper is focused upon the preferred steady-state option but the pulsed variant is also considered, requiring a rise in R_o from 7.5 – 10m for the same net output power to the grid of $1GW_e$. A much larger power than noted in the previous studies was assigned to the pumping of the helium coolant assumed for some of the PPCS designs, ≈400MW (essentially independent of the pulsed versus steady-state selection, of course). Curiously there is an assertion that the effects of cyclic operation were not assessed for that report and yet a pulsed DEMO was confidently stated by Maisonnier to be significantly more reliable than a steady-state one. This might be because of the anticipated unreliability of ultra-long-pulse plasma heating and current drive systems (extrapolated from present-day tokamak operational experience), compared to the relatively simple engineering of a high-flux solenoid.

The final paper selected for review is only a few months old and is by Pamela *et al*. This refers to the earlier finding that the capital cost of the tokamak is about the same as the sum of the balance of

plant and all the buildings. 50% thermodynamic efficiency in generating the electrical power was assumed, with an energy multiplication factor of 1.18 in the blanket. The Greenwald scaling was adopted for the projected average plasma density, which is likely to be conservative in an ignited or very high Q machine, since it was largely derived from tokamaks with relatively modest ratios of total plasma heating power to Ohmic heating power.

The importance of ARM design methodology was emphasised, and the extremely high proportion of the electrical output that had to be committed to the helium pumping (≈200MW), the current drive system (≥300MW_e) and the balance of plant was bemoaned: about a third, depending on the overall current drive efficiency used. Pamela does not comment on the impact on the economics of such a large fraction of the generated electrical output being consumed in recycling on site, but it is a necessary part of the overall equation in balancing the finances of a pulsed machine against that of a continuous one.

Pamela's report was essentially only about steady-state tokamak reactors. It does however include an interesting section on 21st century materials development, such as "nanostructured oxide dispersion strengthened ferritic steels", said to be good for sustained operation at 750°C without undue creep.

2.5. Review Summary

It is evident that from the beginning of the development of tokamaks, almost from their inception in the early 1970's, the fundamental balance of plant costs and operational risk in considering reactors to be either pulsed or steady state had been recognised. Pulsed machines were closer to operational experience but required large energy storage to cope with the burn dwell, and large Ohmic heating power supplies, while continuous output versions needed very large recycled electrical power for the (then largely unproven) non-inductive current drive systems. By the mid-1980's, non-inductive current drive had been convincingly demonstrated with neutral beams, lower hybrid and electron cyclotron waves, but the overall efficiency from mains plug to mega-amps in the plasma was discouragingly poor. Understanding of the pressure driven "bootstrap current" was gained during this period but even in the following decade, although the power conversion efficiency of the various types of plasma heating system improved significantly, the efficiency of plasma current drive at the plasma densities necessary in reactors remained disappointing. Unfortunately, theory can now explain this in detail for each type of current drive and suggests little prospect of a radical shift in the right direction, so even authoritative papers on DEMO from less than a year ago talk of about one third or more of the generated electrical power having to be recycled.

It is interesting to note which of the premises of these older studies, many reflecting the experimental emphases of the times, have now been dropped as the level of understanding of tokamak physics has improved, appropriate materials tests have been made, and technological developments have moved forward. This is a fairly short list and could be summarised as follows:

- limiters giving way to divertors
- the "internal transformer" or solenoid recharge by over-driven plasma current
- superseded forms of beta-limit scaling
- poloidal field coil sets arranged to decouple the principle functions
- inclusion of a 1GWe gas-fired generator to level the dwell
- plasma "Second Stability Region"
- AC plasma current
- monolithic solenoid

No further action would appear to be warranted to consider any of these in greater detail. Many, however, seem merely to have become "unfashionable" and it would seem prudent (as part of future work in this area) to check the reasons for their demise. These would include:

- VCrTi alloy being preferred over SS 316
- use of the vacuum vessel as the toroidal field coil support structure
- incorporation of steel bands into the solenoid layers to strengthen it
- use of the vertical field supply to charge the solenoid
- pressurised high-temperature water made to flash into steam for rapid energy release
- varying the coolant flow to try to level the thermal output power across dwell periods
- the extent to which other electricity generating suppliers care about cyclic grid loads
- using the specific heat capacity of a liquid metal as a thermal energy store
- Availability, Reliability and Maintainability from the earliest design considerations
- difficulty in controlling the plasma pressure and current profile shapes at very high Q
- use of the neutron shield as an energy store, via decay heat and coolant flow tailoring
- a significant degree of load following while remaining at high overall efficiency
- titanium nitride as an insulating layer to reduce MHD drag in liquid metal coolant
- inclusion of a consistent free-boundary equilibrium solver in PROCESS
- ferritic inserts to reduce the toroidal field ripple (ie. to enlarge the radial ports)
- layering of the superconductor current density for higher maximum field strength
- choice of plasma regime (Advanced, L-Mode, H-Mode, ITB, ELMy, sawteeth…)
- constraints on "t_{He}*/t_E" and their experimental validation eg in JET
- helium density profile peaking extinguishing the core
- density–limit disruptions occurring in the plasma ramp-down phase
- relative overall reliability of pulsed and steady-state reactors
- punitively large pumping power for helium coolant
- blanket energy multiplication factor
- thermodynamic energy conversion efficiency
- validity of Greenwald scaling in a very high Q plasma
- nanostructured oxide dispersion strengthened ferritic steels and similar developments

Although the fusion reactor experts in CCFE are probably able to dismiss many of these for very sound reasons, it would seem likely that several of them will survive the cull and may therefore provide a focus for some of our further work in this area.

2.6. References

[2.1] D.A. Ehst et al, A Comparison of Pulsed and Steady State Tokamak Reactor Burn Cycles. Part II: Magnet Fatigue, Power Supplies and Cost Analysis, Nuclear Engineering and Design/Fusion 2 (1985) 319-336

[2.2] F.Najmabadi et al, Assessment of Tokamak Plasma Operation Modes as Fusion Power Plants: The Starlite Study, Department of Electrical and Computer Engineering and Fusion Energy Research Program, University of California, San Diego, 16th IAEA Fusion Energy Conference, Montreal, Canada, October 7-11, 1996

[2.3] C.G.Bathke et al, A Comparison of Steady-State and Pulsed Tokamak Power Plants, Los Alamos National Laboratory, PO Box 1663, Los Alamos, NM 87545, USA, SOFT 1994

[2.4] F.Najmabadi et al, Overview of the Pulsar Study: A Pulsed Tokamak Fusion Power Plant, US-Japan Workshop on Power Reactor Studies (Q185), March 14-17, 1994

[2.5] F.Najmabadi et al, Comparison of Steady-State and Pulsed-Plasma Tokamak Power Plants, IEA Workshop on Technological Aspects of Steady State Devices Max-Planck-Institut Fur PlasmaPhysik Garching, Germany, February 20-23, 1995

[2.6] Y.Ogawa et al, Advanced Design of a Pulsed Tokamak Fusion Reactor, Faculty of Engineering, University of Tokyo, Bunkyo-ku, Tokyo, 1994

[2.7] J.D.Galambos et al, Commercial Tokamak Reactor Potential with Advanced Tokamak Operation, Nuclear Fusion, Vol 35, No 5, 1995

[2.8] J.Pamela et al, Efficiency and Availability Driven R&D Issues for DEMO, Fusion Engineering and Design, 2009

[2.9] D.Maisonnier, European DEMO Design and Maintenance Strategy, Fusion Engineering and Design 83, 2008, 858-864

[2.10] J.F.Wang et al, Conceptual Design of a Poloidal Field Coil System and Operation Scenario for an Inductively Operated Day-Long Pulsed Tokamak Reactor, Fusion Engineering and Design 29, 1995, 69-77

[2.11] Electrowatt, Pulsed Fusion Reactor Study, AEA Fusion, Culham Laboratory, Abingdon, Oxfordshire, OX13 3DB, September 1992

3. The Effect of Pulsing on DEMO First Wall

3.1. Introduction

The effect of pulsing on the first wall of a future fusion power plant is manifested mainly as thermal fatigue of the structure. Due to the pulsing mode the temperature cycles result in varying stress in the first wall which is lifetime limiting as opposed to a steady-state mode where the number of heat-up – cool-down cycles is negligible in comparison with that of the pulsed mode.

There are papers considering dynamic effects of first wall designs (not restricted to DEMO) [3.1], on the other hand recent DEMO first wall related papers [3.2], [3.3] seem to consider steady-state operation mode only.

In order to estimate the range of stresses and the expected lifetime, a series of analyses have been carried out on a "generic" DEMO outboard first wall. The model of this generic first wall is based on [3.4].

3.2. FE Model

The FE model is a section of the outboard first wall; the dimensions are based upon the above mentioned paper [3.4], and it contains two cooling channels (Fig. 3.1-3.2) in order to take into account cross-flow. In this study the coolant is pressurised water (10 MPa); in the future helium coolant will be considered as well. The wall material is EUROFER 97 (low activation steel).

The modelling has been carried out using ANSYS Workbench 12, the fluid flow was modelled using the CFX module, and the results of this analysis were used in the subsequent transient thermal and structural analyses. The workflow in the ANSYS Workbench can be seen on Fig. 3.3.

The figure shows the link between the different analyses. The wall heat transfer coefficients are imported into the transient thermal analysis from the CFX results. The body temperature data is imported into the transient structural analysis from this transient thermal analysis results. Constant pressure is applied on the channel walls instead of importing it from the CFX results in order to speed up the process, also to avoid errors by offsetting these results (the reference pressure is 10 MPa in CFX which is not included in the imported results).

The basic geometry and material properties are shared among all the analyses.

The lifetime of the first wall can vary depending on the geometric features: three models with different geometry have been analysed and these will be referred as "original", "modified model 1" and "modified model 2".

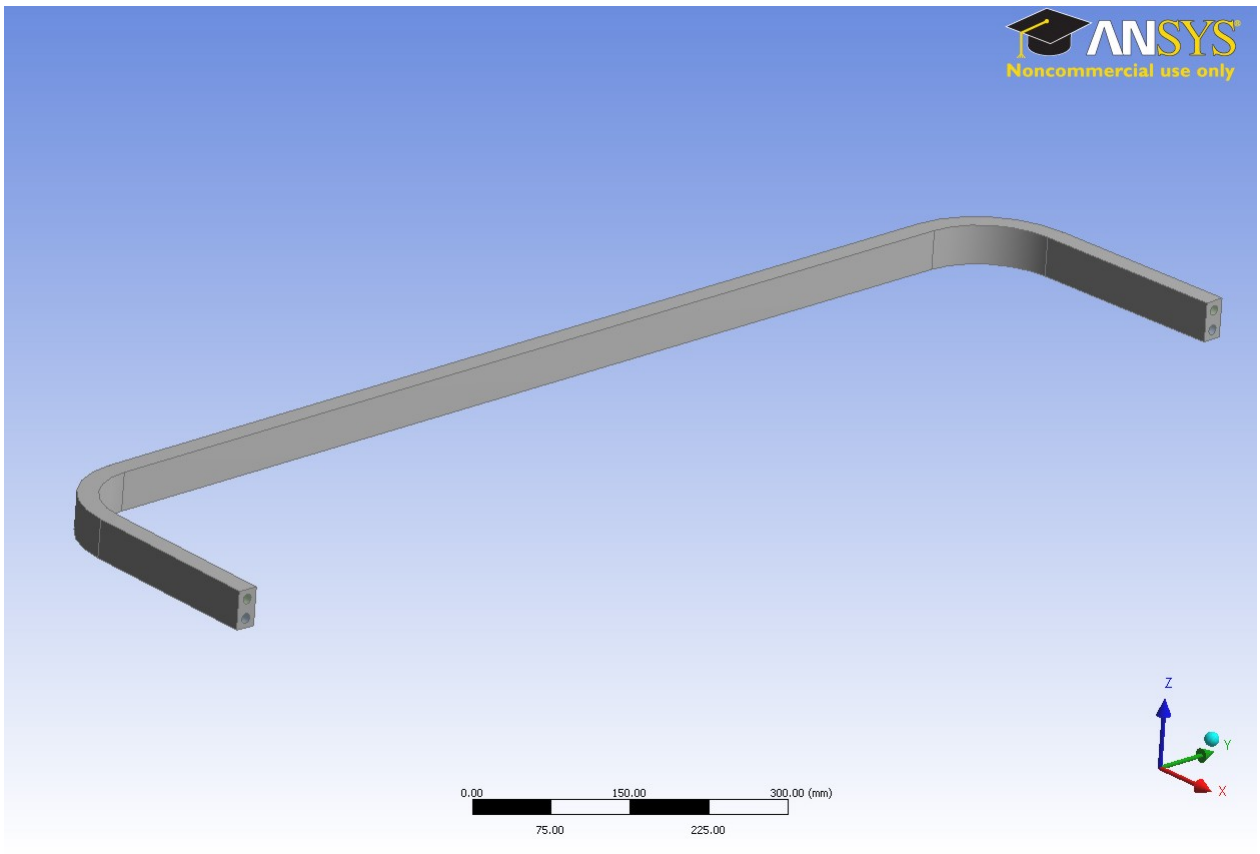

Fig. 3.1: Model for the first wall segment.

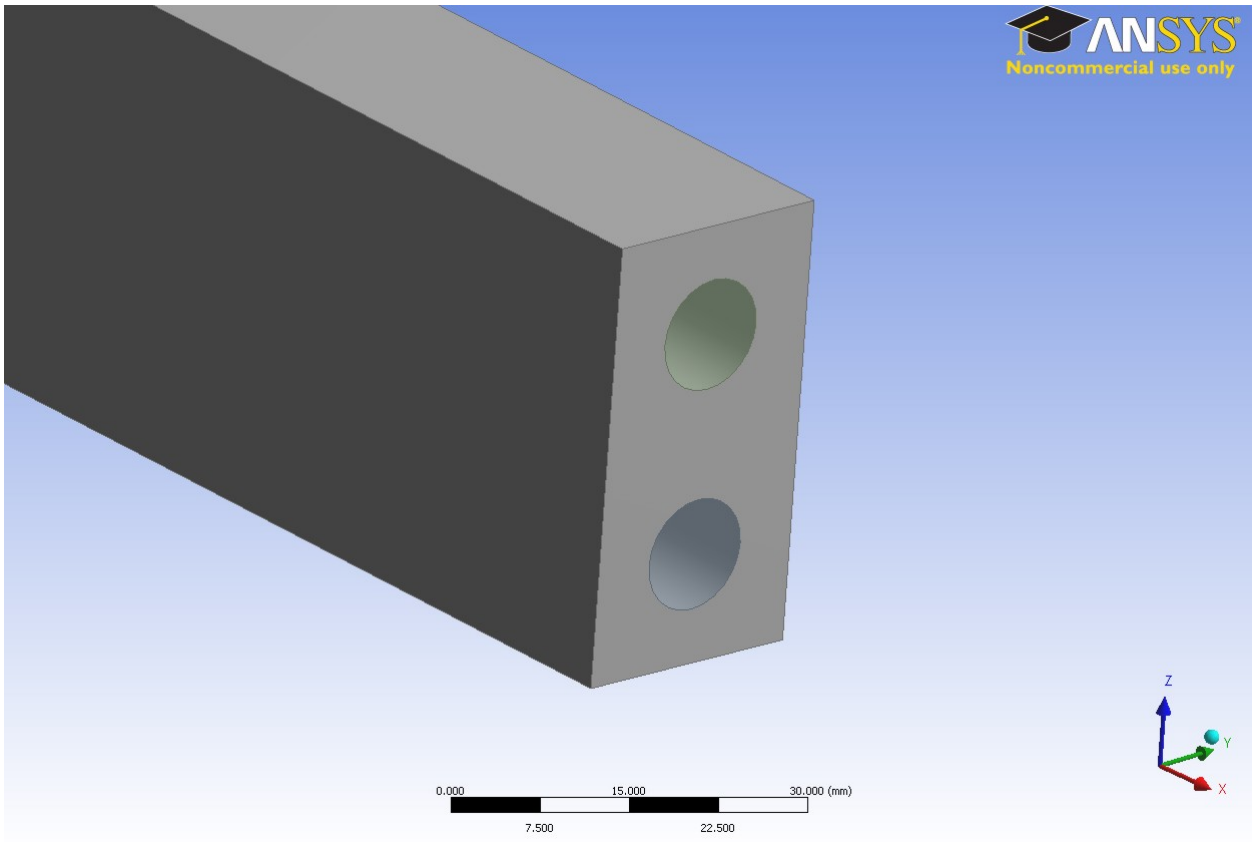

Fig. 3.2: Close view of the cooling channels.

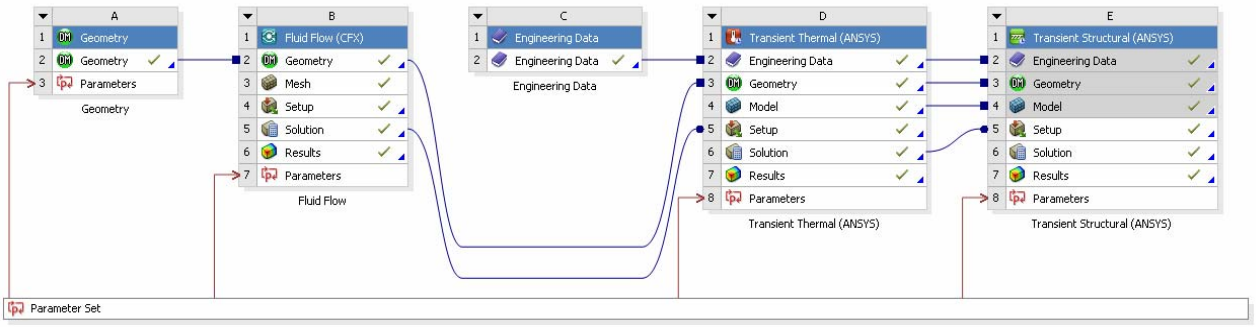

Fig. 3.3: ANSYS Workbench project overview.

3.3. Material properties

The detailed properties of Eurofer 97 and pressurised water can be found in the Appendix 9.2. In order to conclude the fatigue analysis, fatigue curve(s) (S-N curves) are required. The available data regarding the fatigue curve or design curve in the literature is somewhat limited. Fig. 3.4 shows the fatigue curves from three references ([3.5], [3.6], [3.7]) summarised in one graph (the irradiated data is fission data).

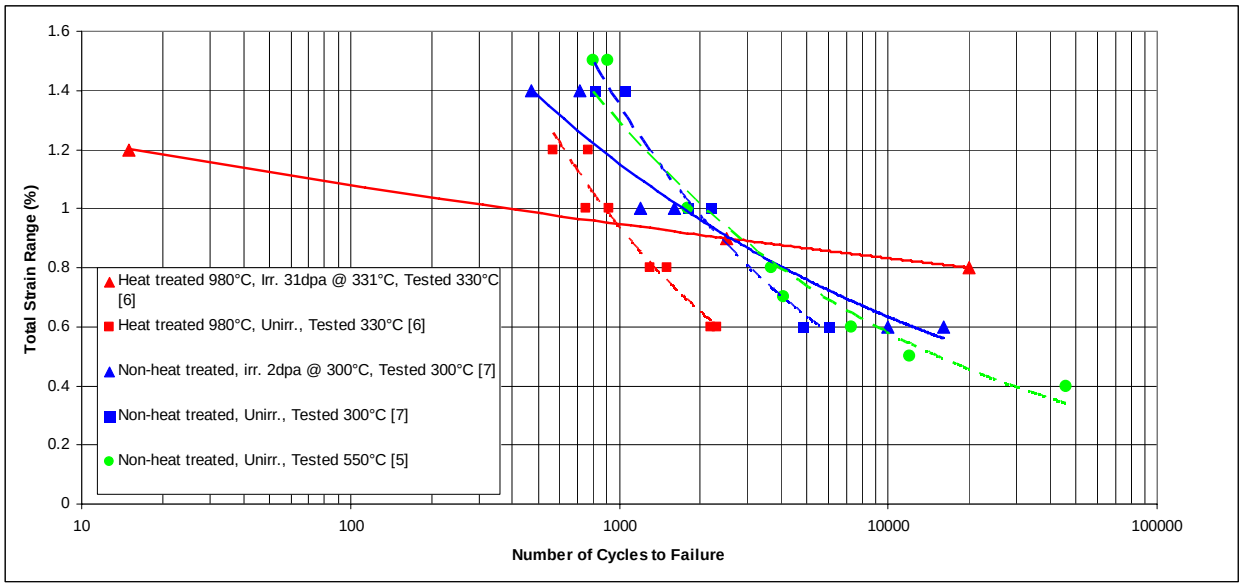

Fig. 3.4: Experimental fatigue curves

The curves for unirradiated Eurofer 97 at 300 °C and 550 °C would seem to be the best choice for the current analysis. In order to obtain a design curve from these data, a factor of 2 has to be applied on the strain range or a factor of 20 on the number of cycles, whichever is the more conservative. This method is usually recommended by different codes in order to allow for effects not included in the measurements [3.8], [3.9].

Trend lines have been fitted using Microsoft Excel and the equations of these trend lines have been used to derive the design curves for unirradiated material at 300 °C and 550 °C (fig. 3.5).

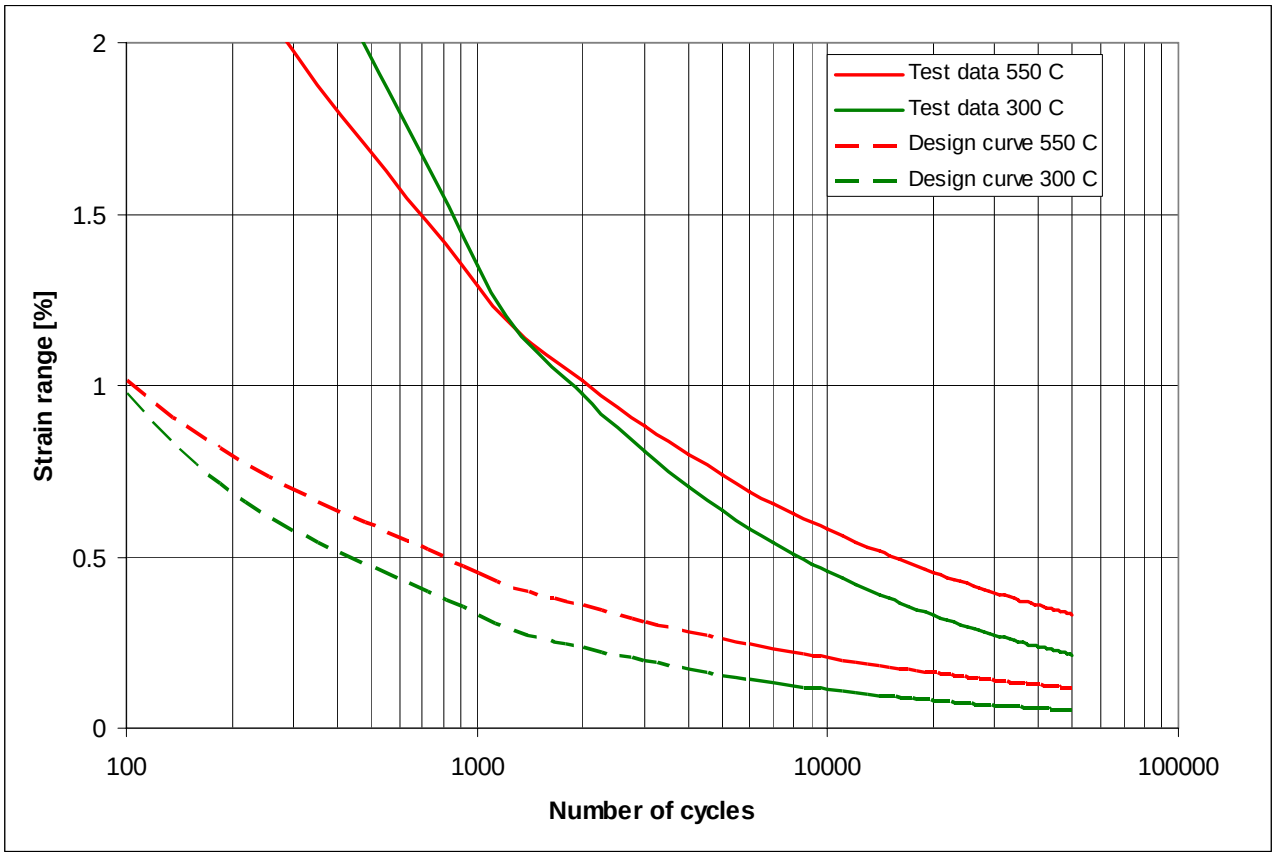

Fig. 3.5: Derived design curves for Eurofer 97

The results will show that the peak temperature in all of the cases falls between 300 °C and 400 °C. For this reason and because it is more conservative, the design curve for 300 °C will be used.

3.4. Analysis

It is assumed that the channels in the wall are 10 mm diameter and their centres are 20 mm from each other in the case of the "original" geometry. The lifetime of the first wall could be extended if the alternating stress and strain is smaller. In order to decrease the alternating stress and strain, the cooling effect can be increased. The first modified model shown on fig. 3.6 has 15 mm diameter channels and more importantly the minimum distance from the front surface is only 3.5 mm.
The second modified model (fig. 3.7) has 10 mm diameter channels as in the original model but the wall itself is thinner, its thickness being only 17 mm instead of the initial 21 mm, and so the distance from the front surface is only 3.5 mm as in the first modification. Fig. 3.8 shows the modifications superimposed on the original design.

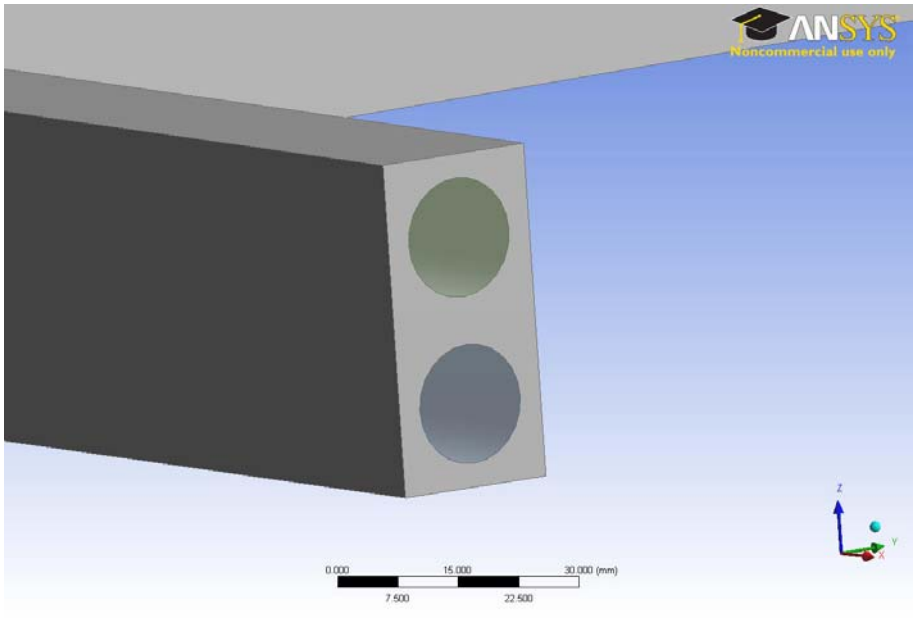

Fig. 3.6: Channel diameter increased to 15 mm.

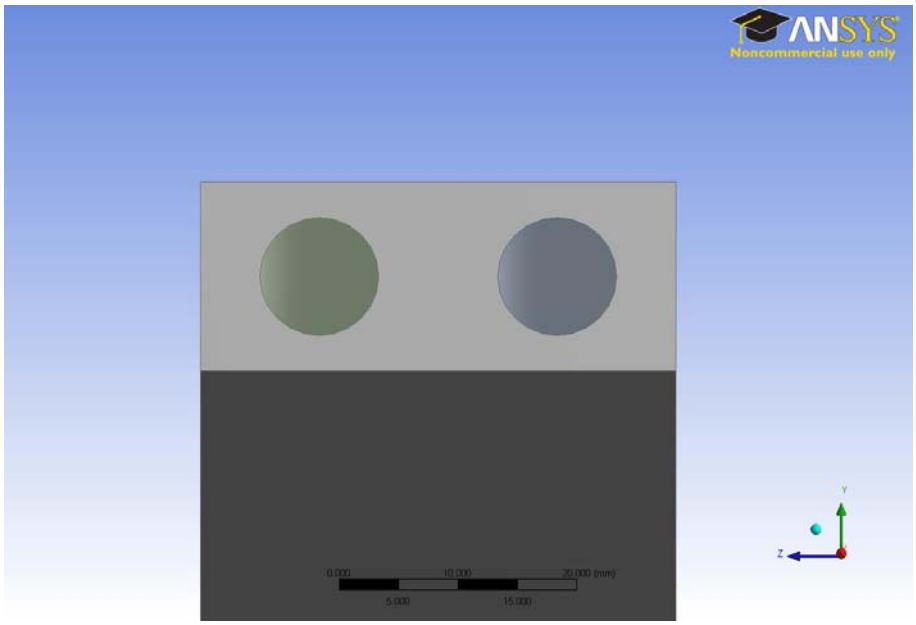

Fig. 3.7: Channel diameter 10 mm.

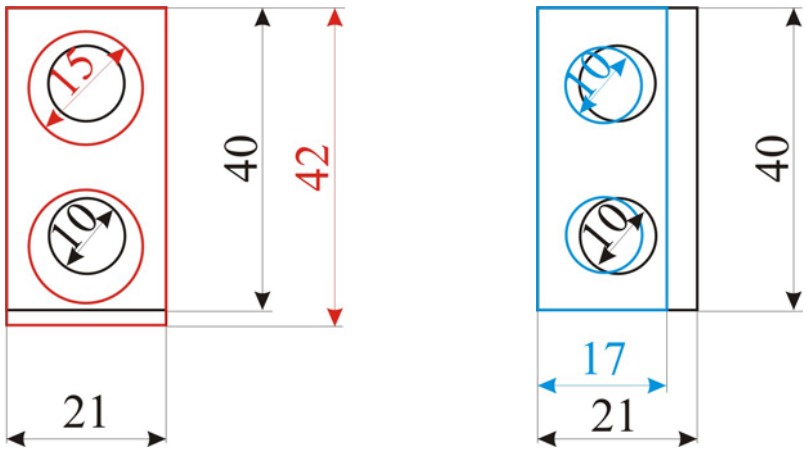

Fig. 3.8: The original geometry overlapped by the modifications.

The fluid flow was modelled using the CFX module of ANSYS 12. The coolant enters the channels with 10 m/s velocity. The aim of the fluid flow calculations is to extract the wall heat transfer coefficients from the simulations. The coolant velocity is the same in all cases, as it has little effect on the surface temperature of the wall. The wall heat transfer coefficients can be imported into the transient thermal analysis in order to calculate the maximum and minimum temperatures in a cycle which drives the maximum and minimum stress and strain in the wall.

Further assumptions are that one cycle lasts 8 hours and the front face of the wall sees a heat flux of 0.5 MW/m^2. No other heat sinks are present apart from the water cooling.

Once these results were evaluated, changes were made in order to find out to what extent the fatigue life can be improved by changing some parameters. Neutron heating at 25 MW/m^3 has been taken into account as well, and the results will be presented in the Appendix 9.2 for each model after the results without neutron heating.

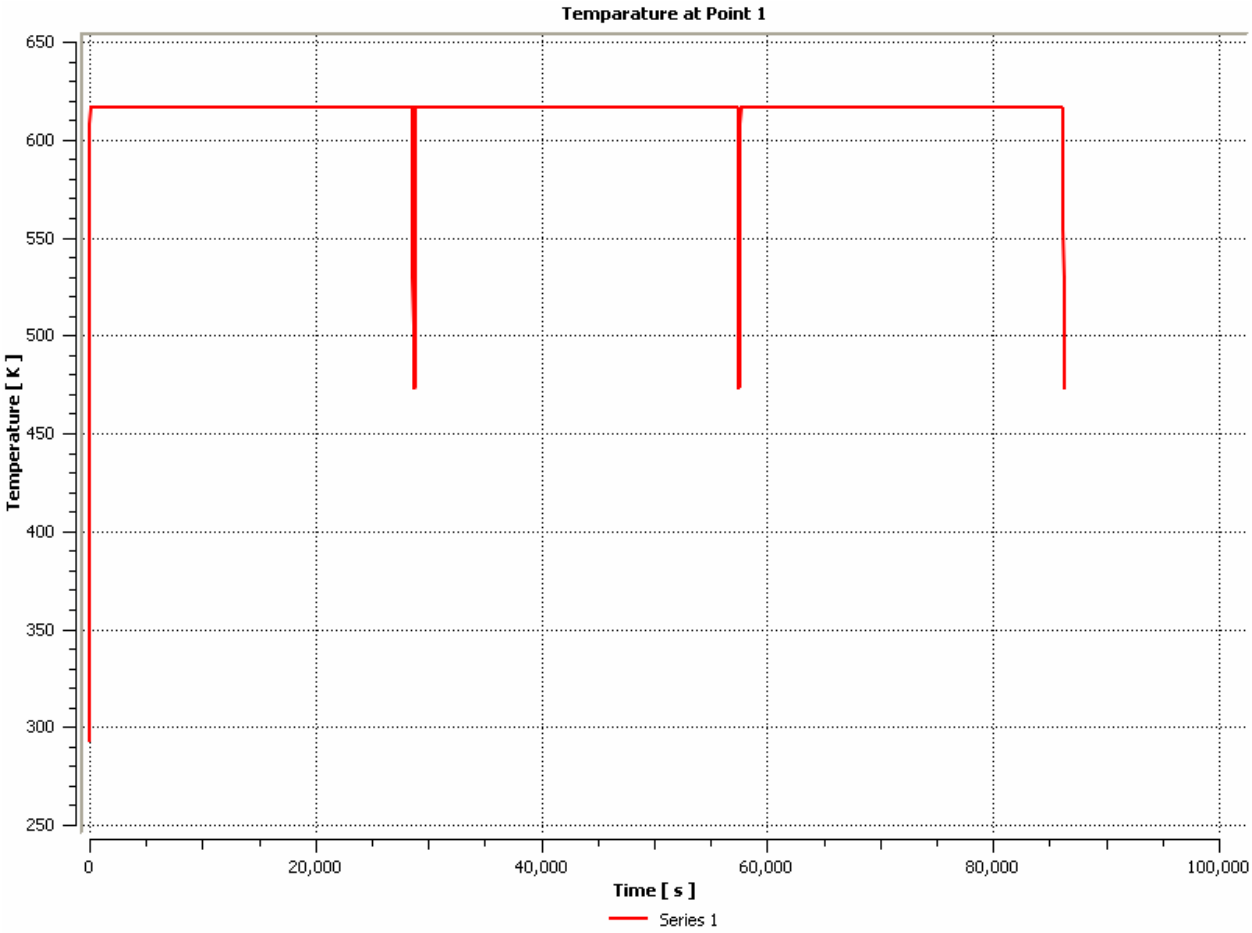

Fig. 3.9: Maximum temperature during 24 hours (CFX).

Fig. 3.9 shows the temperature vs. time in a surface point for three 8 hour pulses. The heat-up phase is 1 minute as is the cooling down and there is a two minute pause after the pulse. The figure suggests that the "flat top" is reached very quickly and therefore it is unnecessary to model the whole 8 hours. Hence a modified pulse was used which lasts for only 30 minutes including the one minute heat-up, one minute cool-down and two minutes pause (fig. 3.10). The starting temperature of the system is 200 °C.

The temperature at the beginning of the cool-down phase can be seen on fig. 3.11. The peak temperature on the surface is 350 °C. The temperature of the coolant changes only slightly, the outlet being only 6 °C warmer than the inlet (200 °C).

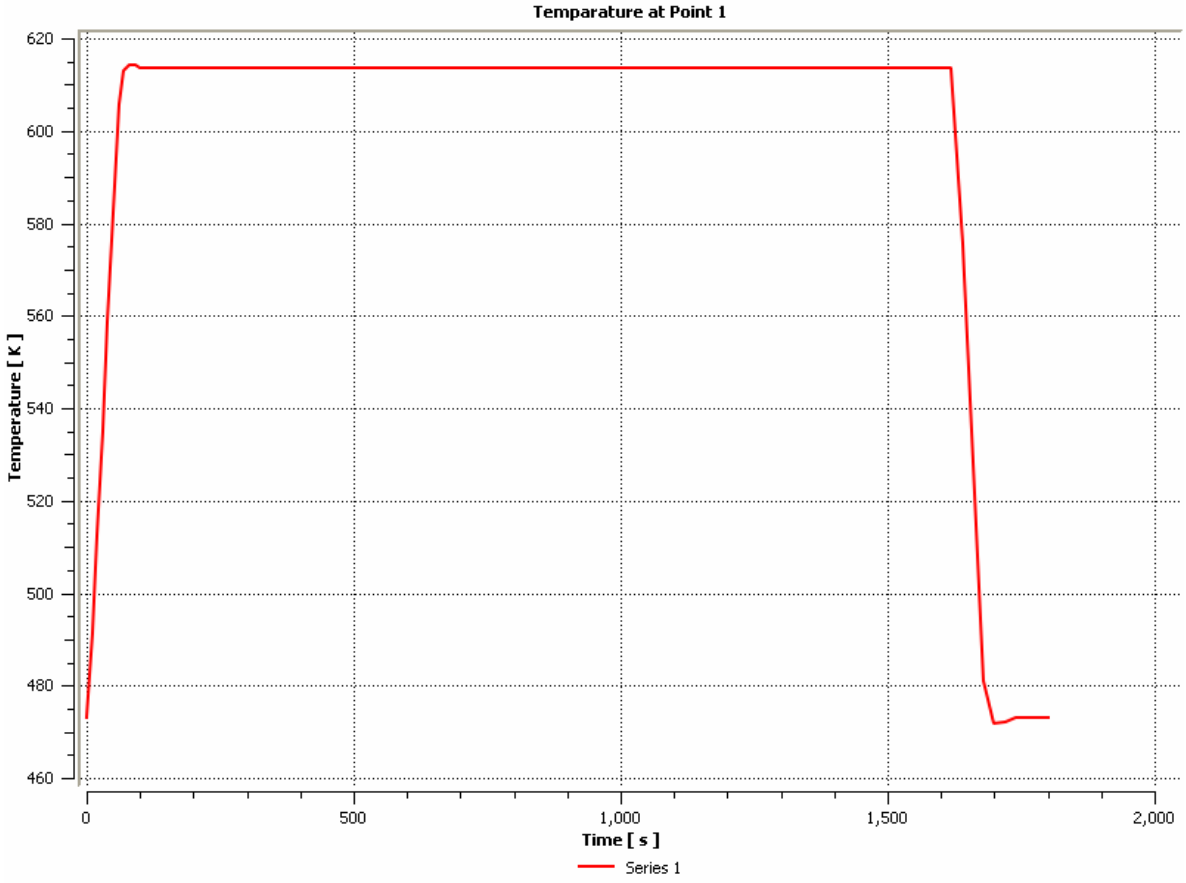

Fig. 3.10: Modified pulse: 30 minutes (CFX).

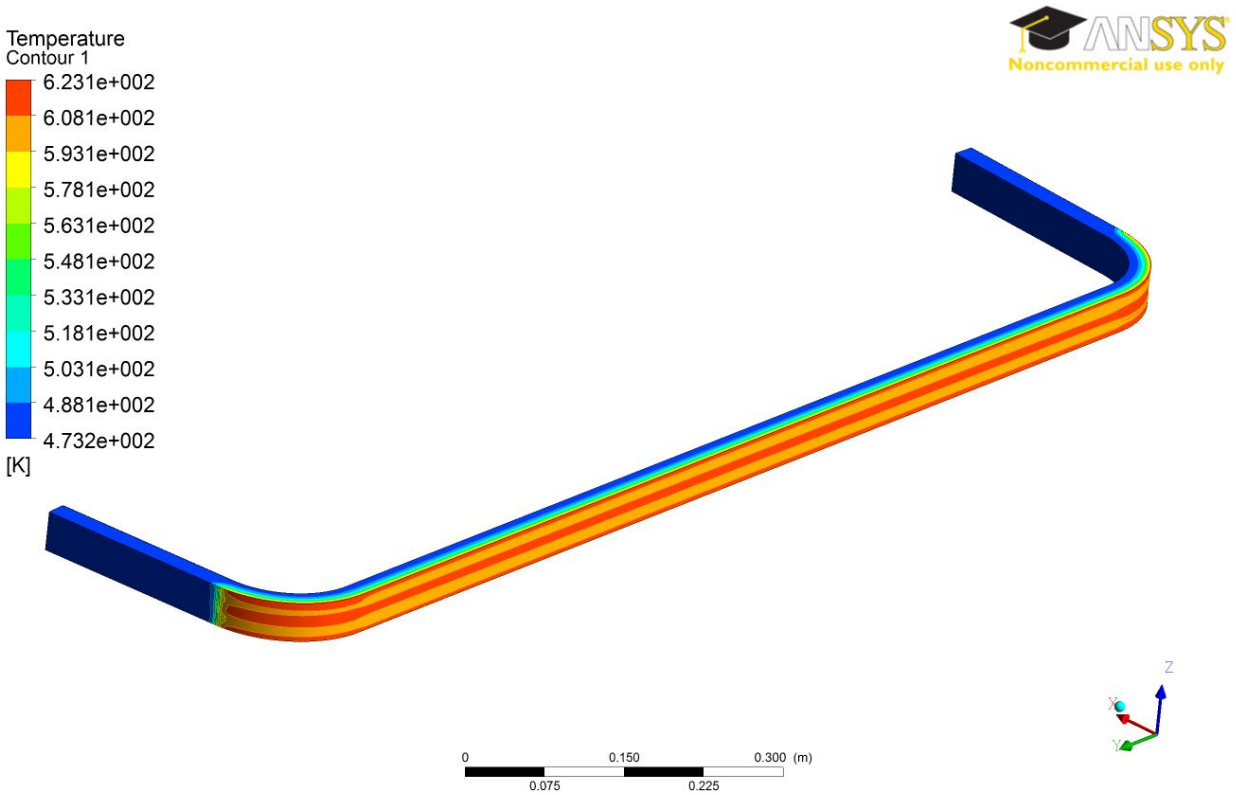

Fig. 3.11: Temperature at 1620 s – original model (CFX).

In order to obtain the stress and strain due to the thermal load, the heat transfer coefficients of the fluid flow solution have to be transferred to the transient thermal module (the CFX thermal solution cannot be transferred to the transient structural module). Fig. 3.12 shows the temperature distribution on the surface. It is slightly lower than in the CFX module peaking at 338 °C (Note that in the cross-section (fig. 9.11 in appendix), the peak temperature is 341 °C: the 350 °C peak temperature must apply to only a few nodes).

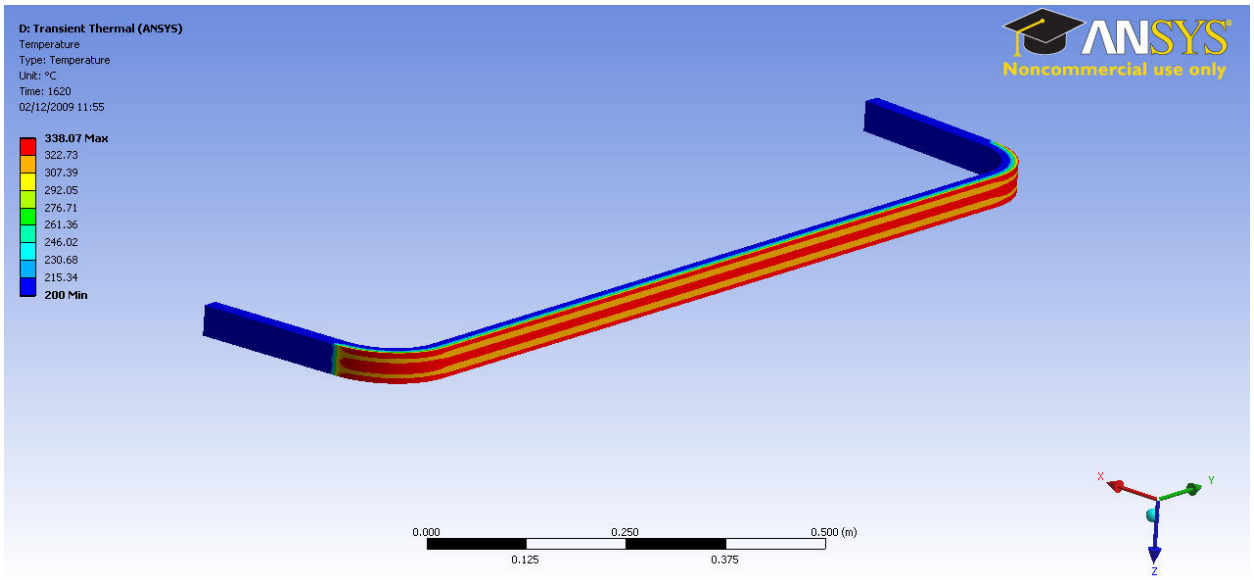

Fig. 3.12: Temperature at 1620 s – original model (ANSYS Mechanical).

This temperature distribution can be transferred to the transient structural analysis. The constraints on the mechanical model are minimalist. The bottom plane has zero displacement in the z direction, and one edge on the side is fixed while the corresponding edge on the other side is free to expand in the y direction.

This means that the stresses and strains are dominated by the thermal effects and the estimated lifetime from these results is an upper limit. Any additional constraints are likely to increase the stresses and strains and even though the stress and strain amplitude due to the alternating temperature would not necessarily change (depending on the constraints) the mean stress and strain would.

The disadvantage of constraining just the edges of the model is that at the constrained nodes we can expect stress concentrations. The reason for this can be that a relatively small number of nodes is constrained and therefore the reaction forces are unrealistically high at these nodes. Basically the reaction forces work like point loads at these nodes.

These local stress concentrations should have negligible effect on the stress and strain distribution in the model.

The fatigue curve we will use is strain vs. number of cycles and therefore the strain intensity results shown on fig. 3.13-3.14 are needed to extract the strain amplitude and mean strain. These strain distributions are typical for all the modelled cases (see Appendix 9.2).

The mean strain intensity based on this is 0.11% and the alternating strain intensity is 0.094%. The total strain range is 0.188%. This means that the number of cycles to failure is about 3500 according to the design curve.

However it has to be pointed out that [3.5] suggests that the thermomechanical cycling causes more damage than isothermal mechanical cycling with the same strain range. Although it is not quantified in the paper how much worse the thermomechanical cycling is, the graph in [3.5] suggests that it could be in the range of a factor of 2. Assuming this, the effective strain range is about 0.376%, and with that the number of cycles to failure is 750.

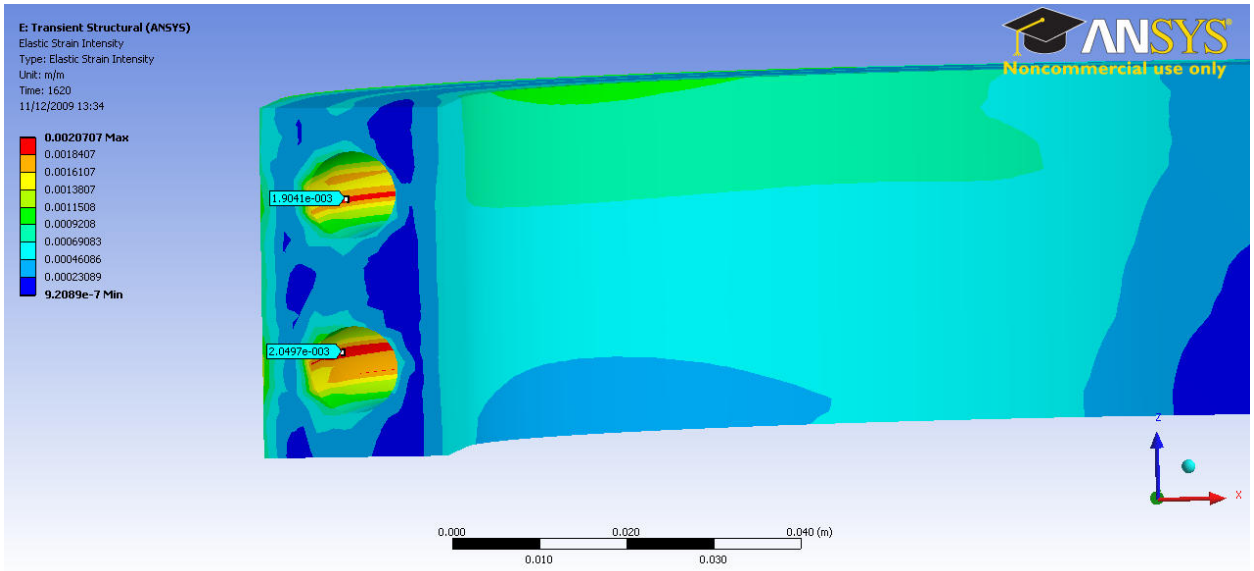

Fig. 3.13: Strain intensity in the elbow region of original model at 1620 s (ANSYS Mechanical).

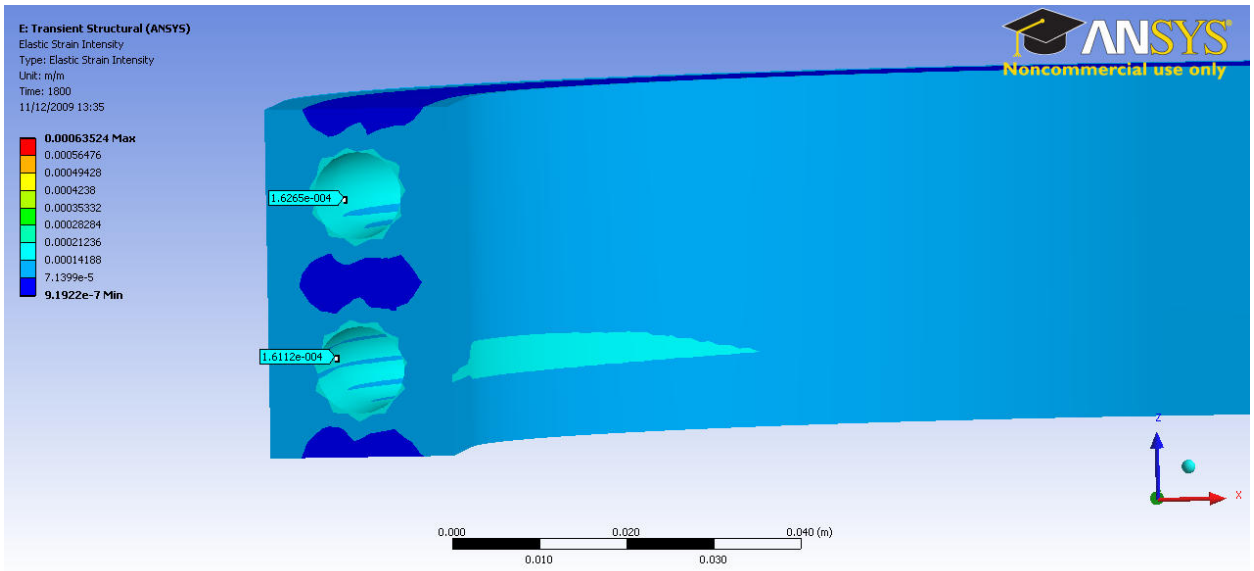

Fig. 3.14: Strain intensity in the elbow region of original model at 1800 s (ANSYS Mechanical).

3.5. Results

The detailed analysis reports of the three modelled geometries are in the Appendix 9.2. Table 3.1 shows the results for all the three models. In the column "Maximum surface temperature", the first number is the CFX and the second is the ANSYS mechanical result. The number of cycles to failure is calculated from the design curves shown in fig. 3.5 and was derived from the test results by applying a factor of 2 on the strain range or a factor of 20 to the number of cycles, whichever is the more conservative to account for uncertainties associated with material and loading conditions that are not taken into account in the tests [3.8], [3.9]. These results should include effects like mean stress and thermomechanical cycling ([3.8] claims that the factor of 2 on stress and 20 on cycle is a quite reasonable limitation, but not excessively conservative for a LWR (light water reactor) environment).

Table 3.1: FE results summary, number of cycles to failure based on the design curve

Model	Max. surface temperature [°C]	Mean strain [%]	Alternating strain [%]	Total strain range [%]	Number of cycles to failure
Original	350/338	0.11	0.094	0.188	***3300***
Original with neutron heating	389/370	0.13	0.115	0.23	***2100***
Modified model 1	309/304	0.08	0.065	0.13	***7000***
Modified model 1 with neutron heating	328/323	0.1	0.073	0.146	***5600***
Modified model 2	320/304	0.082	0.063	0.126	***7700***
Modified model 2 with neutron heating	346/324	0.096	0.079	0.158	***4750***

It has to be emphasised again that the fatigue data for Eurofer 97 is rather limited. More research needs to be done in a fusion context; in particular the effect of thermomechanical cycling at elevated temperatures.

Eurofer 97 does not have very good fatigue properties, for comparison the same strain ranges would allow more than 40 000 cycles for 316 LN stainless steel in the worst case and in the range of 10^8 in the best case. MANET (martensitic steel for NET) would allow 15 000 to 130 000 cycles [3.10]. The Japanese F82H seems to have better response to fatigue as well. The number of cycles would be above 20 000 for the strain ranges in table 3.1 (based on a preliminary design curve [3.11]).

As Eurofer 97 is not a common material that is included in the design codes, the number of cycles to failure can be alternatively calculated by using the curves obtained by the tests (at 300 °C) and

then correcting for non-zero mean strain and a factor of 2 for the thermomechanical cycling. Results for this approach are shown in Table 3.2.

There are several methods to correct for mean stress or strain. The fatigue curves available are based on strain range, therefore those correction methods are preferred that are strain-based as well. In order to make these corrections, one would need the parameters σ_f, ε_f, b and c in the Coffin-Manson formula in elevated temperature:

$$\frac{\Delta\varepsilon}{2} = \varepsilon_a = \frac{\sigma_f}{E}\left(2N_f\right)^b + \varepsilon_f\left(2N_f\right)^c$$

N_f is the cycles to failure, E is the Young's modulus, $\Delta\varepsilon$ is the strain range for zero mean stress, and the other four parameters are fitting constants. These parameters are not known for the relevant cases.

One of the simplest, but generally acceptable approaches could be the correction of the number of cycles to failure by the Walker procedure [3.12], [3.13]:

$$N_W = N_f\left(\frac{1-R}{2}\right)^{\frac{1-\gamma}{b}}$$

R is the ratio of the minimum and maximum stress (-1 for full reversal). There is no data available for Coffin-Manson fitting constants in the case of Eurofer 97, but there are data for other metals. Table 3.2 shows what the expected lifetime would be in case of different *b* and γ values. Typically *b* is in the -0.1 - -0.2 range for steels and γ is between 0.5 and 0.7 [3.13], [3.14]. In our cases, R≈0.

Table 3.2: Number of cycles to failure based on the test curve and corrected for mean stress.

Model	Total strain range		Number of cycles to failure				
	Calculated	Factor of 2 due to thermo-mechanical cycling	Without correction	γ=0.5 b=-0.1	γ=0.5 b=-0.2	γ=0.7 b=-0.1	γ=0.7 b=-0.2
Original	0.188	0.376	15000	468	2678	1875	5357
Original with neutron heating	0.23	0.46	9750	304	1741	1218	3482
Modified model 1	0.13	0.26	32500	1015	5803	4062	11607
Modified model 1 with neutron heating	0.146	0.292	25500	796	4553	3187	9107
Modified model 2	0.126	0.252	35000	1093	6250	4375	12500
Modified model 2 with neutron heating	0.158	0.316	21500	671	3839	2687	7678

These results suggest that the non-zero mean stress can reduce the lifetime of the first wall dramatically. It strongly supports the need for accurate material property measurements for Eurofer 97. The correction formula is very sensitive to the parameters and most of the parameter combinations suggest that the lifetime can be more restricted (including the effect of thermomechanical cycling – multi-axial stress state) than the design curves suggested.

3.6. Summary and future work

A pulsed version of DEMO with 8 hour long pulses would have 1095 heat-up cool-down cycles in a year if it operated 365 days per year. The results show that from a fatigue point of view, the lifetime of the analysed DEMO outboard first wall designs could extend to about 8.3 years in the best case or only 101 days in the worst case (including neutron heating), depending on the design and the parameters used for mean stress/strain correction. Using the design curve simplistically, the expected lifetime in the best case would be about 5 years.

The results indicate that more accurate data is required in respect of fatigue of EUROFER 97, including irradiation effects. The different fatigue and design curves show that there is more research to be done in order to obtain reliable fatigue data for Eurofer 97. The effect of thermomechanical fatigue has to be explored, also the parameters in the Coffin-Manson formula have to be measured and/or calculated. The results were corrected in the analyses above for non-zero mean stress using typical parameters for steels in applying the Walker method. This dramatically reduced the projected number of cycles to failure.

These results are principally dominated by the effect of thermal pulsing, where the means of support can influence both the mean and alternating stress and strain, which will have a significant effect upon the expected lifetime, both in steady-state and pulsed mode.

Other thermal effects like creep, irradiation creep, creep fatigue, the effects of over-power and under-power transients during a pulse have to be covered in future works.

In the models, the wall thickness was very small. Due to the plasma interaction, the first wall will be eroded from the outside, and also due to water corrosion there are likely to be problems arising inside the coolant channels. More research should be carried out to find low activation steels (or coolant additives adequately stable in the neutron radiation field) that can withstand corrosion.

Due to the corrosion problems with water, other coolants may have to be used. Helium cooling is a preferred option in this context and therefore helium-cooled first wall designs will be a key part of these analyses in the future.

3.7. References

[3.1] P. J. Karditsas: "Lifetime and thermal-structural performance of various first wall concepts and implications of creep-fatigue for design and licensing", Fusion Engineering and Design 39-40 (1998) 575-584.

[3.2] B. G. Hong, D. W. Lee, S. J. Wang, Y. Kim, W. K. In, K. H. Yoon: "Basic concepts of DEMO and design of a helium-cooled molten lithium blanket for a testing in ITER", Fusion Engineering and Design 82 (2007) 2399-2405.

[3.3] P. Chaudhuri, C. Danani, V. Chaudhari, C. Chakrapani, R. Srinivasan, I. Sandeep, E. R. Kumar, S. P. Deshpande: "Thermal-hydraulic and thermo-structural analysis of first wall for Indian DEMO blanket module", Fusion Engineering and Design 84 (2009) 573-577.

[3.4] F. Zacchia, N. Cerullo, C. Fossa: "Proposal for an alternative type of helium-cooled blanket for DEMO", Fusion Engineering and Design 41 (1998) 569-575.

[3.5] J. Aktaa, M. Weick, C. Petersen: Reduced softening of EUROFER 97 under thermomechanical and multiaxial fatigue loading and its impact on the design rules, Journal of Nuclear Materials 386–388 (2009) 911–914.

[3.6] Petersen et al, Tensile and Low Cycle Fatigue properties of different ferritic/martensitic steels after the fast reactor irradiation 'ARBOR 1', J. Nuc. Mat. 386-388 (2009) 299-302

[3.7] J. Rensman, NRG Irradiation Testing: Report on 300°C and 60°C Irradiated RAFM steels, NRG Report #20023/05.68497/P, Aug. 2005

[3.8] O. K. Chopra, W. J. Shack: "Review of the Margins for ASME Code Fatigue Design Curve - Effects of Surface Roughness and Material Variability (NUREG/CR-6815, ANL-02/39)", Division of Engineering Technology, Office of Nuclear Regulatory Research, U.S. Nuclear Regulatory Commission, Washington, DC 20555-0001, September 2003

[3.9] ITER Structural Design Criteria for In-Vessel Components

[3.10] NET Material Data N/I/3300/5/A, 14/09/1990

[3.11] A-A. Tavassoli: "DEMO Interim Structural Design Criteria" Draft A3.S18F Revision 1, Appendix A, Fig. A3.S18F.6.4.2 pp53.

[3.12] K. N. Smith, P. Watson, and T. H. Topper: "A Stress-Strain Function for the Fatigue of Metals", ASTM Journal of Materials, Vol. 5, No. 4, December 1970.

[3.13] N.E. Dowling, "Mean Stress Effects in Stress-Life and Strain-Life Fatigue," Fatigue 2004: Second SAE Brasil International Conference on Fatigue, São Paulo, Brasil, SAE Paper No. 2004-01-2227, Society of Automotive Engineers, June 2004.

[3.14] http://www.fatiguecalculator.com/cgi-bin/StrainShowMatProp.pl

4. The Divertor

4.1. Introduction

The divertor will be a critical component within commercial fusion plants. It will be subject to high heat flux and significant ion bombardment. It will also need to be designed to produce usable heat for electricity generation, using the coolant as the working fluid in a suitable power cycle. As part of the Power Plant Conceptual Studies (PPCS) programme, three near-term concepts (PPCS-A, PPCS-B, PPCS-AB) and two advanced concepts (PPCS-C, PPCS-D) have been developed. Each of the plant concepts has a different divertor concept. These range from a modification of the water-cooled ITER configuration (PPCS-A), through helium-cooled divertors (PPCS-AB, B, C) to an advanced liquid metal-cooled divertor concept (PPCS-D).

The advanced concepts may eventually be more suitable for use in a commercial power plant, but these will be more complex and will require much more research and development. The discussion here will focus on divertors within the near-term PPCS concepts, as these technologies have a greater possibility of being developed in time for DEMO. A distinction will be made between pulsed and continuous-mode operation in DEMO, as the two present different environments for the divertor, and also have different economic consequences for the feasibility of DEMO as a step towards commercial reactors.

4.2. System Level Considerations

The EU fast track scenario envisages electricity production by fusion to be achieved by 2030. The following 'system level' considerations affect the divertor design.

1. The early generation fusion reactors would need to utilise electricity generation technology from combustion and/or nuclear fission power stations. The best electricity generating cycle used by 'conventional' power stations at the time of fusion plant design would be one of the factors used to determine the coolant, and hence the thermal efficiency of power generation [4.1]. Efficiency is a major factor in the cost of electricity (COE) from fusion. Figure 4.1 shows the maximum theoretical efficiency η_{max} of any heat engine at a given coolant outlet/power cycle inlet temperature exhausting to atmosphere (20°C), where $\eta_{max} = 1-(T_{cold}/T_{hot})$. Shown alongside are typical efficiencies of steam and gas power generation cycles.

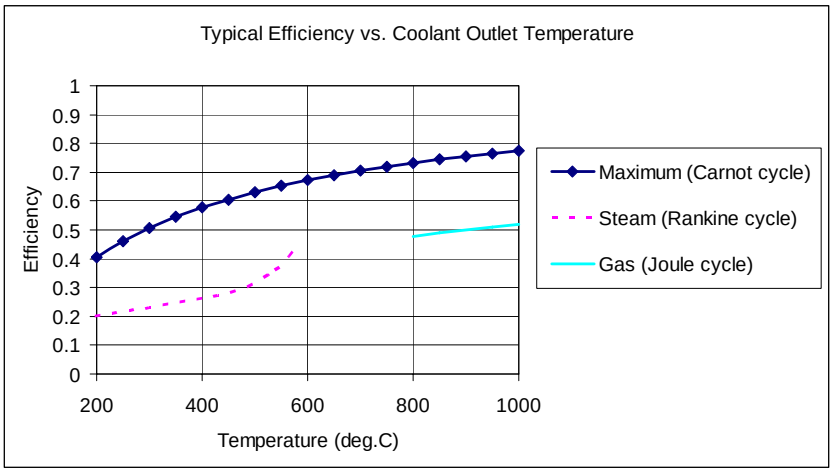

Fig. 4.1: Typical Cycle Efficiencies vs. Maximum Coolant Temperature

Increased efficiency by using higher coolant temperatures is limited by the availability of divertor materials and joining processes which can withstand these conditions.

2. The desire to have less waste from fusion leads to the need to use 'reduced activation' materials. RAFM (reduced activation ferritic/martensitic) steels have an upper temperature limit of 550-600°C as the tensile strength rapidly reduces with increasing temperature over this range [4.2]. This material temperature limit is compatible with generating technology using supercritical water. Managing tritium contaminated water would need consideration.

3. For a gas cooled system, efficiency at around 500°C is lower than that possible with a water cooled system, due to the higher pumping power required per unit of heat transferred. Modern direct cycle gas turbines need temperatures 900°C and above to be efficient. These temperatures require development of SiC composite materials to be developed, if required in fusion reactors. Temperatures above 600°C and below 900°C have no proven power plant technology available for fusion applications. Use of these coolant temperatures would require development of generating technologies.[4.1]

4. Economics of fusion electricity also depend heavily on plant availability; downtime needs to be kept to a minimum. Lifetime of the divertor should be maximised, and design should be as robust as possible to minimise risk of damage.

5. Since the divertor will have to handle a high heat flux, the choice of coolant outlet temperature presents a compromise. Low temperature will provide a large thermal gradient across the divertor between the plasma and the coolant, and will help achieve high heat flux. High temperature is required for high thermal efficiency of power generation, but this means the divertor will have to be designed to allow high heat flux (up to 15MW/m^2) across a relatively small temperature gradient.

4.3. Divertor Requirements

An ideal divertor would have several functions and features including the following [4.3, 4.4]:

1. Extraction of helium and fuel atoms and high Z contaminants from the plasma.
2. Efficient recovery and conversion of the fusion thermal power incident on the divertor (estimated at ~15% of total). Pumping power in the divertor coolant circuit should be no more than 10% of the thermal power recovered.
3. Compact design for cost effectiveness
4. Handling of high heat flux (up to 15MW/m^2) at high operating temperature (>600°C), requiring high thermal conductivity and high melting temperature. The divertor will also have to withstand significant cyclic thermal stresses, and so issues such as creep fatigue may become critical. This is especially true for pulsed operation, where pulses are long enough to induce creep fatigue, but have a much greater number of pulses per year than for continuous working mode.
5. Handling of high neutron fluence, and resistance to sputtering erosion in the plasma facing components, and resistance to irradiation damage in the structural component, such that operability is maintained for at least 2 years under DEMO conditions. The lifetimes of critical components such as the divertor impact on plant availability and hence the cost of electricity. It is more cost-efficient to use divertors which are able to withstand operating conditions for 2 years of operation. They can then be replaced only during scheduled downtime, with little or no impact on plant availability.
6. Compatibility with good core confinement and stability

4.4. Divertor Concepts

4.4.1. PPCS-A (Water Cooled)

The divertor concept for ITER uses high conductivity CuCrZr as a heat sink. However, operating conditions in DEMO and future commercial fusion power plants are likely to be harsher than in ITER. CuCrZr is known to suffer from embrittlement at high neutron flux, as well as a reduction in fracture toughness at a neutron damage of 0.3dpa. This is more evident at high temperatures. In the high neutron flux, high temperature environment expected in the DEMO divertor, this behaviour is obviously undesirable. PPCS-A is therefore strongly based on the ITER divertor reference design, but with a W-alloy monoblock acting as plasma-facing armour and a CuCrZr water coolant tube embedded within. Oxygen free high conductivity (OFHC) Cu is used as a compliant layer inserted between the CuCrZr tube and the W-alloy monoblock [4.3]. Coolant conditions are similar to that in the ITER divertor, with a coolant outlet temperature of ~166°C and pressure of 4.2MPa.

This low-grade heat is of little use in generating power directly, and hence this design goes against the 'ideal divertor' concept above. However, the exhaust heat may still be used effectively elsewhere in order to increase overall plant efficiency. For example, it may be possible to integrate the divertor cooling circuit into the reactor blanket power conversion cycle, by preheating the feedwater for the steam generator. A system of this type could potentially increase the overall efficiency of the PPCS-A reference plant from 31.0% to 32.9%, although the net efficiency is only 31.6% after accounting for pumping power in the divertor circuit [4.5].

A modified design was proposed, with an RAFM (EUROFER) tube and a compliance layer of soft graphite ('Papyex') in order to achieve a higher water temperature (and hence higher conversion efficiency). This design operates at 325°C coolant outlet, and 15.5MPa pressure. The two designs are shown in Figure 4.2, taken from [4.3]. The coolant at 325°C could be used as the heat input for a low pressure ratio steam generator, but Figure 4.1 shows conversion efficiency at around 325°C (assuming a temperature gap $\Delta T \approx 25°C$ between maximum coolant and steam temperatures) is very poor. Direct use of this heat may prove uneconomical, considering the extra plant (heat recovery steam generator, steam cycle plant, and generator) required. However, the waste heat could be used in the same way as for the initial PPCS-A concept, with the higher-grade heat improving overall plant efficiency by more than 0.6%. Further studies are required, for example a cost-benefit analysis for this scheme.

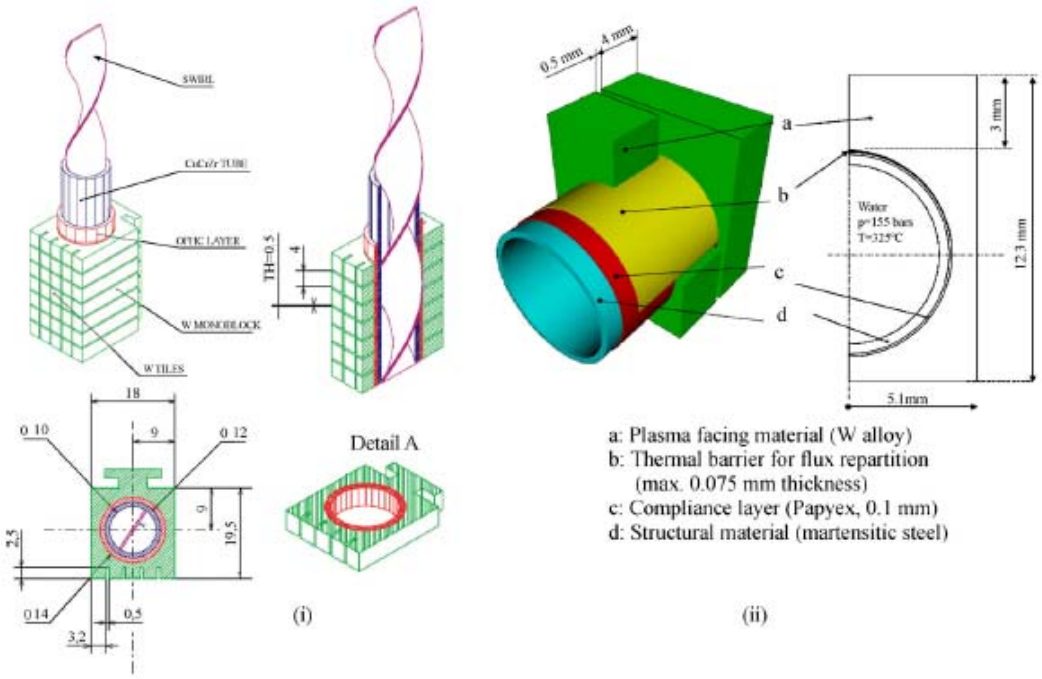

Fig. 4.2: (i) PPCS-A design (W/CuCrZr/OFHC); 2(ii) Advanced concept (EUROFER/W/Papyex)

4.4.2. PPCS-AB, B, C (Helium Cooled)

Helium cooling has several advantages over water cooling: it is chemically and neutronically inert, capable of working at higher temperature than water (hence allowing a higher power conversion efficiency), and at lower pressure. Additionally, since helium gas is to be used for FW/blanket cooling, overall plant design can be simplified (leading to reduced capital and ongoing costs) by using the same coolant in divertor loops.

This concept also presents fewer technical challenges and relies on more proven technology and materials than the more advanced liquid metal-cooled concepts such as PPCS-D. The main disadvantage is that much greater volumetric flow is required to achieve the same flow of "heat transfer units" $\dot{m}c_p$, due to its low density (ρc_p= 0.93kJ/m^{3}K for helium, 4200 for water). The low density of helium will be a disadvantage in designing effective cooling circuits. Effective designs will have to counteract this disadvantage, by providing a large heat transfer area and/or promoting turbulent flow. However, this will mean a high pumping power will be required to pump the fluid at high speed across a large pressure drop. Some initial designs are shown in Figure 4.3.

The first features a porous 'wick' material providing the coolant with a large surface area to volume ratio for high heat transfer. The second is a simpler design with a narrow (~0.1mm) slot to provide a large contact area. The third is a modification of the slot concept, with geometry changed to reduce the length of the conduction path between plasma and coolant, and also using a pin array at the top of the cooling channel to increase the contact surface area further. This enhances heat transfer, from 5 up to 10MW/m^2.

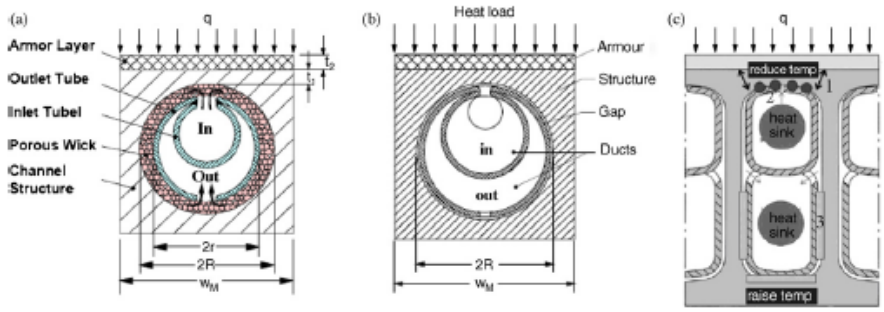

Fig. 4.3: Some initial HCD designs: (a) porous medium concept (Q=5MW/m2), (b) simple slot (Q=5MW/m2) , (c) modified slot (Q=10MW/m2)

4.4.3. Advanced He-cooled Concepts

Research and development has been undertaken on helium-cooled divertor designs for DEMO and conceptual studies in recent years. Most of the conceptual plant models in Europe, and also the US ARIES-CS study, consider helium-cooled divertors as reference designs. Two main concepts are presented, both of which are designed to operate at DEMO reference conditions of 10MPa and 600°C coolant inlet.

1. HETS

The high efficiency thermal shield (HETS) concept is shown in Figure 4.4. A single jet of coolant impinges on the curved surface shown, then flows downwards through the narrow gap towards the outlet. Simulations predict an incident heat flux of 10MW/m^2 and coolant outlet temperature of 800°C. The top tungsten armour is brazed onto the WL10 tungsten alloy lower structure capable of withstanding the high temperature of the coolant.

2. HEMJ/HEMS

Helium cooled modular divertor with jet cooling (HEMJ) uses multiple jet impingement to achieve high heat transfer. The design is shown in Figure 4.4. A sacrificial armour layer of pure tungsten provides thermal shielding and protection against incident particles from the plasma. As with HETS, the upper section is WL10 brazed onto the W cap, and the structural material below is constructed from ODS EUROFER. To deal with the difference in thermal expansion coefficients, a Cu transition piece is used (shown in red). Coolant temperature is expected to be 600°C (inlet) to 700°C (outlet), and the design is expected to achieve a heat flux of 10MW/m^2.

The HEMS design is similar, with a different mechanism for heat transfer. Instead of using jet impingement, a tungsten slot array is brazed to the top cooling surface, and guides flow radially outwards from the top of the inlet. A higher coolant exit temperature of 713°C is predicted, with the same heat flux of 10MW/m^2.

Although HEMS provides a slightly higher coolant outlet temperature, HEMJ is preferred as a reference design due to the relative simplicity of design and hence lower cost of manufacture.

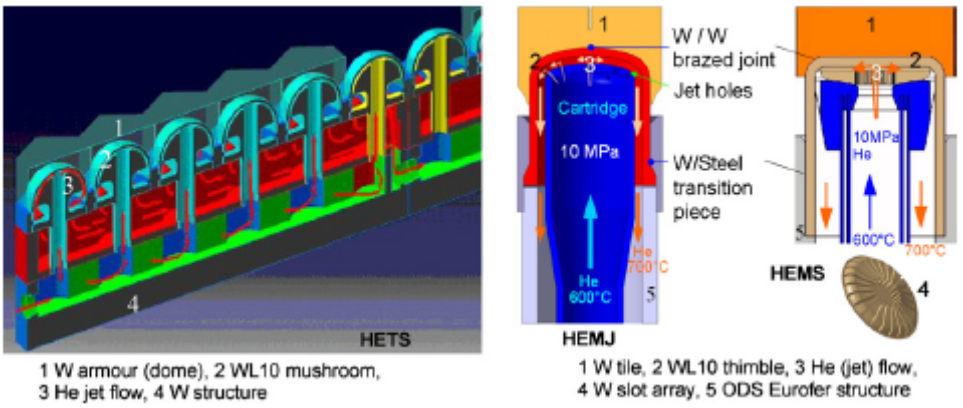

Fig. 4.4: HETS concept (left), HEMJ/HEMS (right)

4.5. Concept Comparison

Table 4.1 shows the main heat transfer design parameters associated with each of the divertor concepts discussed so far, in order to provide a comparison of performance against the two criteria of total heat flux and outlet temperature. The final column, W_{pump}/Q_{in}, is a measure of concept performance: the lower the ratio of estimated pumping power to divertor heat output, the more efficient the power conversion will be. A suggested reasonable limit is 10%. Entries left blank correspond to concepts for which insufficient data is available to calculate W_{pump}/Q_{in}. Appendix 4.1 shows the derivation of these values.

Table 4.1: Divertor Concept Coolant Flow Parameters

Concept	**Heat Flux (MW/m^2)**	**Pressure (MPa)**	**T_{in} (°C)**	**T_{out} (°C)**	W_{pump}/Q_{in}
PPCS-A (CuCrZr)	15	4.2	140	~166	7.2%
PPCS-A (RAFM)	15	15.5	300	~325	12.3%
He (porous medium)	5.5	8	632	800	
He (slot principle)	5	14	600	800	
He (modified slot)	10	10	640	712	
HETS	10	10	600	800	10%
HEMS	10	10	600	713	
HEMJ	10	10	600	700	9.6%

4.6. Material Issues

Several properties are required of materials to be used in the DEMO divertor: high thermal conductivity, high tensile and creep strength, high fracture toughness, high radiation resistance, low residual activation, good compatibility with the cooling medium, a high operating point temperature, and a wide range of tolerable temperatures. Presently the most promising materials for the "near-term" concepts presented so far are RAFM steels such as EUROFER, and W alloys, each with their relative advantages and disadvantages.

4.6.1. RAFM steels

Reduced Activation Ferritic/Martensitic steels such as EUROFER may be suitable for some designs due to their low activation compared to ordinary steels. However, the upper temperature limit on RAFM steels is around 550°C, above which their mechanical strength begins to reduce [4.6].

Oxide dispersion strengthened (ODS) RAF steels can achieve improved strength and creep resistance at high temperature. ODS would effectively increase the maximum operating temperature from 550°C to 650°C. ODS (nano-composited) ferritic steels are a more advanced concept which could possibly raise the maximum operating temperature to 750°C [4.7], but this material is at a much earlier stage in its development compared with EUROFER and ODS EUROFER.

The ARBOR irradiation campaign was performed at the BOR-60 experimental reactor facility, and tested 9 different RAFM steels at two different irradiation levels (~30dpa in ARBOR-1 campaign, ~90dpa in ARBOR-2, as calculated by the SPECTER code). Specimens were irradiated in a fast neutron flux (>0.1MeV) of 1.8×10^{15} n/cm^2 at temperatures between 331°C and 338°C. Tests were then performed to determine the effect of irradiation on the tensile and low-cycle fatigue properties of the RAFM steels. Materials tested included EUROFER 97, EUROFER 97 with varying boron contents, and ODS-EUROFER 97 with 0.5% Y_2O_3 [4.8].

Figure 4.5 shows the effects of test temperature, irradiation temperature, and irradiation dose, on the yield strength ($R_{p0,2}$) of standard EUROFER 97. Results are taken from several campaigns, including ARBOR-1. Figure 4.6 similarly shows the dependence of uniform strain (Ag) for the same test pieces. Figures 4.5 and 4.6 show radiation hardening is a significant issue for EUROFER 97. Tensile test results for EUROFER 97 with different boron contents, and those for ODS-EUROFER 97, are not yet available.

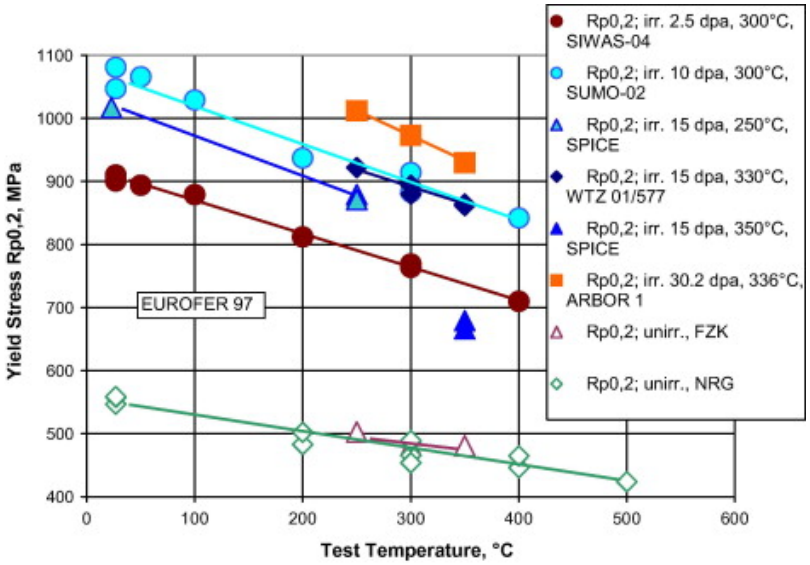

Fig. 4.5: Yield Stress vs Temperature and Irradiation (EUROFER 97)

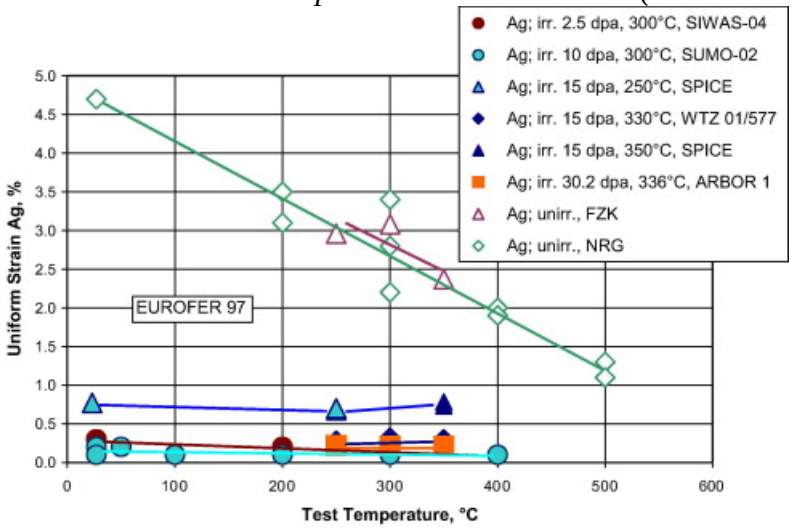

Fig. 4.6: Uniform Strain vs Temperature and Irradiation (EUROFER 97)

The low-cycle fatigue behaviour of EUROFER 97, and ODS-EUROFER 97 with 0.5% Y_2O_3, were also affected by irradiation. Figure 4.7 shows that for standard EUROFER 97, the number of cycles to failure for irradiated specimens is less than that of unirradiated specimens at strain ranges above about 1%. This is because the maximum strain exceeds the reduced elastic limit of the irradiated steel. Conversely, for strain ranges under ~1%, the performance is enhanced compared to the unirradiated steel. A similar effect is observed in ODS-EUROFER.

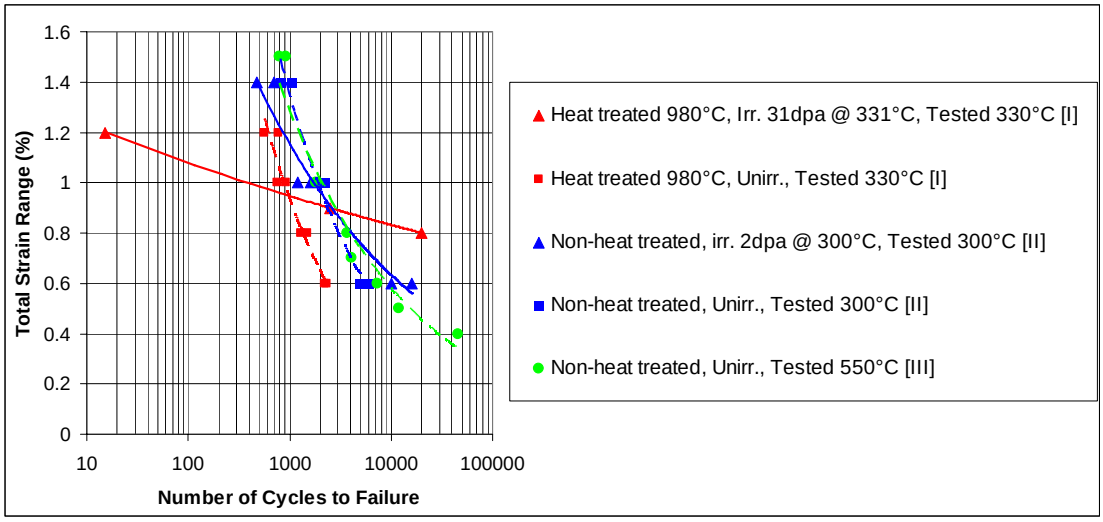

Fig. 4.7: S-N curves for EUROFER 97, various sources

Several other properties of the RAFM steels were also investigated. The ductile to brittle transition temperature (DBTT) of EUROFER-97 was found to increase from 180K to about 380K (107°C) through irradiation. Initial testing gives the DBTT of irradiated ODS-EUROFER 97 at 382°C, however it is expected that this can be reduced significantly [4.9]. Creep properties such as stress exponents, 1% strain limits, and creep rupture times (up to 30,000 hours) were as expected for design relevant conditions (<100MPa and 720-870K), so that performance under a range of operating conditions can be well approximated using appropriate scaling laws. One issue identified by Petersen et al.[4.6] is creep fatigue. Strain controlled fatigue tests were performed on RAFM specimens from room temperature to 820K, with no hold times. When the same tests were performed with hold times of 1000s, the lifetime of specimens in compression and tension was found to reduce by up to one order of magnitude. More experimentation is required to investigate this behaviour.

4.6.2. W and W alloys

Tungsten and its alloys are well suited to the high temperature environment in the divertor: high melting point, high creep resistance, high thermal conductivity, low vapour pressure [4.6]. However, they also suffer from a high Ductile to Brittle Transition Temperature (DBTT) of around 800°C, making them undesirable for use at temperatures lower than this. The behaviour of W-alloys is less well documented than RAFM steels. R&D continues on understanding the micromechanical behaviour of W-alloys (in particular brittle failure mechanisms within the metal). This knowledge can be used to help develop W-alloys with improved “low”-temperature ductility.

4.6.3. Unresolved Issues

The full effects of irradiation on the mechanical properties of EUROFER, W and W alloys for use in DEMO are unknown. The work done so far to characterise the materials' behaviour under irradiation has involved fission reactors [4.6]. These produce a different neutron energy spectrum and hence are of limited use in qualifying materials for use specifically in DEMO. The effect of the expected irradiation on thermomechanical properties (such as creep, creep rupture, creep fatigue, fracture toughness and material strength) need to be accurately determined. Another significant issue is the production of He and H via transmutation, which has not been reproduced in any of the experiments performed so far on these alloys.

The advantages of the HEMJ divertor concept are its relative simplicity of design and the benefits of using helium as a coolant. However, one key problem with this design (and others) is the temperature profile during operation. Tungsten should be kept above its DBTT of around 800°C, however the EUROFER structure beneath must be kept below 550°C to retain satisfactory mechanical properties. The issue is illustrated in Figure 4.8, showing that it is difficult to reach a design which satisfies both temperature limits. Advances in materials such as nano-composited ferritic steels and tungsten alloys may reduce the temperature gap. If a combination of a steel and tungsten alloy could be developed which had an intermediate temperature (above the DBTT of the W-alloy, and below the maximum operating temperature of the steel), it would resolve this issue. Work is ongoing to develop ODS ferritic steels with higher operating temperature (an earlier literature review indicated a possible limit of around 800°C, approaching the DBTT of tungsten [4.6].

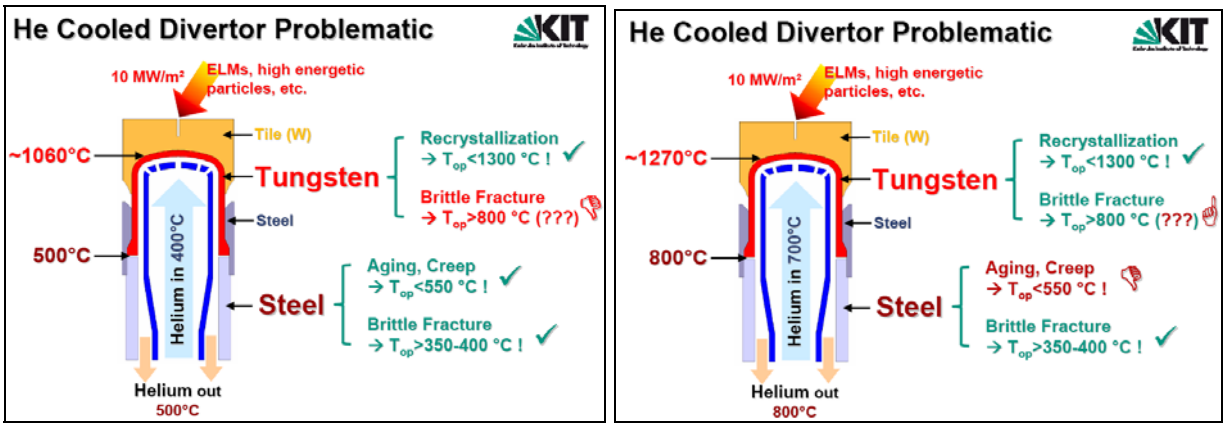

Fig. 4.8: Temperature Profile within HEMJ (M Rieth, P Norajitra - DEMO Technical Meeting 29-30 Sept. 2009)

As EUROFER is the reference material for the European breeder blanket [4.10], a significant amount of R&D has been undertaken to investigate manufacturing and joining techniques. Performance of joints using Hot Isostatic Pressing (HIP) and diffusion bonding in particular has been assessed. However, since EUROFER and the HIP technique have never before been used in nuclear components, a significant amount of qualification work (including investigations into the effect of post-weld heat treatment on mechanical and micro-structural properties) remains.

One other possible major hurdle is the joining of ODS steel to tungsten. Both have very different thermal expansion coefficients and Young's Moduli, possibly creating high differential stresses at the interface. Both materials are also highly chemically reactive and may form brittle phases at the interface, known as "Laves phases" [4.6].

4.7. Prototypes and Testing

The HEMJ design described above is defined as the reference design for DEMO by Norajitra et al. [4.3] at Forschungszentrum Karlshruhe (FZK), who have been progressing the concept for several years. Physical test modules have been created from 9 individual cooling "fingers" as shown in Figure 4.9. A combined helium loop and electron beam facility (60kW, 27keV) has been built at the Efremov Institute in St. Petersburg (Figure 4.10) in order to test these modules [4.11]. A technological study on manufacturing of the finger modules was also performed.

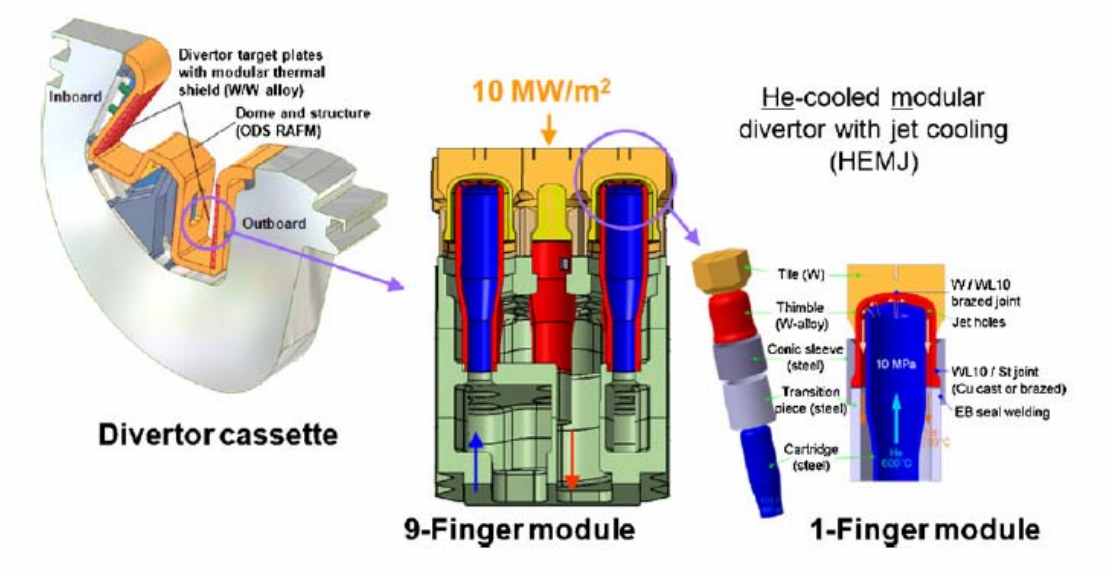

Fig. 4.9: Buildup of divertor cassette from finger elements

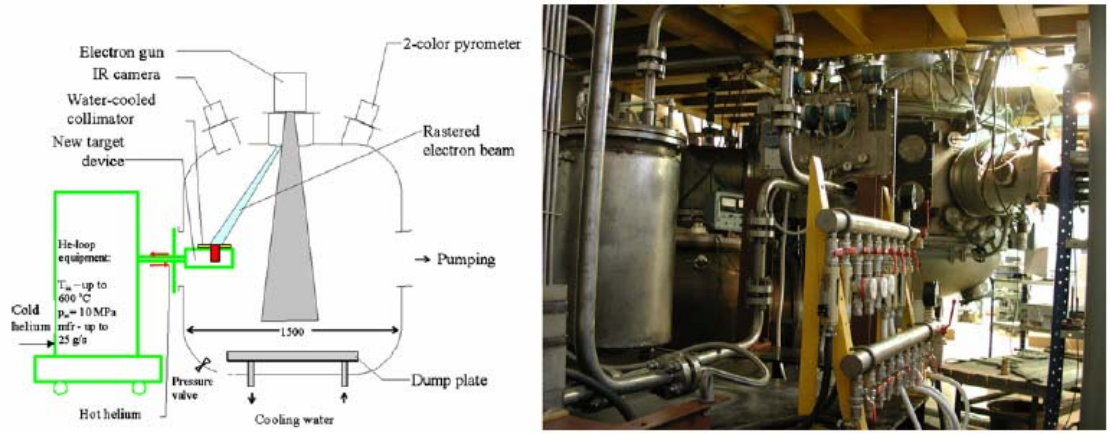

Fig. 4.10: TSEFEY Test Facility, Efremov Institute

The first test series involved periodically applying and removing a heat load of 5-13MW/m^2 over intervals of 30-60s, to simulate thermal cycling. It was found that the modules tested could already achieve a heat transfer rate of 10MW/m^2 under these conditions. Furthermore, no recrystallisation of the W thimble occurred. Neither was brittle failure observed anywhere at this design load, however destructive post-examination showed small-scale defects in the W armour which could potentially lead to sudden brittle fracture.

The second series of tests used modified test fingers which were improved in two ways: optimised geometry to reduce thermal stresses; and a secondary grinding process of electrical discharge machining (EDM). The second test series showed the test pieces surviving for over 100 cycles at 10MW/m^2 with no damage.

A third test series was intended to investigate the effect of various factors on performance: tile design; material used; brazing filler metal; and type of machining (EDM vs. turning alone) [4.11]. Work continues in order to demonstrate that the existing modules are capable of handling 10MW/m^2 for 1000 cycles, and to test the latest generation of finger designs developed since the previous tests.

4.8. The 'Super X' Divertor

The Super X Divertor (SXD) concept proposed by Valanju et al. [4.12, 4.13] can potentially ease many of the design problems for reactor-scale devices. Figure 4.11(a) shows the basic concept as applied to the current upgrade of the MAST spherical tokamak, which is being fitted with a Super X divertor.

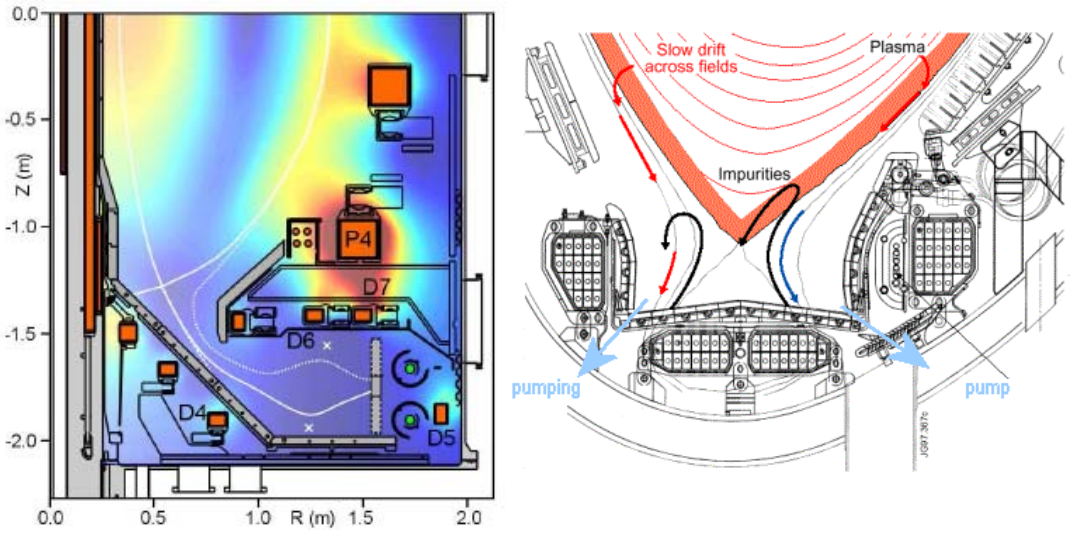

Fig. 4.11: (a) MAST divertor region with SXD, (b) JET divertor region

Several divertor poloidal field coils are added to move the outer strike point, where the scrape-off layer (SOL) hits the divertor target, to a location further out from the centre of the tokamak (larger major radius R). This increases the plasma wetted area, and hence reduces the heat flux density on the divertor target.

A further improvement is associated with the enlargement of the SOL in the region around D6 - in this area the radial component of outward flow has slowed, leaving the flow mainly toroidal. The path length before particles hit the divertor target is hence greatly increased, allowing more collisions and reducing the temperature in the SOL by the time it reaches the divertor target. The overhang shown also shields the outer divertor target from bombardment by neutral particles [4.14].

The reduced heat flux, reduced SOL temperature, and reduced neutral particle bombardment on the divertor target plates will all help to alleviate the demands placed on the divertor, making it easier to find a design which will operate safely under operating conditions throughout the design life, without exceeding any material limits.

The concept will necessarily increase the size of the machine, to accommodate the extra divertor coils and longer outer SOL leg, and so goes against the compactness requirement of an 'ideal' divertor above. However, further work may show that the advantages of SXD outweigh this disadvantage.

Although the SXD concept is favourable for spherical tokamaks such as MAST and NSTX, the geometry of a conventional tokamak means the advantages do not apply to the same extent. By extending the divertor leg by 1m, the major radius R of the outer strike point on MAST will increase by a factor of 3 as shown in Figure 4.11(a). In a conventional tokamak, the torus shape means the outer strike point of a 'standard' divertor is already at a large R. This R will be larger still on reactor-scale machines such as DEMO, so that a 1m extension of the divertor leg will have a relatively small effect on R, and hence heat flux density on the outer divertor target.

The TF coils could also potentially be an issue preventing SXD in conventional tokamaks. There is a relatively large amount of space in the divertor region on MAST (Figure 4.11(a)) compared to JET (Figure 4.11(b)). Expanding the vessel size enough to incorporate an SXD in a conventional tokamak may cause it to enclose part of the TF coils also. Unlike the TF coils in MAST, those in DEMO will be superconducting, so that placing them inside the vacuum vessel, relatively unprotected from the high temperature plasma, could cause serious thermal issues. The cyclic thermal loading caused by pulsed operation would cause still more problems.

4.9. Conclusions: Pulsed vs. Continuous operation of the Divertor

Initial results from testing of HEMJ modules indicate that this design could allow the divertor to fulfil the requirements listed above. The helium-cooled concept has several advantages as discussed. Tests have shown that a heat flux density of 10MW/m^2 is achievable, sufficient to satisfy the requirements of PPCS-B and C. This seems to be the preferred concept, providing a good compromise between performance and attainability:
Coolant outlet temperature (and hence maximum theoretical work output and overall plant efficiency) is higher than for the water-cooled concept.
A significant body of R&D has already been done to prove the feasibility of the concept.

Although prototypes have already been built and tested, more work is required to characterise the materials and joining processes used in the HEMJ divertor, especially under the conditions expected e.g. irradiation. Extensive testing leading to development of fusion relevant materials and processing databases is now crucial in order to achieve the validation of components and structural materials necessary for use in DEMO.

Previous studies [4.15, 4.16] have been performed on the HETS and HEMJ concept in order to analyse their performance. A principal result was the trade-off between maintaining a low divertor temperature (below material limits) and low pumping power (for efficient power conversion). For example, Figure 4.12 shows several variations on the HETS concept which were analysed, along with the acceptable design window in blue. There is only a small overlap between the achievable design space and acceptable performance window, i.e. a limited range of possible 'good' designs.

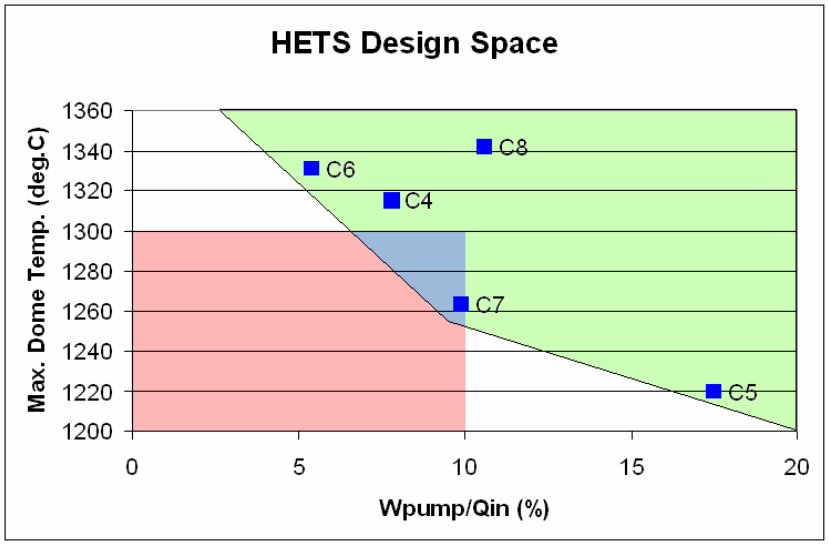

Fig. 4.12: Maximum Dome Temperature vs. Cooling Circuit Performance. Successful designs should achieve coolant pumping power <10% of the thermal power removed, while keeping the front surface below 1300℃, defining the rectangle shown in the figure.

There are several upper limits on temperature, only one of which is active for a given operating mode. The limit of creep fatigue will be important for pulsed and continuous operation, as both result in cyclic thermal loading with prolonged hold times at high temperature operation. However, over the course of two years (the period between scheduled shutdowns of current fission plants) a continually operating reactor may go through around 100 cycles in 2 years due to interrupted pulses, while a pulsed reactor may go through approximately 1 (pulse/hr) × 24 × 365 × 2 ≈ 18,000 cycles. This will mean a much lower creep-fatigue temperature limit will have to be put in place for pulsed operation, in order to ensure the divertor modules survive between shutdowns. It is possible that this lower temperature limit (to be determined, and dependent on materials, geometry, irradiation effects, mode of operation, etc.) may eliminate the overlap between achievable and acceptable design spaces, rendering a given concept unfeasible.

As a rough example to illustrate the point, from Figure 4.7 the predicted strain range which will allow a EUROFER 97 specimen to survive 100 cycles is around 1.1%, compared to around 0.8% for 18,000 cycles. For thermal strain, if the allowable ΔT were 1300°C for continuous operation as in Figure 4.10, the corresponding ΔT allowable for pulsed operation would be 1300°C × 0.8/1.1 ≈ 950°C. This is clearly a much more difficult design target to achieve, and the situation is aggravated by thermomechanical worsening of S-N performance and the necessity of using design curves.

If in this way no divertor concepts are found to be feasible for 2 years of pulsed operation, then interim shutdowns will have to be planned in order to replace the divertor modules. This will raise the cost of electricity (COE) from the reactor as discussed. Creep fatigue is still an issue for continuous operation, but further work may prove that a particular concept may be suitable for 2 years under continuous mode, while no concept can be found which can operate for 2 years in pulsed mode.

4.10. Future Studies

Work is continuing in various fields, for example: the characterisation of W, W-alloys, and EUROFER (especially irradiation effects etc.); increasing the safe operational temperature range of W-alloys and RAFM steels; development of the SXD concept; and prototyping and testing of the

divertor concepts mentioned in this chapter. One important area of future work is to check emerging literature, conference proceedings, etc., in order to keep up to date with current developments and breakthroughs in relevant fields.

Once the full effects of irradiation on these materials are sufficiently well characterised, it would be useful to embark on a program of work again comparing the various concepts discussed in this chapter (or their latest design iterations at that time), in order to get a more realistic idea of their performance under DEMO-relevant conditions (both pulsed and continuous operation). Of particular interest are the issues of creep-fatigue, and irradiation effects, which have not been accounted for adequately in the experiments performed so far. Further studies similar to [4.15] and [4.16] based on time-dependent instead of steady-state analysis, including reliable data on radiation effects, erosion and sputtering etc., would be useful.

The measured quantities from tests on prototypes of the helium-cooled concepts match well with predicted values from finite element analysis. The geometry of prototypes have also been accurately measured in a 'cold' state. However, one important issue is that coolant flows channels may be subject to large deformations or damage during operation (high temperature, high gas velocity and pressure). In all helium-cooled concepts, the channels are designed to be narrow (around 0.1 – 1mm gap). Previous studies have shown how relatively small changes in flow geometry can have a large impact on operating point [4.15]. It is conceivable that relatively small deflections due to thermal gradient could cause a narrowing of the channels and hence a choking effect in the flow. The reduced coolant flowrate could lead to a buildup in temperature in the divertor module, which would aggravate the problem further and eventually cause the module permanent damage through overheating. This is just one example of a failure mode which calls into question the robustness of design of this type of divertor. It would be useful to perform experiments during which the geometry of the divertor module (especially this critical dimension, coolant channel width) was measured "in situ".

Another potential problem with the helium cooled concepts is the possible erosion of the coolant channel walls over time due to the high pressure, high velocity gas flow. This could have a range of consequences, for example fouling of the heat exchanger, activation of the coolant stream, or total blockage of the narrow channel (leading to overheating and permanent damage). This issue will need to be investigated in more detail in order to prove concept viability.

As a separate investigation, it may be worthwhile to undertake a preliminary feasibility study on SXD in DEMO-relevant (conventional tokamak) geometry. Such a modification may result in a relaxation of design objectives for divertor modules as discussed above, making it possible to find a feasible design for pulsed operation even if none can be found for a conventional divertor arrangement.

4.11. References

[4.1] "Discussion on fast track and impact on material R&D strategy – fusion material issues for the energy systems in future", S. Konishi, J. Nuc. Mat. 329-333 (2004) 161-165.

[4.2] "Metallurgical properties of reduced activation martensitic steel Eurofer'97 in the as-received condition and after thermal ageing", P. Fernández et al, J. Nuc. Mat. 307-311 (2002) 495-499

[4.3] "Divertor conceptual designs for a fusion power plant", P. Norajitra et al, FEDG 83 (2008) 893-902.

[4.4] “Evaluation of divertor conceptual designs for a fusion power plant”, M. Ferrari et al, FEDG 56-57 (2001) 255-259

[4.5] “Optimization of a water-cooled divertor for the European power plant conceptual study”, A. Li Puma et al., Fus. Eng. Des. 61-62 (2002) 177-183

[4.6] “Structural materials for DEMO: The EU development, strategy, testing and modelling”, R. Laesser et al, FEDG 82 (2007) 511-520

[4.7] “Overview of the European Union fusion nuclear technologies development and essential elements on the way to DEMO”, R. Andreani et al, FEDG 81 (2006) 25-32.

[4.8] “Tensile and low cycle fatigue properties of different ferritic/martensitic steels after the fast reactor irradiation “ARBOR 1”, C. Petersen et al., J. Nuc. Mat. 386-388 (2009) 299-302

[4.9] “Impact property degradation of ferritic/martensitic steels after the fast reactor irradiation “ARBOR 1”, C. Petersen et al., J. Nuc. Mat. 367-370 (2007) 544-549

[4.10] “The manufacturing technologies of the European breeding blankets”, A. Cardella et al., J. Nuc. Mat. 329-333 (2004) 133-140

[4.11] “Current status of He-cooled divertor development for DEMO”, P. Norajitra et al., Fus. Eng. Des. 84 (2009) 1429-1433

[4.12] Super X divertors for solving heat and neutron flux problems of fusion devices”, P.M. Valanju et al., j.fusengdes.2009.06.001 (article in press)

[4.13] Super-X divertors and high power density fusion devices, P.M. Valanju et al., Phys. Plasmas 16 (2009) 056110

[4.14] Super-X Advanced Divertor Design for MAST Upgrade, S. Lisgo et al., ECA Vol. 33E, O-4.046 (2009)

[4.15] Optimization of the HETS He-cooled divertor concept: Thermal-Fluid and structural analysis, P. Karditsas, Euratom/UKAEA Fusion Association, PPCS/TW3-TRP-001

[4.16] Performance Analysis of the HETS and HEMJ He-cooled divertor concepts

[4.17] D. Maisonnier et al., Fus. Eng. Des. 81 (1123-1130)

[4.18] A. Li Puma et al., Fus Eng. Des. 61-62 (177-183)

[4.19] P. Karditsas, Euratom/UKAEA Fusion/CCFE, PPCS/TW4-TRP-001 (2004)

Data sources for Figure 4.7:

[I] Petersen et al, Tensile and Low Cycle Fatigue properties of different ferritic/martensitic steels after the fast reactor irradiation ‘ARBOR 1’, J. Nuc. Mat. 386-388 (2009) 299-302
[II] J. Rensman, NRG Irradiation Testing: Report on 300°C and 60°C Irradiated RAFM steels, NRG Report #20023/05.68497/P, Aug. 2005
[III] Section on First Wall Cyclic Loading, this report

5. Effect of Pulsed Operation on Coil Stresses and Fatigue

5.1. Introduction

Pulsed reactor operation imposes alternating stresses on all the coils. The Central Solenoid (CS) and some of the PF coils reverse their current fully, cycling both the self-forces and the force due to the TF coils. The TF coil current remains approximately constant, but the forces on the TF coil due to the CS and many of the PF coils reverse.

This section describes a proposed approach to analyse the effects of fatigue on the coils. (Fatigue of the superconductor itself is discussed in another section.) Implementation of this approach has only just begun.

The PROCESS reactor systems code includes a section which calculates the stress in the TF coils. The optimisation code then constrains this stress according to the material properties specified. This is legacy code which is not fully documented or validated.

The structural part of the TF coils is of great importance in determining the overall size and cost of the reactor. In ITER-98 (ITER-EDA) for example, the TF coils and their immediate structures constitute more than half the total weight of the magnet system, as follows.

Table 5.1

TF coils (including winding pack, case and intercoil structures)	15 000 tonnes
PF coils	6 500
CS coil (including inner and outer support cylinders)	1 300
Total of all coils (including intercoil and preload structures and gravity supports for coils and vacuum vessel)	26 000

Furthermore, the TF coils occupy valuable space in the central part of the reactor, competing with the central solenoid and the breeding blanket.

Preliminary PROCESS calculations for a pulsed reactor with some additional current drive give TF coils that are more than 2 m thick in the outboard region. It would be valuable to have a set of robust and documented equations for the TF coils to replace those in PROCESS currently.

Initial work has therefore concentrated on the stresses in the TF coils.

5.2. Load Cases

The alternating and mean stress will be calculated using as load cases the states with the extreme values of the current in the CS, referred to as IM (Initial Magnetization), and EOB (End Of Burn). The currents for these cases are given for ITER-98 below. Two more load cases are also considered. One occurs shortly after EOB, as listed below with the name “1328”. The other occurs after a disruption, when the plasma current is interrupted, and the induced currents in the surrounding components have dissipated, while the currents in the CS and PF coils remain as at EOB.

(This is a simplified form of the sequence used for stress analysis of the TF coil in ITER-98, which was as follows. Depending on the type of stress analysis (local or global) and the amount of detail put in the analysis model, the recommended load cases for stress analysis were:
Dead Weight > Cool Down > TF on Only >IM -> CS current zero > Start Of Flattop > Start Of Burn > EOB.)

Table 5.2: Coil currents for different states of ITER-98, MA-turns

Time, s	Plasma	CS	PF1	PF2	PF3	PF4	PF5	PF6	PF7	PF8	PF9	state
0	0	127.6	5.43	13.56	0.24	0.27	1.76	-4.36	3.93	14.35	5.42	IM
1200	21.0	-138.0	-0.47	-3.94	-7.82	0.0	-12.8	-6.50	6.27	6.18	2.31	EOB
1328.6	15.0	-130.0	-2.00	-5.29	-4.87	0.0	-9.17	-1.00	-0.09	5.50	3.27	"1328"
n.a.	0	-138.0	-0.47	-3.94	-7.82	0.0	-12.8	-6.50	6.27	6.18	2.31	"Disruption"

5.3. Material Properties

The material properties have been taken from those used in [5.1] (ITER-2001). For the winding pack the DDD gives orthotropic (anisotropic) values. In the present simpler analysis we have averaged these to give a single isotropic figure.

Table 5.3

	TF coil case	**Winding pack, smeared properties**
material	EC1 strengthened austenitic as cast sections, as used for TF coil case, outer leg regions	Radial plates AISI 316L (or LN). Conductor jacket modified and aged 316LN.
elastic modulus	190×10^9 Pa	70.7×10^9 Pa
Poisson's ratio	0.3	0.213
Paris constant *C*	5.77×10^{-14} m/cycle	5.77×10^{-14} m/cycle
Paris constant *m*	3.73	

5.4. Fatigue data

Fatigue-life data measured at 4 K exists for a number of relevant materials, but it is not clear if it has been fully evaluated and reviewed. Fatigue analyses for the ITER magnets generally use crack growth analysis, but for simplicity we propose to use stress-cycles (S-N) fatigue life curves. The data shown below are from the "Current Configuration" part of the ITER document management system (ref. [5.2]), together with the comment,

> At this writing, the data are too limited to permit determination of recommended fatigue-life values. The provisional minimum fatigue strengths at 10^5 cycles at 4 K of the alloys that have been tested are listed here:
> JN-1 — 1400 MPa; 316LN — 1100 MPa; RF alloy — 600 MPa.

Using a safety factor of 2 in stress, as is conventional for S-N curves, this gives a design fatigue strength at 10^5 cycles = 550 MPa for 316LN at 4K.

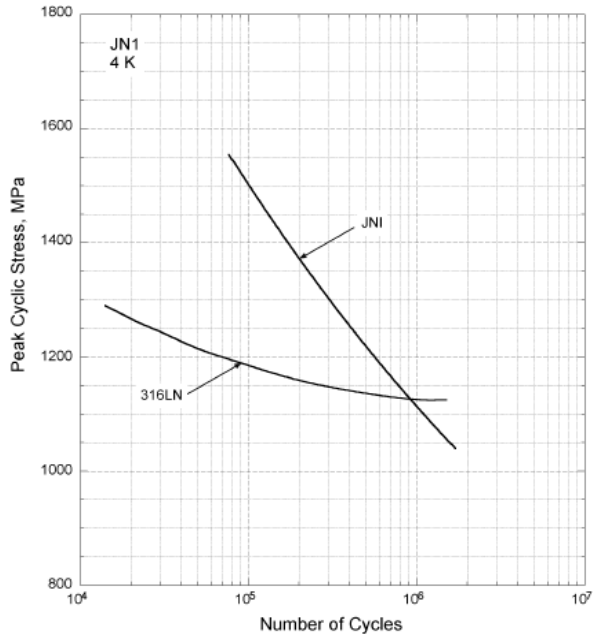

Figure 3.4.1. Stress-controlled, axial, tensile fatigue-life data for JN1, a strengthened austenitic steel intended for large structural components. Data from Umezawa et al. [1994].

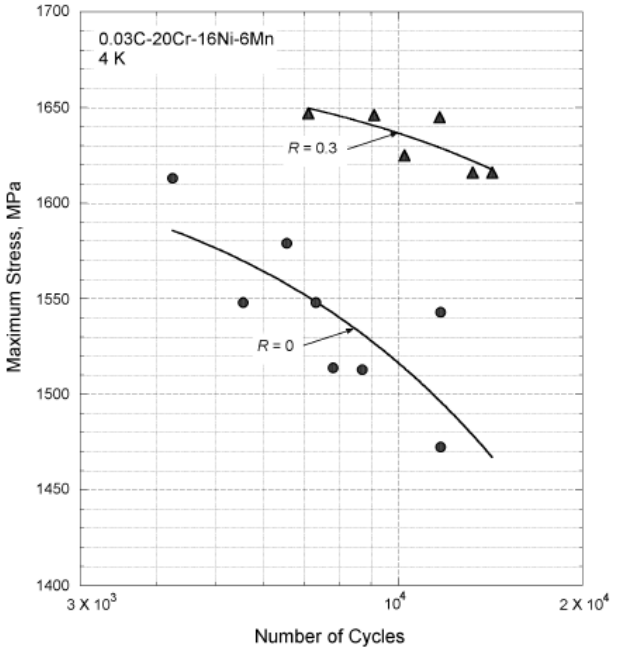

Figure 3.4.2. Stress-controlled, axial, tensile, low-cycle fatigue-life data on the RF austenitic steel 0.03C–20Cr–16Ni–6Mn, $R = 0$ and 0.3 (Alekseev et al [undated]; Anonymous [1993]).

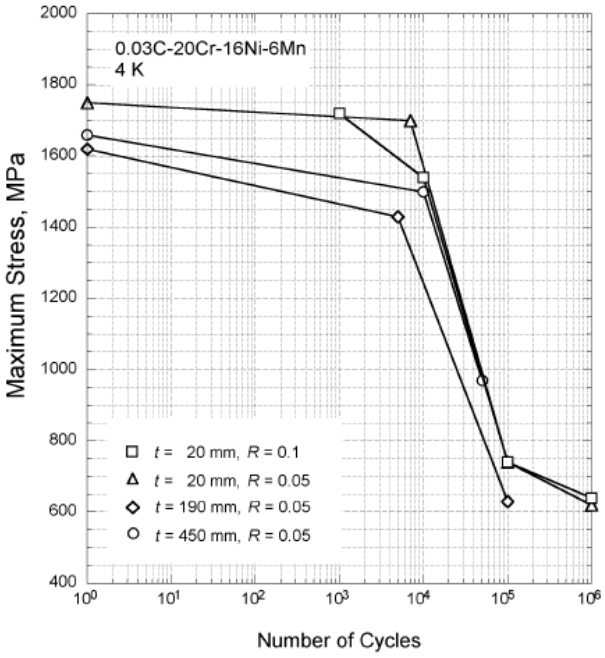

Figure 3.4.3. Stress-controlled, axial, tensile, high-cycle fatigue-life data on the RF austenitic steel 0.03C–20Cr–16Ni–6Mn (Anonymous [1993]); Stepanov [1993]).

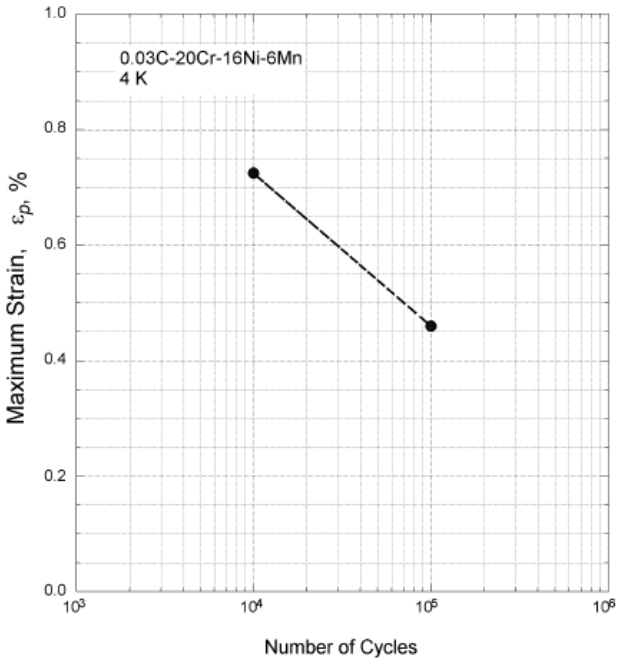

Figure 3.4.4. Strain-controlled, axial, tensile, fatigue-life data on the RF austenitic steel 0.03C–20Cr–16Ni–6Mn (Anonymous [1993]); Stepanov [1993]). Specimens were obtained from 190-mm-thick plate.

Fig. 5.1

However, it is likely that more comprehensive data exists for crack growth. Fatigue life curves can if necessary be calculated by integrating the Paris law of crack growth, provided a suitable (constant) value of the shape factor for a likely defect can be chosen. Three examples are below. The life does not depend sensitively on the crack length at which failure occurs, but the size of the assumed starting crack is critical.

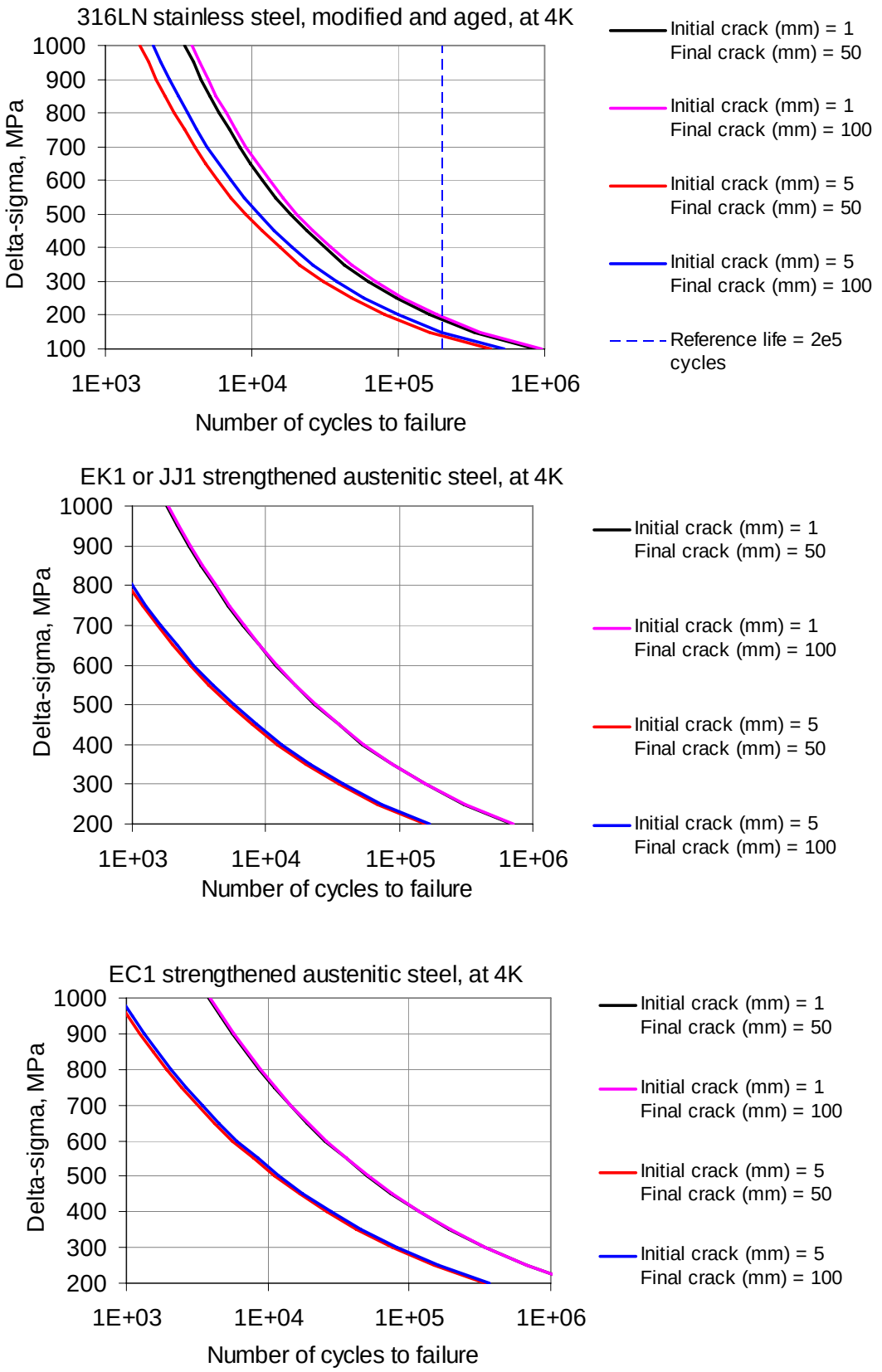

Fig. 5.2: *Fatigue life of austenitic stainless steels, estimated from Paris constants (ref. [5. 1]), as a function of the alternating component of the maximum principal tensile stress. Shape factor for stress intensity factor = 1.12*

Using the safety factor of 2 in number of cycles, as recommended in [5.1] for crack growth analysis, we derive a design fatigue strength at 10^5 cycles = 150 – 200 MPa for 316LN at 4K – about a third of the value derived above from S-N data. We conclude that there is considerable uncertainty involved in using the S-N approach for these materials at 4 K. In this report we will use the design curve below, which includes the safety factor.

EC1 strengthened austenitic as cast sections.

Initial crack depth = 5 mm
Crack depth for failure = 50 mm.

Safety factor = 2 (cycles), i.e.
Design life = ½ Number of cycles to failure (predicted)

Paris constant C = 5.77 x 10^{-14}
Paris constant m = 3.73 (units MPa, m)

Shape factor for stress intensity factor = 1.12.

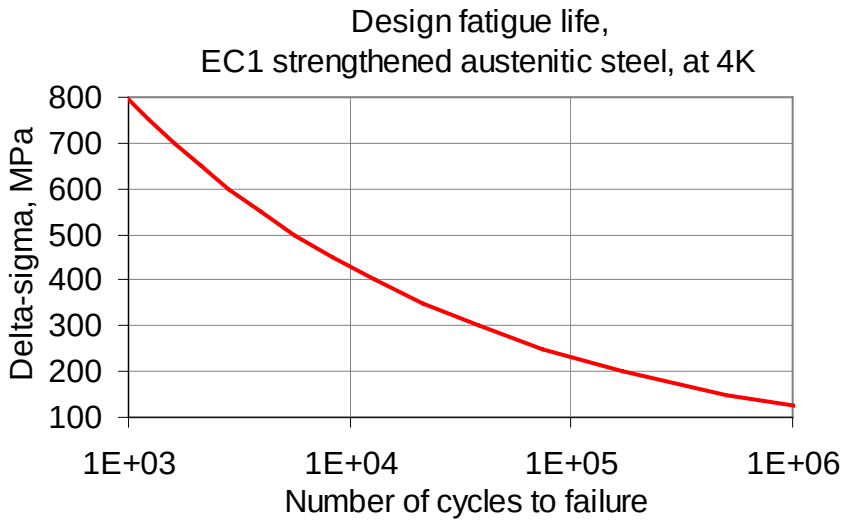

Fig. 5.3: Alternating component of the maximum principal tensile stress

5.5. Present state of the finite element model

The PF coils, CS and plasma are modelled as current sources with uniform current density, with no structural information. The sizes and locations are based on the ITER-98 design.

The TF coil is an approximate constant-tension D. It consists of four circular segments, whose radius of curvature is proportional to the major radius, as required by the constant tension form. In addition there is a vertical straight inboard leg. The coil consists of a winding pack, which includes the superconducting cable and its immediate support components, surrounded by a case. The cross-section of the case is square, and then sliced at the planes where adjacent coils are wedged together. The winding pack is modelled as a single homogeneous component. It is a trapezium, symmetrically placed in the case.

The inter-coil support structure forms a double segmented toroidal shell as shown. This represents a simple design which is nevertheless appropriate for the intercoil stresses. The model includes one sector of the intercoil support structure, with the TF coil in the centre. Cyclic boundary conditions are used. The displacement vector at each node on the left-hand face of the sector is constrained to be equal to that on the corresponding node on the right-hand face. Angled apertures for neutral beams are included (3 m x 1.5 m). The intercoil shells are locally joined to stiffen the structure around the apertures. This model is of course over-optimistic, as in reality other apertures will also

be required. The structure has been made substantially thicker in the toroidal direction where the vertical leg meets the curved section, to reduce localised stresses in the inter-coil shells.

The gravity support is modelled in a simplified way as a short cylinder attached to the case in the outboard region. The base of this part is constrained to move only in the radial direction. Although gravity has not yet been taken into account, this constraint is required to prevent unphysical vertical and toroidal movement.

The TF coils winding packs are modelled as uniform electrical conductors. Consequently the current is not distributed uniformly, but concentrates on the inside where it can take a shorter path. This is physically incorrect for a coil, but is considered an adequate approximation for the present. The magnetic field in the TF coil winding pack due to all the coils is calculated using the Biot-Savart law. This gives the Lorentz force in the winding pack, which is then used for the stress-strain calculation.

The following quantities are used to validate the calculation of Lorentz force:

The total Lorentz force (centering force) per coil,
The Lorentz force on the upper half coil (vertical tensile force per half coil)
Maximum total B field
B field at the plasma major radius.

The figures below show the present state of the finite element model and some example preliminary results. The stresses due to the magnetic field of the TFC are shown separately, as these dominate. The total stresses are the sum of those due to the TFC field and those due to the other fields, provided a strictly linear model is used. The results are shown as with the deformations exaggerated for clarity. The edges of the undeformed shape are also shown. The maximum and minimum values of the quantity plotted are shown at the extremes of the contour legend.

The volumes and masses of the modelled volumes are as follows.

Table 5.4

	Volume, m^3	Density, kg/m^3	Mass, tonne
Case (including gravity support and intercoil shells)	76.3	7930	605
Winding Pack	38.0	7500*	285
Total for 20 coils			17 800

*Taken as 95% of density of stainless steel.

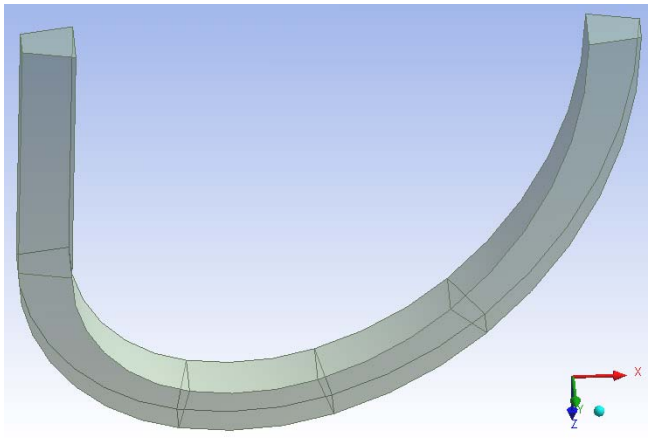

Half of TFC winding pack

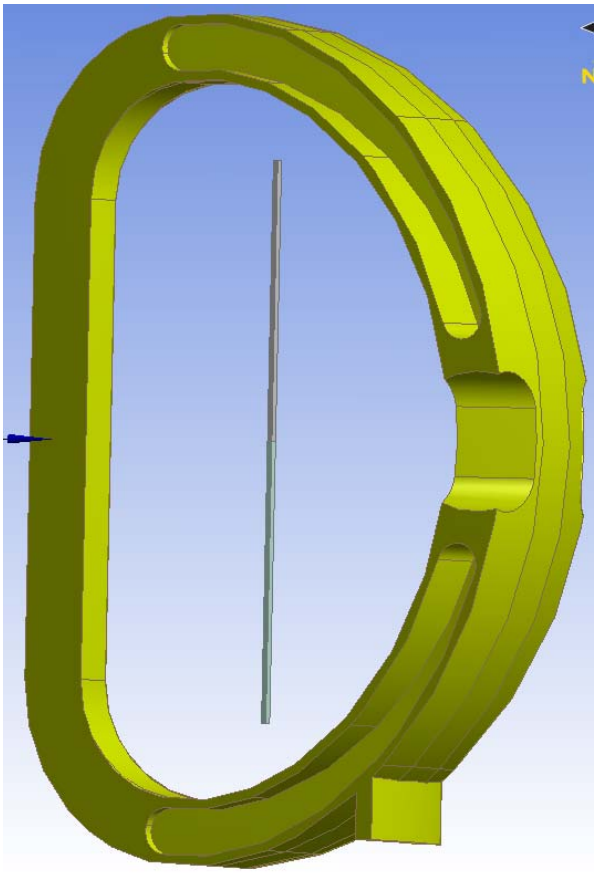

Lower half of TFC coil sector

Fig. 5.4

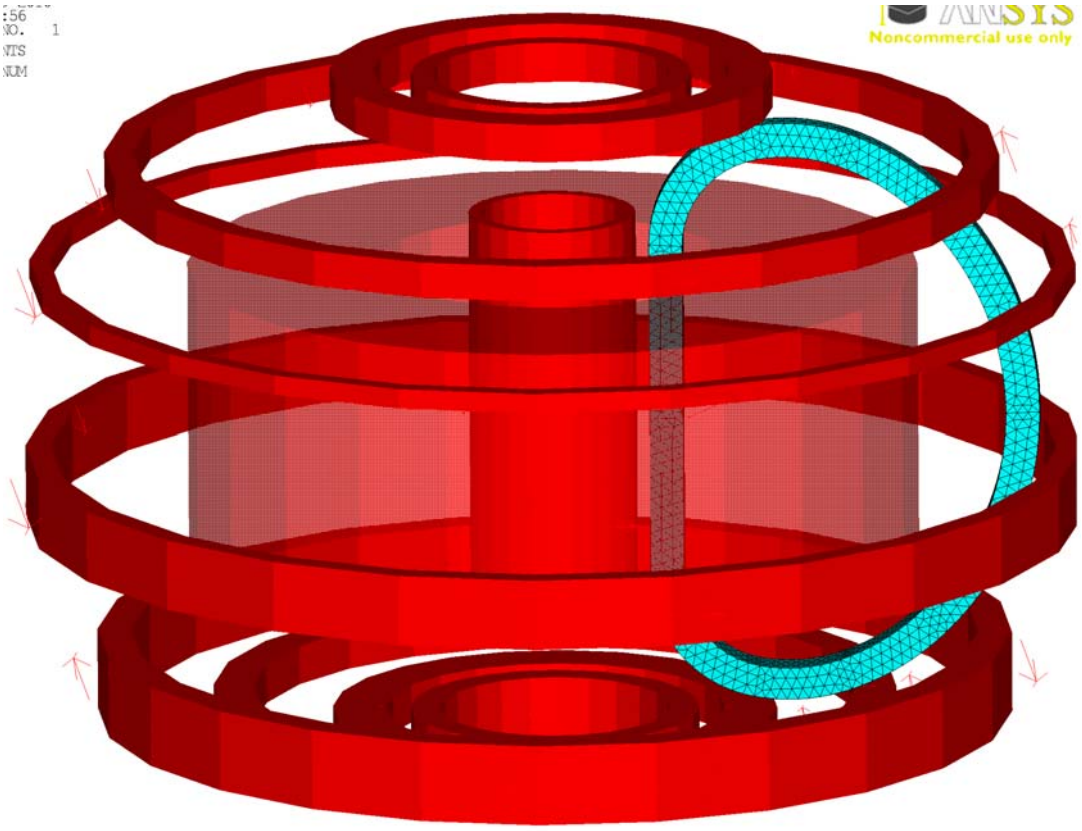

Fig. 5.5: All coils and plasma. Plasma is shown translucent so the CS can be seen.

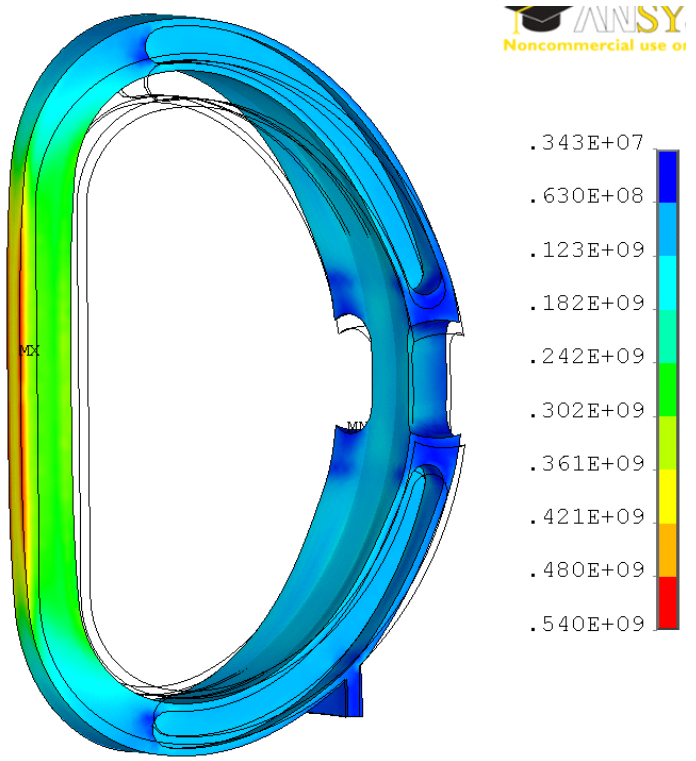

Von Mises stress in the TFC case due to self-forces only

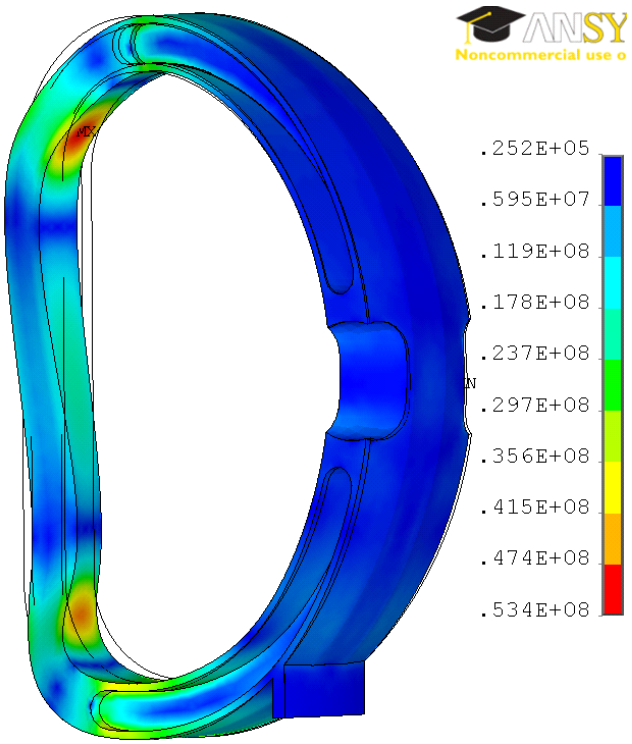

Von Mises stress in the TFC case due to the field of PFC and CS only, Pa. Initial Magnetisation

Fig. 5.6

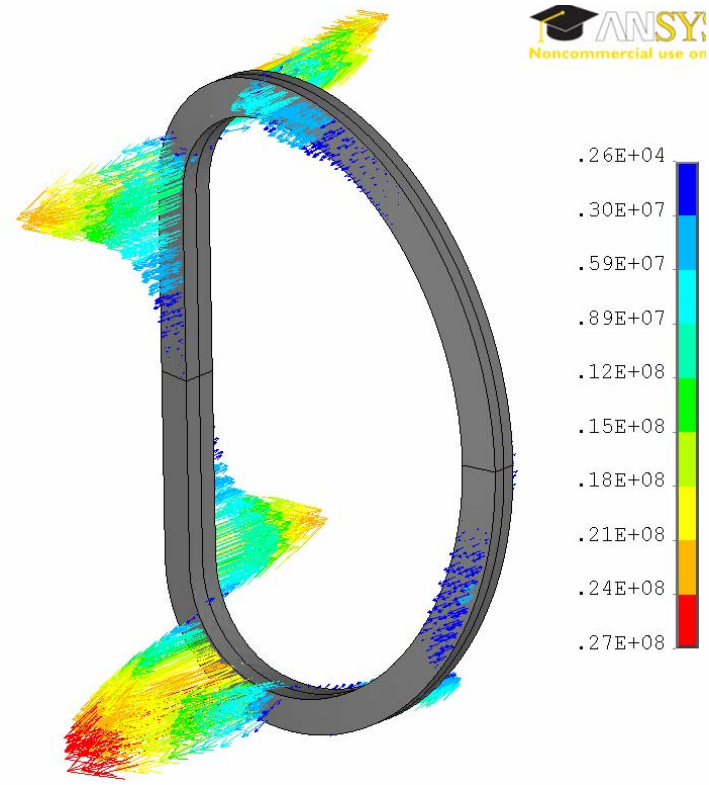

Force per unit volume in the winding pack, due to the field of the PFC and CS only, N/m^3. Initial Magnetisation.

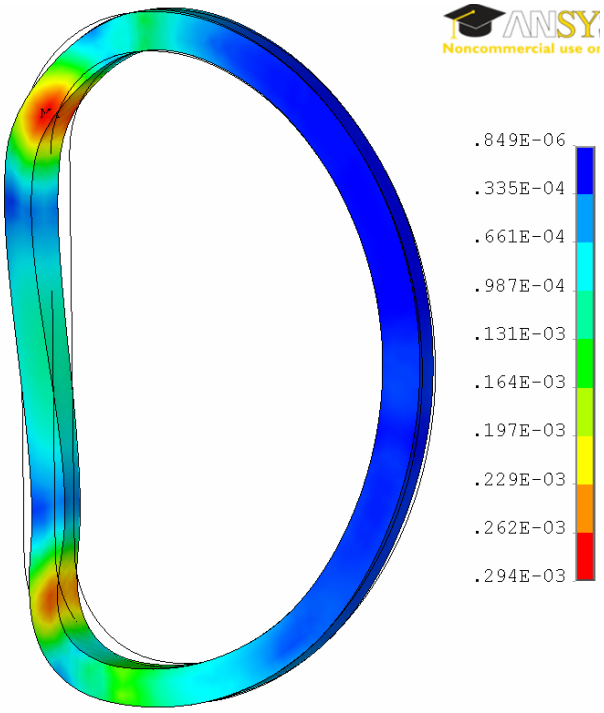

Von Mises strain in the TFC winding pack due to the field of PFC and CS only, Pa. Initial Magnetisation.

Fig. 5.7

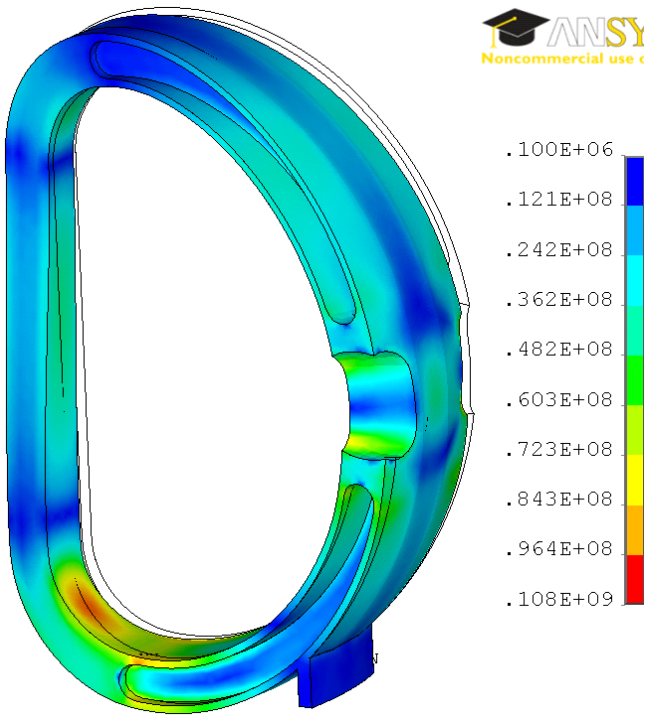

Von Mises stress in the TFC case due to the field of PFC, CS and plasma only, Pa. End of Burn.

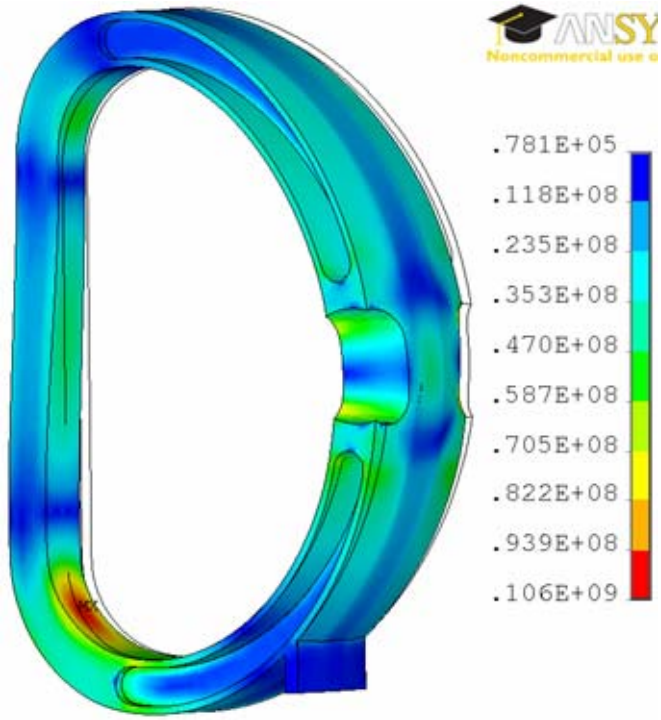

Von Mises stress in the TFC case due to the field of PFC and CS only, Pa. "Disruption"

Fig. 5.7

The alternating stress can be estimated by subtracting the stress tensors between pairs of load cases. The stress due to the magnetic field of the TF coil will of course cancel in the subtraction. Some examples are shown below.

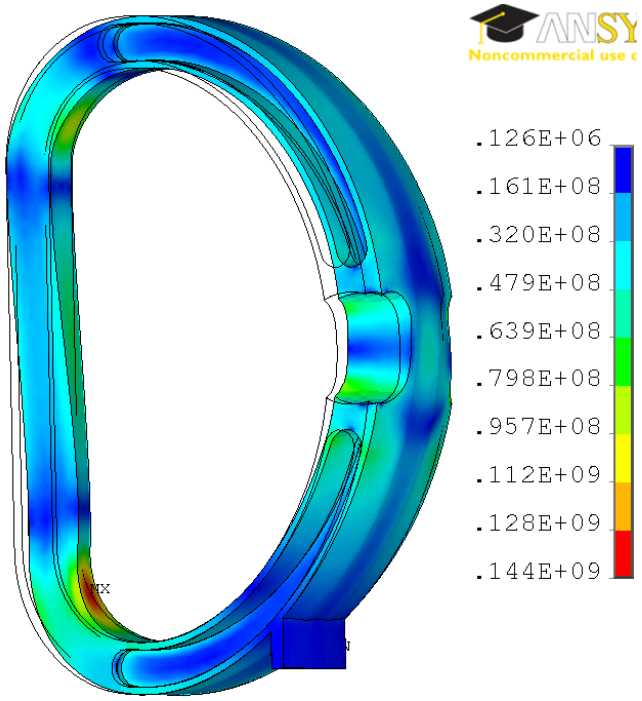

Von Mises stress *difference* in the TFC case, Initial Magnetisation minus End of Burn, Pa.

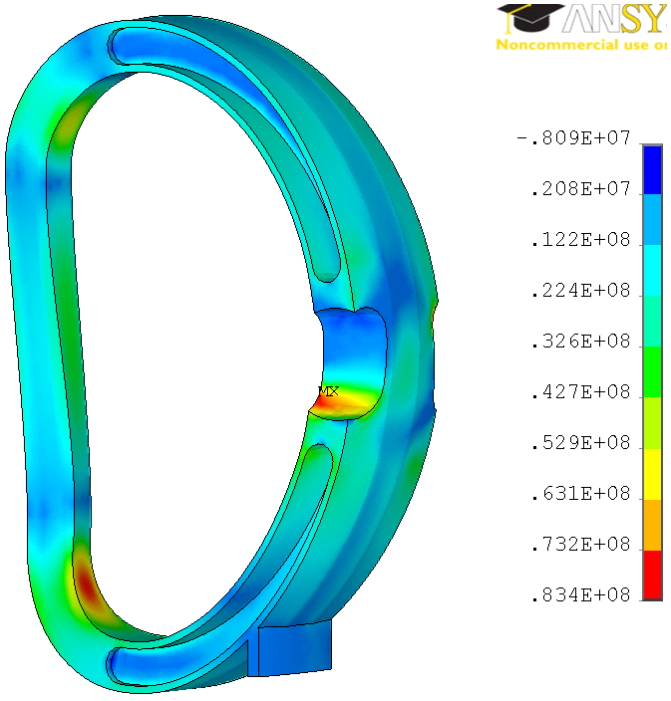

First principal component of stress *difference* in the TFC case, Initial Magnetisation minus End of Burn, Pa.

Fig. 5.8

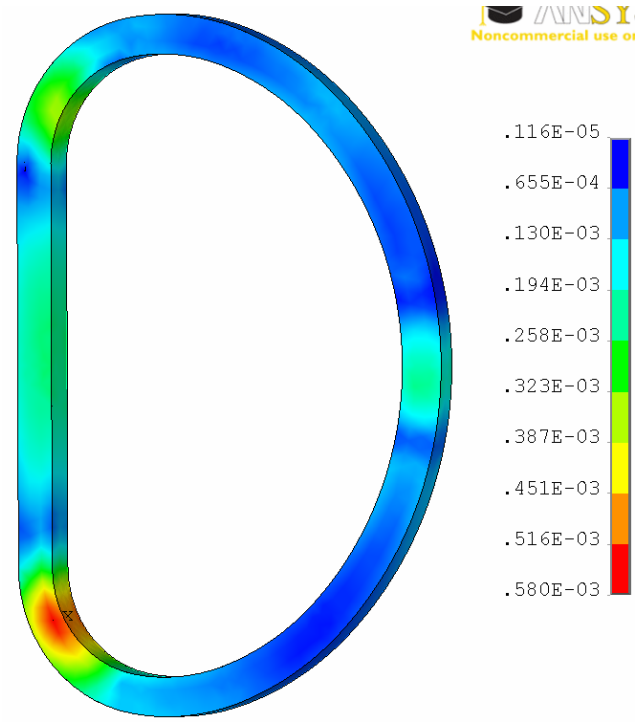

First principal component of strain *difference*, Initial Magnetisation minus End of Burn. (undeformed model)

Fig. 5.9

5.6. Discussion of example preliminary results

Table 5.5: The biggest stress difference found is as follows.

Load cases subtracted	Maximum first principal component of the stress difference	Design life
Initial Magnetisation - End of Burn	83 MPa	> 10^6 cycles

This suggests that in this model the case of the TF coil is much stronger than required for fatigue purposes.
In the winding pack, the maximum first principal component of stress difference in the same subtraction is 55 MPa (0.58% strain - see figure above). We do not yet have a design life curve for the winding pack.

The inter-coil structure has been designed to reduce the localised peak alternating stresses. Nevertheless, stresses are non-uniform. Crack-growth analysis would fully account for the variations in stress, whereas the use of a simple fatigue-life curve assumes that the stress is constant.

We have calculated models with a chamfer on the inboard edges of the case, winding pack or both, but this did not reduce the peak DC stress.

We will need to validate the calculated stresses by comparison with hand calculations.

5.7. Parameterisation for PROCESS

The PROCESS code allows most of the parameters to vary in order to optimise the cost of electricity. The stresses therefore will need to be expressed as simple equations in a small number of parameters. The equations will have to be derived as fits to a family of FE results. The proposed parameters are as follows.

Table 5.6: Independent Variables

	Comments
Major radius of outer leg midline	
Winding pack width	When the winding pack dimensions are changed, its properties will be held constant. This implies that the superconductor fraction remains constant at the ITER-98 value.
Case width	The case is square (except on the wedging surfaces).
Thickness of inter-coil supporting shells	The thicknesses of the two shells will remain equal.
Total TFC current per coil	The PFC, CS and plasma currents are constants for a given load case. By changing the TFC current, the relative value is changed. For given current ratios, stresses will be proportional to the absolute value of the currents.

Table 5.7: Constants

Number of coils
Fraction by which plasma major radius is off-centre in the TFC aperture
Ratios of radii of PF coils, CS, plasma and TF coil
Ratio of radii of outer and inner legs

It is planned to run finite element models for values of each parameter around a set of reference values. For each model the peak alternating equivalent stress in the case will be calculated. For the winding pack, the peak alternating equivalent strain is more appropriate, as the effective (smeared) elastic modulus is reduced because of the presence of the superconducting cable and because the winding pack consists of several disjoint plates. These stresses and strains will then be fitted by simple equations in one variable at a time, which can be included in PROCESS. The optimisation code in PROCESS will then constrain the alternating stresses according to specified fatigue limits.

5.8. References

[5.1] ITER DDD 1.1, Section 2.2 Magnet Structural Analysis (2001). Coil case: p. 19; Winding Pack: p.25.

[5.2] Annex 7, Metallic Materials Mechanical- and Thermal-Property Database, 1997, N. Simon, (.. mechanical- (4 K) and thermal- (4 -295K) property data for the structural alloys that are considered for use in construction of the ITER superconducting central solenoid and toroidal and poloidal field coils.), Section 3, Strengthened Austenitic Steels for Large Structural Components.

6. Fatigue of Superconductors

6.1. Introduction

In a pulsed superconducting reactor the Central Solenoid, PF coils and plasma current are cycled in every pulse, but the TF coils operate in steady-state. The pulsing creates cyclic stresses on all the superconductors, including the TF coils. If the superconductors show fatigue, this will require the design to be modified to provide a bigger performance margin when first built.

The aim of this section is to review the relevant literature on the fatigue of superconducting cables (especially Nb_3Sn ITER cables). It is partly based on a discussion with Dr Matt Jewell of ITER, 27/8/09.

ITER cables are of the "cable-in-conduit" type. The superconducting strands are twisted into ropes inside a jacket (also called conduit), with a flow of helium through the void space and through a central channel. The strands will touch each other intermittently and bend at the crossing points when energised.

Pulsed energisation of superconductors also creates heat dissipation due to AC losses, which are not discussed here.

6.2. Testing

The qualification tests for ITER superconducting cables are being done at the SULTAN test facility at PSI Villigen. The cable sample is placed in a magnetic field and a large current is passed through it, so there are transverse Lorentz forces and locating forces from the case which oppose them. For ITER TF coil samples, the tests are done at 68 kA, 11 T, approximately 1000 cycles (see below).

Strand measurements are done at the TARSIS facility (Test ARrangement for Strain Influence on Strands, University of Twente), which tests the effects of tensile strain, bending and strand crossings. These sources of strain do of course occur in the tests of complete cables – so TARSIS is really a research facility for understanding mechanisms of degradation. The tests are always done in cyclic fashion with incrementing strain, rather than with repetitive cyclic loading, so they are not directly relevant here (refs [6.1] and [6.2]).

The University of Durham does cyclic tests on strands (see below).

It seems that no-one tests the effect of strain (DC or cyclic) on complete cables. Therefore the effect of the deformation of the coil case on the cable inside cannot be estimated.

6.3. Discussion

Strain. The ITER-FEAT Design Description Document (DDD) for the superconductor (ref [6.3]) is completely separate from the DDD on the structural analysis of the magnet (e.g. ref [6.4]). The conductor document seems to ignore the strain imposed on the cable by the deformation of the case, and only considers (1) thermal contraction of the copper and jacket relative to the superconductor, and (2) the transverse forces and strand bending due to the Lorentz force acting on a single cable. In fact these aren't analysed in detail either – but tested in SULTAN.

Dwell time under strain (creep-fatigue). Dr Jewell of ITER believes that the effects of creep-fatigue will be negligible in Nb_3Sn, since it is a brittle material and is very cold. Since brittle materials such as ceramics and rock fail under sustained stress by a mechanism with similar strain vs time curves to plastic creep in ductile materials, this assertion needs to be checked. Creep normally occurs when materials yield plastically when stressed to a significant fraction of the yield stress at a significant fraction of the melting point. Creep-fatigue presumably occurs under somewhat similar conditions – although this has not been confirmed experimentally.

TF coils. The qualification tests for the TF conductors are carried out for 1000 cycles only, because this is the design requirement for energisation cycles of the TF coil. There is of course additional cyclic stress during each plasma cycle, but this is smaller, and not taken into account.

Some samples show degradation continuing up to (and presumably beyond) 1000 cycles, while some show either very little change or a deterioration followed by stabilisation.

The PF coils are NbTi – a ductile material. Fatigue is considered less of an issue. Qualification tests have not been finalised.

The **Central Solenoid** is Nb_3Sn, and is cycled with each plasma pulse. Dr Jewell accepted that this presents a "***unique problem***." The qualification tests for the CS have also not been finalised.

6.4. Conclusion

The effect of cyclic Lorentz forces is measured for ITER cables, but only up to 1000 cycles, which is not enough.
The effect of coil deformation is not measured and cannot be calculated.
It is not possible at present for us to estimate the effect of pulsing on the performance of the superconducting cables in DEMO magnetic field coils.

There is still a need for measurements of the following types.

- Cable and strand.
- Strain cycles 1300 to 50,000
- Dwell time under strain (creep-fatigue)
- Multi-axial strain
- Thermal cycling;

All with

- NbTi and Nb_3Sn
- Critical current measurement
- AC loss properties
- Cold cycling
- Micro-structural analysis.

6.5. Summary of some available data

ITER DDD

Extract from ref 3 follows.

> *Nb_3Sn Degradation*
>
> A number of experiments on Nb_3Sn strands in cable-in-conduit conductors have shown that the full-size conductor can display performance degradation relative to results expected on single strands in isolation. …
>
> The cause of this degradation has been traced to local micro filament fracture within the individual strands …
>
> The local transverse magnetic loads on the cables produce a degradation of the strand superconducting performance. The strands carry two loads. One is a distributed magnetic load, and the other is a cumulative load, as the overall transverse magnetic force is transmitted through the cable to one side of the jacket (about 40t/m in the TF conductor). These loads produce a combined pattern of cyclic bending and transverse compression in the strands, both of which can be expected to affect the local filament superconducting performance. The tensile strains are sufficient to cause filament breakage. Current can locally transfer around these regions of low critical current in the copper/bronze matrix, at the cost of a small electric field. Overall, the cable degrades, displaying an earlier and more gradual superconducting transition.
>
> As will seen in section 6.1 (Figs 6-1 to 6-3), the allowance for degradation of the temperature margin is about 0.7 K in the TF conductor and about 1.5 K in the CS conductor, depending on the operating strain. The difference is due to the high cyclic loading in the CS, which produces significantly more degradation in cyclic conductor tests.

Note that the additional temperature margin required for the CS conductor appears to be determined by judgement alone, since the section mentioned (6.1) does not give or refer to any data on conductor cycling.

Strand Measurements

Effect of axial strain cycling on the critical current density and n-value of ITER niobium-tin wires
D.M.J. Taylor, D.P. Hampshire, ref [6.5]

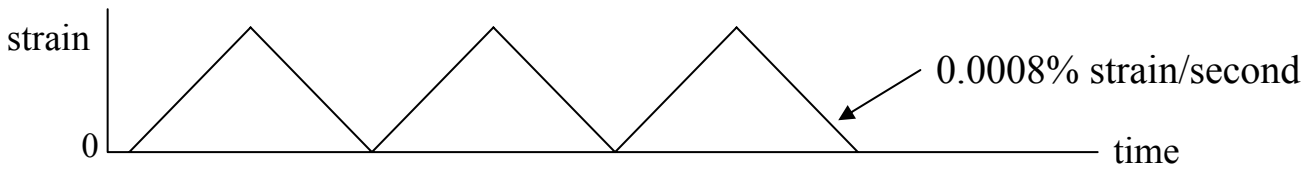

Fig. 6.1

Table 6.1

Number of cycles	Applied strain	Effects on critical current
~500	up to 0.282%	No effect (apart from 1% decrease caused by the first test-cycle for the EM-LMI wire)
1	0.565%	1% − 2% increase
~500	0.339% - 0.565%	increases by 2% - 14% (EM-LMI wire), 6% - 11% (VAC wire)
1	> 0.677% (~0.4% intrinsic strain)	large irreversible decreases
~1300 cycles total		

Influence of cyclic loading at room temperature on the critical current at 4.2 K Nb_3Sn superconducting composite wire,
S. Ochiai and K. Osamura, ref 6.

These measurements were made using cycling at room temperature, so they are of limited relevance. Except for the first cycle (which usually improved the critical current), there was no change in behaviour until the wire failed outright.

Table 6.2

Strain	Cycles to failure
0.35%	>105
0.56%	72,000
0.79%	34,000
1.4%	3,300

Cable Measurements

Qualification tests for ITER TF conductors in SULTAN
P. Bruzzone, *et al*, ref [6.7]

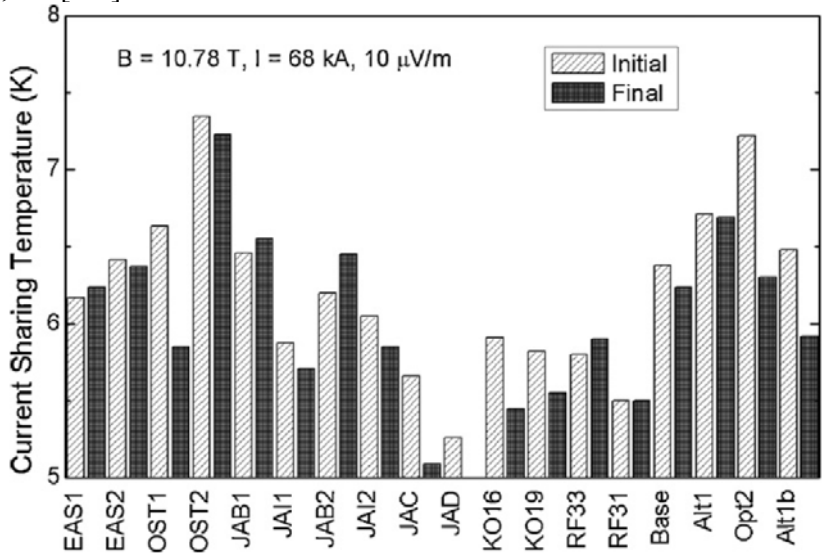

Fig. 4. Summary of the test results for current sharing temperature of the 18 ITER TF conductors at the first and last run of their test campaigns.

Fig. 6.2

A number of load cycles (600–1200) and one thermal cycle (warm-up/cooldown) were included in the test program, along with ac loss tests and dc test at other operating points. Here, only the first and the final critical temperatures (current sharing temperatures) run at ITER TF coil operating conditions are shown.

There is no visible pattern – some conductors improved over 1000 cycles, some deteriorated.

Some examples of the progress during cyclic loading in SULTAN are shown in the graphs below. Details of the conductors are available in the papers – for DEMO purposes we are concerned only to know whether conductors are available that do not show fatigue.

Test Results of Two European ITER TF Conductor Samples in SULTAN
P. Bruzzone et al, ref [6.8].

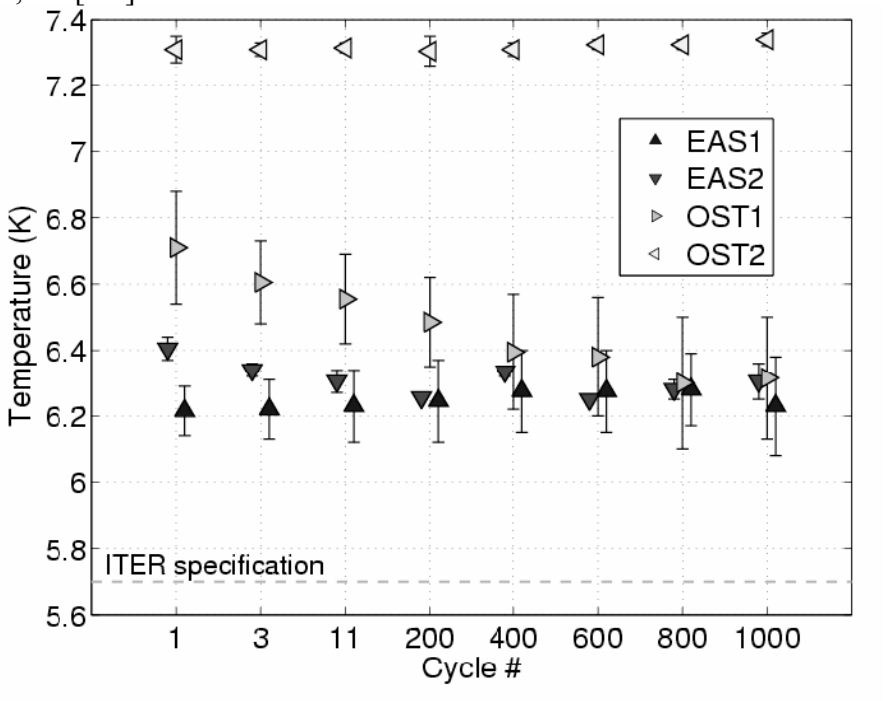

Fig. 6.3

Test Results of the First US ITER TF Conductor in SULTAN
N. N. Martovetsky et al, ref [6.9].

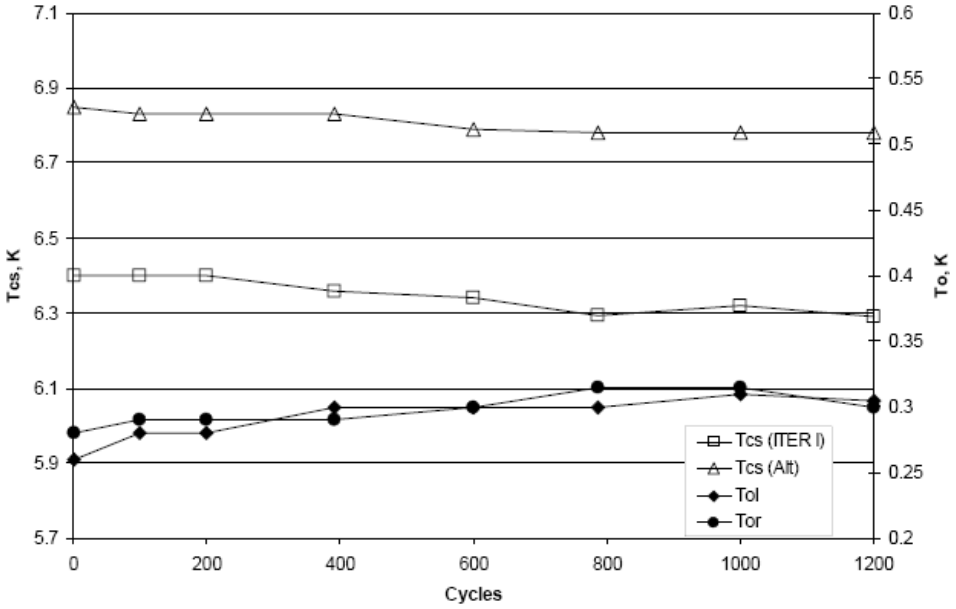

Fig. 4. Evolution of Tcs and To versus number of cycles. Tol is the To for the left leg (ITER) and Tor is for the right leg (Alt)

Cyclic load as above: load 0 - 68 kA and B = 11 T.

Fig. 6.4: Cyclic load as above: load 0 - 68 kA and B = 11 T.

Test Results of a Nb3Sn Cable-in-Conduit Conductor with variable Pitch Sequence
P. Bruzzone *et al*, ref [6.10].

Note that this is not an ITER qualification sample.

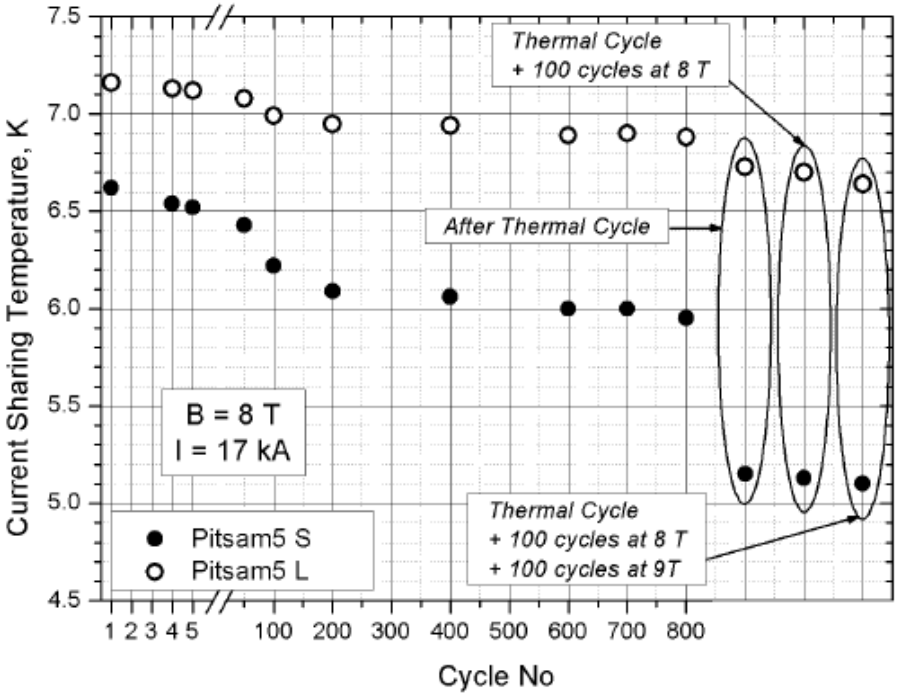

Fig. 5 Evolution of the T_{cs} performance for PITSAM5S and PITSAM5L during the whole test campaign

Fig. 6.5: Test at 17 kA, 8 T .

The process of degradation is continuous and likely not completed at the end of the test campaign.

6.6. References

[6.1] Spatial periodic contact stress and critical current of a Nb3Sn strand measured in TARSIS, A Nijhuis1, Y Ilyin andW A J Wessel, Supercond. Sci. Technol. 19 (2006) 1089–1096, https://user.iter.org/?uid=25DBA7&action=get_document.

[6.2] Nb3Sn strand deformation tests with TARSIS/Pacman, A. Nijhuis et al, https://user.iter.org/?uid=2FPT3L&action=get_document.

[6.3] ITER-FEAT Design Description Document: DDD 11, ITER_D_2NBKXY v1.2, Magnets - 7. Conductors, 09 September 2009 https://user.iter.org/?uid=2NBKXY&action=get_document

[6.4] Design Description Document: DDD 11 Magnets ITER_D_2MVZNX v2.2, 2. TF Coils and Structures, 8 September 2009 https://user.iter.org/?uid=2MVZNX&action=get_document

[6.5] Effect of axial strain cycling on the critical current density and n-value of ITER niobium-tin wires, D.M.J. Taylor, D.P. Hampshire http://www.dur.ac.uk/superconductivity.durham/Axial_strain_cycling.pdf

[6.6] Influence of cyclic loading at room temperature on the critical current at 4.2 K Nb_3Sn superconducting composite wire, S. Ochiai and K. Osamura, Cryogenics (1992) vol 32, p. 584.

[6.7] Qualification tests for ITER TF conductors in SULTAN, Qualification tests for ITER TF conductors in SULTAN, P. Bruzzone, B. Stepanov, R.Wesche, Fusion Engineering and Design 84 (2009) 205–209

[6.8] Test Results of Two European ITER TF Conductor Samples in SULTAN, P. Bruzzone et al; Applied Superconductivity, IEEE Transactions on; (2008) Vol 18 pp 1088-1091, http://crppsc.web.psi.ch/Newsletter/MT20_4I06.pdf

[6.9] Test Results of the First US ITER TF Conductor in SULTAN, N. N. Martovetsky, Applied Superconductivity Conference, Chicago, August 2008, LLNL-PROC-406443, https://e-reports-ext.llnl.gov/pdf/364521.pdf

[6.10]Test Results of a Nb3Sn Cable-in-Conduit Conductor with variable Pitch Sequence, P. Bruzzone, http://crppsc.web.psi.ch/Newsletter/ASC08_1LPD06.pdf

7. Power Supply Cost Analysis for Pulsed Centre Solenoid

7.1. Introduction

The pulsed centre solenoid will require a power supply determined by the inductance, ramp currents (pre-charge and EOB) and dwell time of the solenoid pulse cycle.

The proposed system will use a 2 quadrant supply with reversing switch to swap the quadrants and an opening switch to initiate gas breakdown.

Power supply cost analysis can be achieved by comparing the solenoid theoretical power requirements to known power supply costs either directly or working out a cost per watt value. The data used is estimated and kindly supplied from those noted.

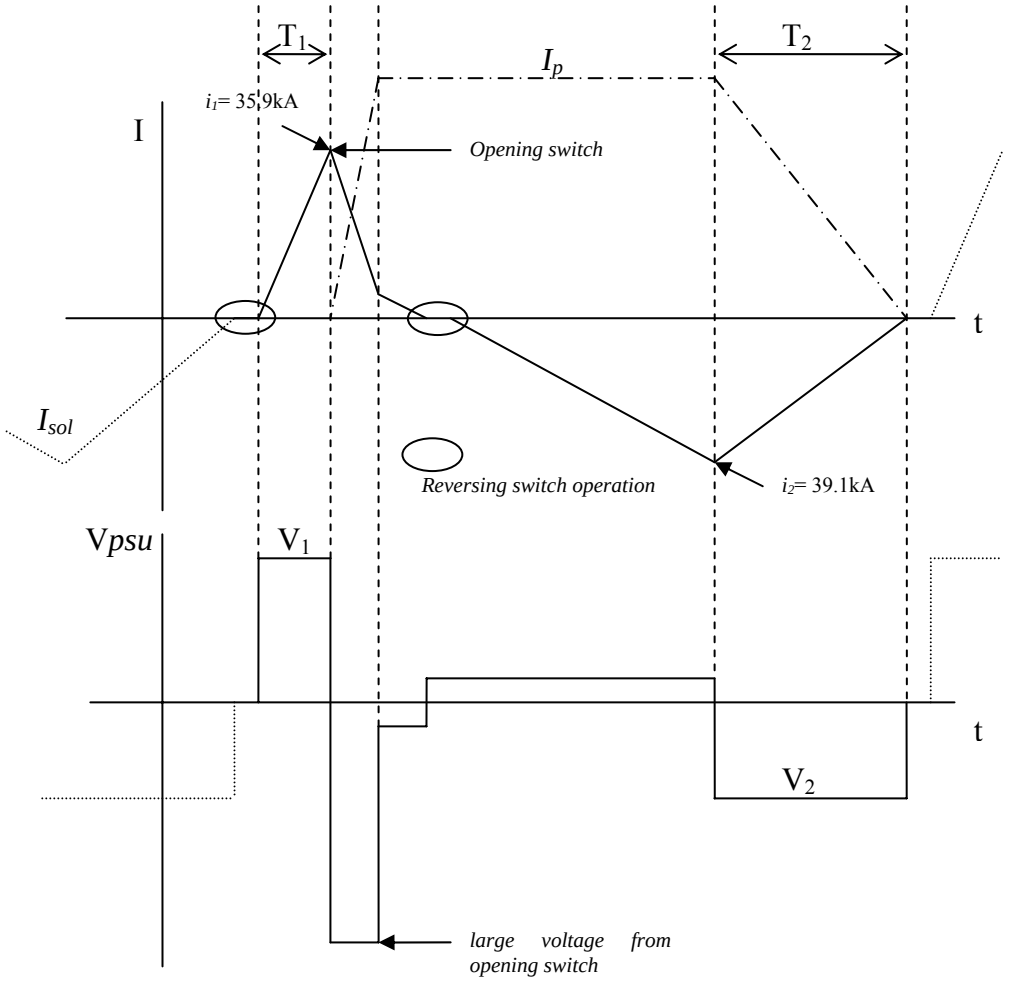

Fig. 7.1: DEMO pulse cycle

7.2. Centre solenoid specification

Inductance = 28H
Turns = 4173
Peak current ramp-up = 35.9kA
Peak current ramp-down = 39.1kA

For the purposes of analysis, the ramps are considered linear and the power supply will be 2 quadrant with a reversing switch, rather than a more expensive 4 quadrant system without a reversing switch.

7.3. Splitting dwell time

$T_{dwell} = T_1 + T_2$

The dwell time is a combination of solenoid current ramp-down and ramp-up times and requires splitting with the following considerations:

- The voltage available in ramp-down can be no more than 2/3 ramp-up voltage ($V_2 = 2/3\ V_1$).
- The cost of the supply is not excessively governed by ramp-down (therefore $T_2 > T_1$)

Due to the 2/3 voltage available in ramp-down, it will be obvious that the ramp-down time will be slower than the ramp-up regardless of the time constraint. There is a slight complication in that there is a rise in current during flattop. Therefore the ratio of dwell time between ramp-up and ramp-down will be split so that ramp-down will be considerably longer than ramp-up.

Using $V(t) = L\frac{di}{dt}$, with linear current ramps:-

Voltage for ramp-up $V_1 = L\frac{i_1}{T_1}$ (1)

Voltage for ramp-down $V_2 = L\frac{i_2}{T_2}$ (2)

Knowing that $V_2 = \frac{2}{3}V_1$, we substitute into (2) and rearrange to get $V_1 = \frac{3}{2}L\frac{i_2}{T_2}$ (3)

Therefore using (1) and (3) $L\frac{i_1}{T_1} = \frac{3}{2}L\frac{i_2}{T_2}$ (4)

Rearranging for T1 and T2 ratio gives $\frac{T_1}{T_2} = \frac{2}{3}\frac{i_1}{i_2}$ (5)

If there is no difference between the magnitudes of the ramp-up current and the EOB current then the dwell time ratio T_2/T_1 would simply be 3/2 (see (5)), however with a known slight increase in current at EOB to be ramped down, and after some trial and error using the known i_1 and i_2 values (figure 7.1), the best ratio as a fraction is 9/5. This ensures that the cost of the power supply is not governed by the ramp-down current.

Note:

1. Only the ramp currents are of interest, i.e. *iR* for current rise during flattop is ignored as it does not govern the cost of power supply.
2. V_1 *and* V_2 are both considered positive for the calculation.
3. As a result of satisfying eq. (4) and (5), only V_1 sets the power supply rating.

7.4. Ramp voltages

Using the dwell split from above, the voltages for ramp-up, V1, and ramp-down, V2, for 30-60-120-300-1000-2000sec dwell times are in shown in table 7.1.

Using $V(t) = L\frac{di}{dt}$, where L = 28H, di = peak current, dt = ramp time, and using peak ramp-up current = 35.9kA, ramp-down current = 39.1kA.

Table 7.1 – Voltage vs dwell time.

Dwell Time (s)	T1 (s)	T2 (s)	V1 (kV)	V2 (kV)	MVA PS rating ramp up	MVA PS rating ramp down
30	10.71	19.29	93.8	-56.8	3370	3330
60	21.43	38.57	46.9	-28.4	1680	1660
120	42.86	77.14	23.5	-14.2	842	832
300	107.14	192.86	9.38	-5.68	337	333
1000	357.14	642.86	2.81	-1.70	101	99.9
2000	714.29	1285.71	1.41	-0.85	50.5	49.9

In conclusion, any dwell time quicker than 120secs would require an extremely large theoretical supply and thus be very costly, especially if the voltage insulation levels are factored in.

A suitable dwell time for cost purposes, from those considered above, would be anywhere between 200-2000secs.

Note V2 is shown as negative as modelled by the waveforms shown at the start of this report.

7.5. Power supply ratings

Included in table 7.1 are the power supply rating requirements for both ramps. Note that the dwell time split results in the ramp-up governing the cost of the supply in MVA terms and not ramp-down.

The MVA rating for the ramp-down is obtained by using the absolute voltage multiplied by 3/2 due to the available power being only 2/3 of the rated power of the supply.

The dwell time vs power comparison is shown in figure 7.2 and 7.3. As can be seen the power supply rating drops off considerably for longer ramp times. This is obvious as a faster ramp requires more voltage and therefore more (reactive) power.

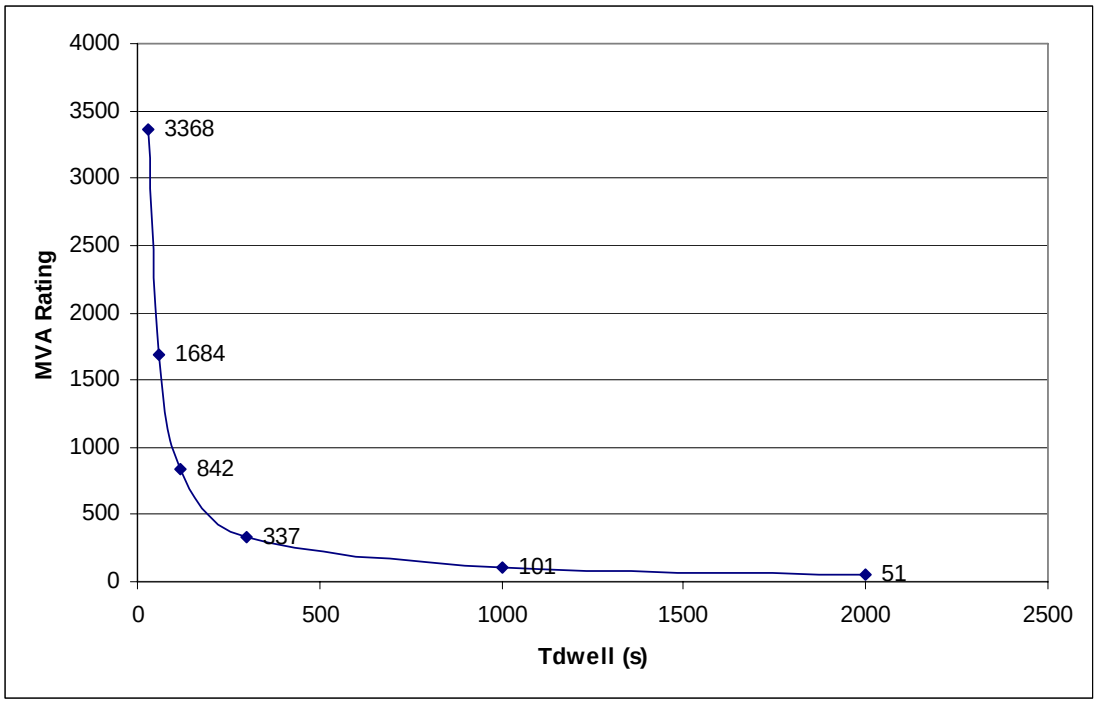

Fig. 7.2: Dwell time vs MVA

7.6. Power supply costs

Cost analysis can be done using a best-estimate approach, comparing the costs to known power supplies, mainly those on high power systems, and working out a guesstimate price per Watt.

Several values have been obtained for comparison only and kindly supplied by those noted. In all cases the MVA for ramp-up is used and the exchange rates are specified. Data tables are attached at the end of this report.

Note:

- Analysis is based purely on MVA required, insulation level for very high voltages have not been factored.
- Costs unless specified do not include other capital costs except power supply parts.

The data for all scenarios is displayed in figures 7.3 and 7.4.

<u>*Scenario 1*</u> – CERN, J.P. Burnet.
A formula used for a single price estimation based on rms power.

$\mathrm{Pr}\,ice(CHF) = k \times P^{0.6}$, where CHF = Swiss Francs
k = 2000 for 2Q thyristor control
P = rms power in kW

1CHF = €0.67

Note: this formula is best used for power <1MVA, giving uncharacteristically cheap costs for any supply significantly above that, where the cost per W reduces dramatically. It is included as reference only (see figures 7.3 & 7.4).

<u>*Scenario 2/3/4*</u> – CERN, J.P. Burnet, cost per kW varies depending on peak power required. The cost per kW decreases as the power required increases:

Peak power < 1MW, 0.5CHF/Watt (scenario 2)
Peak power 1MW – 100MW, 0.3CHF/Watt (scenario 3)
Peak power >100MW, 0.25CHF/Watt (scenario 4)

In figure 7.3, these have been joined together to form the slightly wavering magenta curve.

1CHF = €0.67

Scenario 5 – Based on data supplied by C. Neumeyer (green triangles in figure 7.3).
Data supplied on pulsed and continuous power ratings. These single data points are plotted with the source names.

A reasonable guesstimate was also provided of $100 per kW, shown plotted on figure 7.4.

1$=€0.71

Scenario 6A – Based on data supplied by S. Warder (orange squares in figure 7.3).
Power supply costs vs MVA data are available from the MAST Upgrade project and used for comparison only. These are single data points, i.e. using a single MVA vs cost rather than a "per Watt" approach.

From the data it could be guesstimated that a possible cost ratio could be along the lines of £54 per kW (based on 5.4p/W for a 2Q 12P upgrade project). The error bars if comparing over time on this estimate are likely to be high due to variations in the £ to € conversion. See figure 7.4.

1£=€1.15

Scenario 6B – Based on data supplied by S. Warder.
Similar to Scenario 6A but using £70 per kW (based on 7.0p/W for 2Q 24P upgrade project). The error bars again are likely to be high due to the exchange rate if comparing over time. See figure 7.4.

1£=€1.15

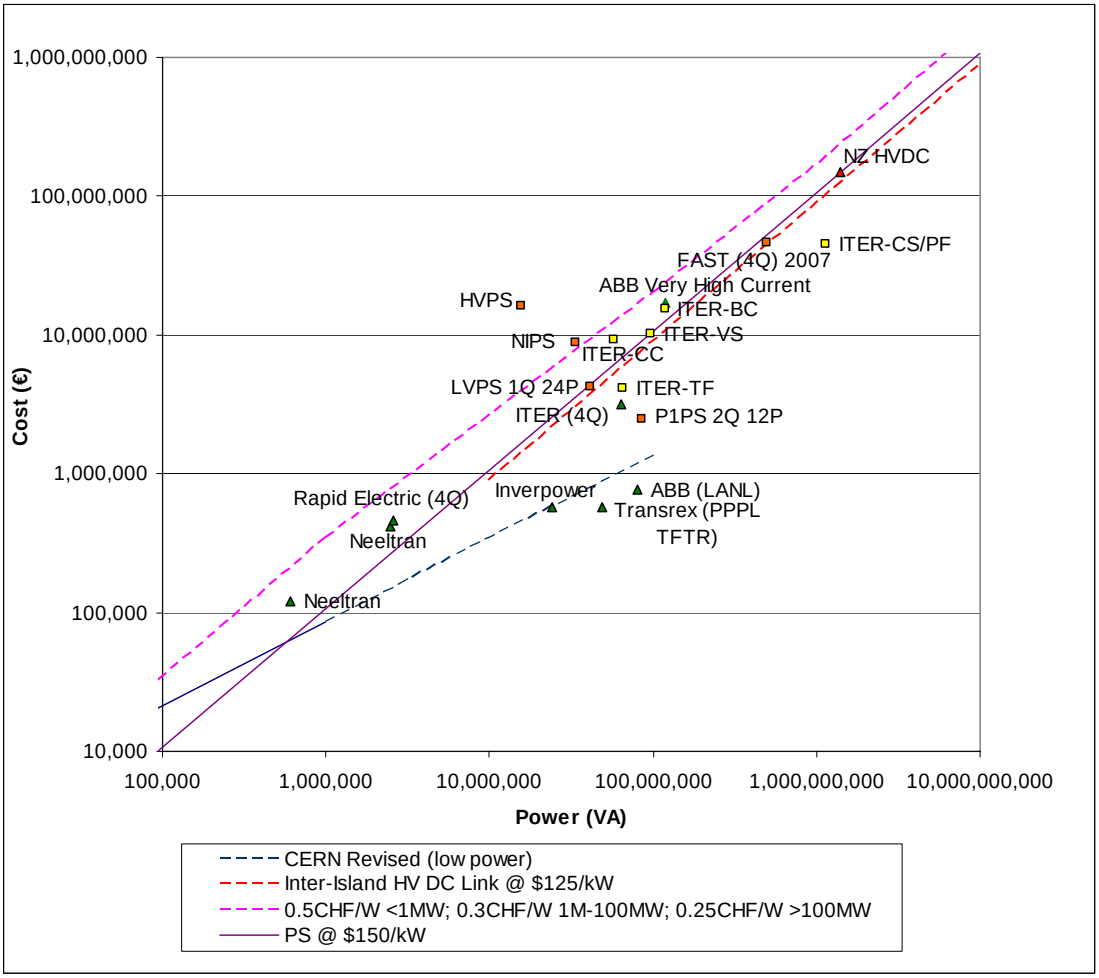

Fig. 7.3: Cost vs power

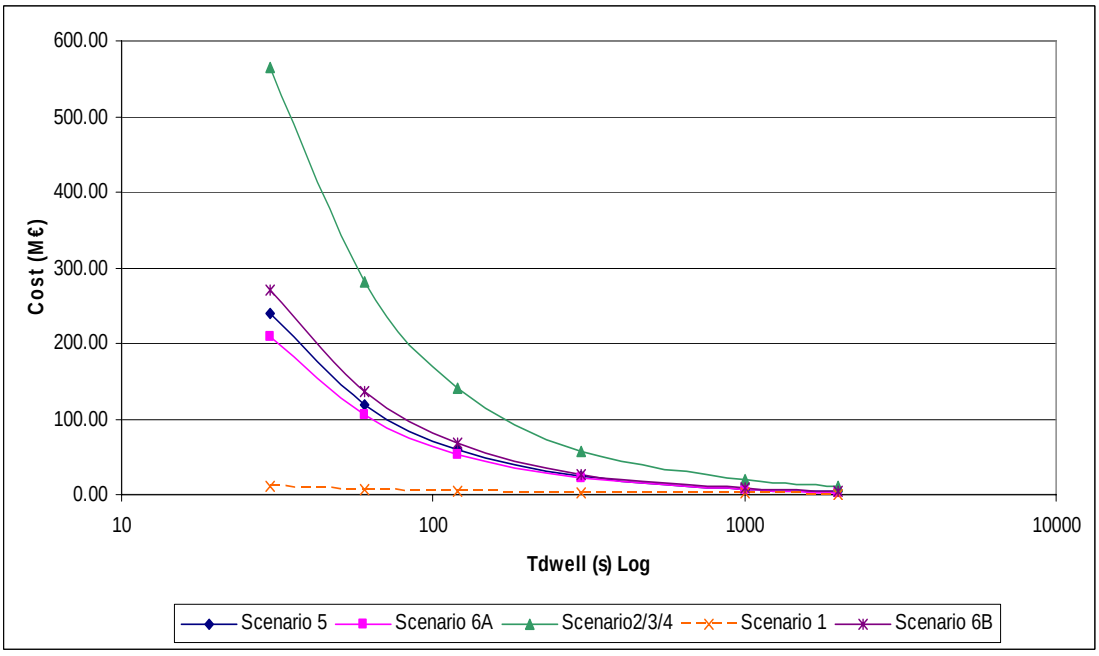

Fig. 7.4: Cost vs dwell time (log scale)

7.7. HVDC link comparison

It maybe beneficial to compare against the cost of ac/dc converters used in HVDC transmission systems as power requirements are likely to be similar (100MW – 1000MW). These have also been plotted in figure 7.3, as follows:

New Zealand inter-island connection replacing 700MW converter with 1400MW NZ$291M (€150M), date 2010 [2]; red triangle.

U. S. Virgin Islands WAPA White Paper, March 2008[3]: "…It is possible to provide a rough estimate for the cost of such a system by examining published cable system prices for inverters and cables. Inverter station costs for a 100 MVA voltage source, HVDC inverter (nominally +/- 100 kV) would be $125/kVA or for two stations a total price of about $25M installed"; red dotted line.

7.8. Thermal storage

This topic is only briefly dealt with here but is fully described in Section 8 of this report.

A thermal storage providing 3GW is required to provide power when the tokamak is not generating plasma. Molten salt (type not detailed) may be used as the storage medium and heated to drive turbines.

The cost of such a system is estimated to be $50/kWh [1]. The cost of the supply is taken to be $100/kW and $150/kW for comparison (these are converted to euro on the plot).

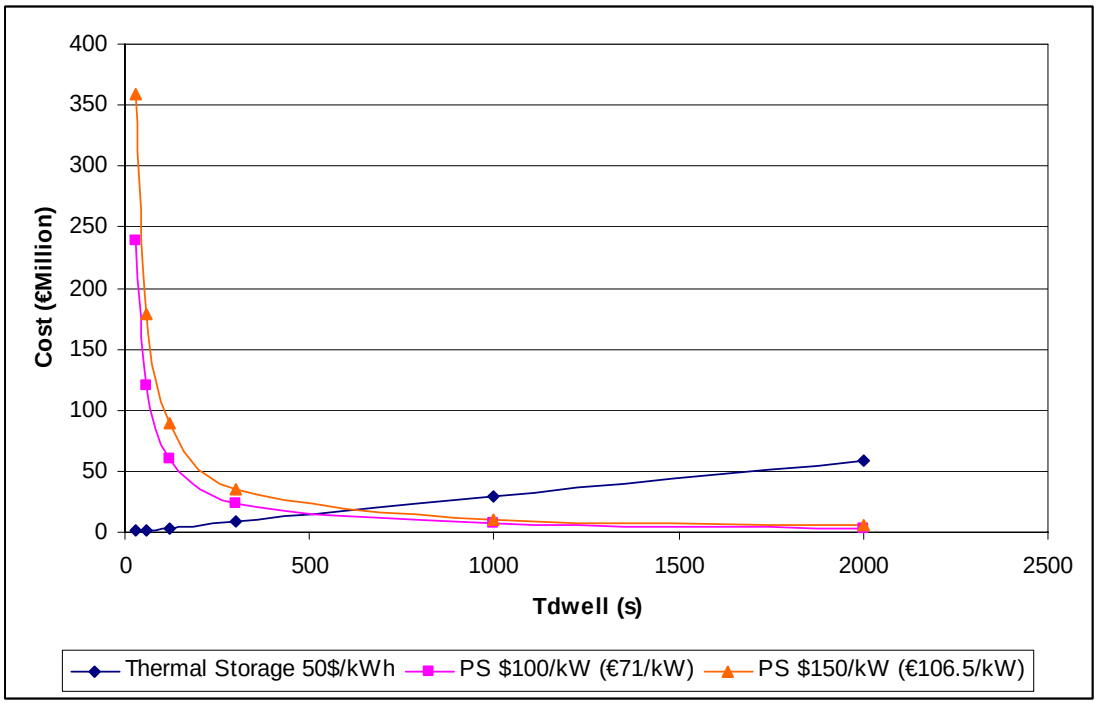

Fig. 7.5: Salt storage & power supply (PS) cost vs dwell time

From figure 7.5 it can be seen that the cost of the power supply falls and the cost of thermal storage rises as dwell time increases. At approx 500secs dwell time, the cost of the supply and storage is approx matched.

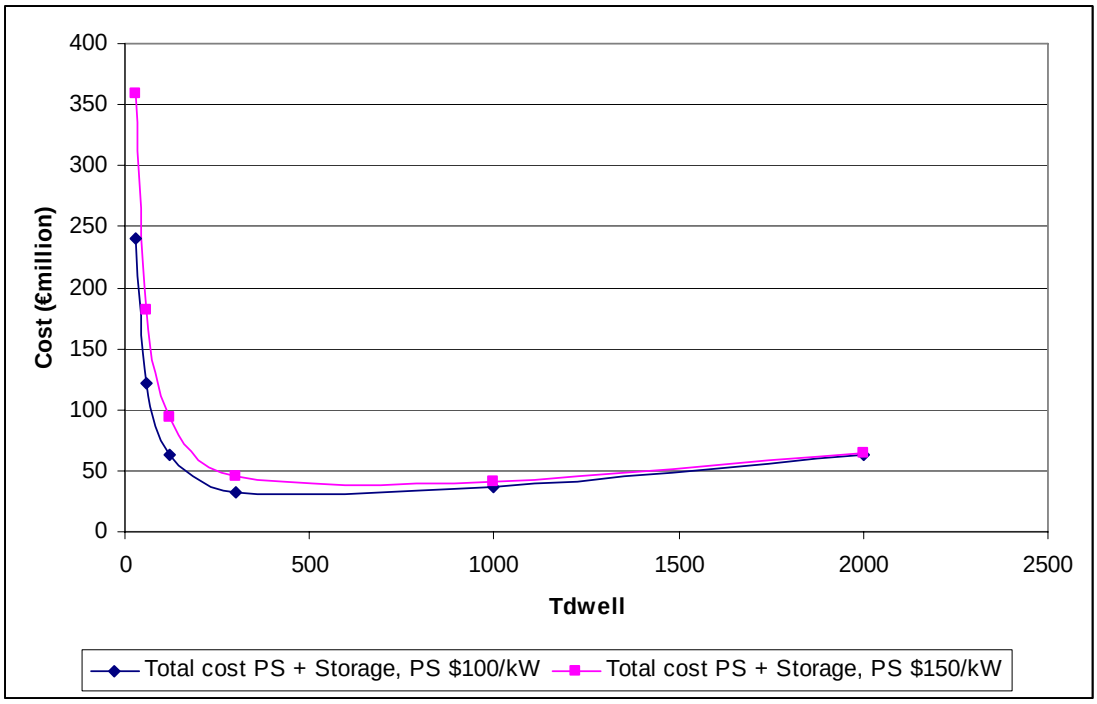

Fig. 7.6: Total cost, storage + power supply (PS), vs dwell time

The cost of storage and power supply, figure 7.6, reaches a minimum of approx €30M and €40M, based on PS costs of $100/kW and $150/kW respectively, when dwell time is approx 500seconds, matching the cost cross-over point on figure 7.5.

The percentage of the storage to the total cost is shown in table 7.2.

Table 7.2

Total cost PS + Storage		**Using PS$100/kW**	**1$=€0.71**
Dwell Time	**Cost (€)**	Storage %	
30	240,021,899	0.4	
60	121,342,200	1.5	
120	63,333,600	5.6	
300	32,788,440	27.1	
1000	36,757,365	80.5	
2000	62,753,683	94.3	

7.9. Conclusion

The result of this analysis gives some idea for power supply ratings and costs given the centre solenoid specification.

7.9.1. Dwell time

To supply the solenoid requirement of approx 150MAt (35.9kA and 39.1kA x 4173 ampere turns) over a short dwell period (i.e. <100secs) is unrealistic as the required supply is huge and the cost

scales dramatically for these low pulse periods. This is shown in figure 7.1, note how the cost increases for shorter dwell times.

From the data collected, a dwell time of >200secs provides a more realistic approach for the solenoid power supply design, with a dwell time split largely in favour of the ramp-down to ensure the cost is governed by the ramp-up only. This dwell period requires a power supply >800MW, figure 7.2. If this still sounds excessive then a dwell time of 1000secs would only require about 100MW.

7.9.2. Power requirement

Figure 7.3 shows the scaling of cost for MVA required. The lines are linear, based on a per Watt figure but this gives some idea of rating costs.

It should be noted that some of the analysis involves voltages of almost 100kV. Scaling of supply cost at this insulation level would be far different than at say 10kV, thus governing the cost of supply, an impact which has not been included.

7.9.3. Cost power supply & energy storage

The cost of supply and storage is governed by the dwell time:

- Shorter dwell time, high power supply cost, low storage cost
- Longer dwell time, low power supply cost, high storage cost

It is estimated that a dwell time of 1000secs will cost in the range of €8M - €15M. This would be a power supply of approx 100MVA, for which the cost is likely to be around €100/kW.

From the cost plot chart figure 7.3, a suitable estimate on a per watt basis taking into account all cost analysis so far would be $150/kW (approx €110/kW).

Energy storage costs will be minimum around a dwell time of 500secs. Longer than 500 seconds, the cost of the storage starts to increase in percentage of the total cost, figure 7.5, and at 2000secs the storage is over 90% of the cost.

7.10. Further work

1. A dwell time analysis could be improved to detail the 200-2000secs range, which would seem mostly likely based on currently projected costs. This would get a better spread of power supply costs and MVA required for these periods.
2. Further HVDC link converter comparison costs may be of interest.
3. The dwell time does not take into account the time after ramp-up and before ramp-down where there is insignificant fusion output power. This will increase the demands upon the thermal storage.

7.11. Acknowledgments

T.N. Todd – Chief Engineer JET, Culham
S. Warder – Power Supplies Unit (MAST), Culham
R. Clarke – Project Support Section Group, Culham
J.P. Burnet – CERN
C. Neumeyer – PPPL
T Bonicelli - ITER
A. Coletti – ENEA

7.12. References

[7.1] How to Use Solar Energy at Night :
http://www.scientificamerican.com/article.cfm?id=how-to-use-solar-energy-at-night
[7.2] HVDC Inter-Island Link Upgrade Project :
http://www.electricitycommission.govt.nz/pdfs/opdev/transmis/HVDC/HVDC-PtIV.pdf
[7.3] http://www.vienergy.org/WAPA%20White%20Paper%20Connection.doc
U. S. Virgin Islands WAPA White Paper, (Spinning Reserve Issues, Inter-connections, & West Indies Power Proposal), prepared by Ben McConnell, Oak Ridge National Laboratory

8. Thermal Energy Storage for Pulsed Fusion Machines

8.1. Summary

The option of having a pulsed DEMO and subsequent reactors in the 2050-2100 timeframe has to be set in the context of changing electricity supply frameworks where the intermittency of renewables is expected to present major challenges for national grids. Nitrate/nitrite molten salt thermal storage systems offer a moderate cost way of reconciling the requirements of a pulsed fusion reactor with a more unpredictable grid dynamic, as well as providing short-term output continuity between pulses. The salts themselves raise interesting questions: they have good, stable high temperature thermal properties but effectively handling salt 'freeze up' and some corrosion issues are topics being worked by the solar thermal community. Pumping powers are reasonable.

8.2. Emerging Grids

It is generally proposed that DEMO will operate from ~2035 [8.1] through to when the first commercial 1GWe reactor (PROTO) emerges in 2050. In this timeframe and towards 2100 fusion is expected to develop a significant role in electricity production and, possibly, energy chemical (hydrogen) supply.

In the same timeframe, it is becoming clear that national electricity grids will probably still be comprised of fossil fuel, renewable and nuclear components [8.2] – the exact proportions depending on the success of carbon markets and energy supply and demand. Other factors, as yet unpredictable, such as the emergence of electric vehicles are potentially disruptive to current thinking.

The UK [8.3], for example, operates – largely – as an energy island but with a DC inter-connector to France [8.4]. As such, National Grid uses frequency control to pull in or drop supply to the grid but in Europe such a scheme is unworkable and is also (in principle) unnecessary since the continent crosses several time zones, so the UK concept of morning and evening peaks in demand is less evident, although EU cross-border connections become power congested. 'TV pickup' is a peculiarly British phenomenon [8.5]. EU frequency control is much tighter than in the UK (+/-0.18Hz compared to +/-0.5Hz) [8.6]. New capacity coming online can be added at 50MW/minute(UK) [8.6] or 120MW/minute in Europe [8.6a]. At all times there is a "spinning reserve" structure available in case a UK maximum credible loss of 1320MW occurs. If this is exceeded some loss of grid capability may be ensue [8.7].

Underlying the conventional UK grid supply model is the notion of a variable demand superimposed on a 'base load', nominally the nuclear generators. Partly this arises from the need to offset the large capital costs of nuclear but it is also claimed to be due to the long cold start times of nuclear capacity ~48h. However, it has to be recognised that this approach is to some extent a vestige of nationalised (CEGB) electricity supply in the UK. In France, where more than 80% of electricity is nuclear, the concept of nuclear base load is irrelevant but, of course, France does have the option of importing/exporting significant power to surrounding countries and this smoothes demand considerably. There is also a certain amount of French hydro-power that can be modulated [8.7a].

With wind generation expected to pick up substantially over the next two decades, there is a growing realisation that intermittency will pose major problems for the UK (and European Grids

where such problems have already emerged [8.6a]). One option, of course, is to substantially increase the connectivity to Europe [8.3], well beyond the current 2GW DC connector's capacity. Wind turbines pose two problems: availability and predictability. If their nominal output were to comprise 20% of electricity supply, it appears there will be a need to 'back up' that supply with short response open-loop gas turbines (the more efficient CCGT's take 6h to run up from a cold start). Additionally, although advanced meteorological data is used it is still difficult to plan a day ahead, as the electricity market would prefer; even hour-by-hour variability is significant since the market 'gate' closes one hour before supply. However, sudden loss of wind power is much less likely than for large (nuclear) plants.

A distinct possibility is that the direct storage capacity of electric vehicles will play a role in providing short term electricity storage. This would require significant software infrastructure but embodies the kind of thinking favoured by 'smart-grid' proponents i.e. to match supply and demand by actively managing users and micro-suppliers in real time [8.8]. A further extension of this thinking is micro-grids [8.9] where, in theory, segments of demand can be "islanded" completely. This has the advantage of improving heat usage by utilising local generation and in principle makes supply more robust, particularly in areas prone to natural disasters (provided the ultimate fuel source is not in common-mode e.g. the natural gas grid). A factor already noted by National Grid is that neither frequency nor voltage reduction effectively reduces demand as many users' devices are already "smart" in the sense that they compensate for such changes.

What does this all mean for fusion? Energy storage will have value in the new world of renewables (particularly wind), and this might be a feature that enhances the case for pulsed devices with electrical or thermal energy storage. It was clear from the discussions with National Grid [8.6] that the concept of "base load" is becoming archaic. The possibility of fusion being able to "load follow", either in pulsed or steady state mode, is another feature that could be beneficial.

Obviously reliability or availability (A) and power output (P) are key issues, as COE (cost of electricity) is proportional to $A^{-0.6}.P^{-0.4}$ (and physics parameters) [8.10]. However, as illustrated above, when a large station such as Sizewell-B is "lost" the consequences can be severe. In the UK, at least, this would pose issues for single-train fusion plants if their electrical output was larger than the 1320MW (the UK "Infrequent Feed Loss Risk"). Designs of up to 4GWe have been proposed in the Large Fusion Power Plant Study [8.11] which make use of the $P^{-0.4}$ benefit to COE. However, in the LFPPS case, co-generation of hydrogen was proposed potentially enabling such large plants to back themselves up albeit at very poor "round trip" efficiency because of the notable inefficiency and poor cost scaling of electrolysers. The underlying assumption in the LFPPS study seems to be that hydrogen would be co-produced as an energy vector for transportation use. That remains an open question.

As far as can be determined the largest single shaft generator in Europe is to be at Flamanville Nuclear, France using an Alstom 1750MW turbine. This may be the current engineering limit but in terms of overall capacity, of course, this is relatively small compared to the multi-generator output of large dams such as Three Gorges or Itaipu [8.12] which has 18 x 715MW water turbines. Nonetheless, even with such a sure supply (hydropower) and generator redundancy, with giant single-node power sources there can still be grid outages leading to massive blackouts [8.13].

8.3. Thermal Energy Storage

There is renewed interest in thermal storage as a means of delivering electricity into the evening from solar power plants [8.14]. The Spanish Andasol-1 plant incorporates a molten salt system that enables high grade heat to be stored during the day for later use in raising steam for evening power

generation. Underlying this concept is the fact that extra solar collector capacity can be added at marginal cost.

The principle is simple enough. An over-sized solar generator (concentrating solar tower) provides enough thermal power for daytime power generation with the balance being held for several hours in the form of sensible heat in high temperature molten salts. In practice, however, the use of molten salts presents several challenges:

(a) at all times the salt must remain molten (in all parts of the circuit): failure to do so may cause a cascading freeze-up due to salt blockages, significant outage and an expensive electrically driven re-melt
(b) the salt must not get too hot: although the vapour pressure is low, the reactivity of some salt-metal interactions can cause corrosion
(c) molten salt leakage presents a serious hazard to personnel, partially in terms of fumes (or aerosols) but mainly because of severe burns and fire hazards
(d) salt-steam interactions, although not nearly as challenging as the sodium-steam heat exchanger problems experienced in the Fast Reactor [8.15], do nonetheless create debris, dust and vapour explosion hazards
(e) physical property deterioration over time (hydroscopic = impurity build up?) may lead to higher viscosity and higher melting point

The benefits of molten salts are their high thermal conductivity, low viscosity, low vapour pressure and high volumetric heat capacity ($\rho.c_p$). A typical salt used in thermal storage is HTS, a potassium-sodium nitrate-nitrite eutectic (minimum melting point) mixture which is usable over the range 142^{o}C (m.p) to 550^{o}C (thermal instability). The density is typically 1750kg/m^3 at 450^{o}C and the specific heat is ~1550J/kg.^{o}C [8.16].

Through inherently safe design, continuous monitoring and good reactor control the drawbacks (b), (c), (d) and (e) can largely be addressed. There are many hundreds of salt compositions available and extensive data exists for a number of prime candidates. The main drawback (a) remains a critical item in solar energy research because of the operational havoc a freeze-up can cause. A promising (although more expensive) approach is to use lithium based salt which can have very low freezing points, possibly below 100^{o}C [8.14]. At these temperatures standard trace heating can be used to guard against cold spots. Many of the proposed salts are readily available in bulk and the "round trip" cycle efficiency can be as high as 93% because of the good heat transfer properties of many salts.

More background on salt technology is given in Appendix 9.6.1 and is based on a paper by Kelly et al.[8.14a] connected to Sandia Laboratories, a key salt research centre. This paper was suggested by researchers at the German Aerospace Centre (DLR), Stuttgart. Dr. Thomas Tamme is their expert on salt technology and they may be interested in collaboration on this topic.

The use of molten salts for energy storage and as a heat transfer medium should not be confused with the use of the FLiBe family of salts proposed as moderators and breeder blanket material. Although these salts are, of course, heat transfer media the central issues with FLiBe are nuclear (neutron effects). A summary of the benefits and drawbacks of FLiBe blankets are summarised in Appendix 9.6.2.

8.4. Pulsed fusion reactor: thermal plant analysis

A first analysis is made here of the opportunity of coupling a fusion reactor to the molten salt technology described above. In an earlier (1993) study it was established that a pulsed fusion device could not rely on the steam drum of a conventional steam cycle to provide ongoing power output during minimum reactor "dwell period" of 300 seconds [8.18]. The key purpose is to determine the likely cost impact of incorporating a molten salt thermal store into a pulsed fusion power plant. A simple spreadsheet analysis (the details are in Appendix 9.6.3) used the basic parameters outlined in Table 8.1.

Table 8.1: Underlying data assumptions used in the model

Parameter	**Value**	**Data source or rationale**
Nominal reactor power	2500 MWth	Nominal DEMO value
Thermal efficiency	40%	Advanced power plant value, this may not be achieved in pulsed reactor but salt loop will help
Minimum salt operating temperature	400^{o}C	This is not fixed, but is used in Andasol-1 to generate steam at 377^{o}C and 100bar [8.19]
Maximum salt operating temperature	550^{o}C	This may be limited by reactor components or salt properties; this value is >PPCS model B [8.10]
Salt (HTS) specific heat	1550 J/kg.^{o}C	From Singh J. "Heat transfer fluids and systems for process and energy applications", Dekker, 1985, pp.224-226 [8.16]
Minimum pulse length	5 hours	Han W. and Ward D. "Reference Design for Pulsed DEMO" 23rd September 2009 [8.20]
Maximum pulse length	10 hours	
Inductive current drive energy pre-pulse (energy derived from salt plant thermally)	10^{11} J (heat to electricity efficiency ignored)	Unknown: 10^{10} J has insignificant effect; 10^{12} J could not be met by heat transfer from salt (maximum 10^{11} J / 0.2h ~140MWe could be met by site steam plant prior to delivery to grid))
In vessel radiant heat loss out of pulse	~20MW	At 500^{o}C divertor/blankets assuming black body radiation to 1000m^2 surface at 20^{o}C
Other static thermal load on salt plant	25MW	This might be heat losses or heat converted into auxiliary power
Capital cost of salt thermal capacity	$20 per kWh (thermal) [8.14a]	Value proposed by US NREL senior engineer Greg Glatzmaeir [8.14] the $50 figure is for kWh(e)
Variables: Output programs that might be sent to grid; salt inventory; inductive current drive switchover time (0.2-1h); plant capacity margin required to meet specified output		

One of the key assumptions in Table 8.1 is that the salt temperature can be allowed to swing between the lower and upper limit temperatures (400-500^{o}C). In practice this may be too much. The Andasol-1 plant contains 28000 tonnes of nominally HTS salt and is expected to produce 50MW for 7.5 hours after sunset. This implies that only a 30^{o}C temperature swing can be tolerated. If this is so, then the predicted salt masses in this study are ~3 times too low. However, as Glazmaier of US NREL (Golden, CO) points out [8.14] the salt plant "doesn't add much to the cost of the resulting electricity because it allows the turbines to be generating for longer periods and those costs can be spread out over more hours of electricity production". Electricity from a solar-thermal power plant costs roughly 13 cents a kilowatt-hour [2009], according to Glatzmaier, both with and without molten salt storage systems.

The in-vessel radiant heat load has been included after discussion with Zsolt Vizvary who suggested that it would be preferable to reduce stresses on the divertor etc by maintaining their temperature near reactor conditions during inter-pulse periods. (The question of whether salt or helium or some

other heat transfer fluid would be used for divertor and blanket cooling is discussed at the end of this chapter). David Ward has pointed out that a compensating factor is the ~100-200MW of decay heat emerging from short-lived isotope decay in the steel wall etc. of the reactor, but this has not been explicitly included in the modelling reported here. While this will be beneficial to the salt thermal storage it is important to ensure that all components that emit this heat must be cooled in some form, by primary coolants, to prevent melting even though they might not be plasma facing [a reactor loss of coolant accident (LOCA) analysis should be considered if it has not already been done]. Decay heat has not been explicitly included in the modelling reported here.

8.5. Six Scenarios

Table 8.2 shows 6 hypothetical programs of supply to the grid using a pulsed reactor (fusion burn periods are shown in pink, off no output periods are grey and grid supply / no fusion periods are shown in orange). The 6th scenario arose from discussion at the pulsed demo workshop on 05/02/10.

Table 8.2

time of day	Program1 Peak Only	Program2 PeakSpread	Program3 BaseMin	Program4 BaseMax	Program5 LoadFollow	Program6 AlwaysOn
0			1000		500	1000
1			1000		500	1000
2			1000	1000	600	1000
3				1000	700	1000
4			1000	1000	800	1000
5		1000	1000	1000	1000	1000
6	**1000**	**1000**	**1000**	**1000**	**1000**	**1000**
7	**1000**	**1000**	**1000**	**1000**	**1300**	**1000**
8	**1000**	**1000**	**1000**	**1000**	**1300**	**1000**
9		1000		1000	500	1000
10			1000	1000	500	1000
11			1000	1000	600	1000
12			1000		700	1000
13			1000	1000	800	1000
14		1000		1000	1000	1000
15	**1000**	**1000**	**1000**	**1000**	**1000**	**1000**
16	**1000**	**1000**	**1000**	**1000**	**1300**	**1000**
17	**1000**	**1000**	**1000**	**1000**	**1300**	**1000**
18		1000	1000	1000	1000	1000
19			1000	1000	500	1000
20				1000	500	1000
21			1000	1000	500	1000
22			1000		500	1000
23			1000		500	1000
utilisation	25%	42%	83%	79%	50%	100%

The suggested purpose of each program and its utilisation of the reactor is indicated by the short titles above. In all the programs it is assumed that the hour prior to pulse is dedicated to the switchover; this is a generous assumption. In Program 1 (Peak Only) the utilisation is very poor because the plant is only providing morning and evening peak cover. In Program 2 (Peak Spread) the minimum pulse length (5h) is used just twice a day, again to cover peaks. In Program 3 (BaseMin) the 24h day is packed out with 2x5h, 1x4h and 1x6h pulses to maximises reactor utilisation (giving the best figure of 83%) and still covering the two daily peaks. In Program 4 nearly the same utilisation is achieved with 2x10h pulses (it is probably not efficient to run a 2h pulse from 11PM to 1AM).

In Program 5 a load following strategy is developed where a much more massive salt system is delivering power to grid even when the reactor is off (reactor "on" periods are shown shaded pink in each program). This program has a low utilisation so, with the greatly increased salt costs, it is probably an expensive option. Finally, in Program 6, the full 1GWe output is maintained to the grid during dwell periods, by making use of high reactor utilisation and a manageably large salt store.

As can be seen in all the above programs the reactor utilisation ranges from very poor (25%) to fair (80%). If the pre-pulse (dwell) periods could be shortened perhaps the utilisation could be increased as far as 85% but the advantages of this might be offset by the other design implications of such a change, requiring the overall reactor system design to be considered in any optimisation.

Results of Scenarios

Program 1 – Peak Only

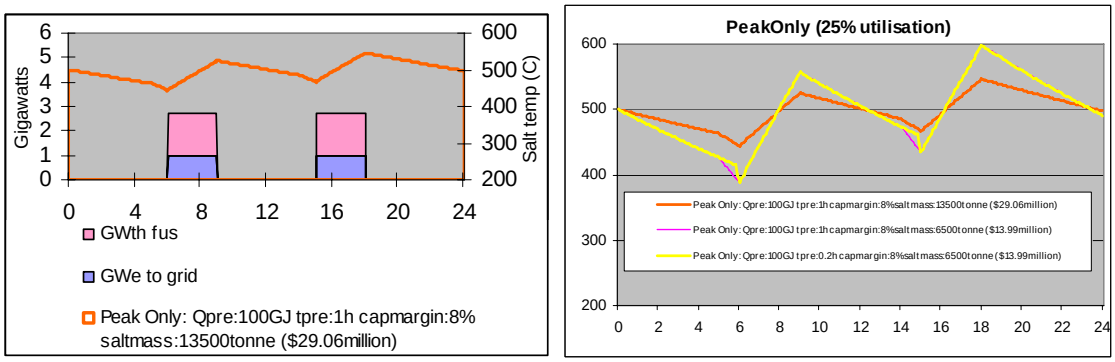

Fig. 8.1

The left-hand plot shows the two periods when the reactor is on during a typical day. The lower block (blue) is GW to grid, the upper block (pink) is thermal power. The orange line (salt temperature) shows the gain achieved during pulses which is lost during interpulse periods through thermal radiation (in vessel) and other static losses. In the right hand diagram other options are explored for this, and all the other, Programs: (a) using half the salt mass and (b) using half the salt mass with a shorter switchover time (0.2h).

In this Program the required mass of salt to contain the salt temperature within the 400 to 550°C temperature band is 6500-13500 tonnes, costing $14-29million. If the NREL cost figure ($50/kWh-e) is credible this suggests that even if three times as much salt is required then the salt costs as compared to reactor costs are just a few percent. If it is cost-effective to use 28000 tonnes of salt on a 50MW solar plant then it is probably similarly cost-effective on a pulsed fusion plant. The reason that the salt volume is less in Program 1 is that during off (dwell) periods no power is being sent to the grid, because the basis this Program is a type of load-following defined to have no demand from the grid in the dwells.

An 8% capacity margin is required to cover the long interpulse periods.

Program 2 – Peak Spread

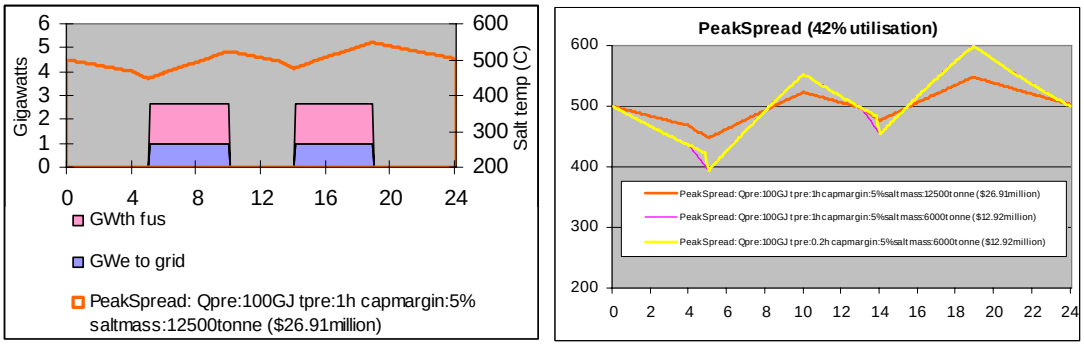

Fig. 8.2

In this Program there are longer pulsed periods, so the capacity margin is reduced as is the volume of salt required (12500 tonnes, $27million). With half the volume of salt the temperature variations (right hand figure, yellow and mauve lines) are probably unacceptable. Wide salt temperature swings will make control of the steam cycle problematic.

Program 3 – BaseMin

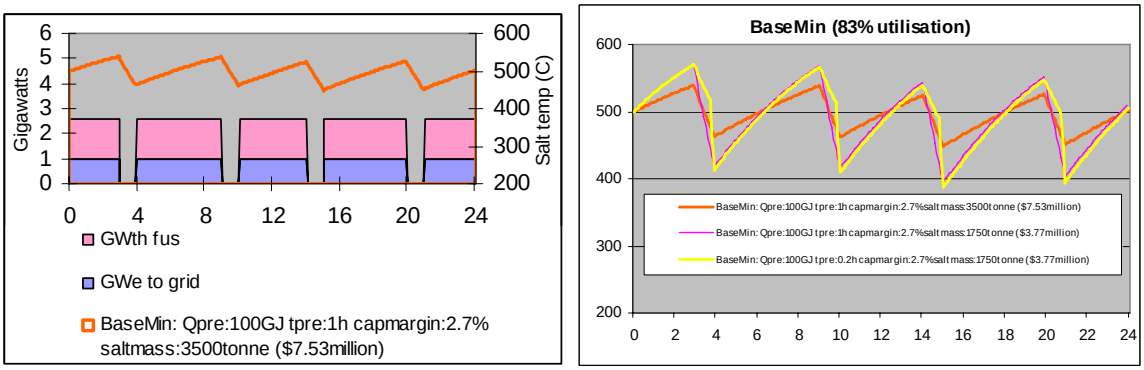

Fig. 8.3

Here the fairly minimised inter-pulse periods result in a low salt inventory (3500 tonnes, $7.5million) and low capacity margin (2.7%). However, there may be an unacceptable consequence: during pre-pulse switchover the salt temperature drops dramatically suggesting there would be heat transfer and control issues for the generation plant. At half salt volumes this drop becomes high, although the low salt volume results in a rapid recovery during pulses. Again, that would not be ideal either, since the salt could overheat.

Program 4 – BaseMax

In this case the maximum pulse length (10h) is used twice a day. The salt mass is larger than in Program 3 because of the need to cover the early hours inter-pulse period (see next page). However, it is the long pulse period that could cause a large temperature excursion if the salt mass is too low.

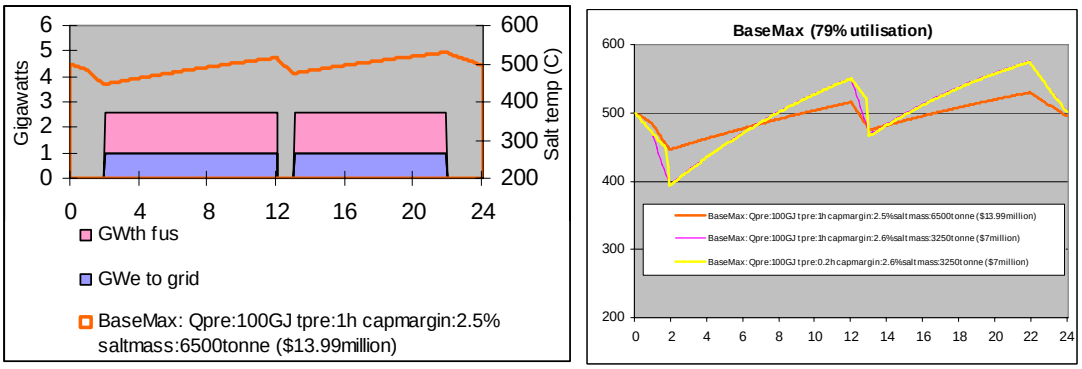

Fig. 8.4

Program 5 – Load Follow

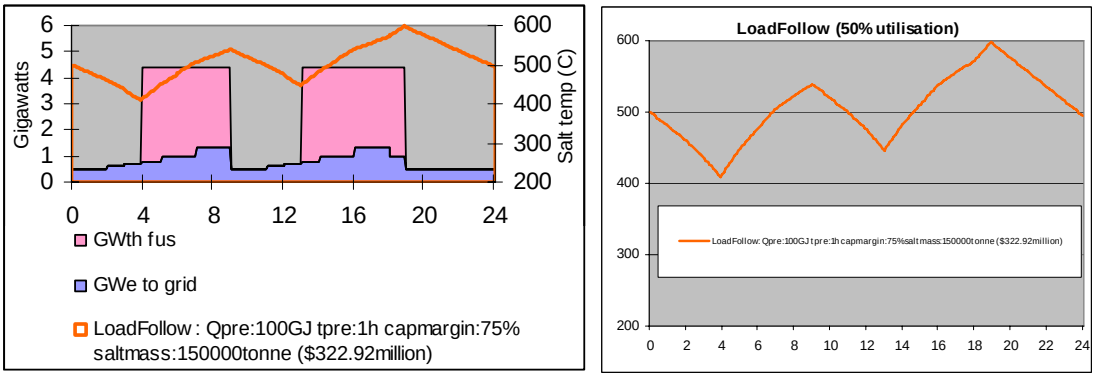

Fig. 8.5

This Program requires a massively increased salt volume to cover the inter-pulse period where power is still being supplied to the grid (blue area in left hand figure). The pulsed periods (5h) would, in practice, be extended if possible. No attempt is made to show the effect of reduced salt column because, as it is, the temperature excursions are too high. The 150,000 tonne salt volume starts to make the salt plant a major physical item as well as a significantly costly one ($322million). Additionally, the plant margin is 75% which, coupled with the poor utilisation (50%) makes this option very uneconomic. Kelly et al [8.14a] suggest that salt storage should be viable up to at least 3.6GWh(thermal) i.e. 10x Andasol or 280,000 tonnes.

Program 6 – Always On

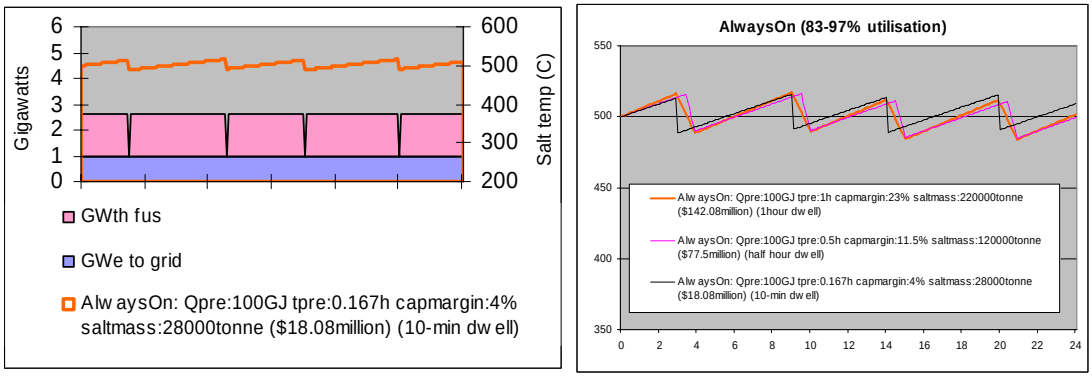

Fig. 8.5

'Always On' effects on COE (A, P)			
1.12	A effect	1.05	1.02
0.93	P effect	0.97	0.99
1.04	overall	1.02	1.01
1h dwell		0.5h dwell	10m dwell
24/(24-4)	margin	24/(24-2)	24/(24-0.67)

If the fusion plant has to provide 1GWe continuous (blue, top left) then the salt store has to cover ancillaries and 2.5GWth to power the turbines during the dwell. The salt store size is larger, of course, but costs are still within reasonable limits.

For a 10 minute dwell case more salt may be required because rate of temperature drop may be too rapid (black line). Bear in mind that all these temperatures are calculated as if the salt were 'well mixed'. In reality, some large salt volumes (many tonnes per second) need to be pumped. The overall effect on COE ($A^{-0.6}.P^{-0.4}$ of reduced availability (A) and increased plant size (P=(1+margin).1GWe) is shown in coloured table. The net effect on COE could be quite small.

For a 1-hour dwell it is estimated that a 220,000 tonne salt store is required (within the limits suggested by the DLR group) at a cost of $142million. This could drop significantly if the optimum dwell is nearer 10 minutes.

8.6. Conclusions from thermal study

Maximisation of plant utilisation not only increases availability (A) and thereby reduces COE, it also reduces the salt mass and plant margin required. Defining a figure of merit (FOM) as utilisation / (1 + plant margin%) confirms this trend.

Figure 8.6 shows the benefit of high utilisation. The points plotted are only for cases where no power is being sent to the grid during dwell periods ie. just auxiliary power and pre-pulse power is demanded.

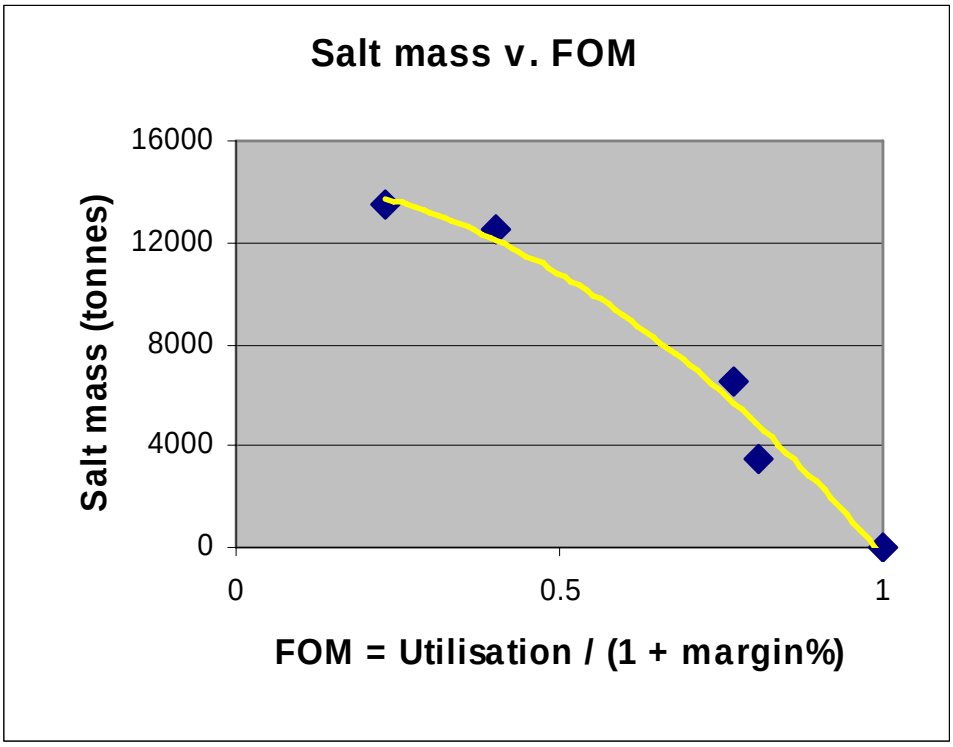

Fig. 8.6

In principle, the capital cost of the salt volumes required suggest that thermal storage would be cost effective in a pulsed fusion reactor. Even if the Andasol-1 salt volumes were used with a pulsed reactor it is suggested that (at 85% utilisation) a maximum if 220,000 tonnes of salt might be

required at a cost of $142million for use in a 1GWe fusion plant. This could be substantially less if a shorter dwell time were adopted.

The question of pumping power has been considered briefly. Pumping power is V.Δp (V m^3/s and Δp, the pressure drop, Pascals). V is set by Q_{load}= ρ.V.cp.T_{diff} which means V is less than 10% of the equivalent helium V even though helium cp is good. Δp could be small because ρ(salt) is high – much higher than for helium. However, the Nusselt number is lower, and this suggests a different heat exchanger layout for salt compared to helium so, without doing a more detailed analysis, it is difficult to scale already predicted helium pumping powers to those of salt. Nonetheless, it is estimated that perhaps a few 10's of MW for salt pumping on 2.5GWth might be required.
..
The next steps in the salt study, if it is decided there is merit in this concept, might be:

- Talk to the salt experts at the German Aerospace Centre (DLR), specifically Dr.Rainer Tamme
- Do some thermal modelling to determine some slat circuit practicalities and pumping power
- Consider the allowable temperature swing
- Analyse the impacts on plant margin and COE
- Keep abreast of developments in salt technology and trace heating (DC heating of pipes is the method used today).

8.7. Non-salt options: high temperature metal hydride energy storage

While investigating the salt technology used in the Andasol-1 (and -2) plants, a report detailing the benefits of magnesium hydride energy storage was accessed [8.22].

In their paper "High Temperature Metal Hydrides as Heat Storage Materials of Solar and Related Applications" Michael Felderhoff and Borislav Bogdanović propose that with suitable catalysts (which have been demonstrated in laboratory studies) it should be possible to create a high cycle thermal store a low cost with high reliability.

The principle is simple $MH_n \rightleftharpoons M + n/2H_2$

The reaction is endothermic, so hydrogen gas is produced when the mixture is heated. The chemical equilibrium obeys van't Hoff's law i.e. the chemical equilibrium is determined by temperature and in this case that involves the hydrogen gas, so as temperature rises so does the gas pressure (in a non linear way).

Magnesium hydride (MgH_2) is useable between 200 and 500^{o}C and the enthalpy of formation is quite large at 75kJ.mol^{-1} H_2. The energy density is also usefully large at 0.9 kWh.kg^{-1} Mg.

Traditionally the concern with metal hydrides is the slow rate of reaction (attainment of equilibrium) in the above reaction. The authors developed methods of nickel doping the hydride. Another approach was to use a ternary hydride Mg_2FeH_6, although the cyclability of this system is not fully developed. The volumetric hydrogen density is 150kg/m^3, double that of liquid hydrogen.

A principle advantage of the solid hydride system is that there is no question of freeze-up as with the salt systems. However, because the thermal store is a solid the key question is now to effect heat transfer to it. The authors demonstrated a heat pipe system (the composition of which was not clear) but how scalable that would be remains a big question. In practice, the metal hydride technology

looks like a neat solution for small scale thermal storage e.g. small system power with a solar concentrator, short term thermal storage or portable cookers etc.

8.8. Conclusions from this sub-task

An early (1993) [8.18] study indicated that a pulsed fusion reactor could not rely on the energy stored in a conventional steam cycle drum to get through reactor "off" periods. Since that time salt-based energy storage has matured and now forms the basis for a commercial solar thermal plant (Andasol-1) to provide electricity after sunset. Even though the mass of salt employed is large (28000 tonnes) for a 50MWe plant, it is claimed that the capital costs (around $50/kWh) are low enough to make this economic. In principle a similar approach could be used for 1 GWe pulsed fusion plant in which short (5h) pulse lengths are used as near continuously as possible so as to achieve a high reactor availability A~85% (and modest COE impact). Under these conditions it is (generously) estimated that 12000 tonnes of HTS salt would be required at an estimated capital cost of $25million. If salt technology is further extended to reactor components then studies suggest FLiBe is the prime candidate, although much safety related work under nuclear conditions remains to be done and the merits of HTS stand independently of FLiBe and these should not be confused.

8.9. References

(Accessed January 2010)

[8.1] http://www.iter.org/proj/Pages/ITERAndBeyond.aspx
[8.2] http://www.energy-regulators.eu/portal/page/portal/LDP_HOME/Research/Policy%20papers/ENERDAY-09-report.pdf
[8.3] http://www.energyefficiencynews.com/i/2470/
[8.4] http://www.kellogg.northwestern.edu/Faculty/ottaviani/homepage/Papers/Cross%20Border%20Electricity%20Trading%20and%20Market%20Design.pdf
[8.5] http://www.bbc.co.uk/britainfromabove/stories/people/teatimebritain.shtml
[8.6] Meeting UKAEA-CD/National Grid [Phil Shepherd et al] 13th November 2009, Wokingham NGC centre
[8.6a] http://www.contratom.de/news/newsanzeige.php?newsid=18808
[8.7] http://www.cigre.org/fr/events/download/3-%20UK%20Frequency%20Excursion.pdf
[8.7a] http://www.world-nuclear.org/info/inf40.html
[8.8] http://www.energyboom.com/electric-vehicles-grid-energy-storage
[8.9] http://eetd.lbl.gov/CERTS/pdf/mg-pesc04.pdf
[8.10] http://www.ipp.mpg.de/ippcms/eng/presse/pi/02_06_pi.html
[8.11] http://aries.ucsd.edu/LIB/MEETINGS/0003-USJ-PPS/WAGANERH/LgFusPPS_USJA_W_3_00.ppt
[8.12] http://www.solar.coppe.ufrj.br/itaipu.html
[8.13] http://laht.com/article.asp?CategoryId=14090&ArticleId=347179
[8.14] http://www.scientificamerican.com/article.cfm?id=how-to-use-solar-energy-at-night
[8.14a] http://nrelpubs.nrel.gov/Webtop/ws/nich/www/public/Record?rpp=25&upp=0&m=1&w=NATIVE%28%27TITLE_V+ph+words+%27%27adopting+nitrate%2Fnitrite+salt+mixtures%27%27%27%29&order=native%28%27pubyear%2FDescend%27%29
(gives full reference, the author has a copy)
[8.15] http://www.iop.org/EJ/abstract/0305-4624/9/3/I04

[8.16] http://books.google.co.uk/books?id=9YL0aUXr2jUC&dq=%22heat+transfer+fluids+and+systems%22+singh&printsec=frontcover&source=bl&ots=o9qnFrlNup&sig=lcfd7sYGiS8gOyoZ2QreM4WrV04&hl=en&ei=Ti5TS6HcBo740wTr_oSsCg&sa=X&oi=book_result&ct=result&resnum=4&ved=0CBoQ6AEwAw#v=onepage&q=1550&f=false page 226 data for KNO3-NaNO3-NaNO2 eutectic
[8.17] http://www.absoluteastronomy.com/topics/FLiBe
[8.18] http://62.173.95.116/webview/?session=45325252&infile=authsecsearch.glu&nh=20&calling_page=hitlist.glu&key=186205
[8.19] http://www.solarpaces-csp.org/Tasks/Task1/andasol.htm
[8.20] Han W. and Ward D. “Reference Design for Pulsed DEMO” 23rd September 2009
[8.21] http://www.osti.gov/bridge/servlets/purl/752080-IbRXGs/webviewable/752080.pdf
[8.22] http://www.ncbi.nlm.nih.gov/pmc/articles/PMC2662468/

9. 9 Appendices

9.1. Topics Identified at the Study Group Kick-Off Meeting

First thoughts on report topics and related issues – 21st Jan 2009

Have we been thinking about this?

- What number of pulse cycles is optimum for reactor economics? ✓
- How should fatigue considerations be allowed for in PROCESS? ✓
- Is divertor sweeping necessary, good, bad, or disastrous? ✗
- What data is available on generic and fusion-specific plant failure rates? ✗
- What radiative power fraction can be assumed, and where does it shine? ✗
- What are all the plant structures affected by pulsing?
  - Coils: superconducting cable, conduit, internal and external supports ✓
  - Divertor: tiles, interface bonds, pipes, welds δ
  - First wall: *ditto* δ
  - "Port plugs" or similar: vacuum boundaries, pipe-work, welds ✗
  - Plasma heating plant ✗
  - Power supplies: transformers, switch-gear, dump resistors ✗
  - Cryoplant? ✗
  - *Many other things, TBD!* *See report summary!*

CCFE CULHAM CENTRE FOR FUSION ENERGY

9.2. First Wall: Supporting Analyses

The appendix contains the detailed material properties, analysis results and verifications of the models.

9.2.1. Material properties

The wall material is EUROFER 97, its properties are shown in table 9.1 and 9.2. The thermo-physical properties are also shown on fig. 9.1-9.5.

Table 9.1: Thermo-physical properties of EUROFER 97

T (C)	Rel (microΩcm)	DENS (kg/m^3)	k (W/mK)	CTEm (1E-6)	CTEi (1E-6)	Cp (J/kgK)	E (GPa)	G (GPa)	NU
20	49.882	7870.740	28.064	10.354	11.306	439.227	217.261	84.253	0.300
50	52.300	7862.532	28.867	10.471	11.465	461.604	215.209	83.373	0.300
100	56.330	7848.402	29.782	10.661	11.730	489.805	212.230	82.115	0.300
150	60.360	7833.712	30.252	10.845	11.995	509.304	209.658	81.055	0.300
200	64.390	7818.462	30.380	11.023	12.260	523.174	207.327	80.118	0.300
250	68.420	7802.650	30.265	11.195	12.525	534.490	205.074	79.232	0.300
300	72.450	7786.278	30.008	11.360	12.790	546.324	202.732	78.321	0.300
350	76.480	7769.344	29.709	11.520	13.055	561.750	200.137	77.313	0.300
400	80.510	7751.850	29.470	11.674	13.320	583.843	197.124	76.134	0.300
450	84.540	7733.796	29.389	11.822	13.585	615.676	193.527	74.711	0.300
500	88.570	7715.180	29.568	11.963	13.850	660.324	189.183	72.968	0.300
550	92.600	7696.004	30.107	12.099	14.115	720.859	183.926	70.834	0.300
600	96.630	7676.266		12.228	14.380	800.355	177.590	68.233	0.300
650	100.660			12.351	14.645	901.887	170.011	65.093	0.300
700				12.469	14.910	1028.529	161.025	61.339	0.300

T - temperature
Rel – electrical resistivity
DENS – density
k – thermal conductivity
CTEm – secant thermal expansion coefficient
CTEi – instantaneous thermal expansion coefficient
Cp – specific heat
E – Young modulus
G – shear modulus
NU – Poisson ratio

Table 9.2: Tensile properties of EUROFER 97

TEMP	σ_Y ave	σ_Y min	σ_U ave	σ_U min
C	MPa	MPa	MPa	MPa
20	545.57	515.56	667.83	619.74
50	528.39	499.32	648.49	601.8
100	507.1	479.21	621.58	576.82
150	492.97	465.85	599.67	556.49
200	483.63	457.03	580.87	539.05
250	476.72	450.5	563.3	522.75
300	469.88	444.04	545.07	505.83
350	460.76	435.42	524.28	486.53
400	447	422.41	499.05	463.12
450	426.23	402.79	467.48	433.82
500	396.11	374.32	427.69	396.89
550	354.26	334.77	377.78	350.58
600	298.33	281.92	315.87	293.13
650	225.96	213.53	240.07	222.79
700	134.8	127.39	148.48	137.79

TEMP – temperature
σ_Y ave – average yield stress
σ_Y min – minimum yield stress
σ_U ave – average ultimate strength
σ_U min – minimum ultimate strength

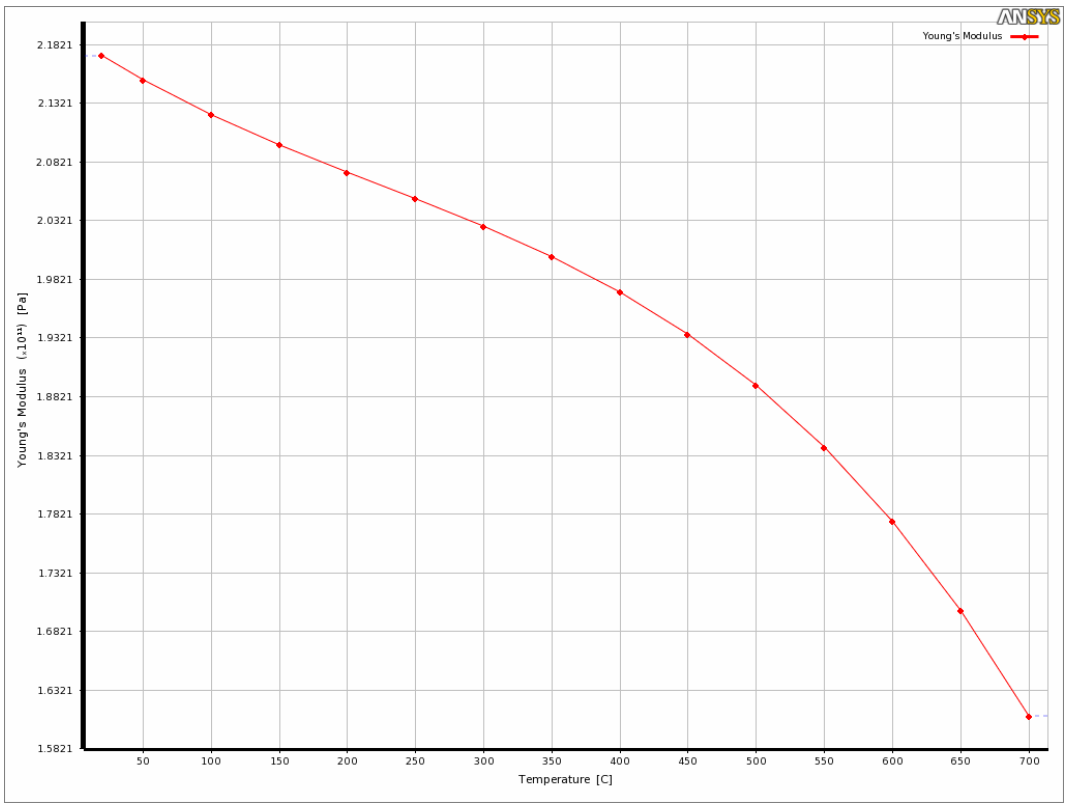

Fig. 9.1: Young modulus of EUROFER 97.

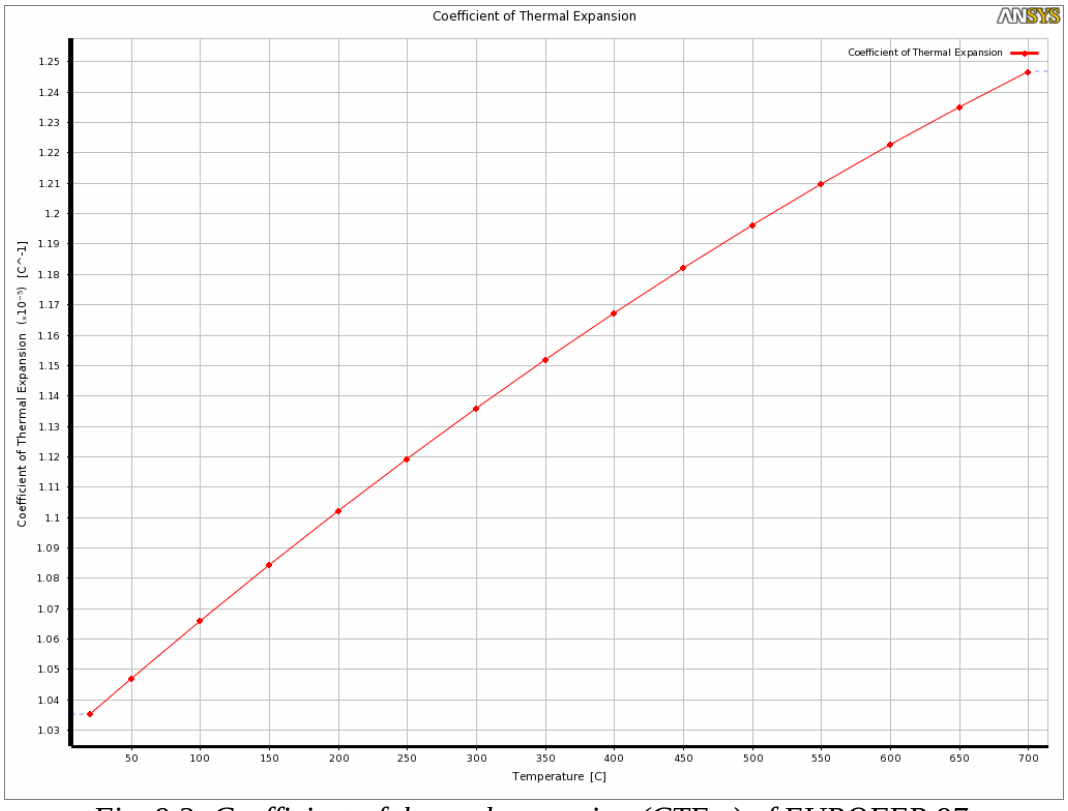

Fig. 9.2: Coefficient of thermal expansion (CTEm) of EUROFER 97.

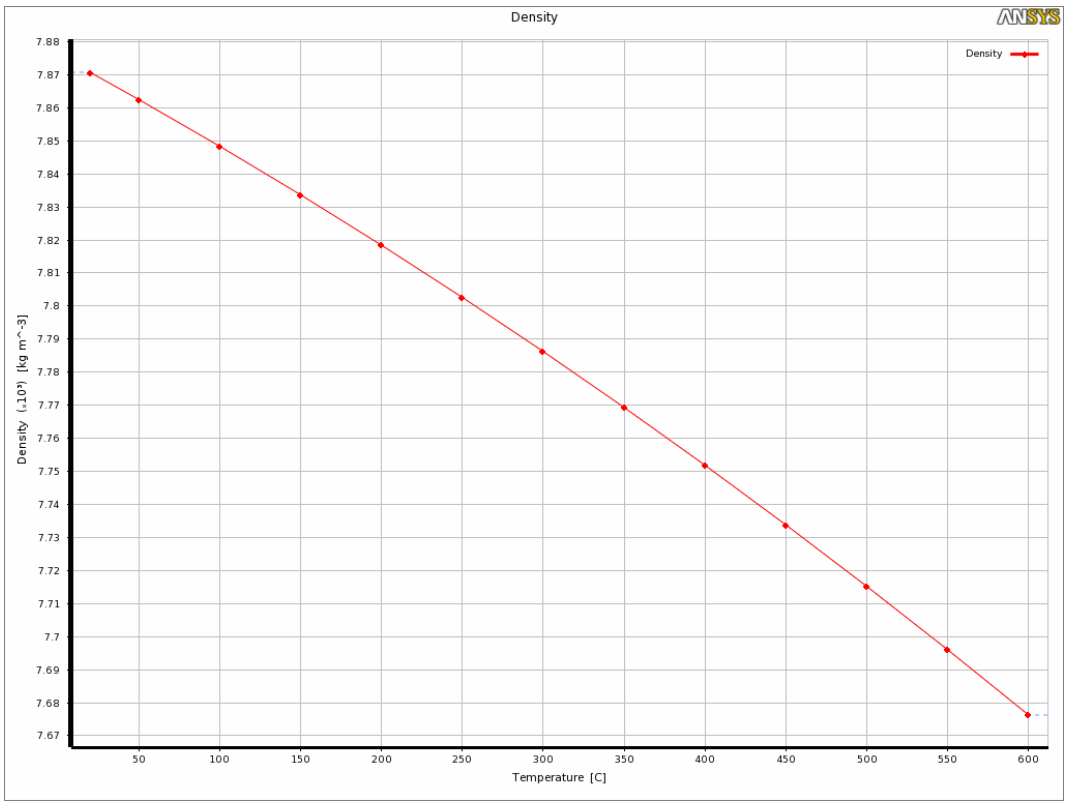

Fig. 9.3: Density of EUROFER 97.

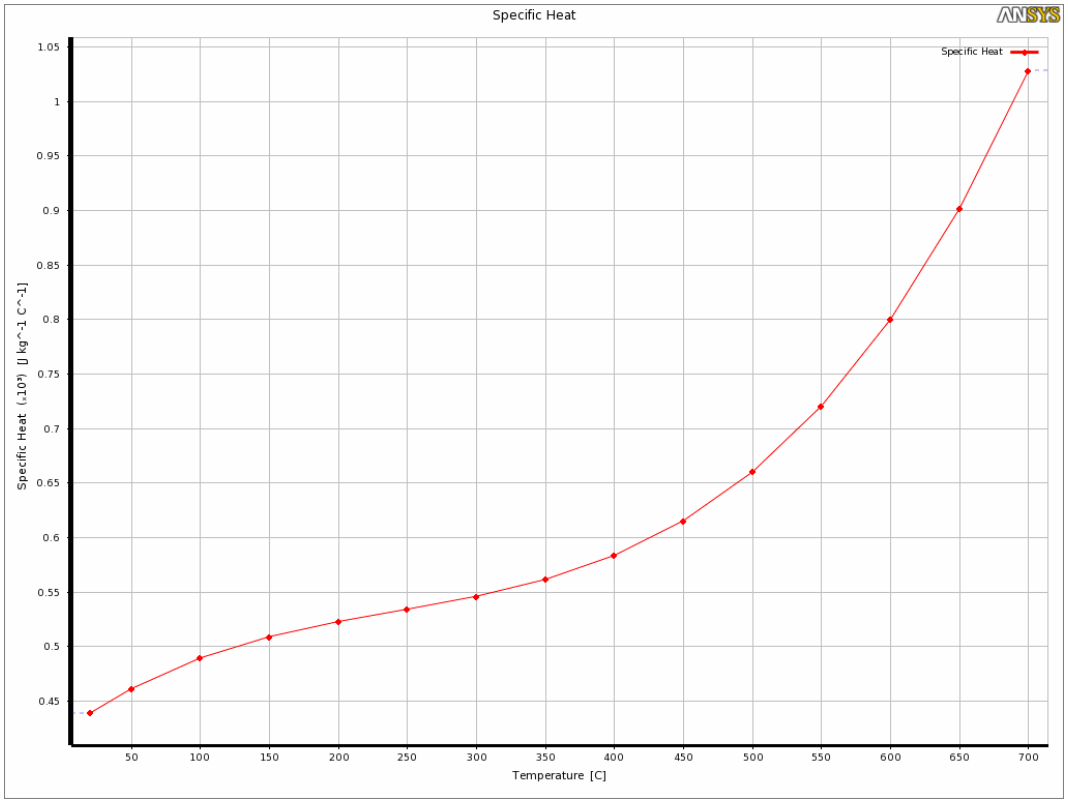

Fig. 9.4: Specific heat of EUROFER 97.

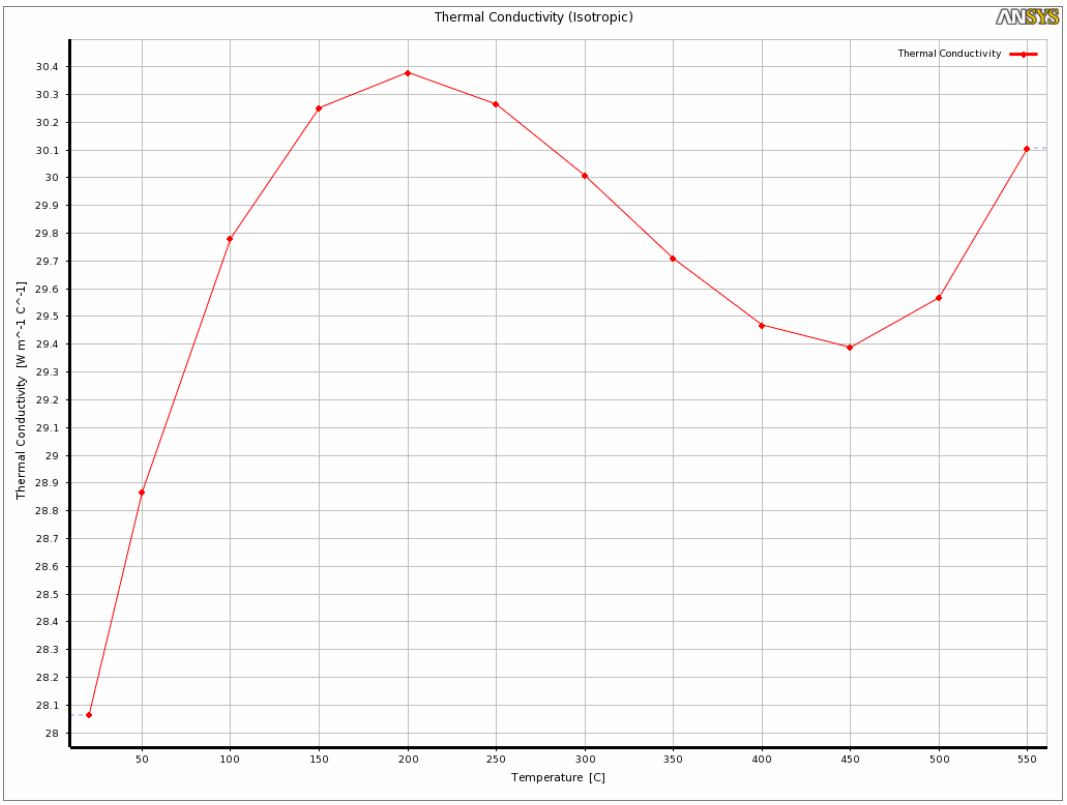

Fig. 9.5: Thermal conductivity of EUROFER 97.

The coolant is pressurised water at 10 MPa, its properties are shown in Table 9.3.

Table 9.3: Water properties at 10 MPa

TEMP (C)	TEMP (K)	SPVOL (m^3/kg)	DENS (kg/m^3)	VISC (kg/ms)	K (W/mK)	cp (W/mK)
20	293.1	0.000997	1003	0.000998	0.5965	4152
40	313.1	0.001003	996.6	0.000654	0.6255	4155
60	333.1	0.001013	987.5	0.000469	0.6479	4163
80	353.1	0.001024	976.1	0.000357	0.6644	4175
100	373.1	0.001039	962.8	0.000284	0.6757	4194
120	393.1	0.001055	947.8	0.000235	0.6823	4221
140	413.1	0.001074	931.2	0.000199	0.6843	4258
160	433.1	0.001095	912.9	0.000173	0.6822	4307
180	453.1	0.00112	892.9	0.000152	0.6759	4369
200	473.1	0.001148	871.1	0.000137	0.6657	4450
220	493.1	0.001181	847.1	0.000124	0.6514	4556
240	513.1	0.001219	820.5	0.000113	0.6328	4698
260	533.1	0.001265	790.7	0.000103	0.6096	4898
280	553.1	0.001322	756.4	9.48E-05	0.5809	5196
300	573.1	0.001398	715.4	8.65E-05	0.5455	5692
311.5	584.7	0.001456	686.9	8.16E-05	0.521	6172

TEMP – temperature
SPVOL – specific volume
DENS – density
VISC - dynamic viscosity
k – thermal conductivity
cp – specific heat

9.2.2. “Original” model

Neutron heating excluded

The fluid flow was modelled using the CFX module of ANSYS 12. It is a conjugate heat transfer analysis, the model mesh and boundary conditions are shown on Fig. 9.6-9.8. The coolant velocity is 10 m/s, the heat load is 0.5 MW/m^2.

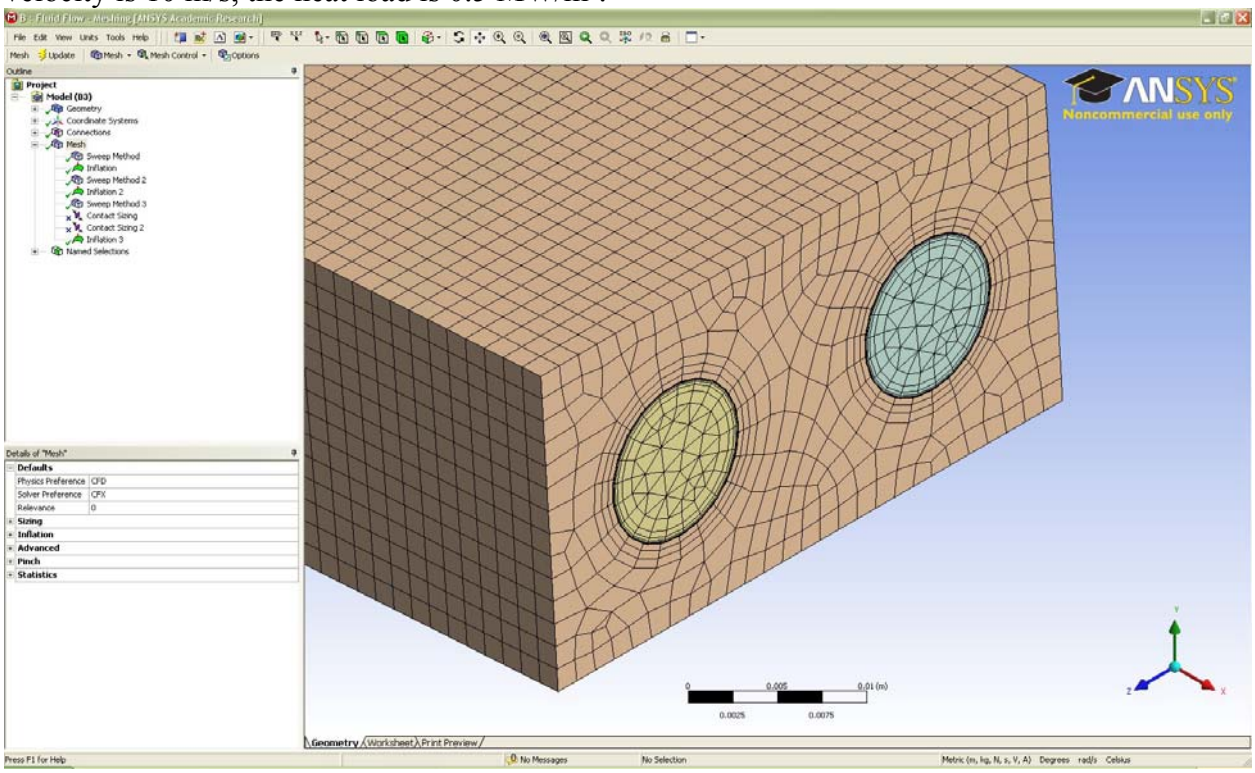

Fig. 9.6: CFX mesh (CFX).

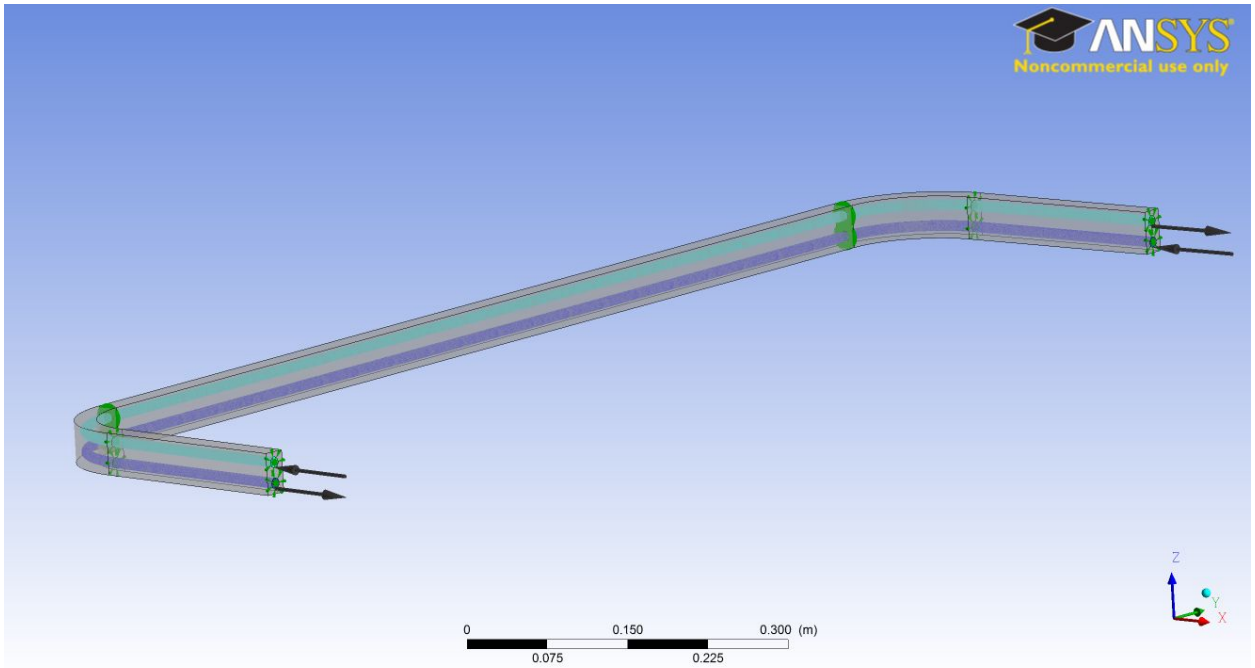

Fig. 9.7: Boundary conditions for fluid flow modelling (CFX).

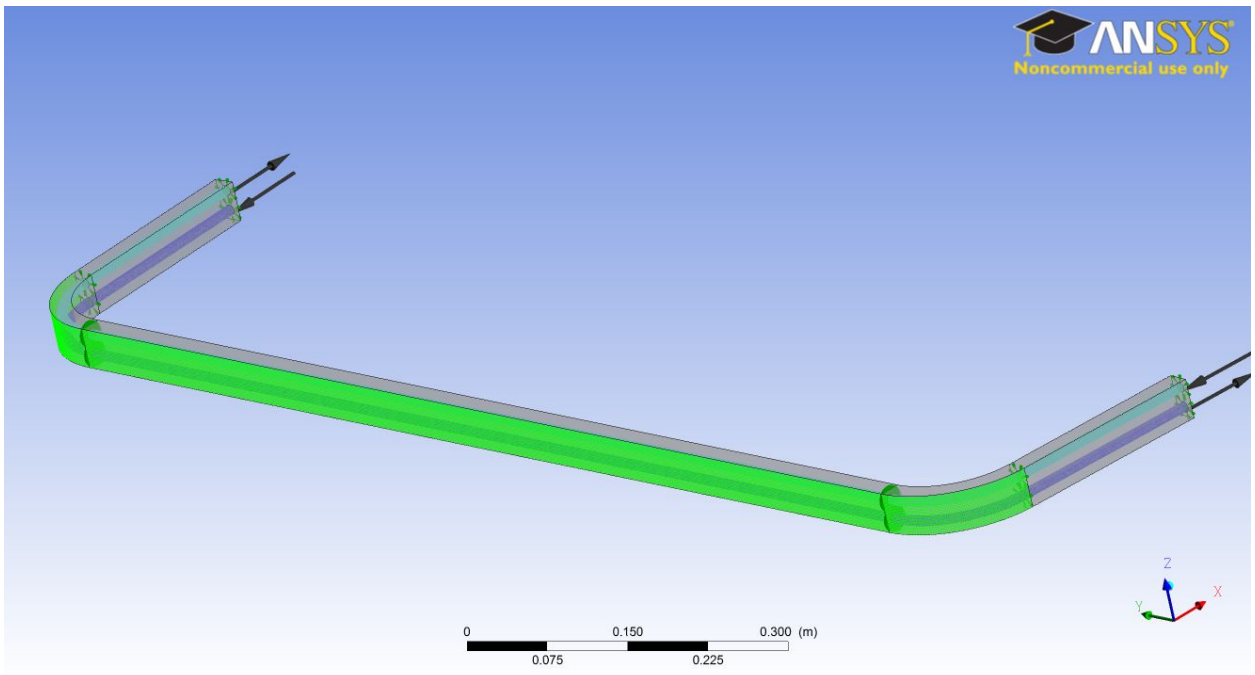

Fig. 9.8: Heat flux applied on the front surface (CFX).

Fig. 9.9 shows the y^+ number (at 1620 s – right before the beginning of the cooling-down) on the channel walls. This number can indicate whether the mesh is good enough. It is a dimensionless distance of the first node from the wall. Its recommended value is between 11 and 200, but it can depend on the application. In this model it is between 22 and 40, suggesting the mesh is sufficiently fine.

The temperature at the beginning of the cool-down phase can be seen on fig. 9.10. The peak temperature on the surface is 350 °C.

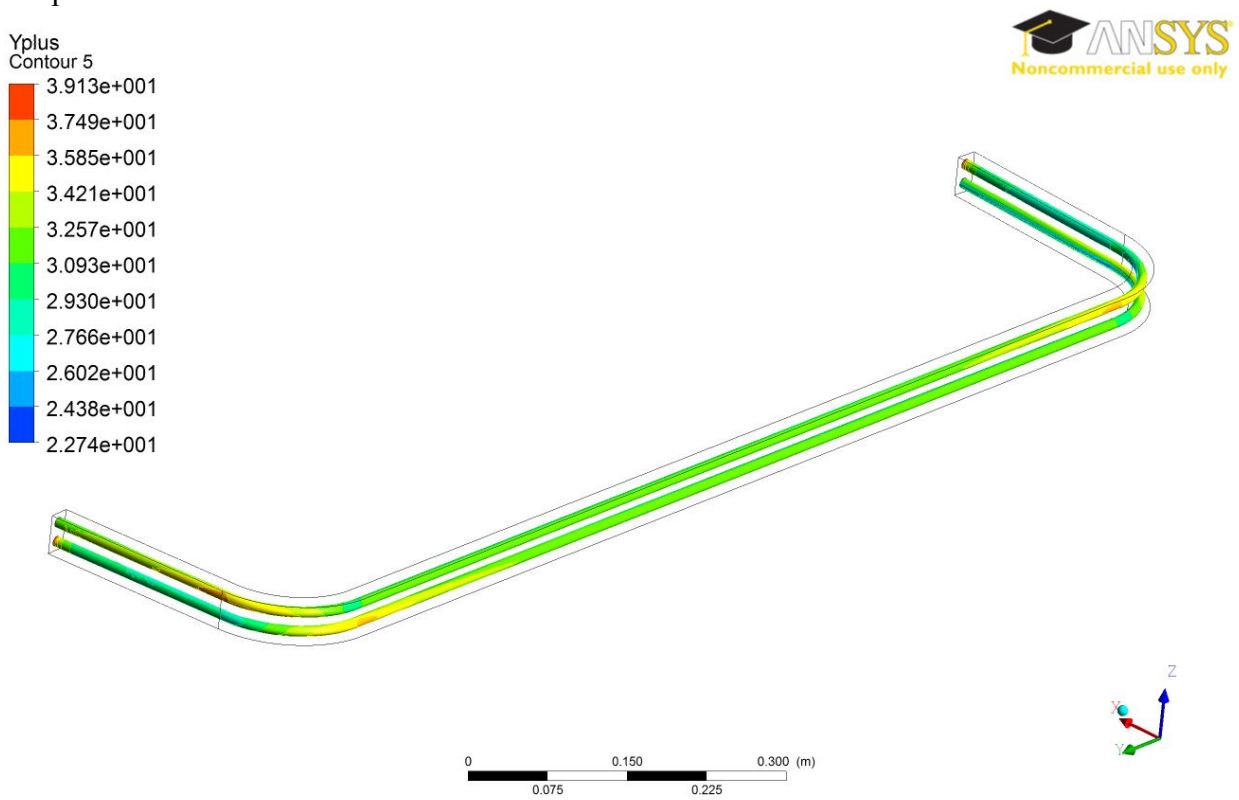

Fig. 9.9: The y^+ value at 1620 s (CFX).

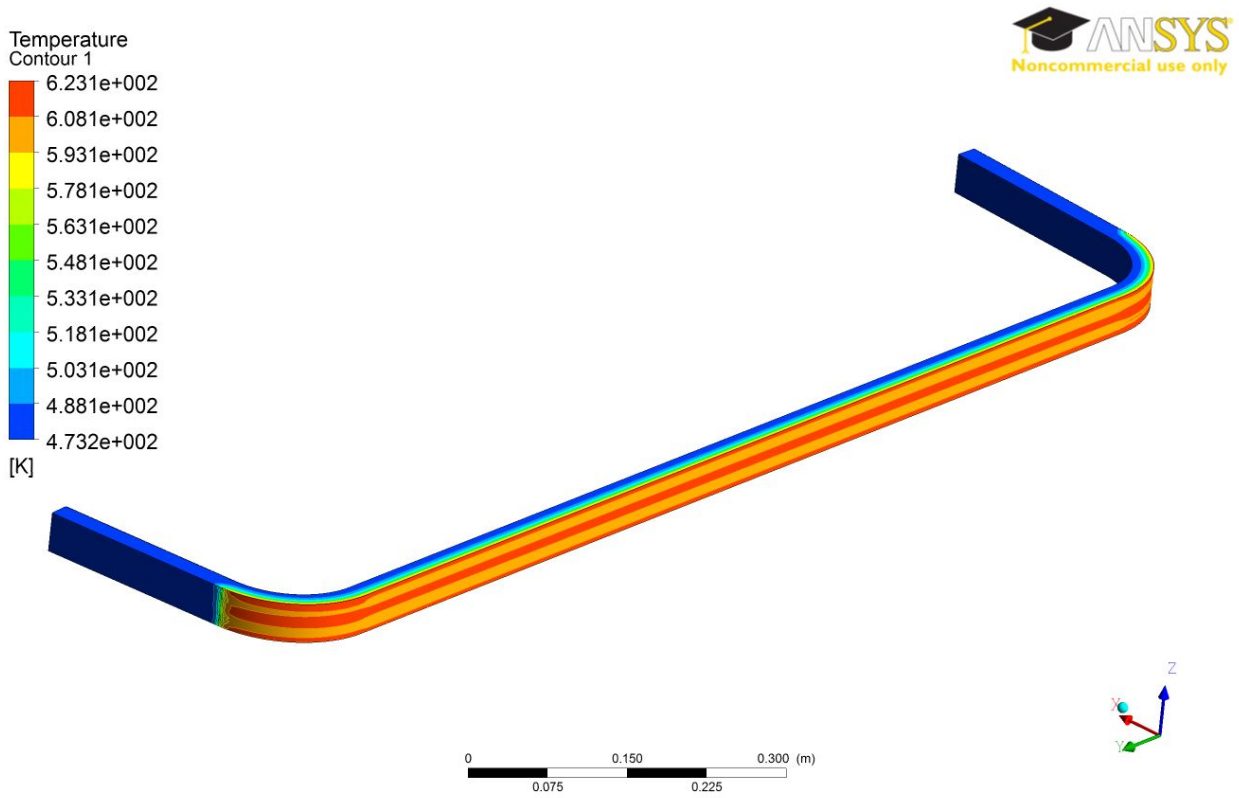

Fig. 9.10: Temperature at 1620 s (CFX).

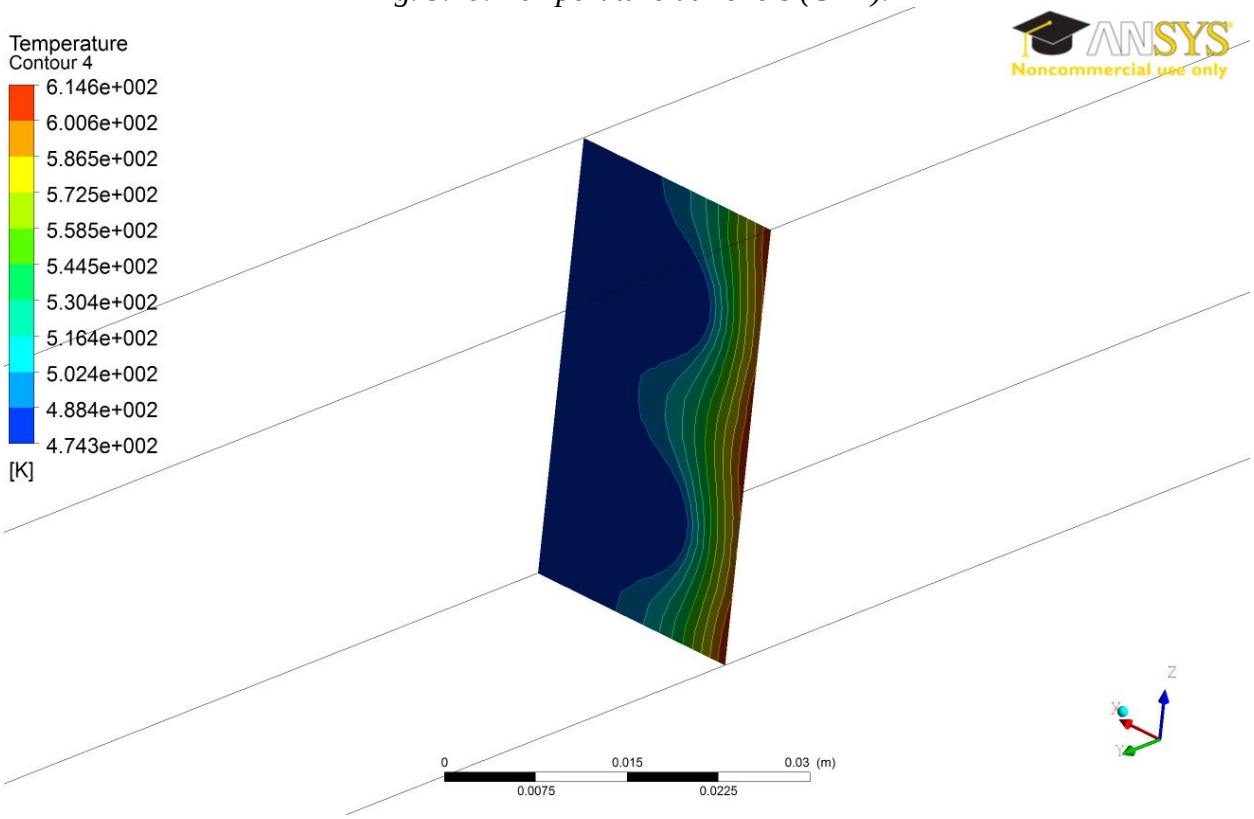

Fig. 9.11: Temperature distribution in an arbitrary section at 1620 s (CFX).

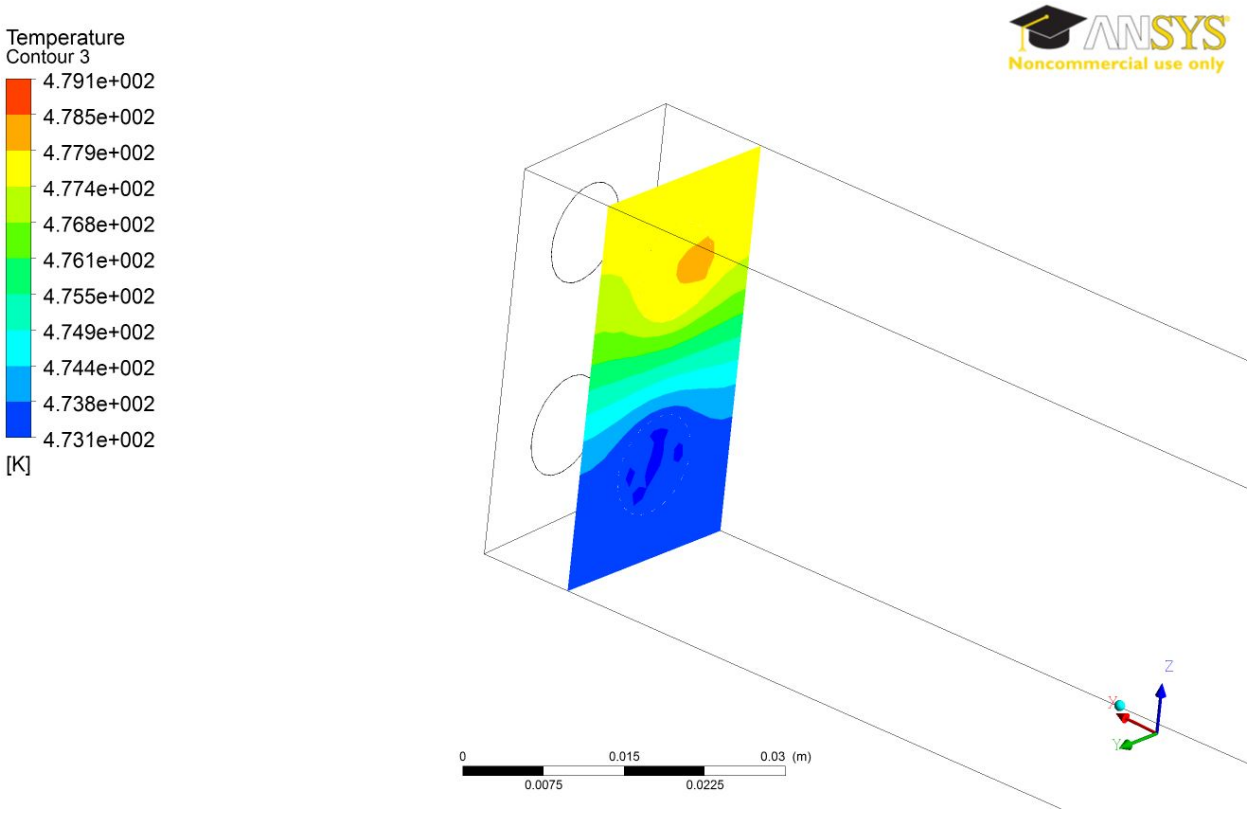

Fig. 9.12: Temperature distribution in a section close to the inlet/outlet at 1620 s (CFX).

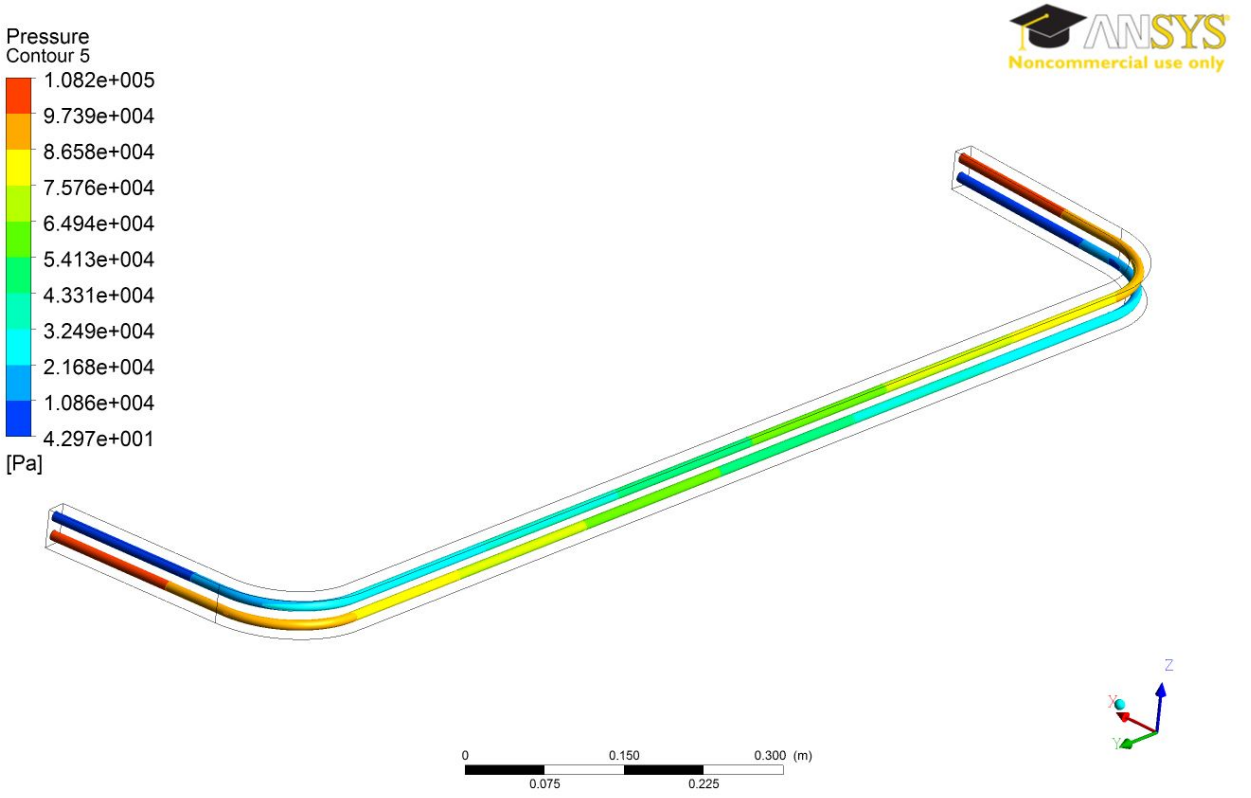

Fig. 9.13: Pressure distribution along the channel walls (CFX).

Fig. 9.12 suggests that the outlet temperature of the coolant is just slightly warmer than the inlet temperature; the increase is 6 °C.

The pressure along the channels can be seen on Fig. 9.13. The pressure drop is about 0.1 MPa which is negligible compared to the 10 MPa pressure of the water. The maximum velocity of the

water is ~12 m/s in the elbow, the dynamic pressure ($\rho \cdot v^2/2$) from this is 0.062 MPa. The boiling point of water on 10 MPa is 310.96 °C on 9.8 MPa 309.48 °C. There is no risk of cavitations.

Fig. 9.14 shows the temperature distribution on the surface. It is slightly lower than in the CFX module peaking at 338 °C
(Note that on Fig. 9.11 the peak temperature is 341 °C, the 350 °C peak temperature must apply only a few nodes).

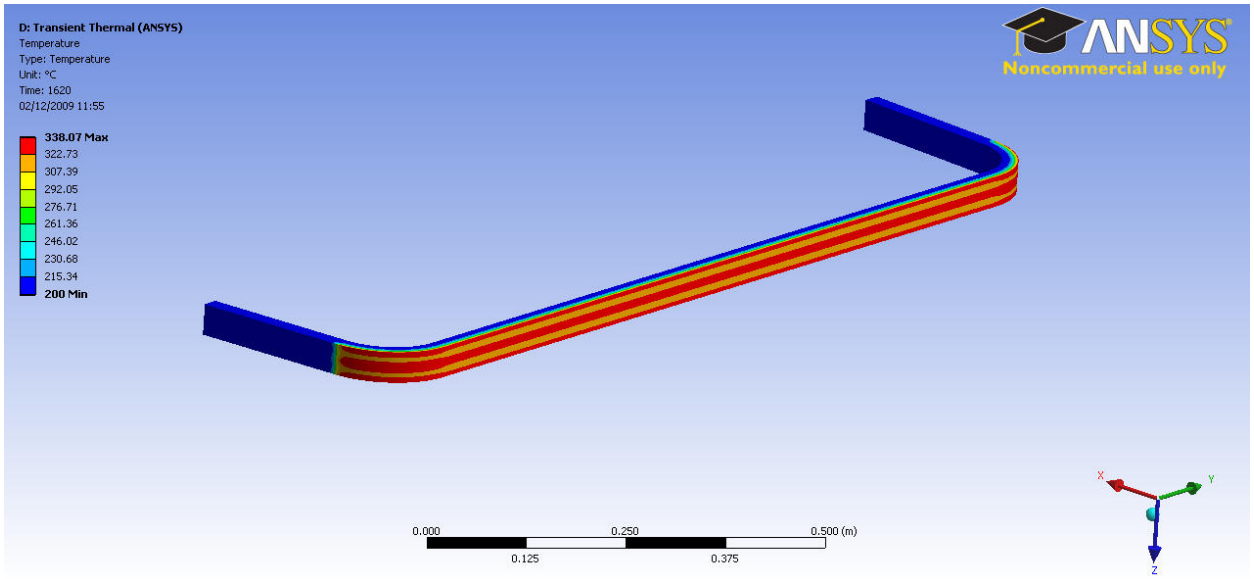

Fig. 9.14: Temperature at 1620 s (ANSYS Mechanical).

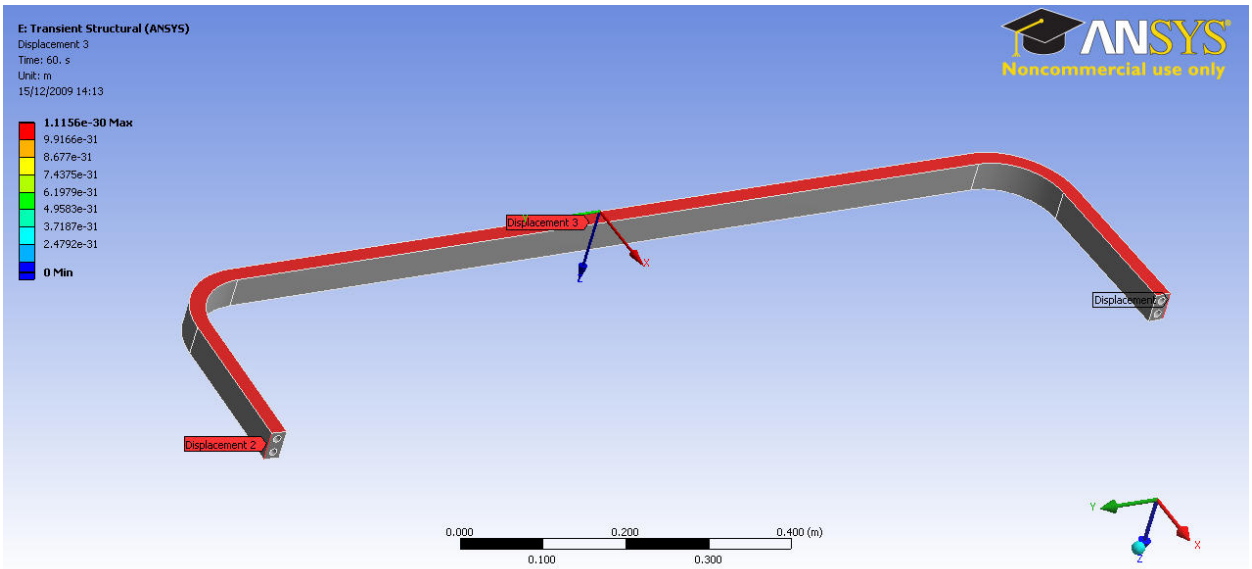

Fig. 9.15: Constrains for mechanical analysis (ANSYS Mechanical).

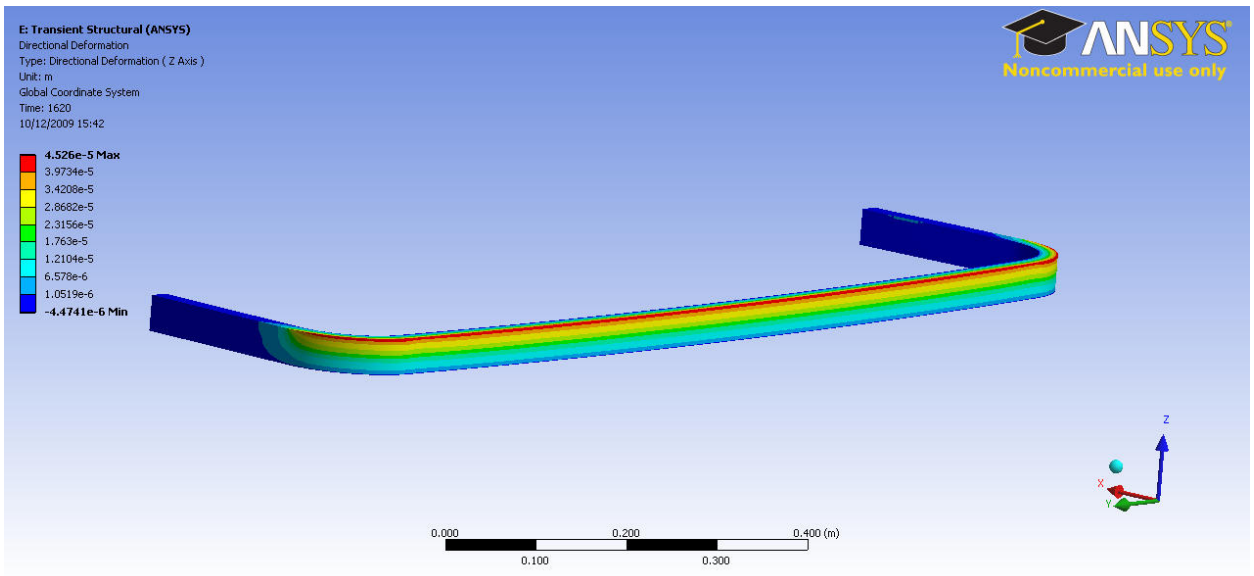

Fig. 9.16: Displacement in z direction at 1620 s (ANSYS Mechanical).

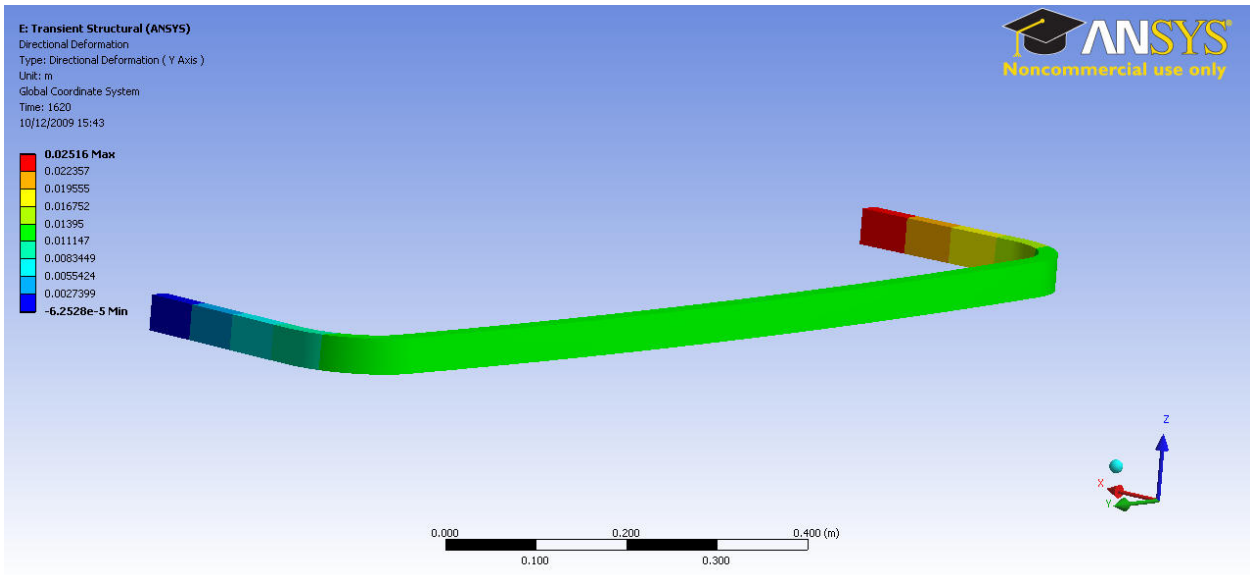

Fig. 9.17: Displacement in y direction at 1620 s (ANSYS Mechanical).

Fig. 9.16 and 9.17 show the displacement in z and y direction just before the cool-down phase. Fig. 9.18 and 9.19 shows the stress intensity distribution along the model and at the elbow.
The fatigue curves we will use are strain vs. number of cycles therefore the strain intensity results shown on fig. 9.20-9.22 are needed to extract the strain amplitude and mean strain.

The mean strain intensity based on this is 0.11% and the alternating strain intensity is 0.094%. The total strain range is 0.188%. However it has to be pointed out that the [5] suggests that the thermomechanical cycling causes more damage than isothermal mechanical cycling with the same strain range. Although it is not quantified in the paper how much worse the thermomechanical cycling the graph suggest that it is about a factor of 2. Assuming this the effective strain range is about 0.376%.

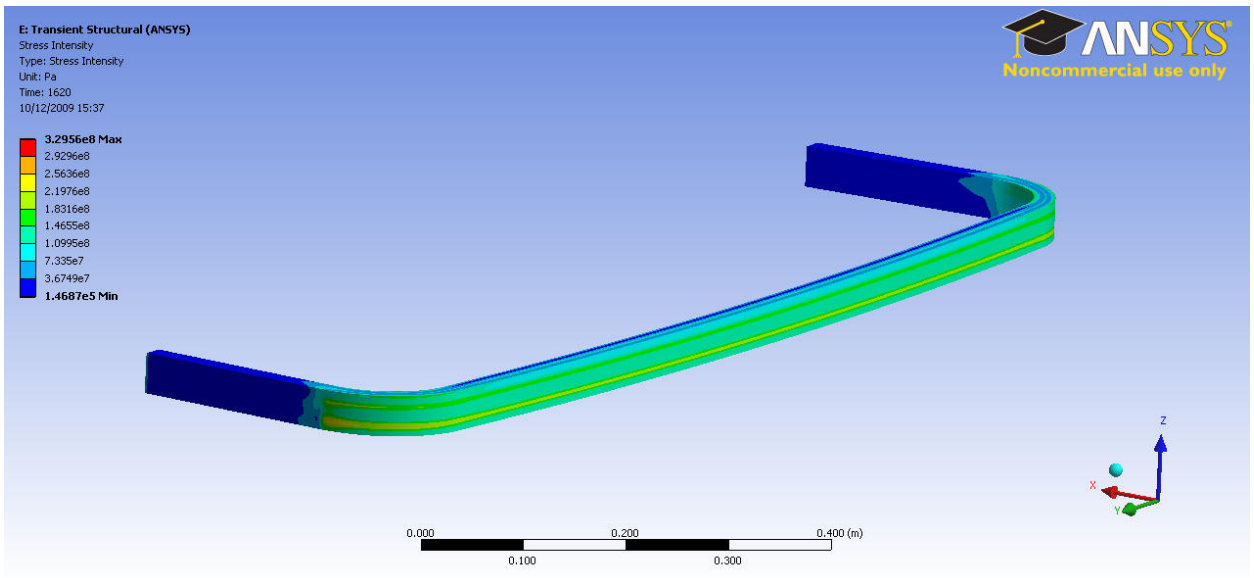

Fig. 9.18: Stress intensity at 1620 s (ANSYS Mechanical).

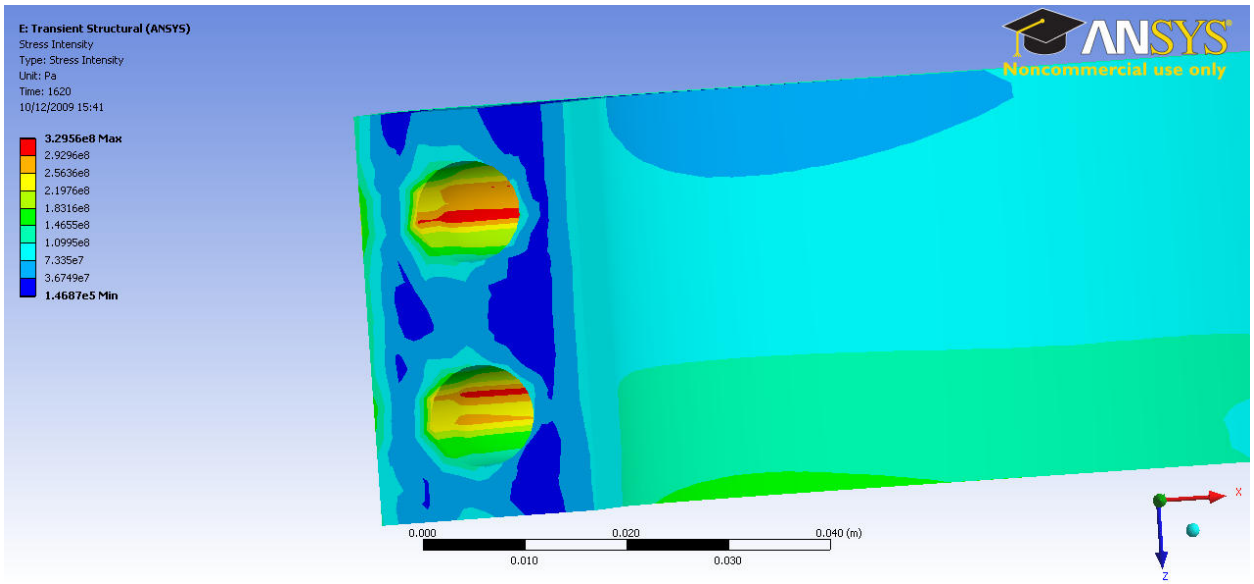

Fig. 9.19: Stress intensity in the elbow region at 1620 s (ANSYS Mechanical).

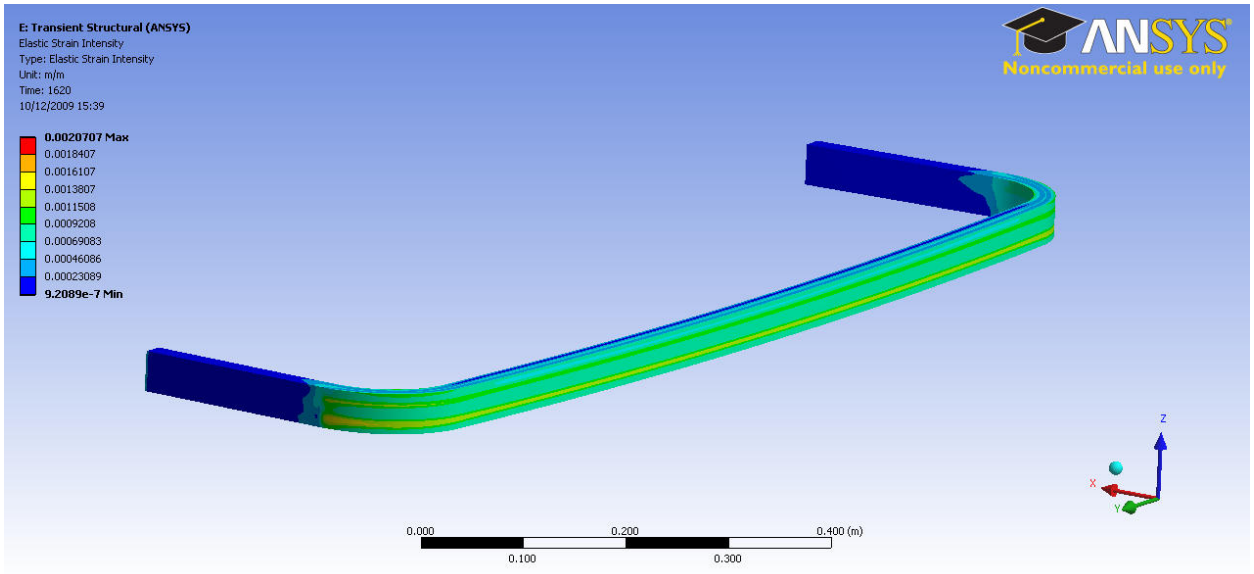

Fig. 9.20: Strain intensity at 1620 s (ANSYS Mechanical).

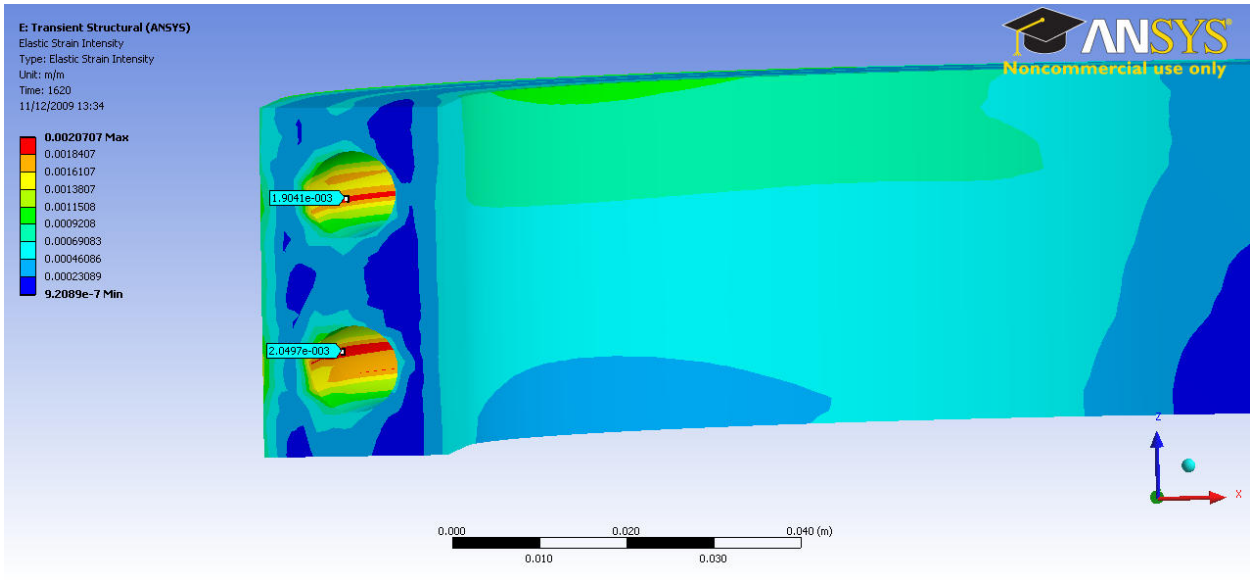

Fig. 9.21: Strain intensity in the elbow region at 1620 s (ANSYS Mechanical).

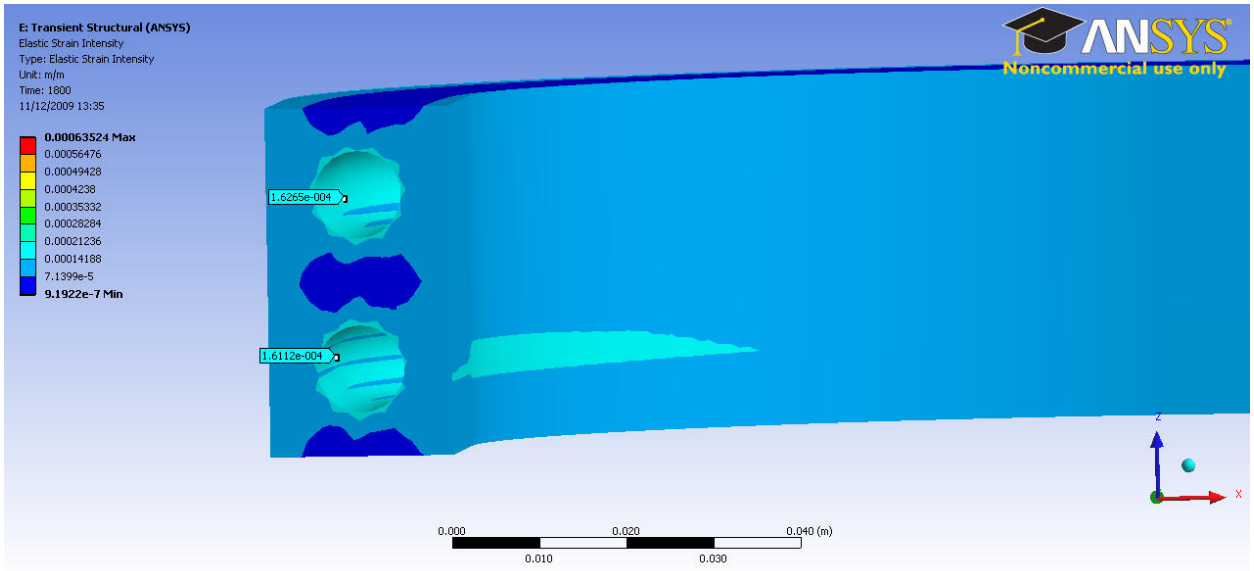

Fig. 9.22: Strain intensity in the elbow region at 1800 s (ANSYS Mechanical).

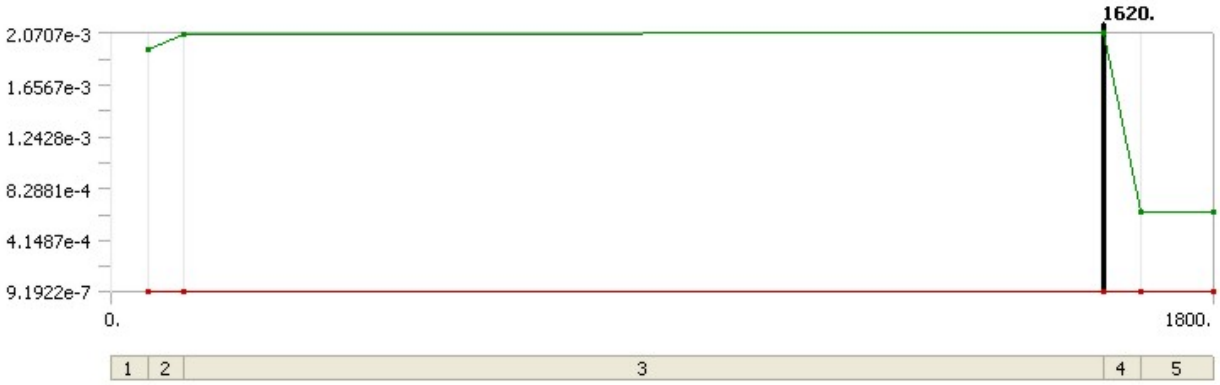

Fig. 9.23: Maximum (green) and minimum (red) strain intensity along time (ANSYS Mechanical).

Neutron heating included

The above set of calculations has been carried out including the neutron heating. The fluid flow modelling basically the same, the effect of the 25 MW/m^3 neutron heating results in a peak temperature of 389 °C (fig. 9.24), 39 °C more than without neutron heating.

The outlet temperature is 12 °C warmer than the inlet temperature (fig. 9.26).

Again, ANSYS mechanical transient thermal analysis gives lower temperature, the peak temperature is 370 °C (the difference is 32 °C between this model and the one without neutron heating) (fig. 9.27).

The maximum stress and strain occurs at the constraints these have to be excluded the areas of interest are still the channels in the elbow region. The stress intensity (fig. 9.28-9.29) at the wall of the channels reaches into the 400-450 MPa range, which is the limit of the elasticity (435 MPa minimum, 460 MPa average yield strength at 350 °C).

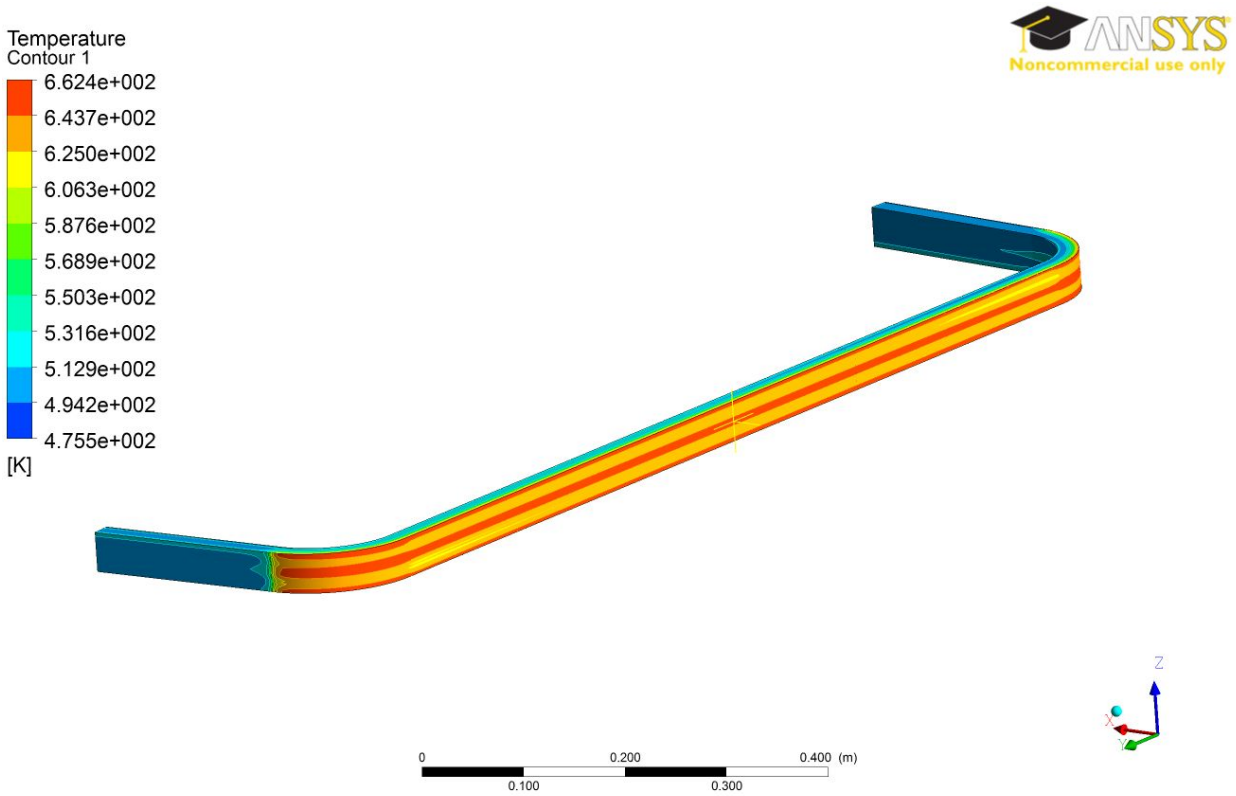

Fig. 9.24: Temperature at 1620 s (CFX).

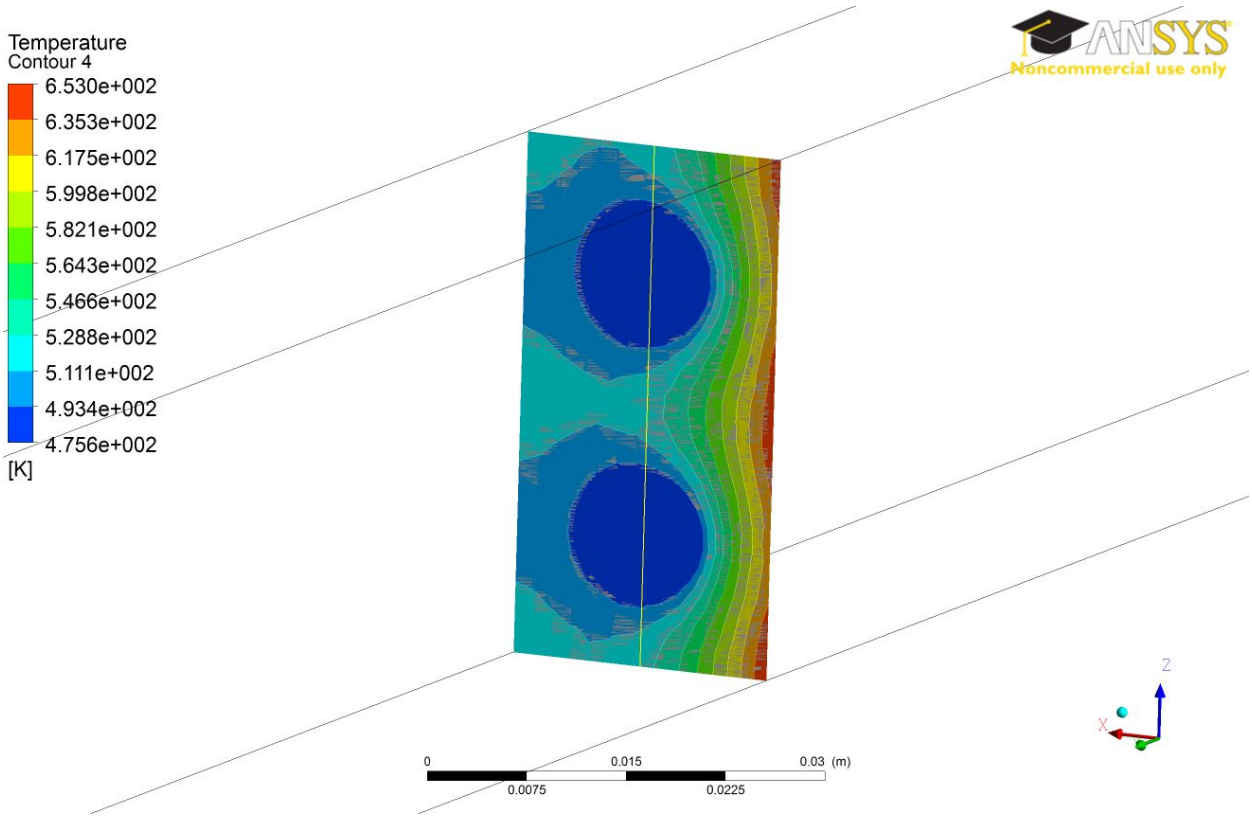

Fig. 9.25: Temperature distribution in an arbitrary section at 1620 s (CFX).

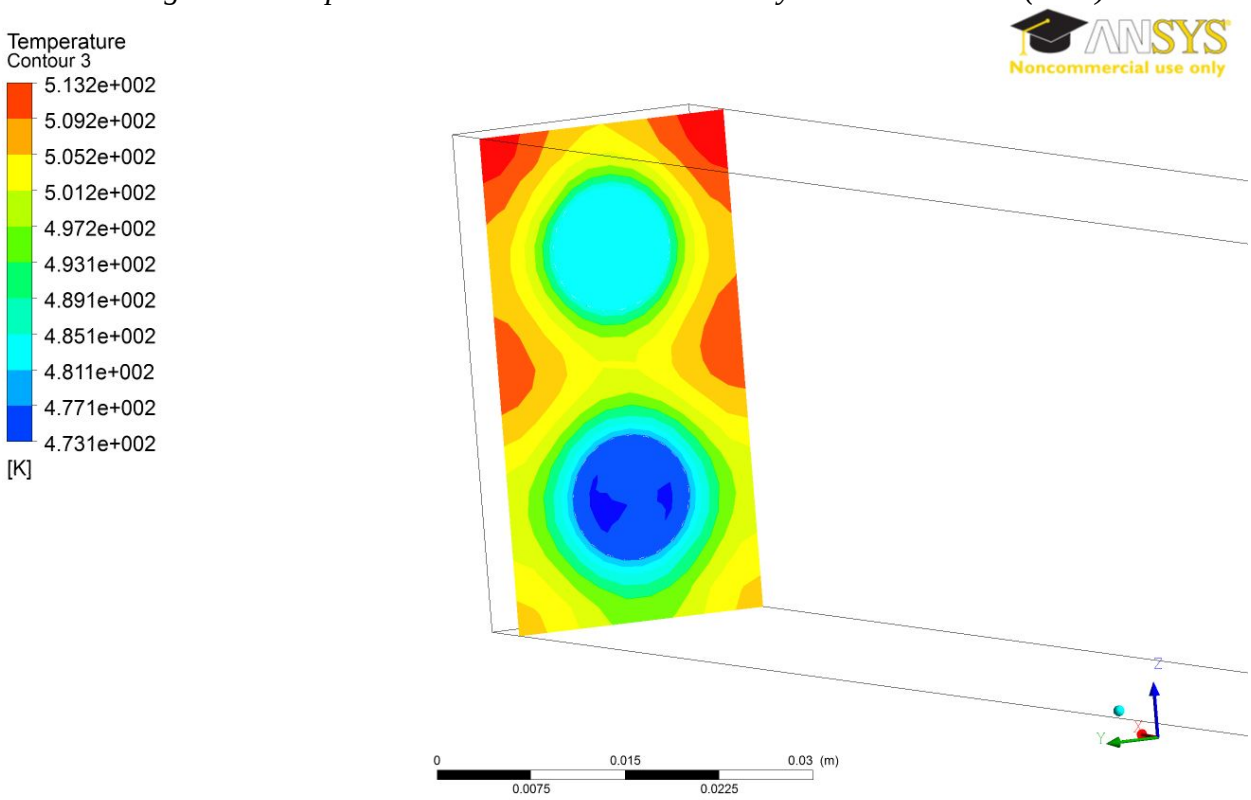

Fig. 9.26: Temperature distribution in a section close to the inlet/outlet at 1620 s (CFX).

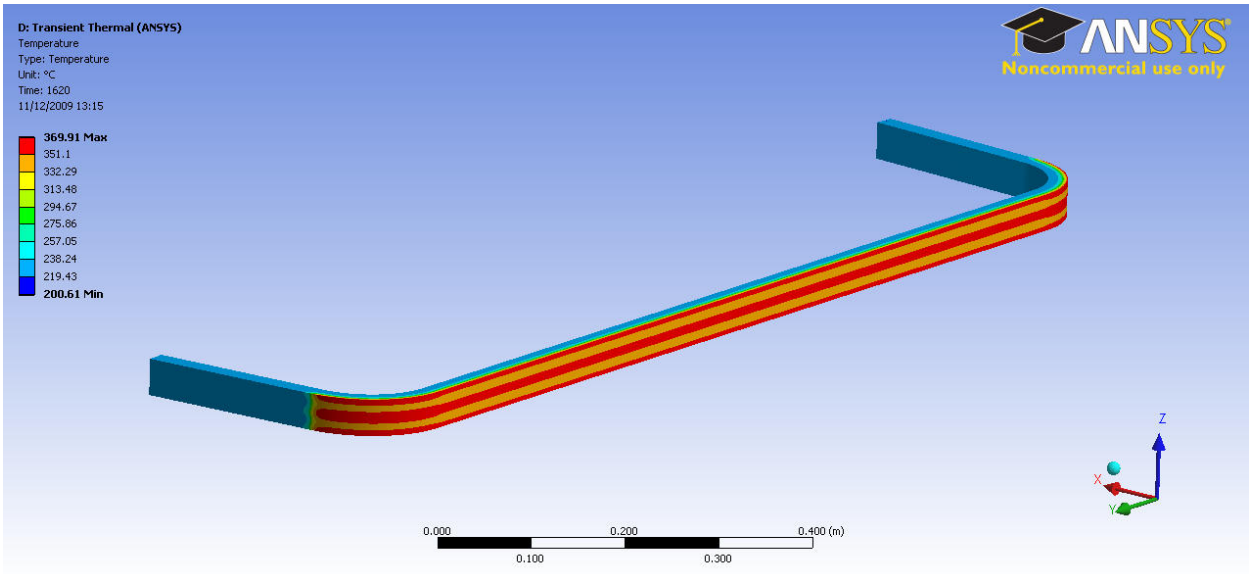

Fig. 9.27: Temperature at 1620 s (ANSYS Mechanical).

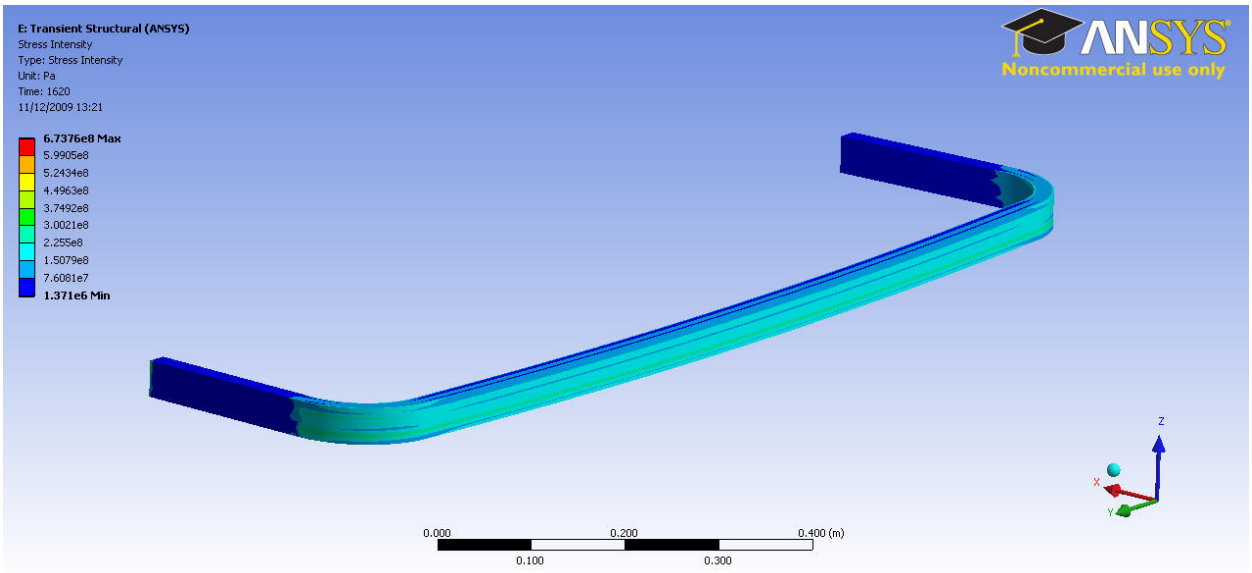

Fig. 9.28: Stress intensity at 1620 s (ANSYS Mechanical).

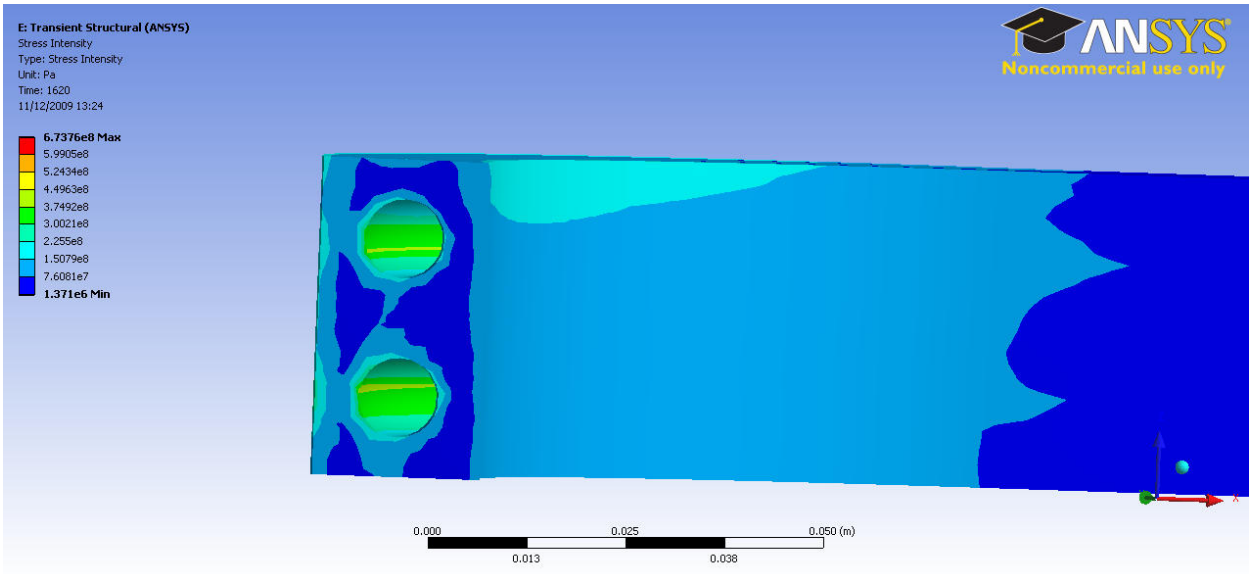

Fig. 9.29: Stress intensity in the elbow region at 1620 s (ANSYS Mechanical).

The strain intensities are shown on fig. 9.30-9.32. The mean strain intensity 0.13% and the alternating strain intensity is 0.115%. The neutron heating increased both the alternating and mean strain. The total strain range is 0.23%.

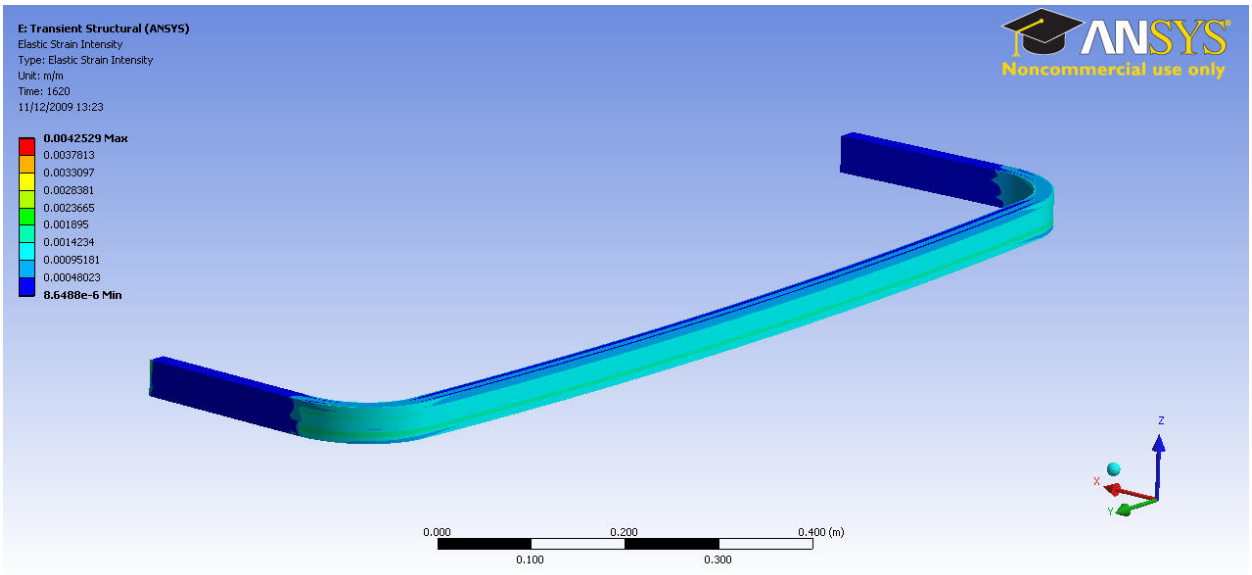

Fig. 9.30: Strain intensity at 1620 s (ANSYS Mechanical).

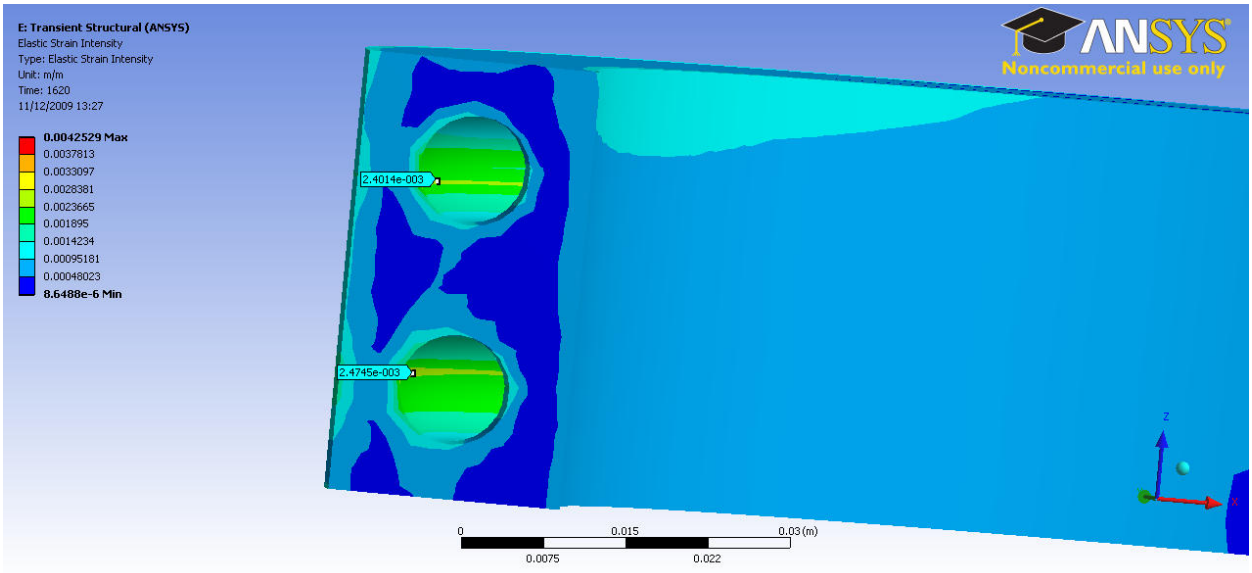

Fig. 9.31: Strain intensity in the elbow region at 1620 s (ANSYS Mechanical).

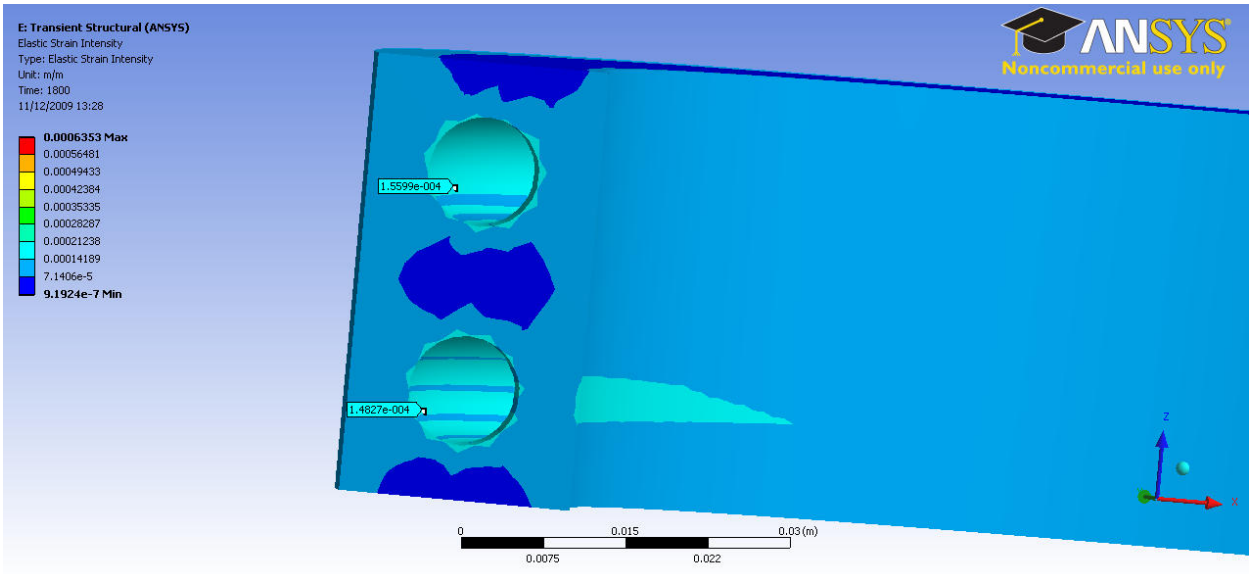

Fig. 9.32: Strain intensity in the elbow region at 1800 s (ANSYS Mechanical).

9.2.3. Modified model 1

Neutron heating excluded

The modelling method is the same as for the original model.

The peak surface temperature is 309 °C (fig. 9.33), the outlet temperature is only about 2 °C warmer than the inlet temperature (fig. 9.35). ANSYS mechanical transient thermal analysis gives lower temperature; the peak temperature is 304 °C (fig. 9.36).

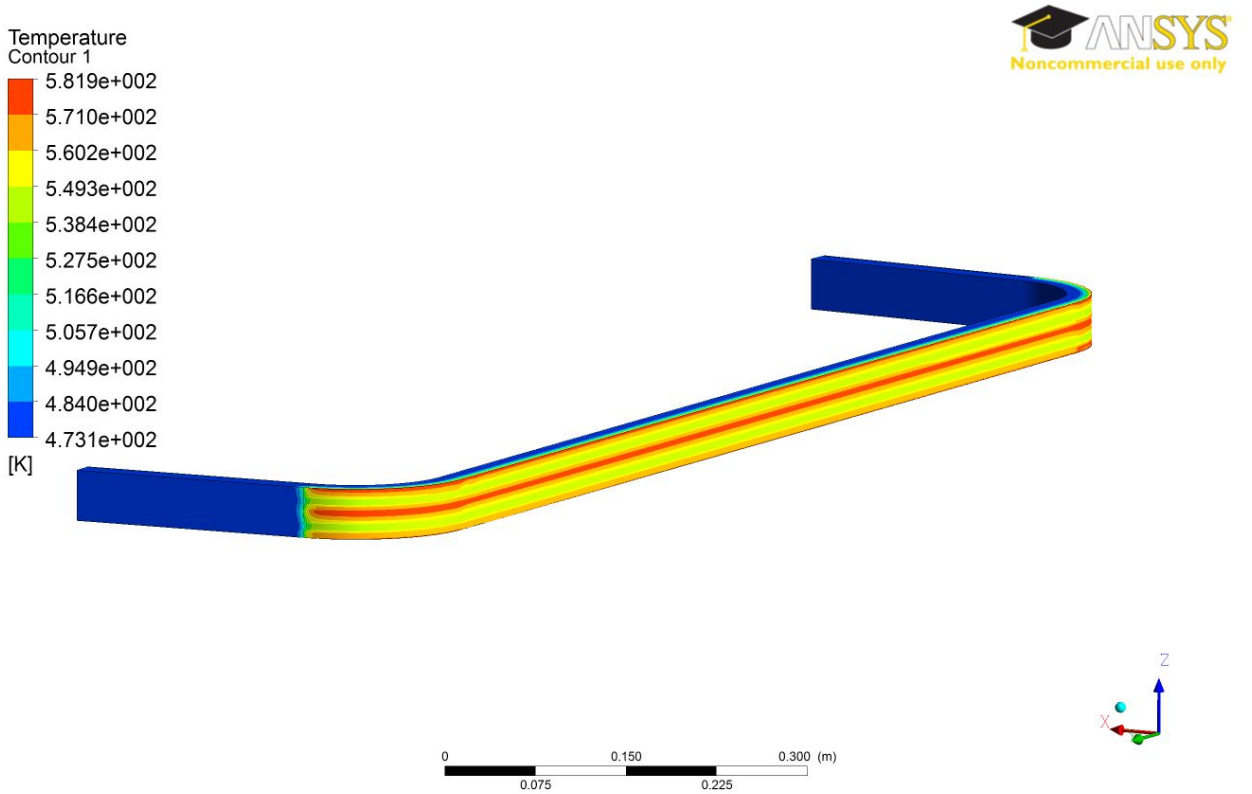

Fig. 9.33: Temperature at 1620 s (CFX).

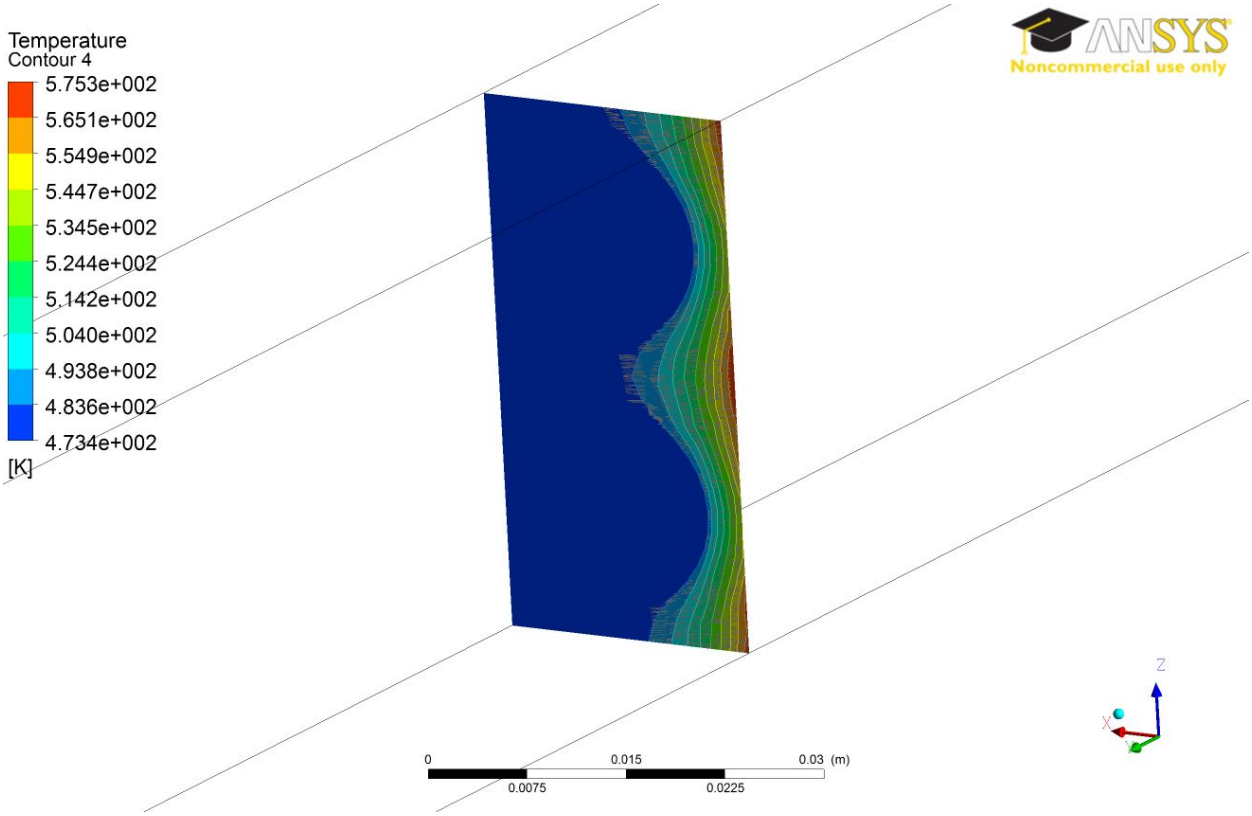

Fig. 9.34: Temperature distribution in an arbitrary section at 1620 s (CFX).

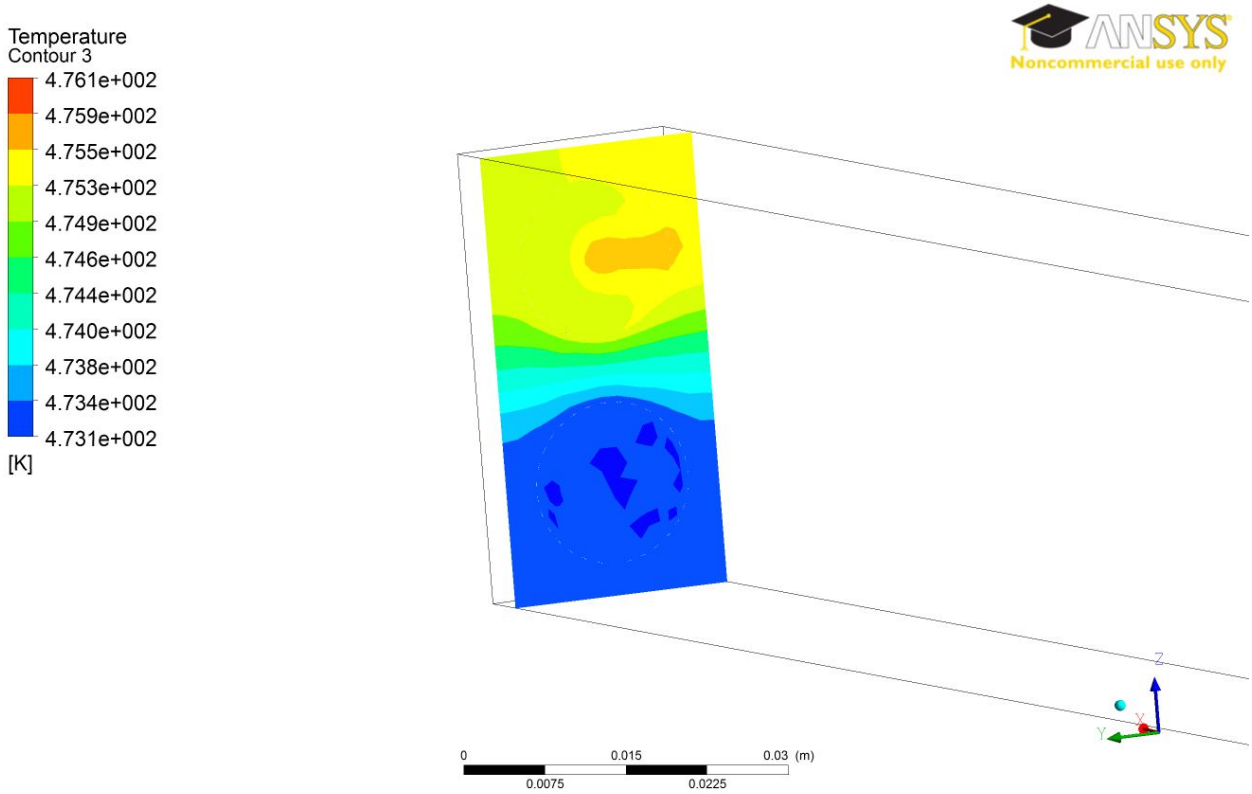

Fig. 9.35: Temperature distribution in a section close to the inlet/outlet at 1620 s (CFX).

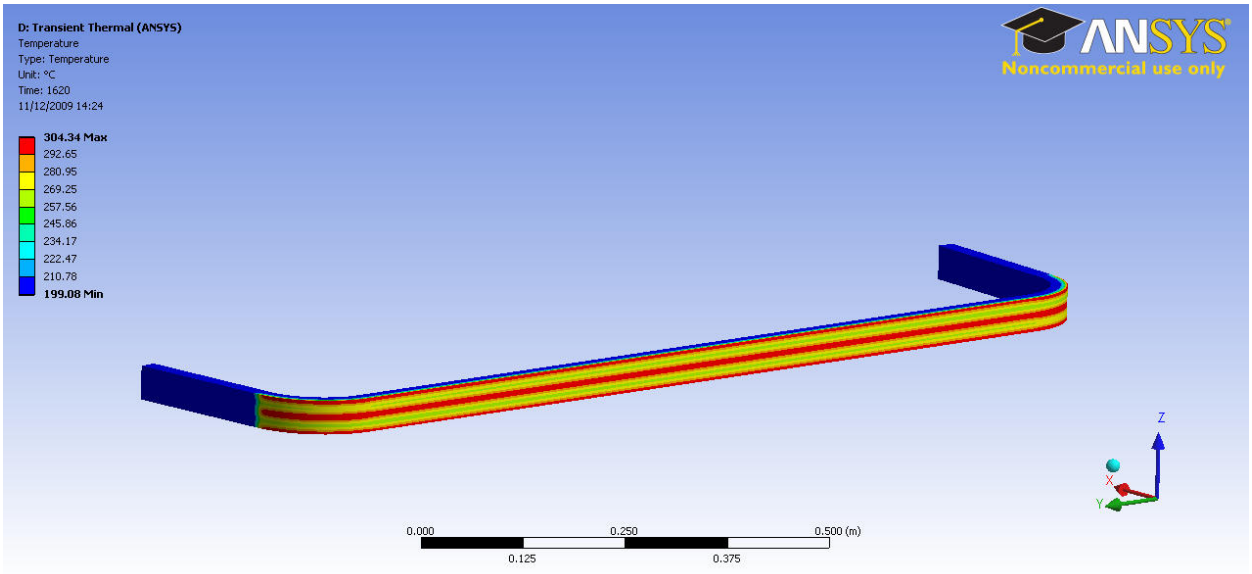

Fig. 9.36: Temperature at 1620 s (ANSYS Mechanical).

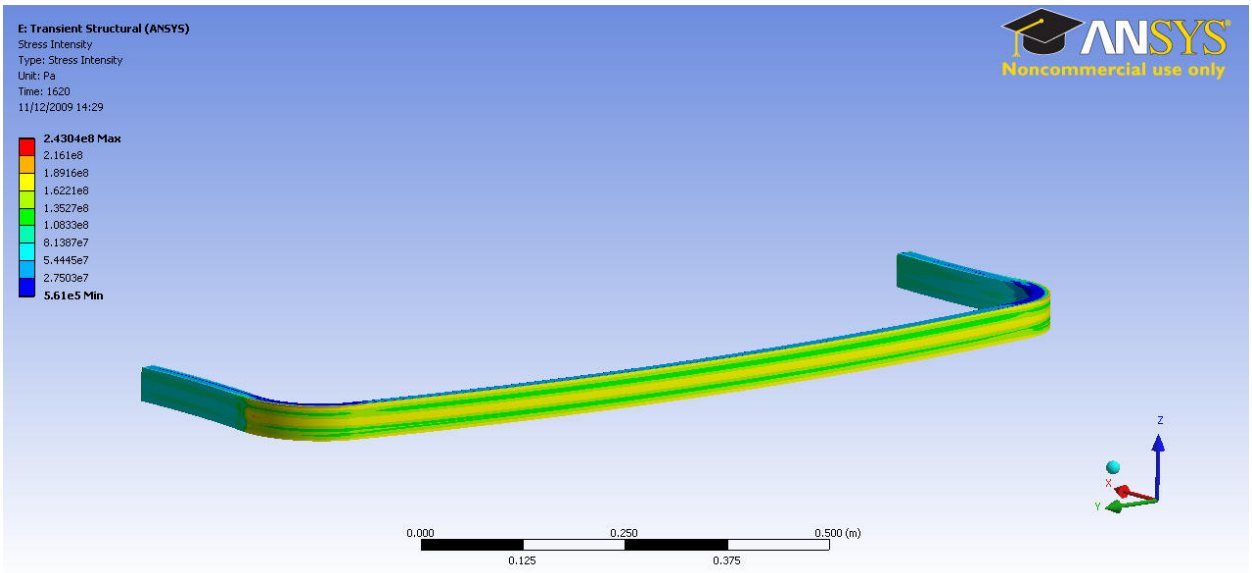

Fig. 9.37: Stress intensity at 1620 s (ANSYS Mechanical).

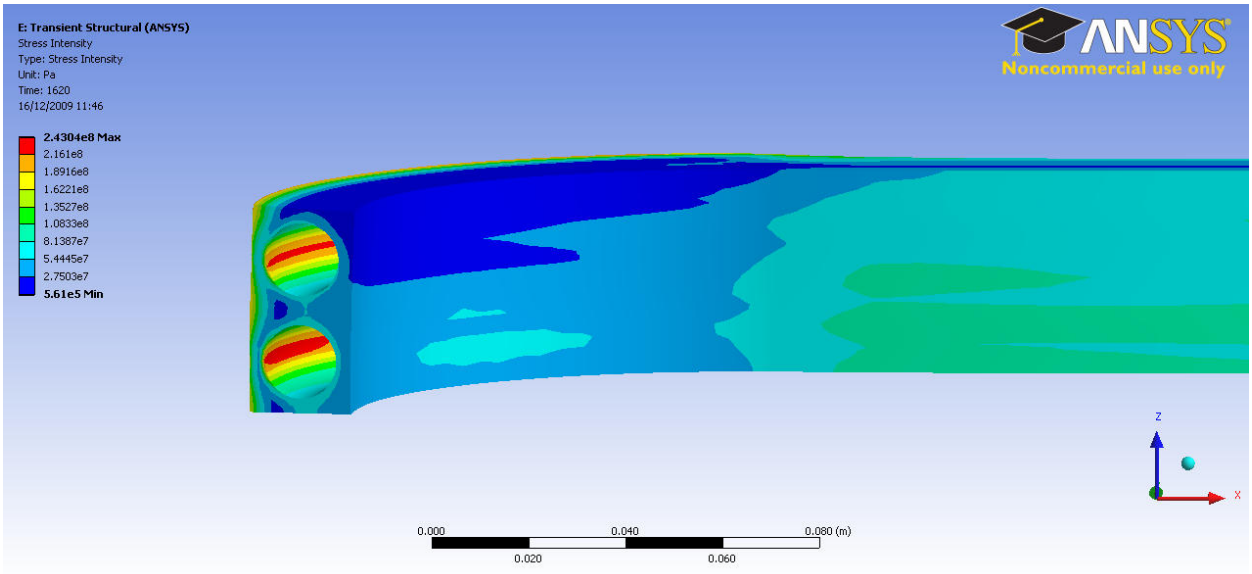

Fig. 9.38: Stress intensity in the elbow region at 1620 s (ANSYS Mechanical).

The strain intensities are shown on fig. 9.39-9.41. The mean strain intensity 0.08% and the alternating strain intensity is 0.065%. The total strain range is 0.13%.

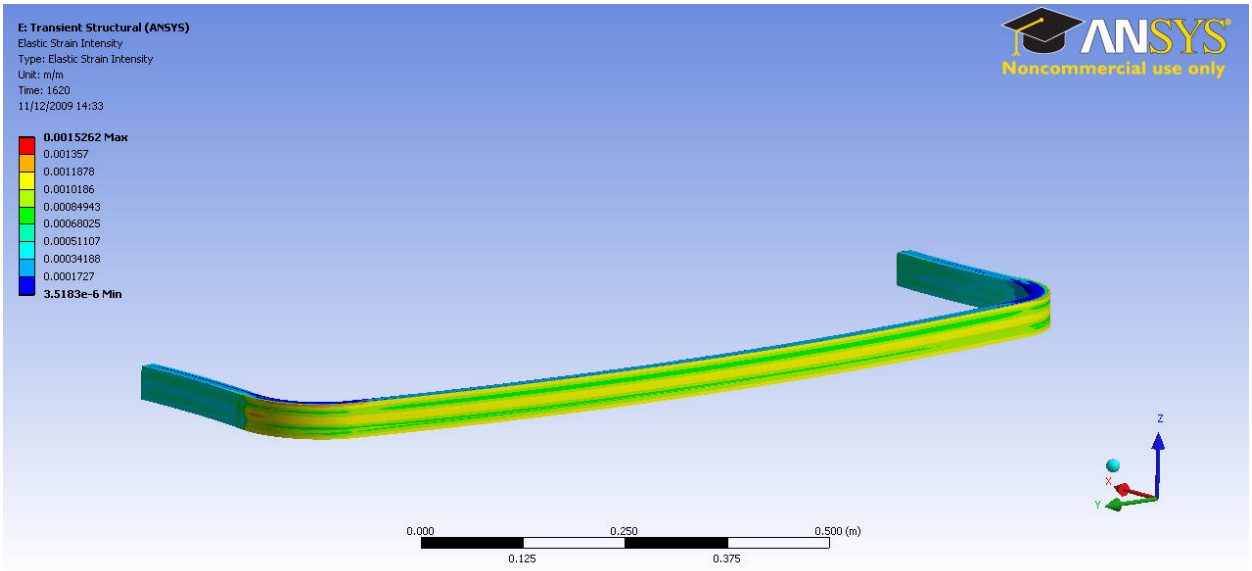

Fig. 9.39: Strain intensity at 1620 s (ANSYS Mechanical).

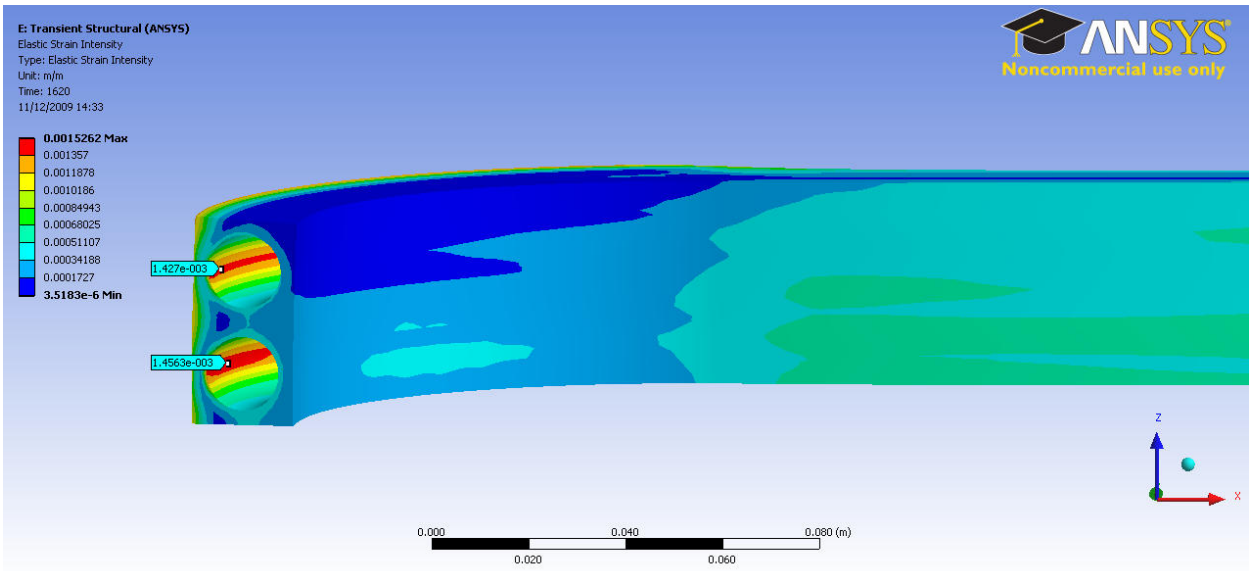

Fig. 9.40: Strain intensity in the elbow region at 1620 s (ANSYS Mechanical).

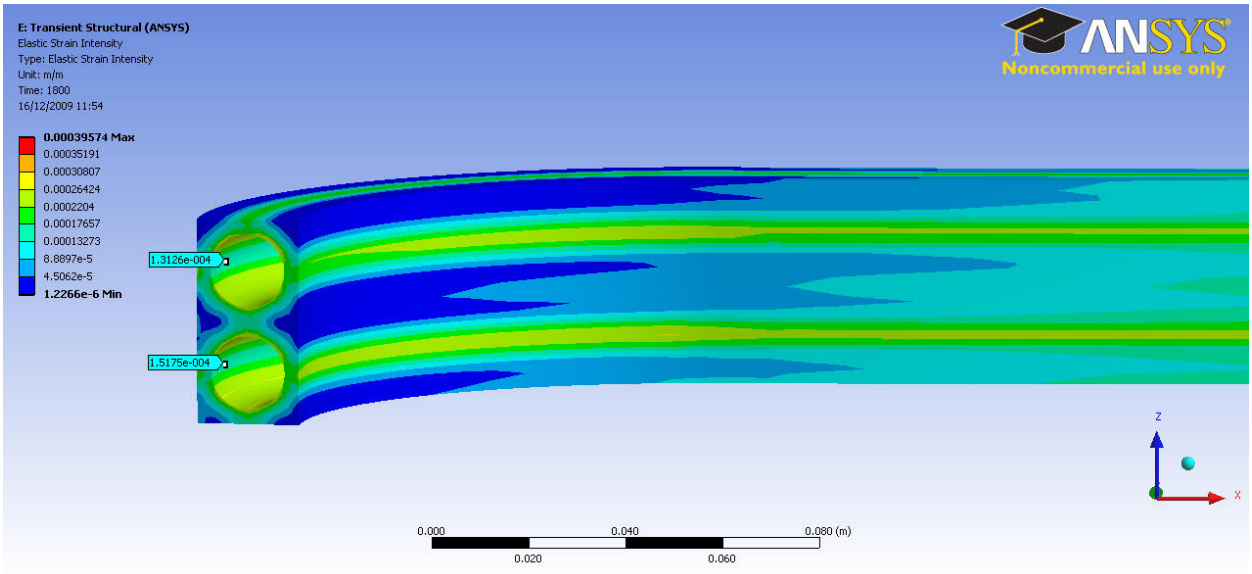

Fig. 9.41: Strain intensity in the elbow region at 1800 s (ANSYS Mechanical).

Neutron heating included

The peak surface temperature is 328 °C (fig. 9.42) if the neutron heating is included; the outlet temperature is only about 2 °C warmer than the inlet temperature (fig. 9.44).

ANSYS mechanical transient thermal analysis gives lower temperature; the peak temperature is 323 °C (fig. 9.45).

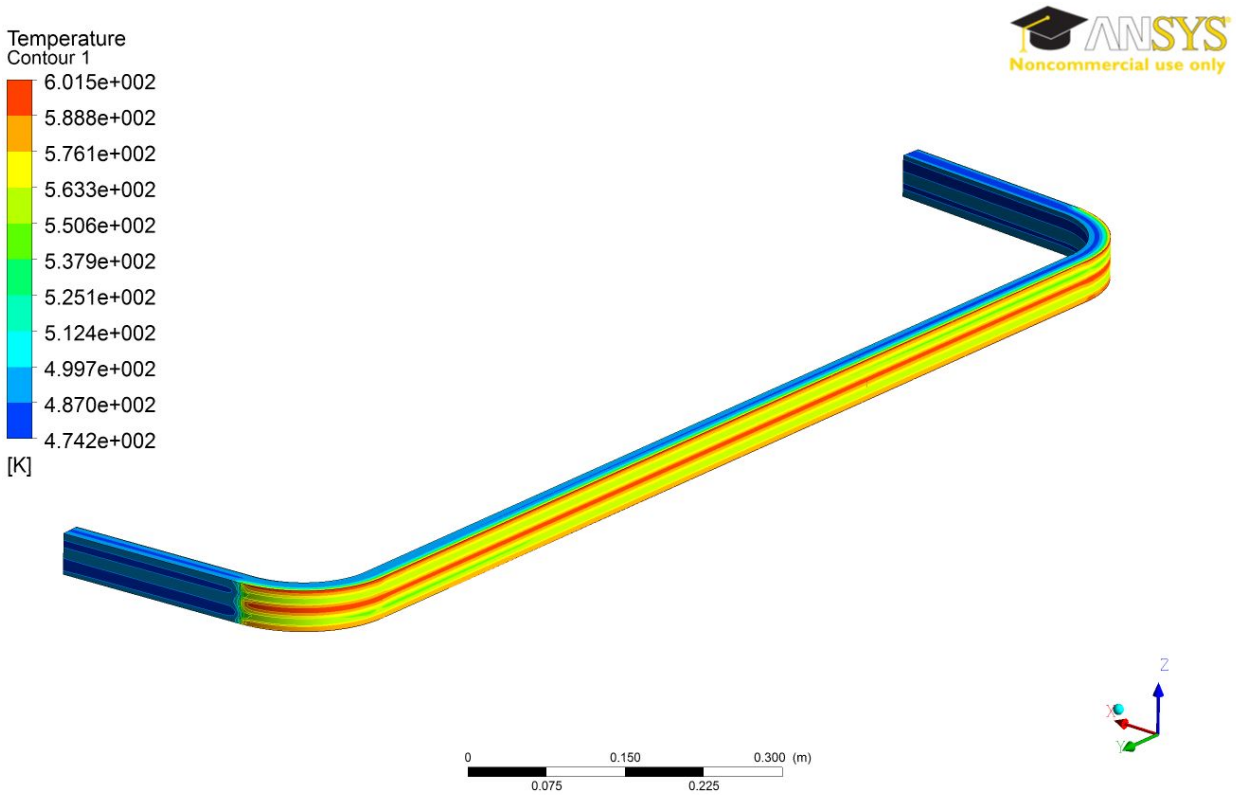

Fig. 9.42: Temperature at 1620 s (CFX).

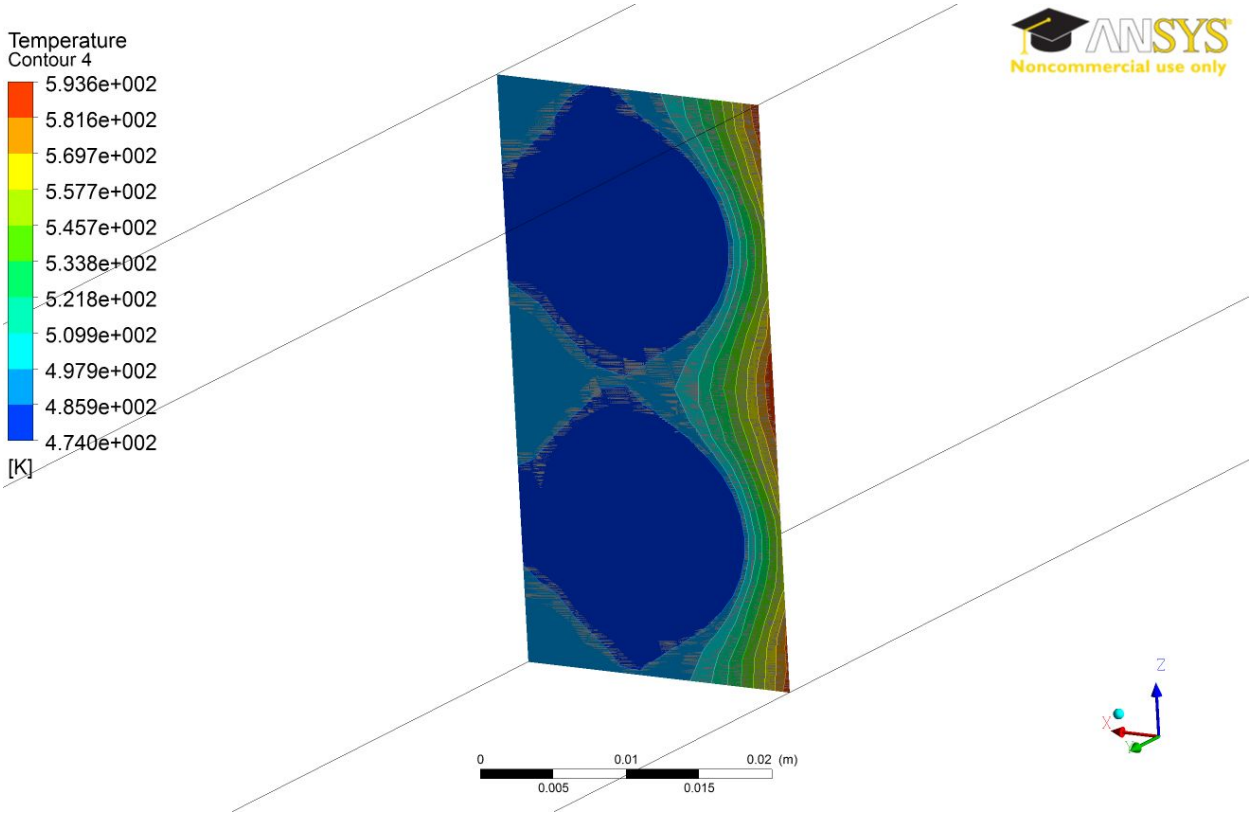

Fig. 9.43: Temperature distribution in an arbitrary section at 1620 s (CFX).

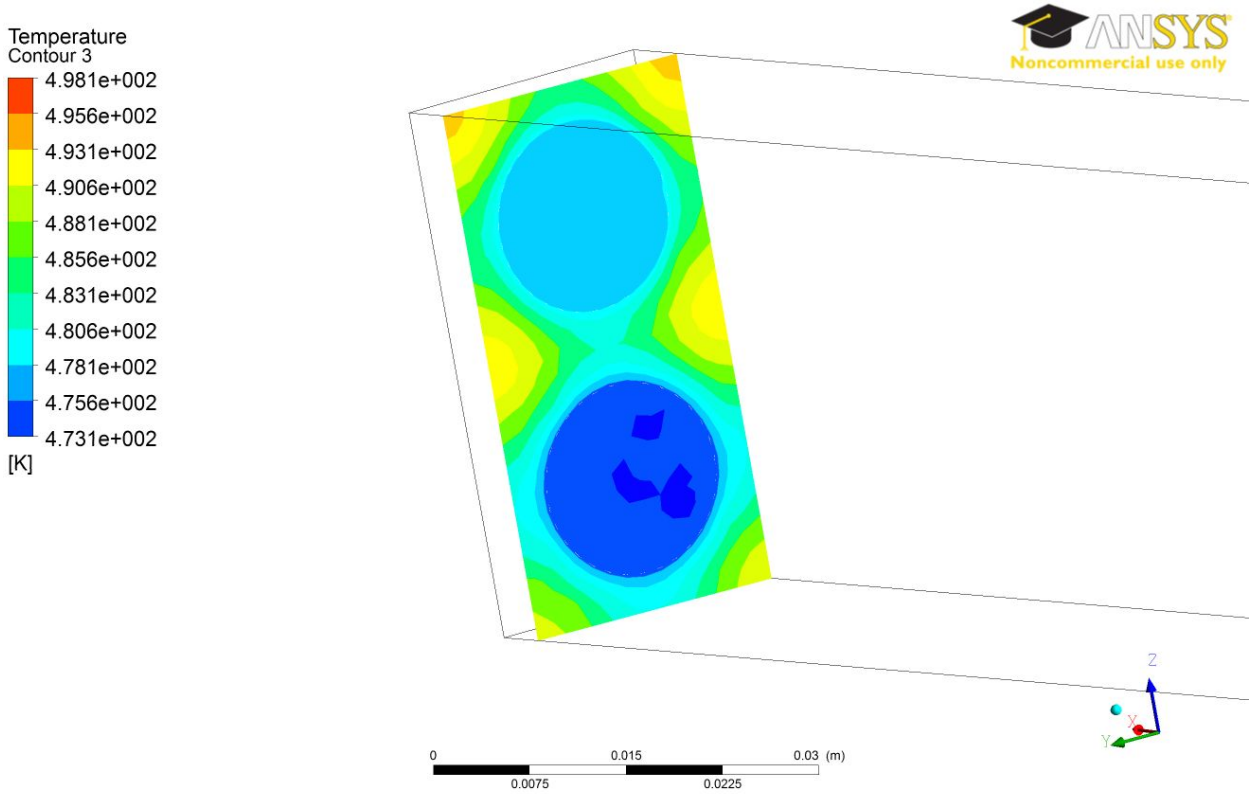

Fig. 9.44: Temperature distribution in a section close to the inlet/outlet at 1620 s (CFX).

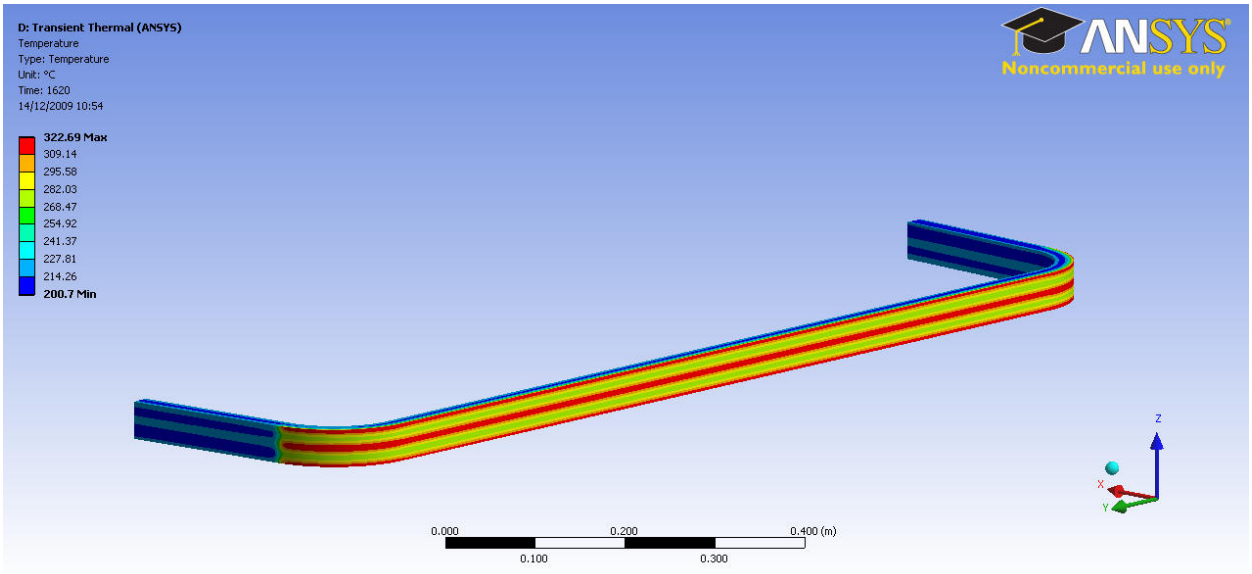

Fig. 9.45: Temperature at 1620 s (ANSYS Mechanical).

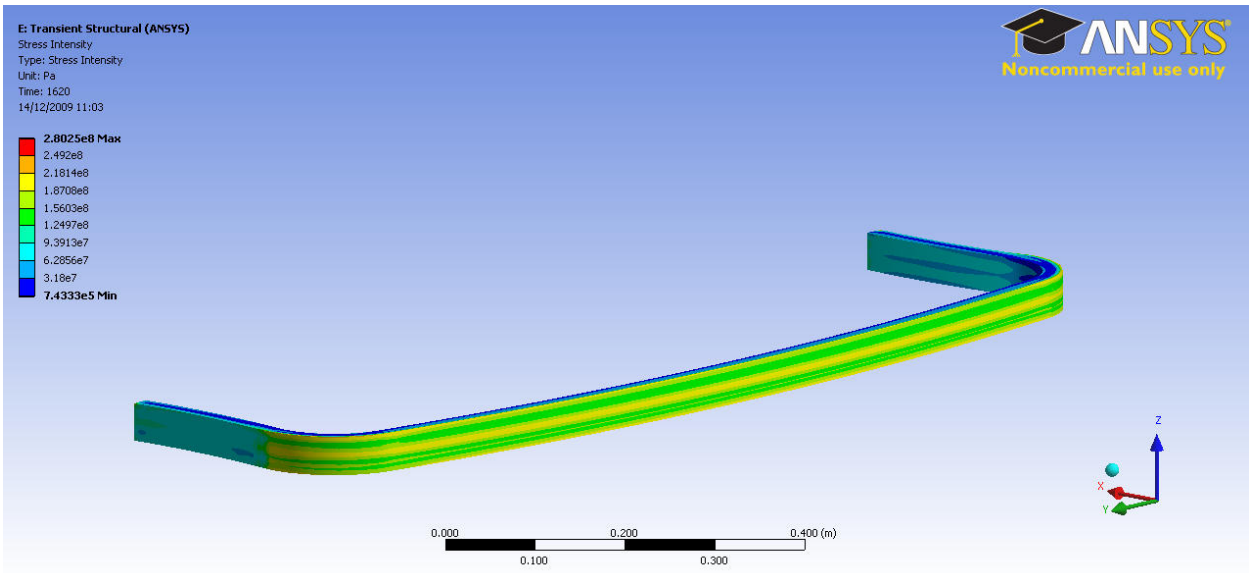

Fig. 9.46: Stress intensity at 1620 s (ANSYS Mechanical).

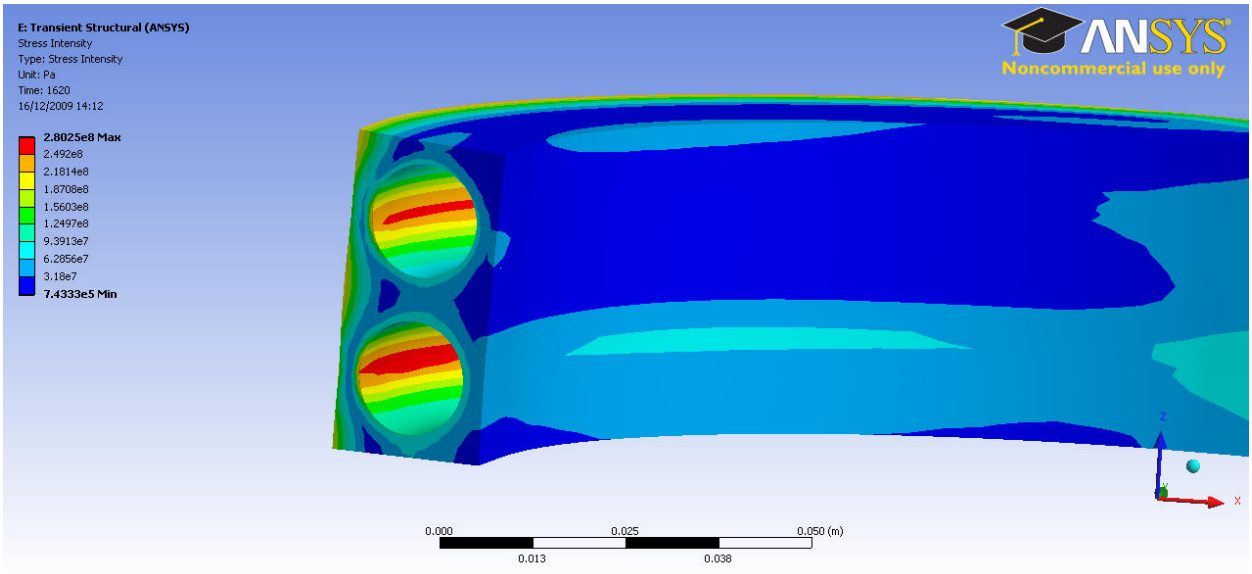

Fig. 9.47: Stress intensity in the elbow region at 1620 s (ANSYS Mechanical).

The strain intensities are shown on fig. 9.48-9.50. The mean strain intensity 0.1% and the alternating strain intensity is 0.073%. The total strain range is 0.146%.

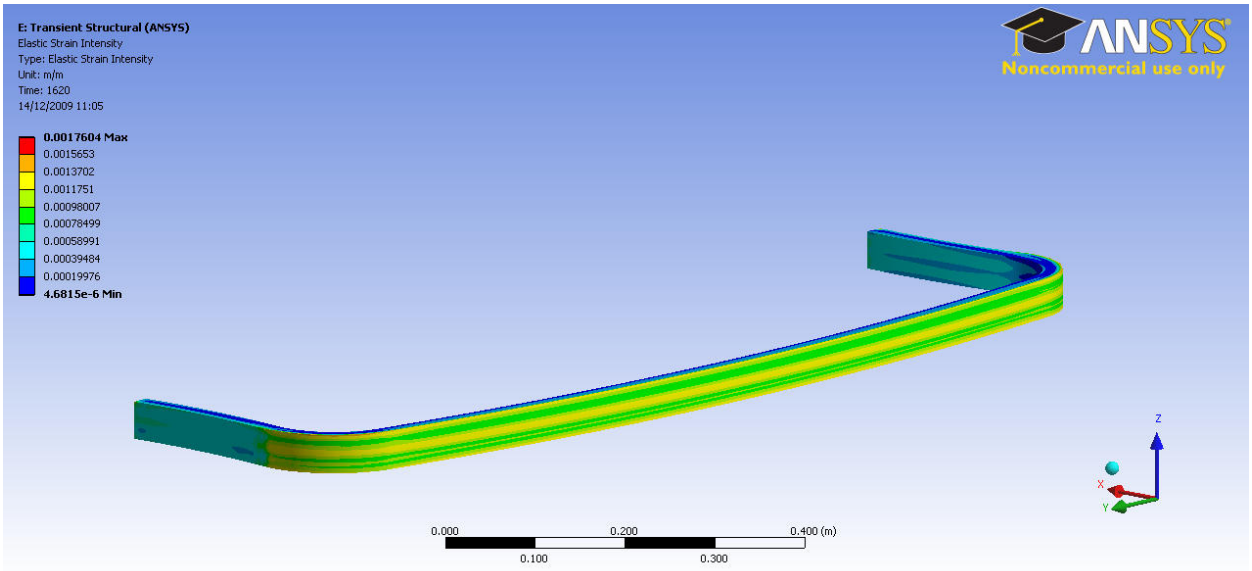

Fig. 9.48: Strain intensity at 1620 s (ANSYS Mechanical).

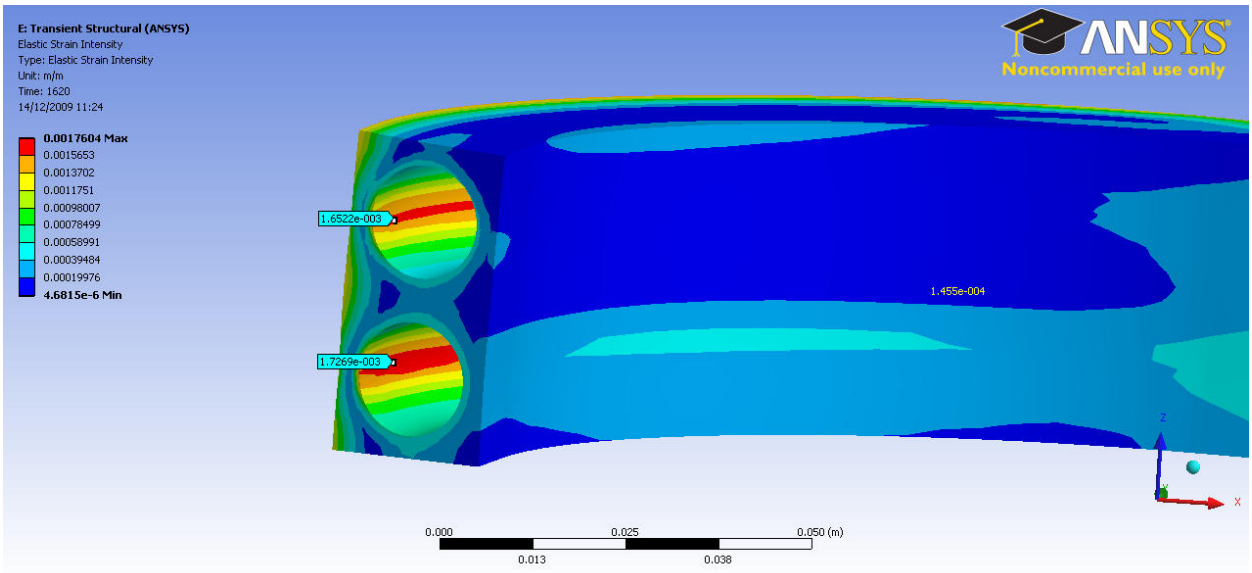

Fig. 9.49: Strain intensity in the elbow region at 1620 s (ANSYS Mechanical).

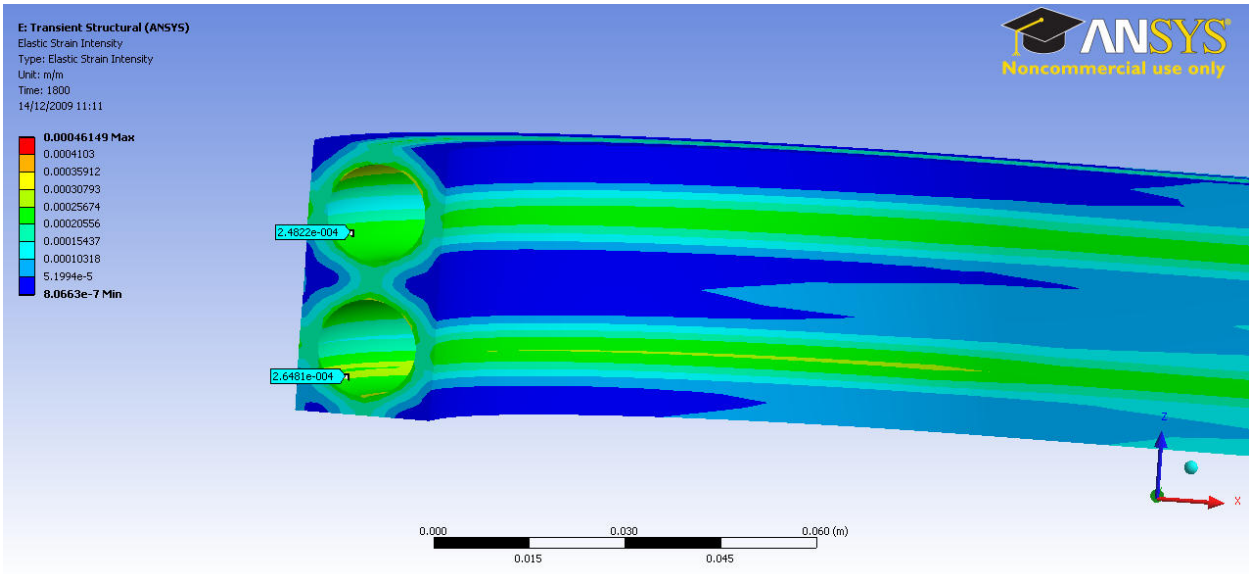

Fig. 9.50: Strain intensity in the elbow region at 1800 s (ANSYS Mechanical).

9.2.4. Modified model 2

Neutron heating excluded

The modelling method is the same as for the previous models.

The peak surface temperature is 320 °C (fig. 9.51), the outlet temperature is only about 5 °C warmer than the inlet temperature (fig. 9.53). ANSYS mechanical transient thermal analysis gives lower temperature; the peak temperature is 304 °C (fig. 9.54). It has to be mentioned that the 320 °C peak temperature in the CFX analysis is very localised, fig. 9.52 suggests it is rather closer to 312 °C.

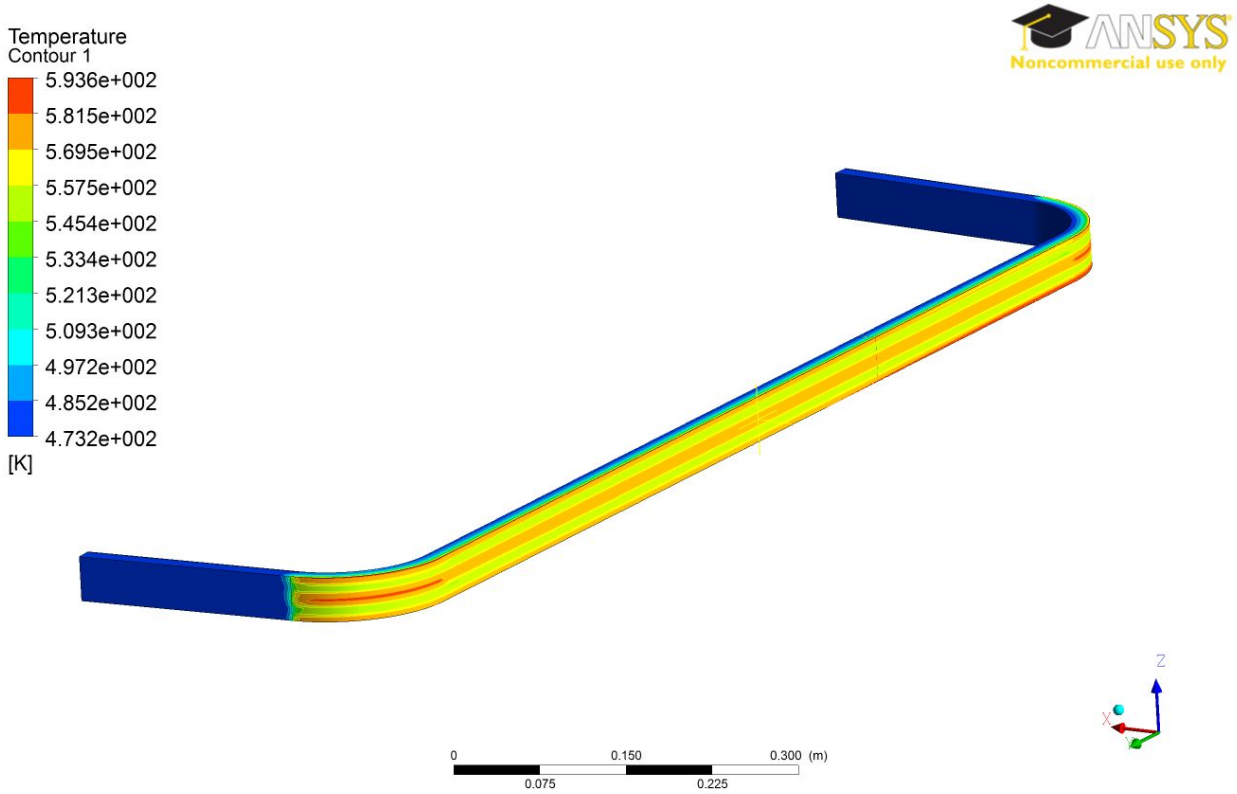

Fig. 9.51: Temperature at 1620 s (CFX).

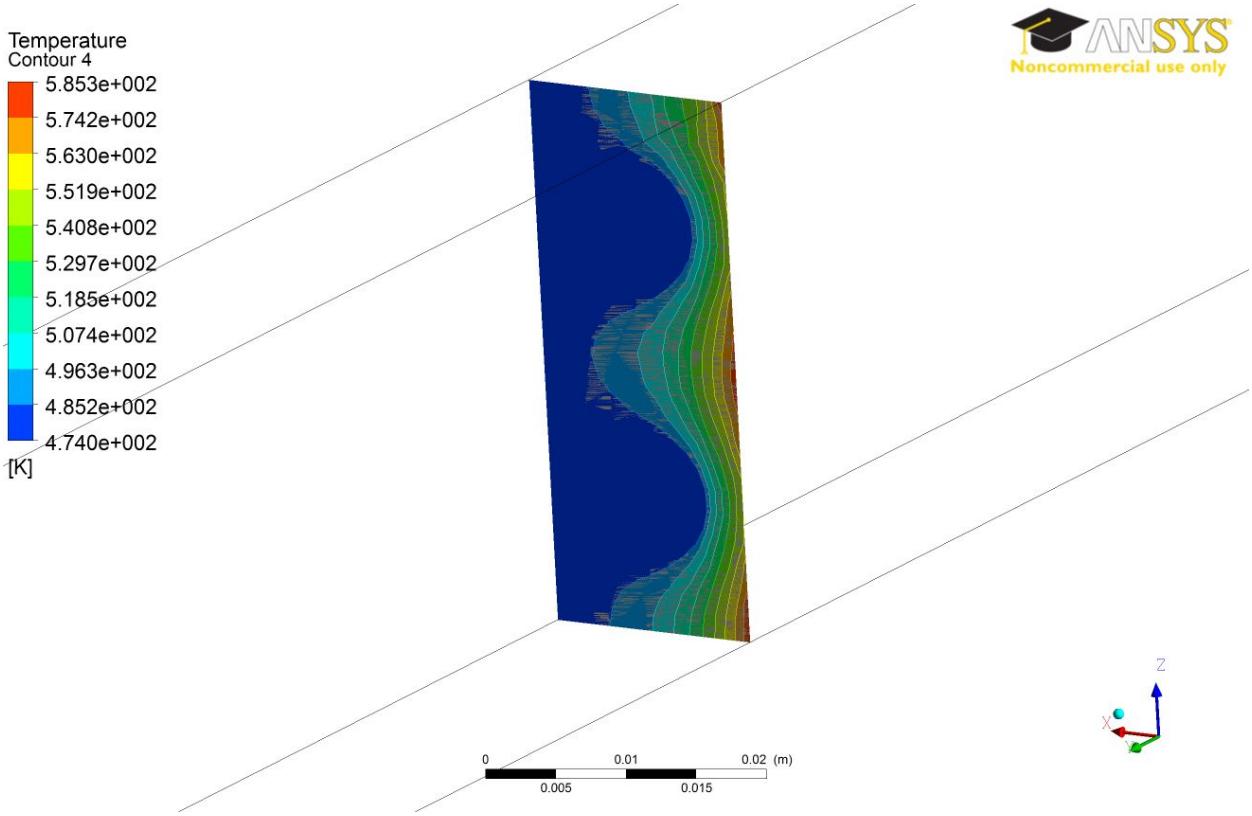

Fig. 9.52: Temperature distribution in an arbitrary section at 1620 s (CFX).

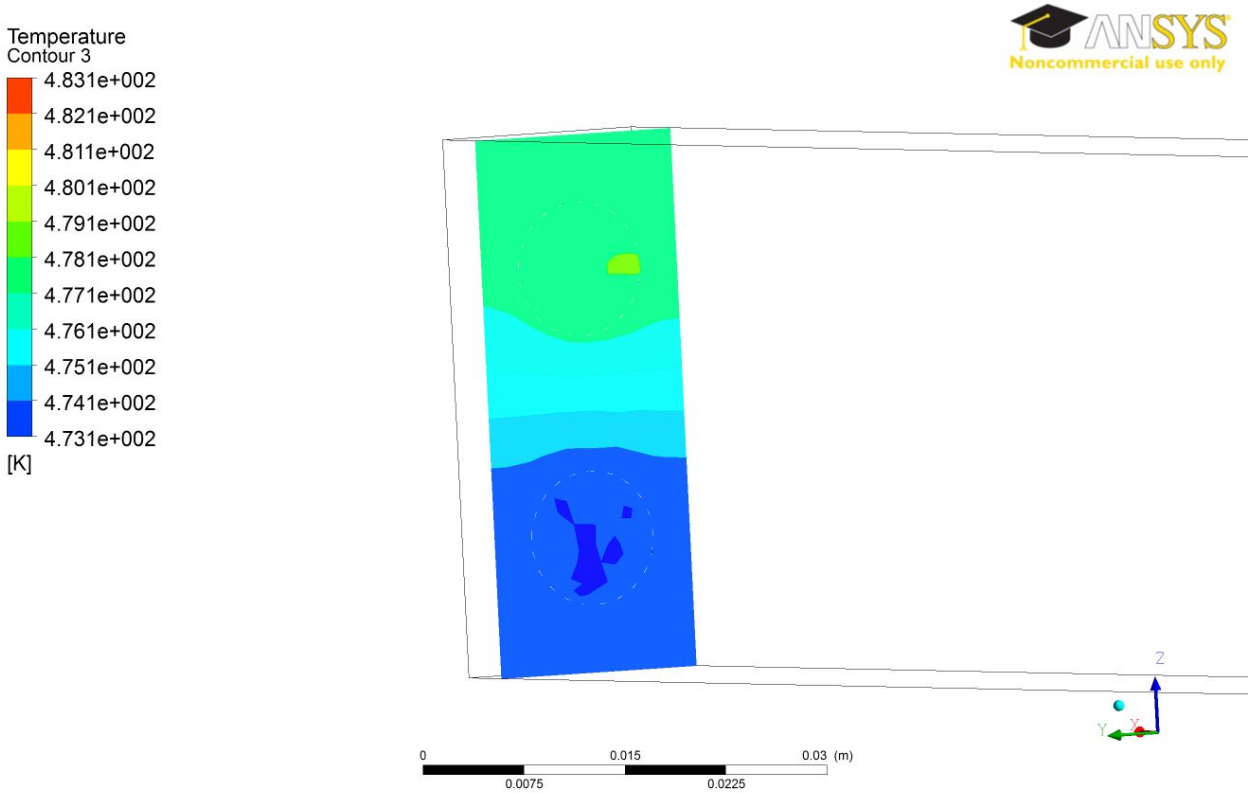

Fig. 9.53: Temperature distribution in a section close to the inlet/outlet at 1620 s (CFX).

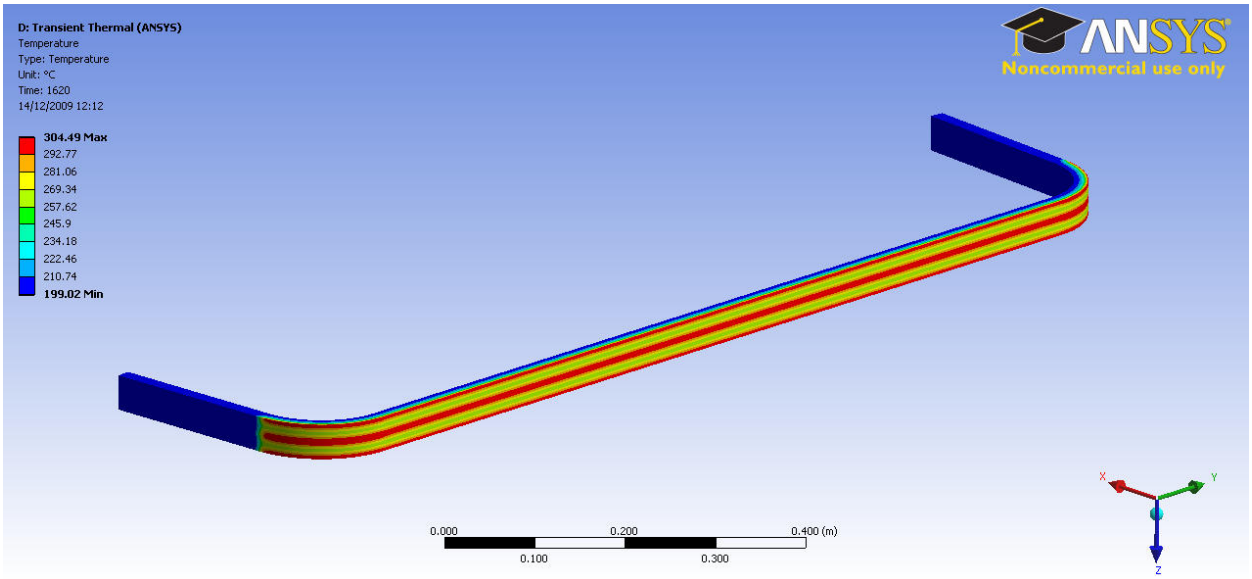

Fig. 9.54: Temperature at 1620 s (ANSYS Mechanical).

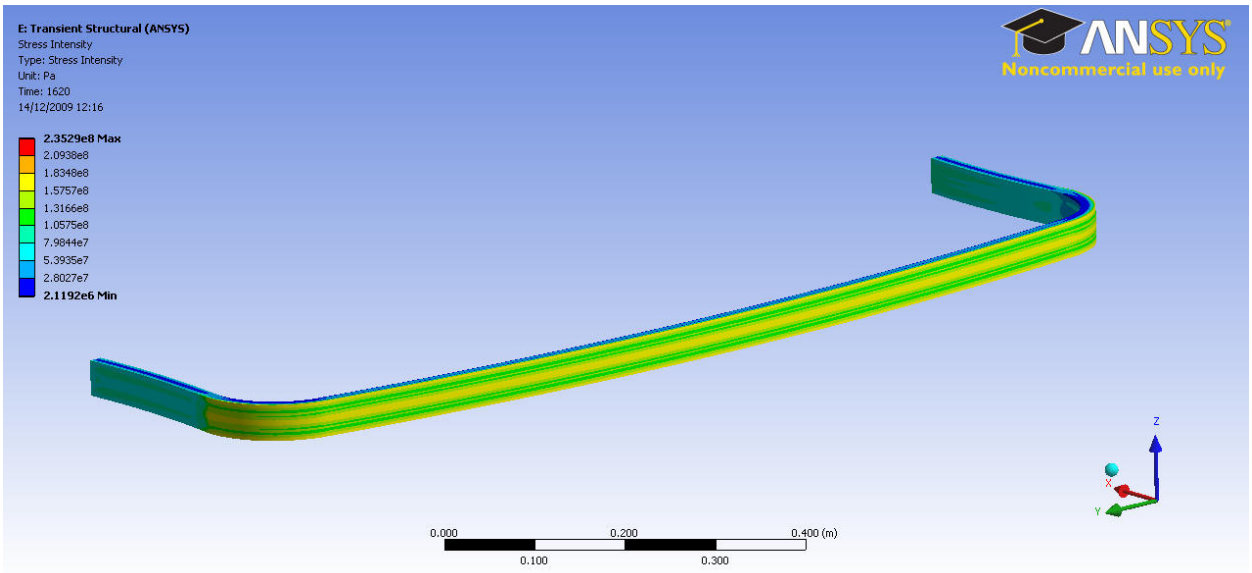

Fig. 9.55: Stress intensity at 1620 s (ANSYS Mechanical).

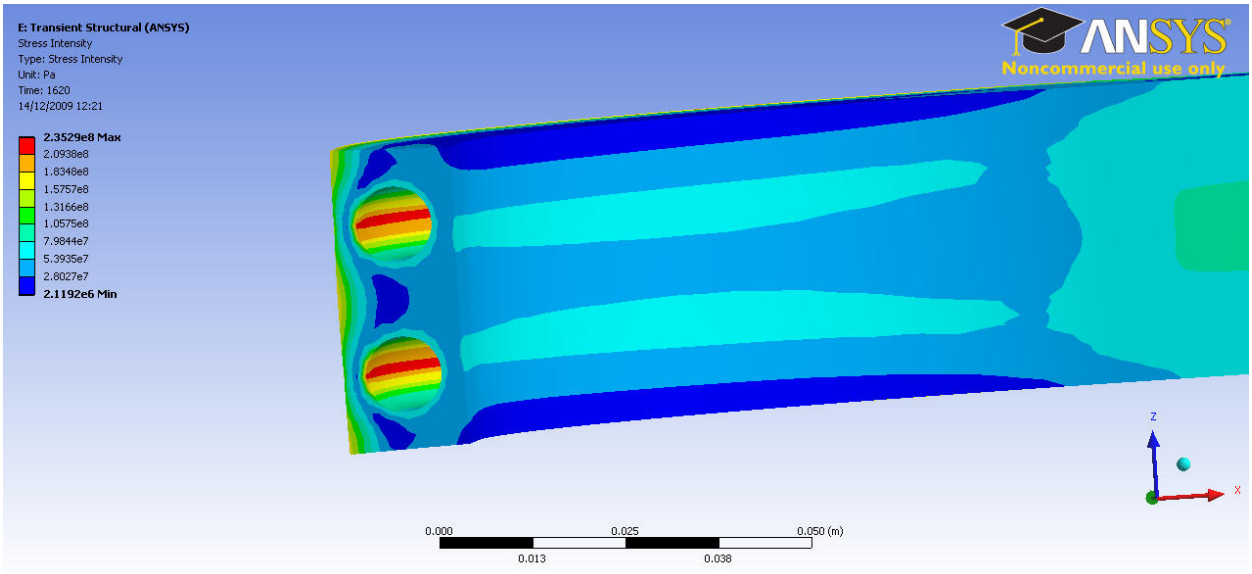

Fig. 9.56: Stress intensity in the elbow region at 1620 s (ANSYS Mechanical).

The strain intensities are shown on fig. 9.57-9.59. The mean strain intensity 0.082% and the alternating strain intensity is 0.063%. The total strain range is 0.126%.

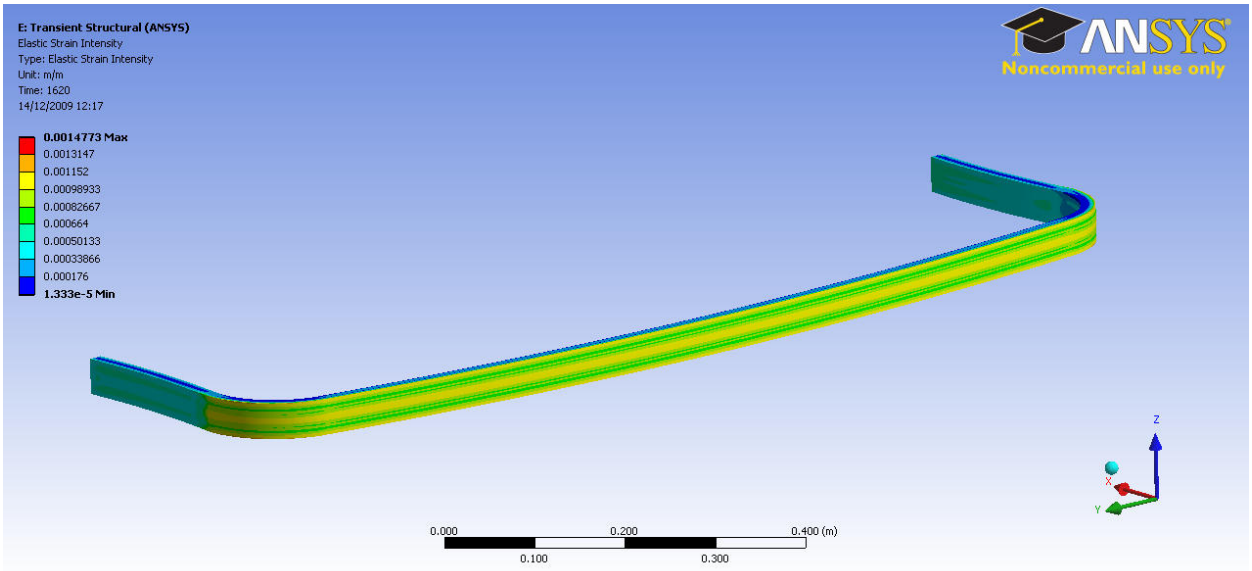

Fig. 9.57: Strain intensity at 1620 s (ANSYS Mechanical).

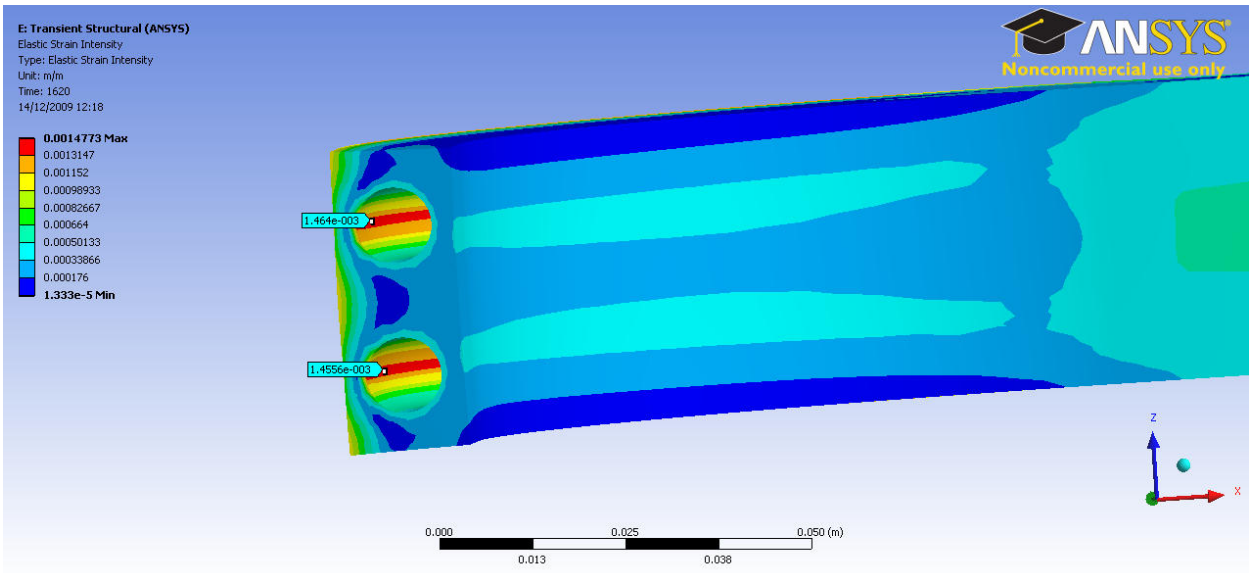

Fig. 9.58: Strain intensity in the elbow region at 1620 s (ANSYS Mechanical).

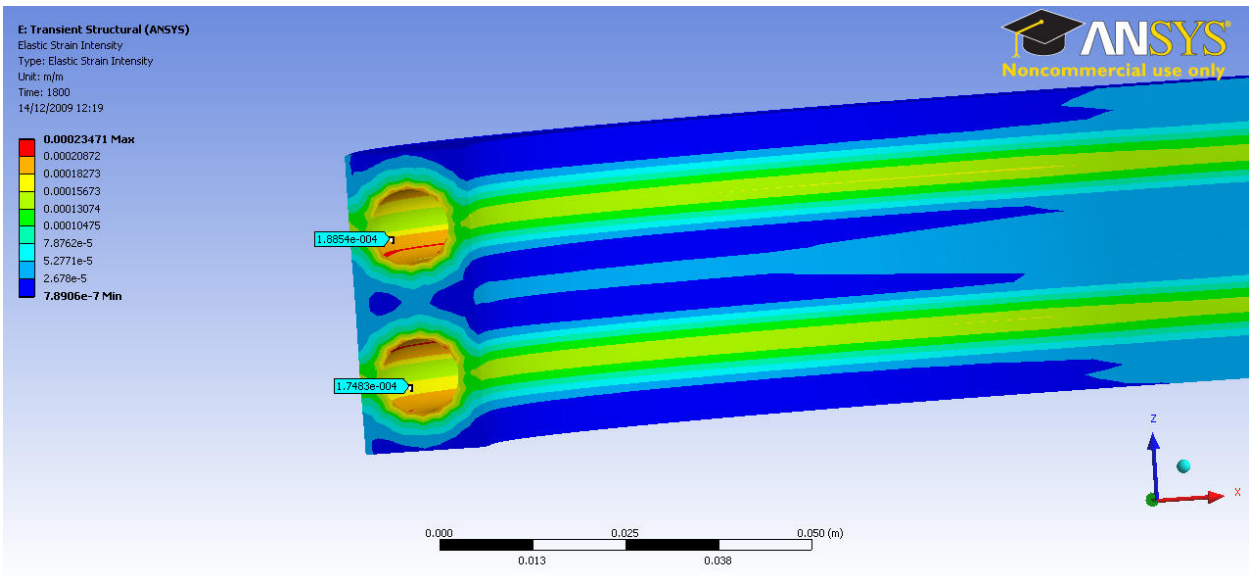

Fig. 9.59: Strain intensity in the elbow region at 1800 s (ANSYS Mechanical).

Neutron heating included

The peak surface temperature is 346 °C (fig. 9.60) if the neutron heating is included; the outlet temperature is only about 10-12 °C warmer than the inlet temperature (fig. 9.62).
ANSYS mechanical transient thermal analysis gives lower temperature; the peak temperature is 324 °C (fig. 9.63). Again, the 346 °C peak temperature in the CFX analysis is very localised, fig. 9.61 suggests it is rather closer to 336 °C.

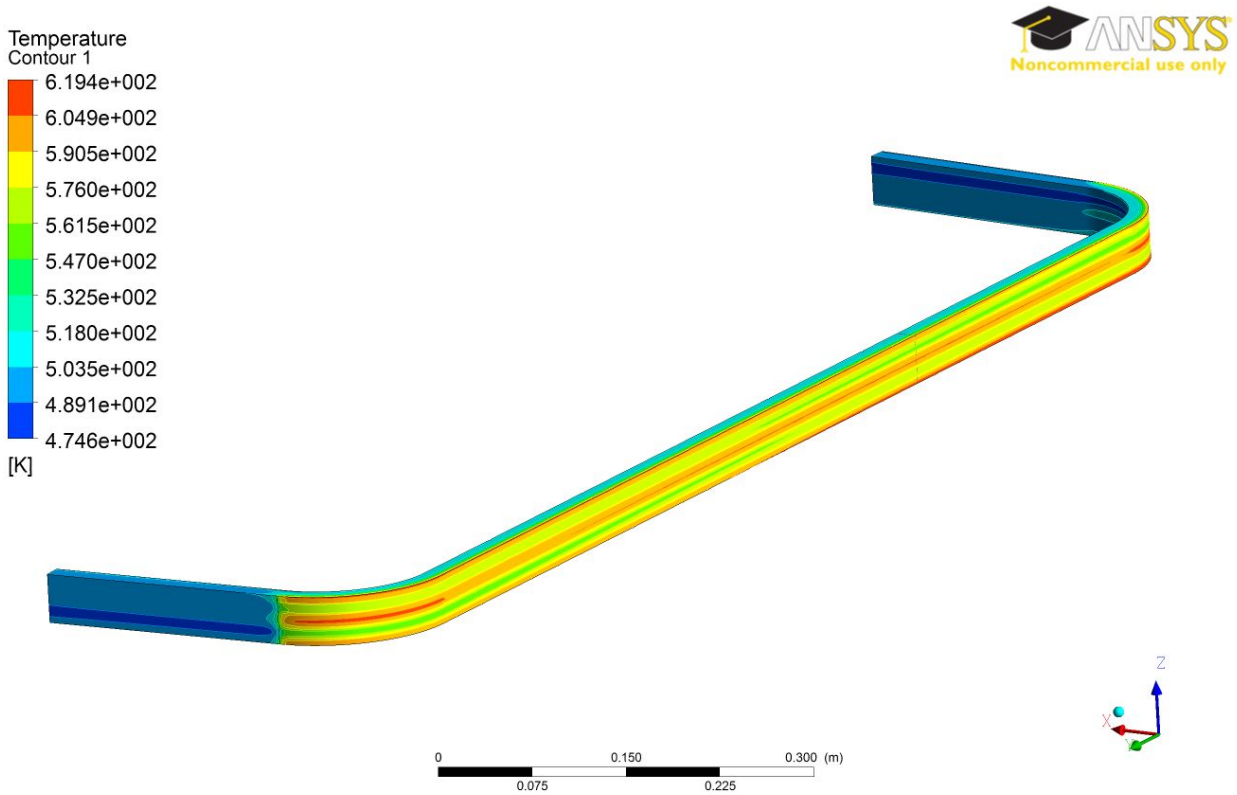

Fig. 9.60: Temperature at 1620 s (CFX).

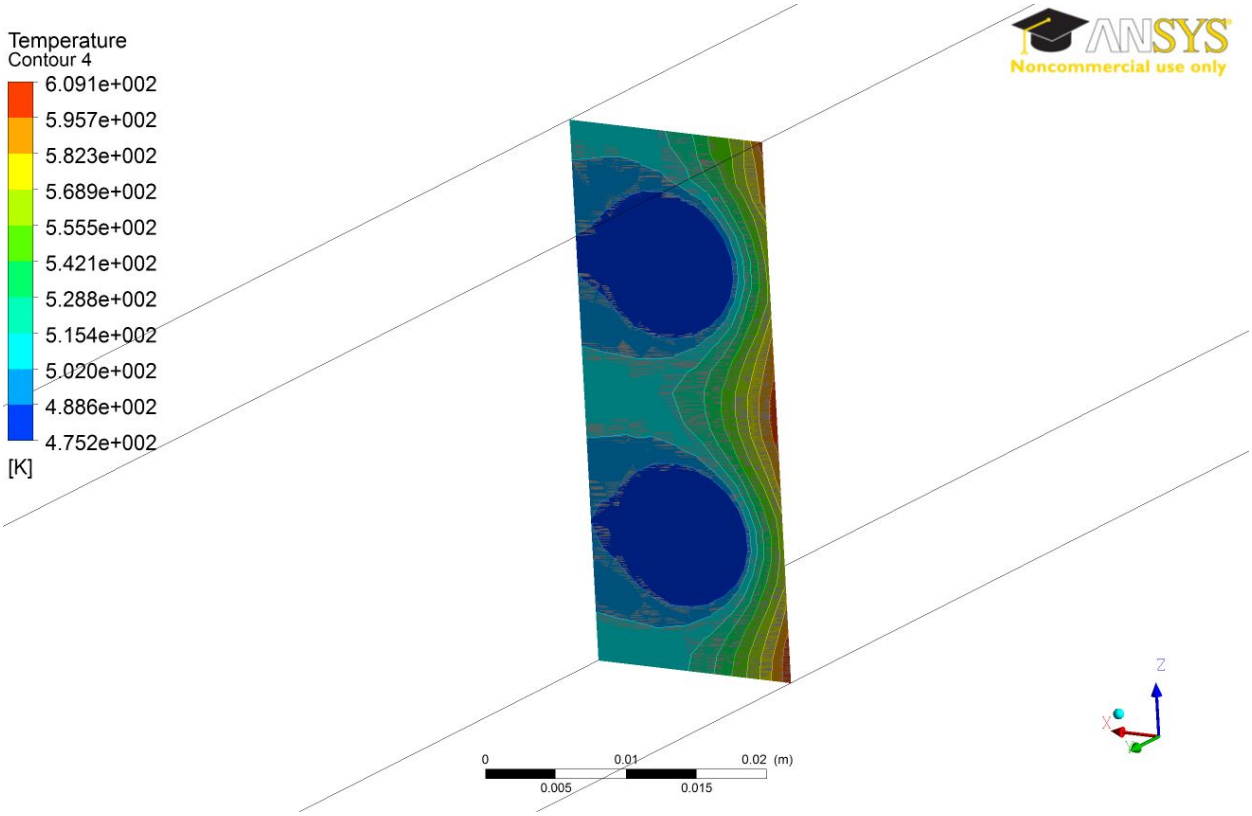

Fig. 9.61: Temperature distribution in an arbitrary section at 1620 s (CFX).

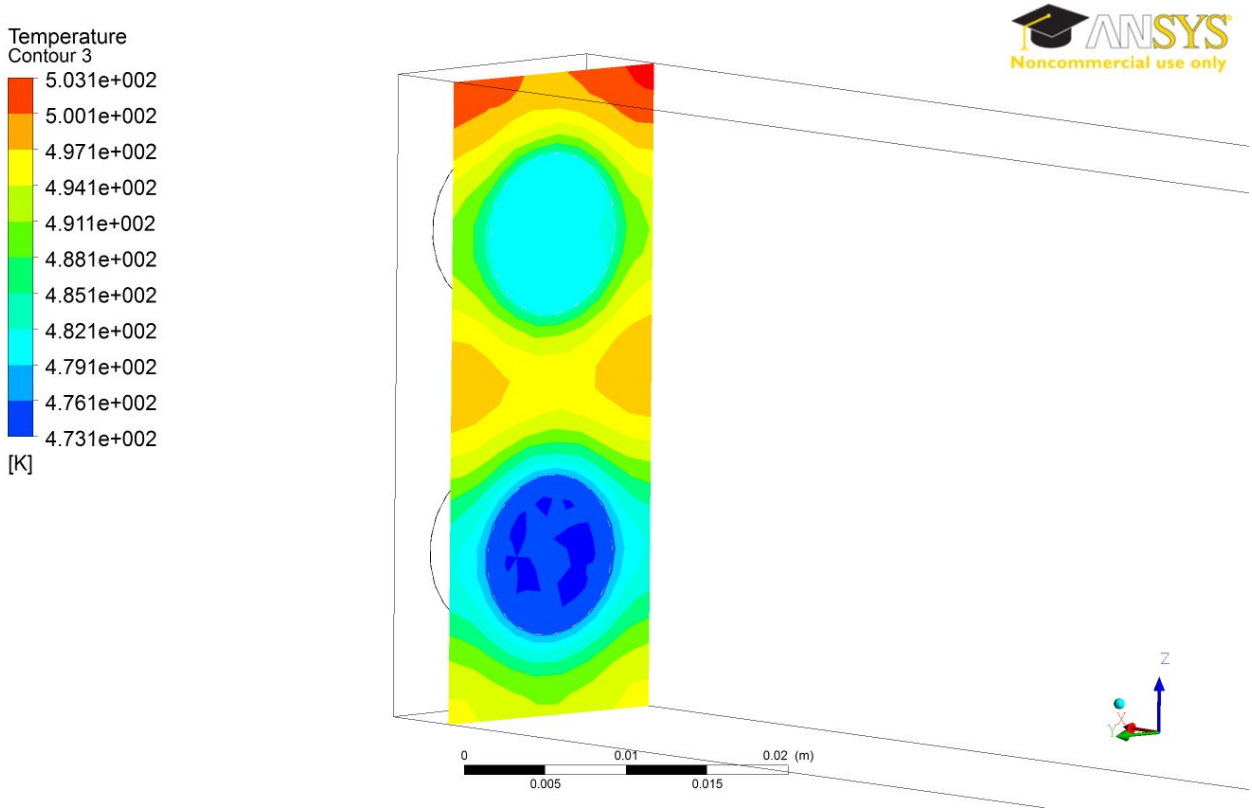

Fig. 9.62: Temperature distribution in a section close to the inlet/outlet at 1620 s (CFX).

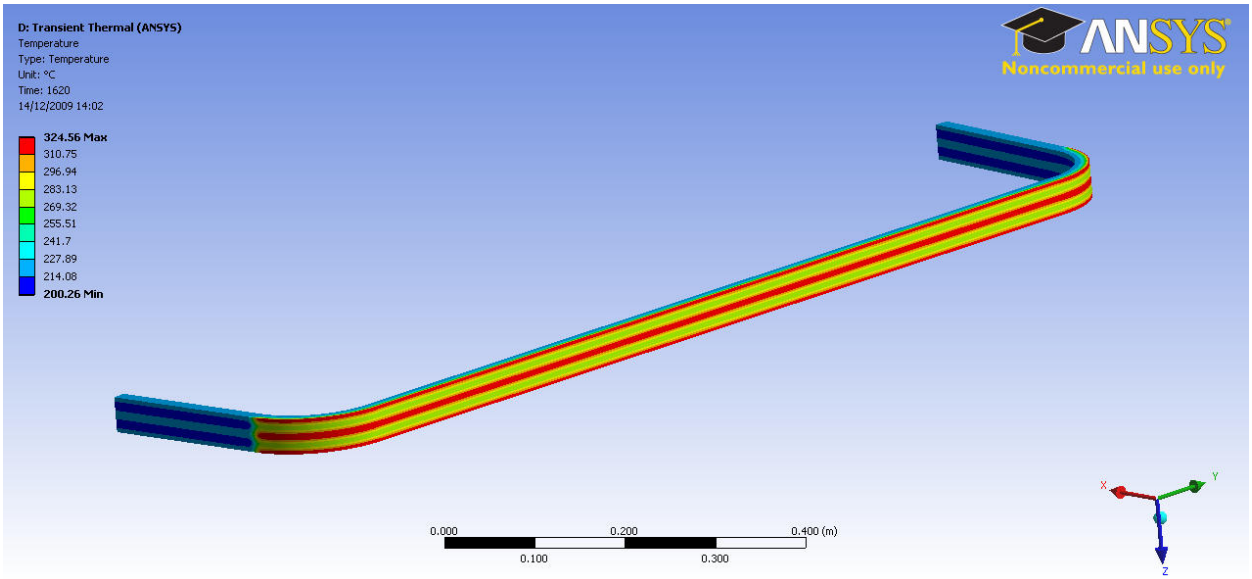

Fig. 9.63: Temperature at 1620 s (ANSYS Mechanical).

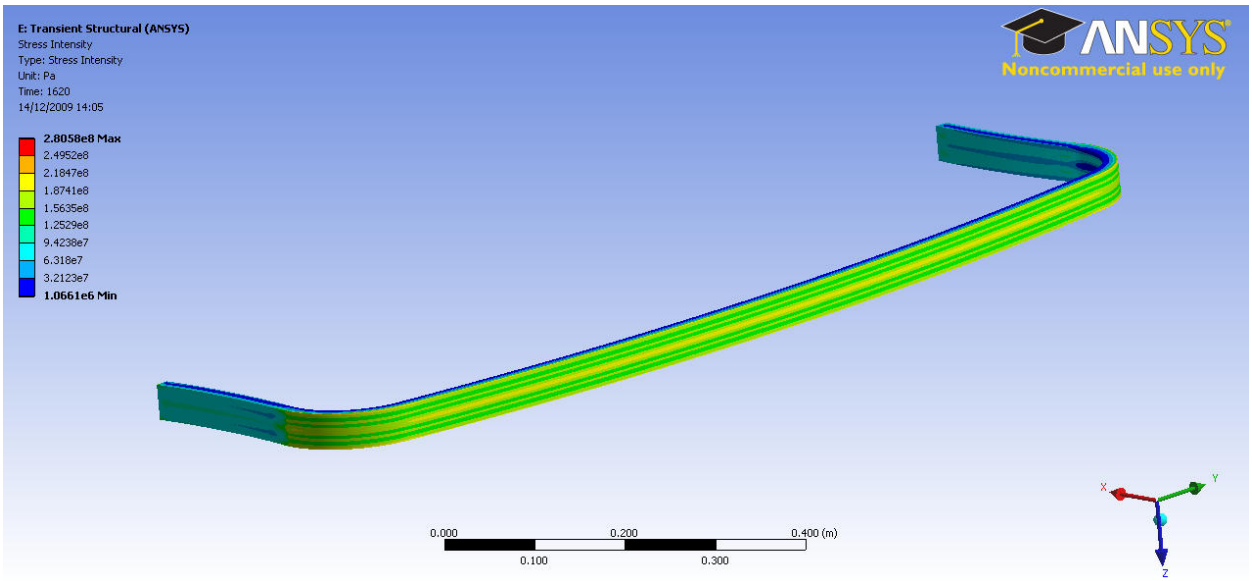

Fig. 9.64: Stress intensity at 1620 s (ANSYS Mechanical).

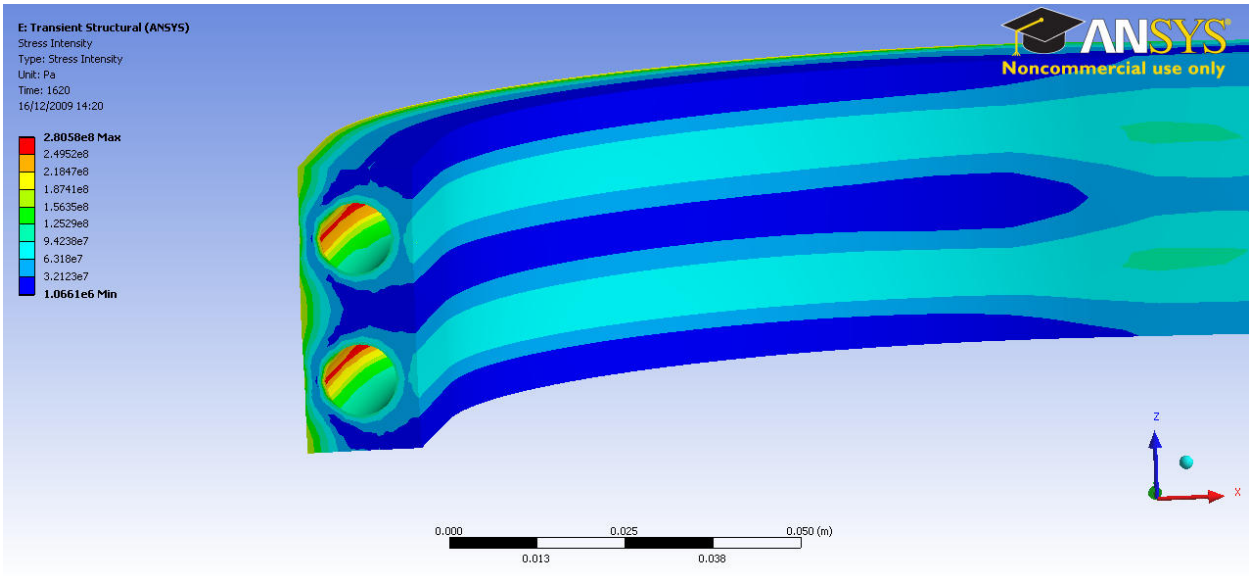

Fig. 9.65: Stress intensity in the elbow region at 1620 s (ANSYS Mechanical).

The strain intensities are shown on fig. 9.66-9.68. The mean strain intensity 0.096% and the alternating strain intensity is 0.079%. The total strain range is 0.158%.

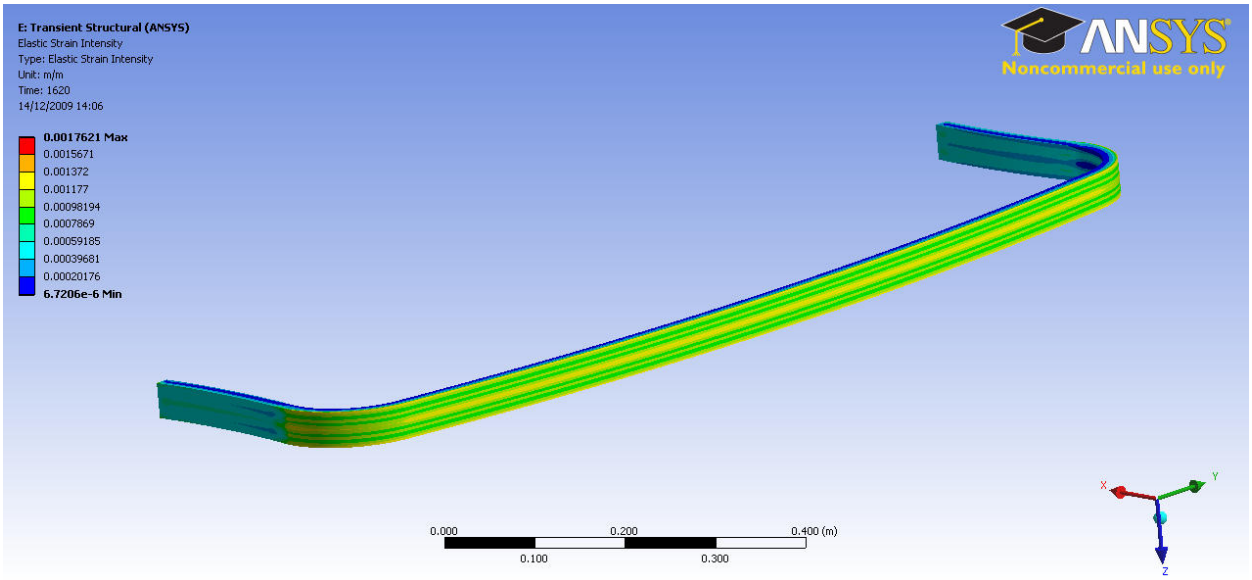

Fig. 9.66: Strain intensity at 1620 s (ANSYS Mechanical).

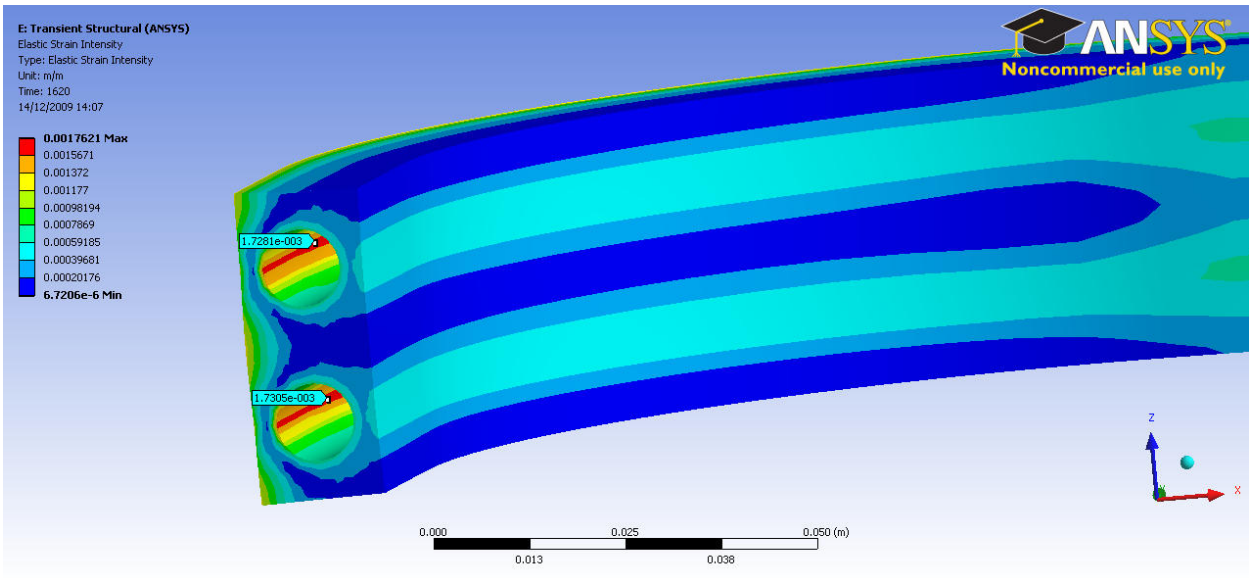

Fig. 9.67: Strain intensity in the elbow region at 1620 s (ANSYS Mechanical).

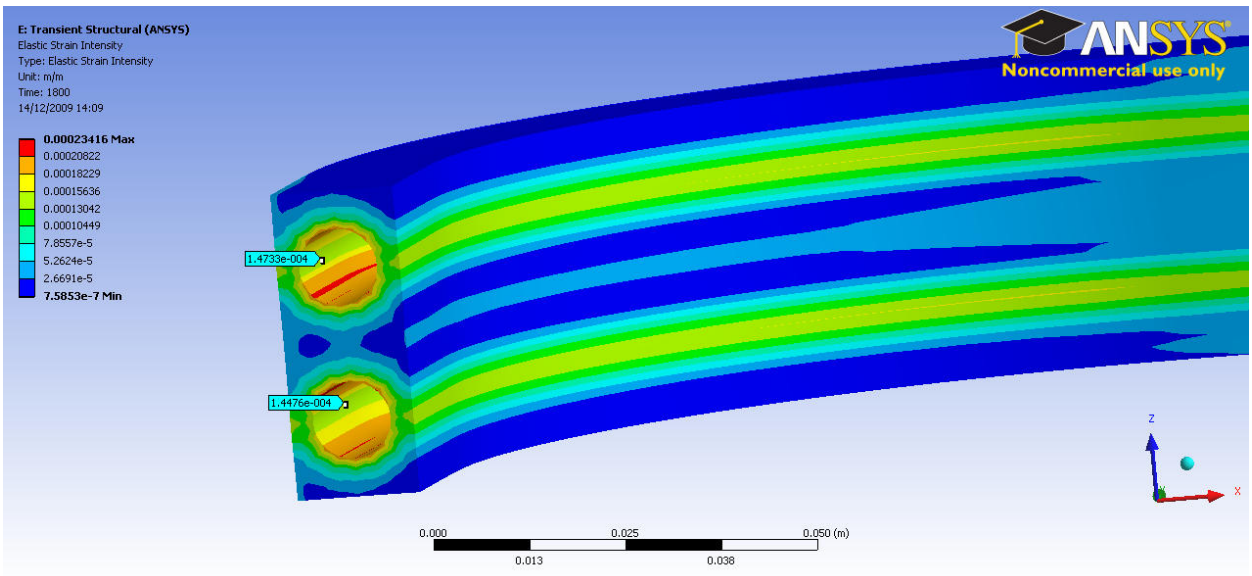

Fig. 9.68: Strain intensity in the elbow region at 1800 s (ANSYS Mechanical).

9.2.5. Monolith

All the analyses were done on a small section of the first wall in order to save computing resources. However it does not mean that it is a restriction. The original model (without neutron heating) is extend to a "monolith" which includes five pairs of cooling channels. The strain distributions at different location of the models are shown on fig. 9.69-9.73.

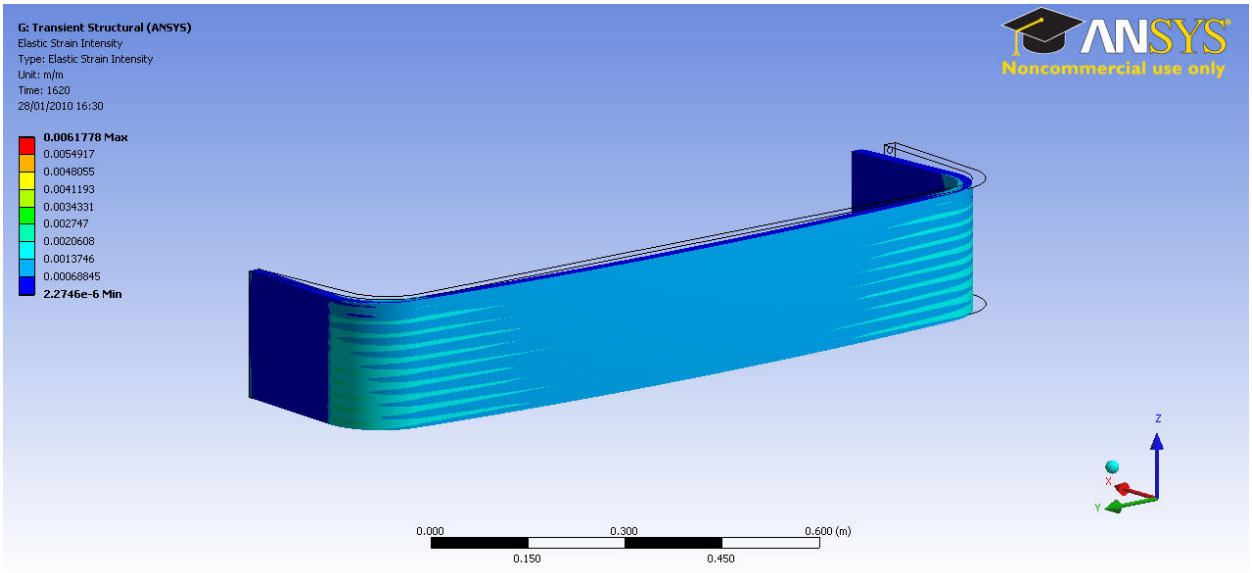

Fig. 9.69: Strain intensity at 1620 s (ANSYS Mechanical).

Fig. 9.70 and 9.71 show strain values inside the cooling channels. Although these values slightly decrease farther away from the constrained bottom plane (where the displacement in z direction is 0), the maximum strain intensity is about the same as it was for the original model (see fig. 2.13).

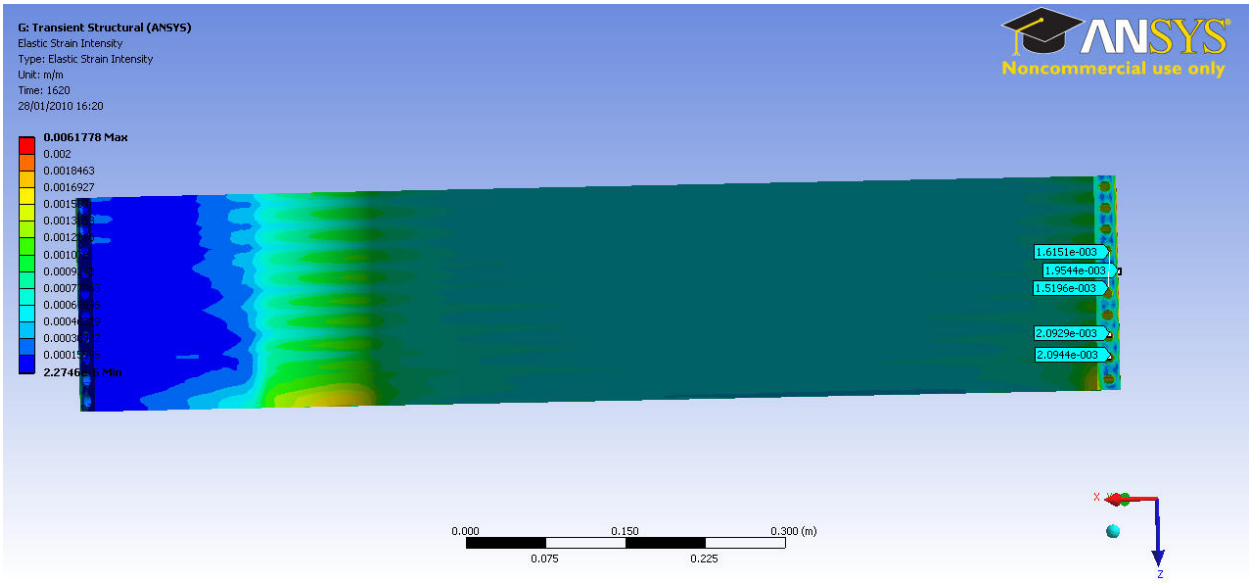

Fig. 9.70: Strain intensity at 1620 s (ANSYS Mechanical).

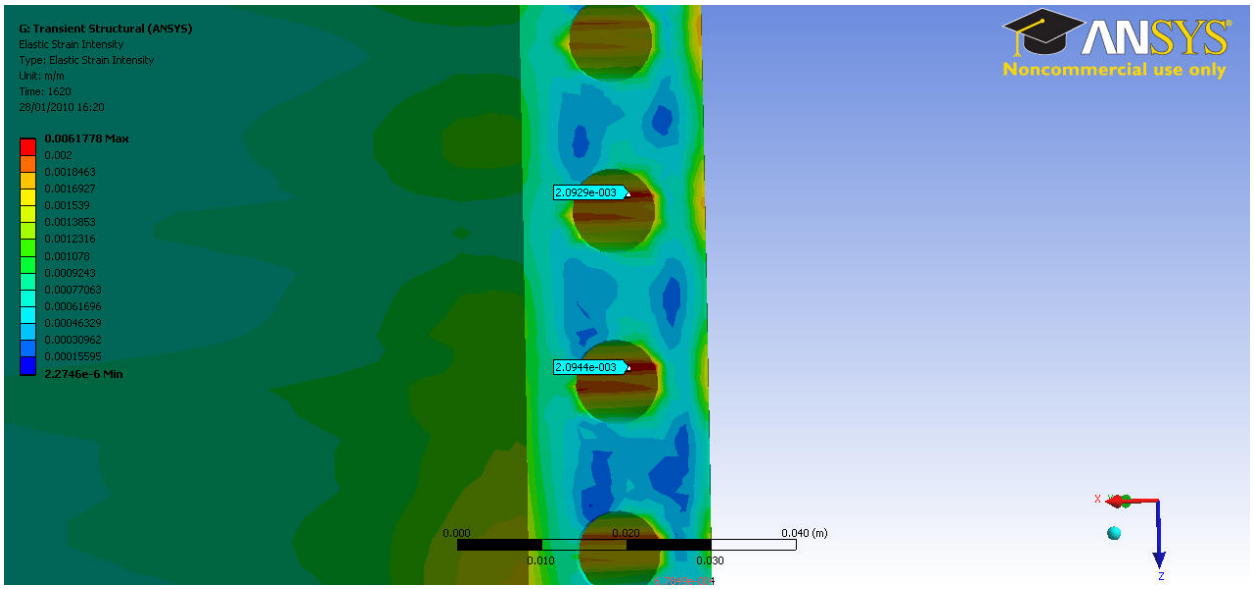

Fig. 9.71: Strain intensity in the elbow region at 1620 s (ANSYS Mechanical).

The location of the maximum strain however is at one of the constrained edges (fig. 9.72). As was mentioned in 2.2, the reason for this can be that a relatively small number of nodes is constrained and therefore the reaction forces are unrealistically high at these nodes. Fig. 9.73 shows the distortion due to the heat load compared to the undeformed wire frame of the model. It shows that the constraints are minimalist; the model can “breath” and the stresses and strains are dominated by the heat load.

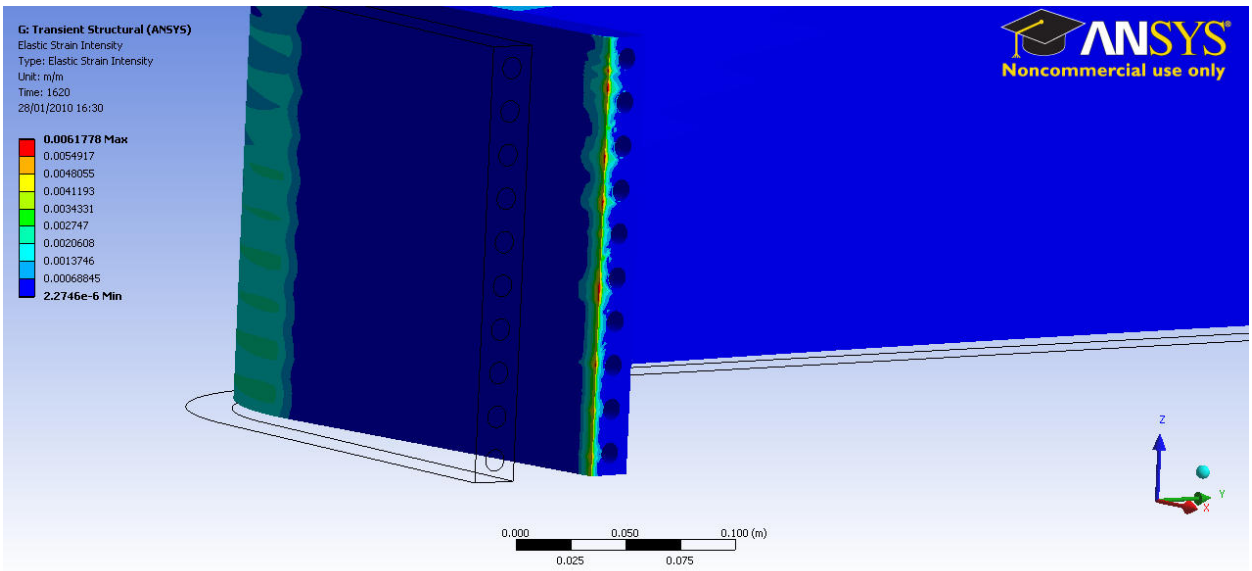

Fig. 9.72: Strain intensity at the constrained edge at 1620 s (ANSYS Mechanical).

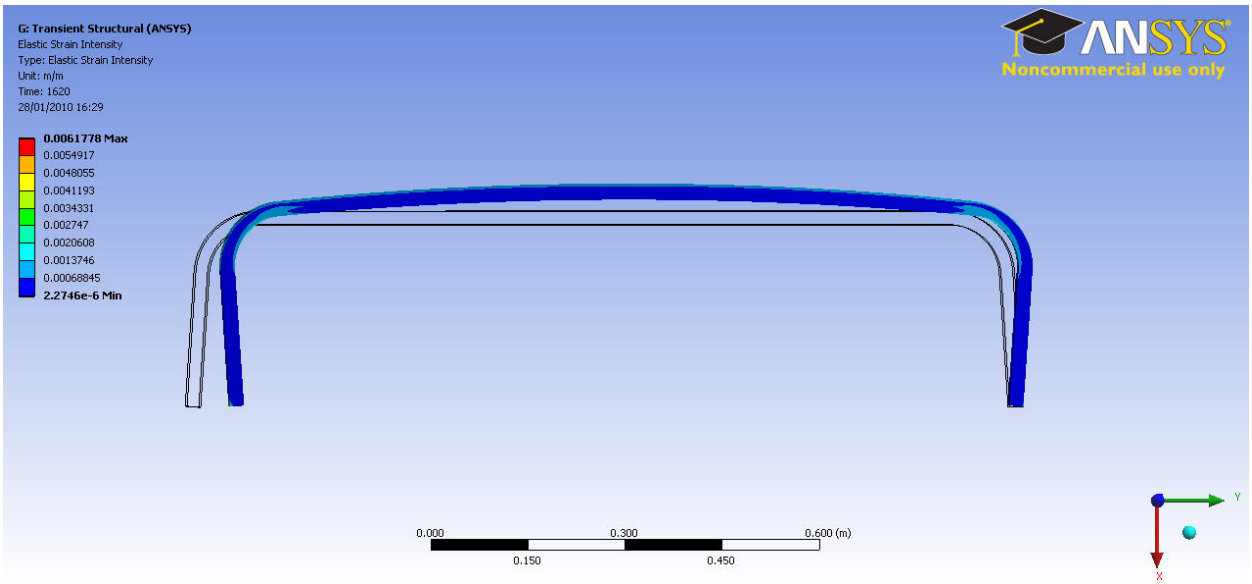

Fig. 9.73: Strain intensity at 1620 s, deformed shape and undeformed wire frame (ANSYS Mechanical).

9.2.6. Verification

The results have been compared to ANSYS Classic results and hand calculations in order to make sure the models worked correctly.
The original model without neutron heating has been analysed with ANSYS APDL 12 (formerly Classic), and so the wall heat transfer coefficients have been calculated using the Dittus-Boelter equation for the Nusselt number. Fig. 9.74 shows the temperature distribution (see fig. 9.10 for comparison). The maximum temperature is almost exactly the same.

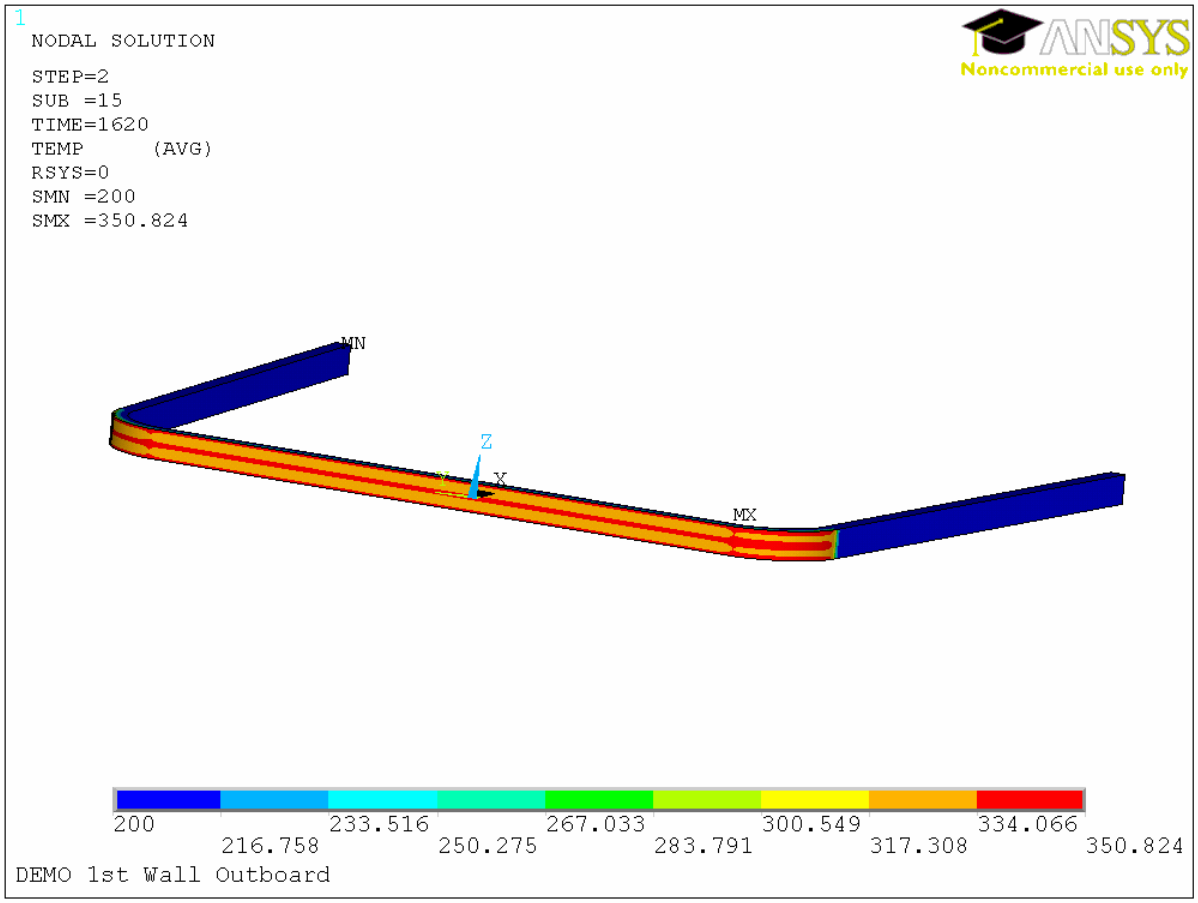

Fig. 9.74: Temperature at 1620 s (ANSYS APDL).

Fig. 9.75 and 9.76 show the stress intensity and elastic strain intensity, but the model does not include the pressure from the water coolant. It can be concluded that the stress and strain values are in the same range (see fig. 9.19 and 9.21 for comparison).

The jagged black boundaries in the “cross section” on fig. 9.75 and 9.76 are due to the fact that in ANSYS Classic the relevant elements are selected to show the inner part of the cooling pipe; they are element boundaries.

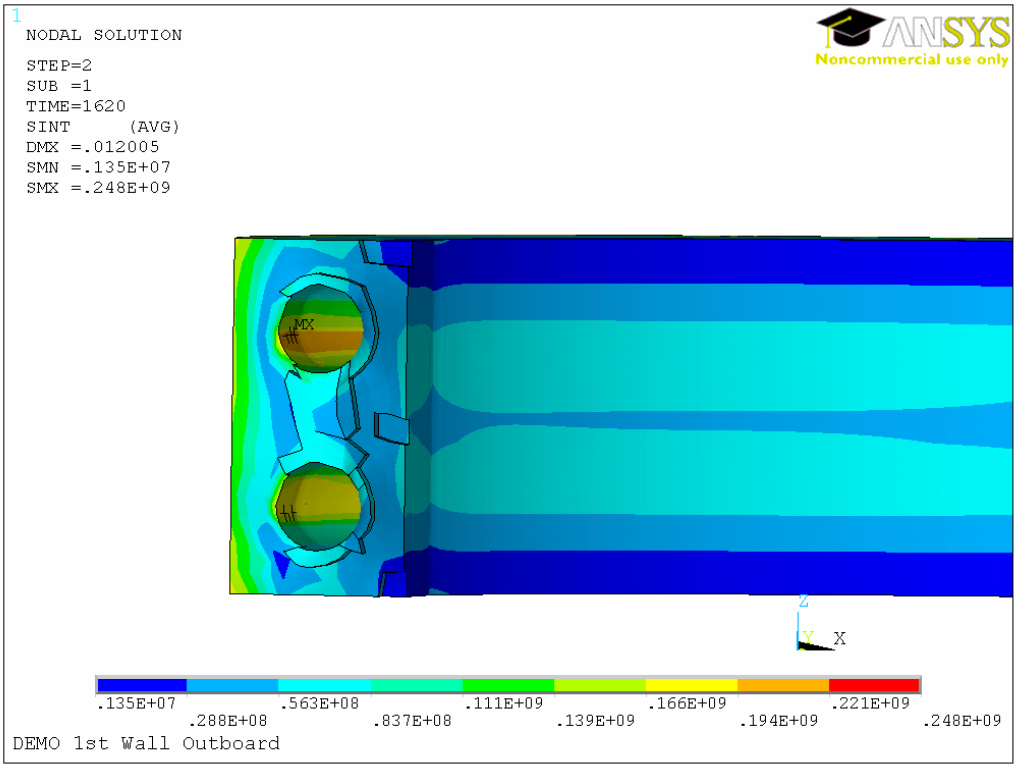

Fig. 9.75: Stress intensity in the elbow region at 1620 s (ANSYS APDL).

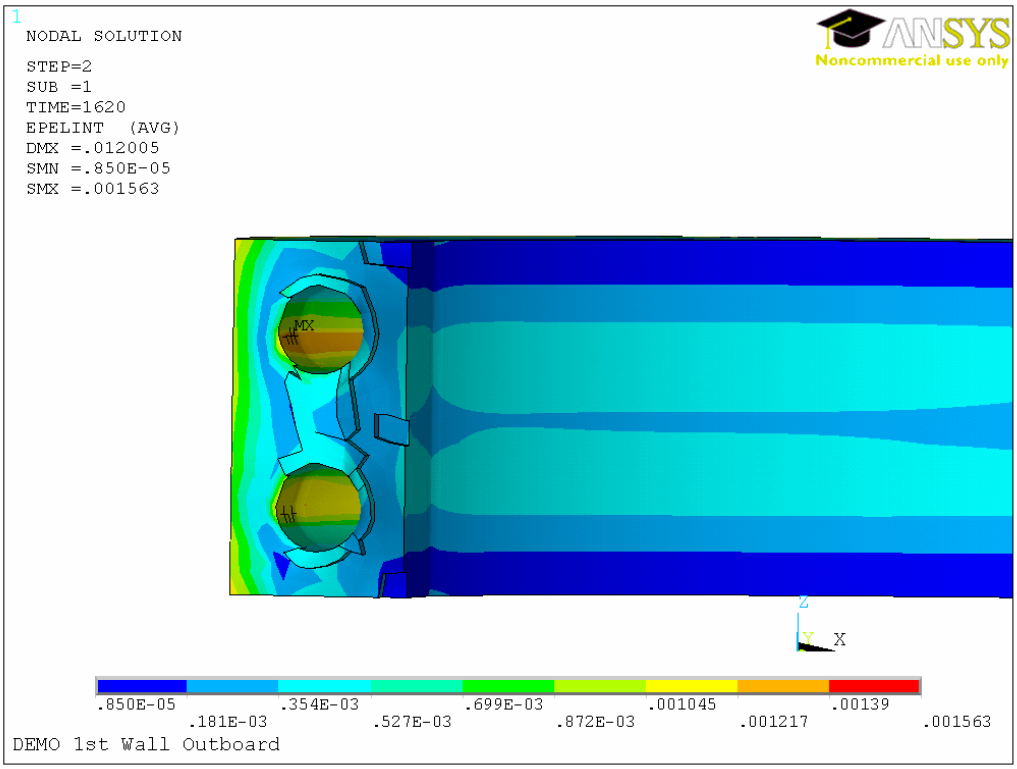

Fig. 9.76: Strain intensity in the elbow region at 1620 s (ANSYS APDL).

The pressure drop in the channels can be estimated by hand calculation. The flow is turbulent with Re>60000. The length of the channel is ~1.664 m (L), diameter 10 mm (D), water velocity 10 m/s (v), density 871.1 kg/m^3 (ρ).

$$\Delta p = \lambda \cdot \frac{L}{D} \cdot \frac{\rho}{2} \cdot v^2$$

The λ coefficient of friction can be taken from the Moody diagram. In this case it is about 0.02, thus Δp = 144951 Pa = 0.14 MPa. This is consistent with the CFX results.

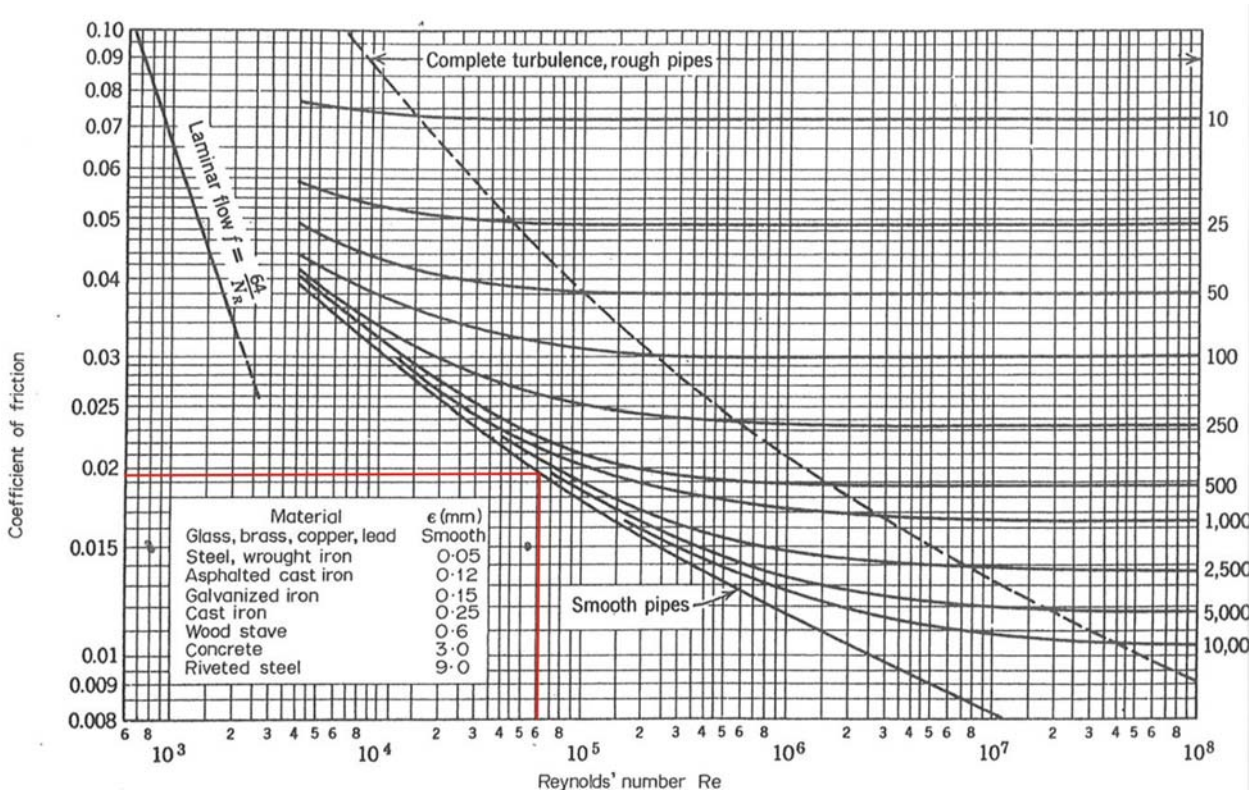

Fig. 9.77: Moody diagram.

9.3. Comparison of Pumping Power for Water vs. Helium-Cooled Concepts

9.3.1. Water cooled concepts

PPCS-A concept is based on 5000MW$_{th}$ fusion power and 1546MW$_e$ net electrical power output, giving a plant efficiency of 31%. Of the 5000MW$_{th}$ fusion power, 894MW$_{th}$ (~18%) is incident on the divertor.

1 Basic Concept (166°C)
The basic PPCS-A concept outputs water at 166°C. This temperature is too low to be practically useful as a heat source for power generation [4.17]. However, this low-grade heat could be used more effectively as an indirect heat source, to pre-heat the feedwater for the blanket steam generator. This would increase overall plant efficiency from 31.0% to 32.9%, falling to 31.6% once divertor pumping requirements are included. Divertor pumping power is hence approximately 65MW, or **7.2% of divertor heat load.**

2 Advanced Concept (325°C)
The advanced PPCS-A water-cooled concept is capable of outputting primary cooling water at 325°C. Assuming a temperature drop ΔT =5K across heat exchanger between primary and secondary water circuits, highest temperature T_{mas} in secondary circuit is 320°C. Typical efficiency of steam cycles at this temperature (see Fig. 4.1) is around 24%, potentially creating an extra $894 \times 0.24 = 214MW_e$ output. This would increase plant efficiency to (1546+214)/5000 = 35.2%. This is subject to a further reduction when considering the input energy for pumping the cooling circuit. This is a rough estimate – [4.17] suggests the net increased efficiency would be 33%, meaning a divertor coolant circuit pumping power of approximately 110MW, or **12.3% of divertor heat load.**

It may be possible to use the 325°C outlet of the advanced PPCS-A concept as pre-heating for the blanket steam generator, as with the basic PPCS-A concept, rather than use this heat directly for power generation. The higher outlet temperature of the advanced concept is likely to improve the scheme, achieving an overall plant efficiency greater than 31.6%. However, unless the resulting efficiency by this method is greater than 33.0%, it would still be most efficient to simply use the heat directly. Further study of the system as a whole is required in order to determine which strategy is preferable.

9.3.2. Helium cooled concepts

PPCS-B concept is based on 3600MW$_{th}$ fusion power and 1332MW$_e$ net electrical power output, giving a plant efficiency of 31%. Of the 3600MW$_{th}$ fusion power, 685MW$_{th}$ (~19%) is incident on the divertor.

Divertor for PPCS-C is identical to PPCS-B, therefore divertor calculations have been made based on PPCS-B.

1 Reference concept (HEMJ)
Experiments on HEMJ 'reference concept' prototypes gave flow conditions in each module as follows:

$p_{in} = 10MPa,\ T = 600°C,\ \dot{m} = 6.8g/s,\ \Delta p = 0.11MPa$

Ideal pumping power is given as:

$$\dot{W}_{pump} = \int_{V_1}^{V_2} p.dV = \int_{V_1}^{V_2} \frac{RT}{V}.dV = RT\ln(\frac{V_2}{V_1}) = RT\ln(\frac{\rho_1}{\rho_2}) = RT\ln(\frac{p_1/RT}{p_2/RT}) = RT\ln(\frac{p_1}{p_2})$$

$T = 873K,\ p_1 = 9.89MPa,\ p_2 = 10.0MPa,\ R_{helium} = 2077J/kgK$

$\dot{W}_{pump} = 2077 \times 873 \times \ln(10/9.89) = 20kJ/kg$

Assuming pump isentropic efficiency of 90%, pumping power becomes 22.3kJ/kg

Mass flow 6.8g/s per module: pumping power $22.3 \times 6.8v \times 10^{-3} = 0.151$kW/module

Total divertor area = 2.3m (target length) × 54.0m (circumference) = 124.2m^2. Pump work 0.151kW/module becomes $0.151 / 281 \times 10^{-6} = 537$kW/m^2 = 66MW total.

Divertor work input is hence 66MW/685MW = **9.6% of divertor heat load.**

Outlet coolant temperature given by $Q=mc_p \Delta T$ (c_p for helium is 5188J/kgK):

$T_{out} = T_{in} + (2.81 \times 10^3 / 6.8 \times 10^{-3} \times 5188) = 680°C$.

Assuming a 10°C drop in the primary/secondary heat exchanger, the maximum power generation efficiency is limited to around 40% by steam cycle (temperatures below 800-900°C are incompatible with gas turbine generators). Work output from the divertor should therefore be around 685 × 0.40 = 274MW.

Net work output from divertor circuit = 274 – 66 = 208MW. Overall plant efficiency is given in [4.17] as 36%.

2 Alternative concept (HETS)

A conceptual study of the HETS concept shows that in order to retain the maximum dome temperature below the allowable limit of 1300°C, the pumping power in the divertor circuit is around **10% of divertor heat load** [4.19]**.**

The effect on overall power plant efficiency is thus expected to be similar to that of the HEMJ concept.

9.4. Coil Stresses: PROCESS Model of TF Coil for Stress Calculations

The PROCESS module SCTFCOIL calculates stresses in a superconducting TF coil. It gives the stresses in the inboard leg at midplane. The alternating stresses are not calculated.

The geometry handled by the first part of the routine is shown below. The coil shape is used for calculating stored energy, but not for stresses. The field from the CS and PF coils does not seem to be included. It is these fields that cause alternating stresses in the TF coils, so it would be desirable to include them in future versions. There is code that would provide for a set of support rings additional to the bucking cylinder, but this does not seem to be implemented.

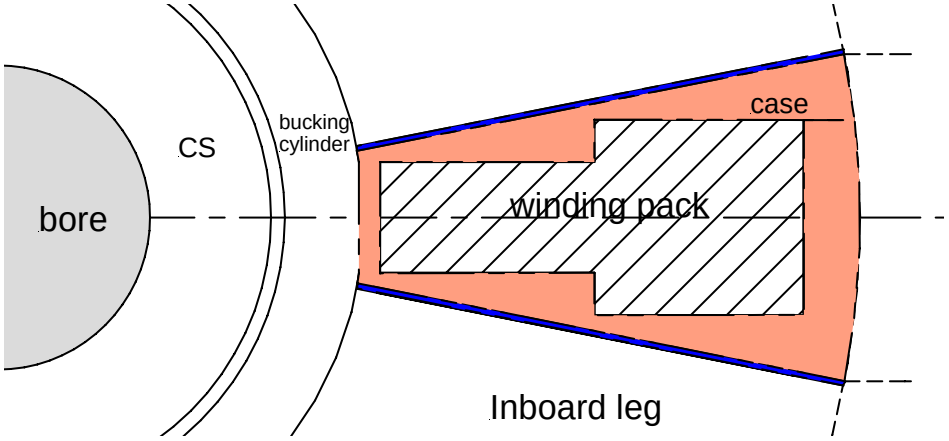

Fig. 9.78

The conductor geometry is input (square cross-section, with rounded edges, conduit and insulation).

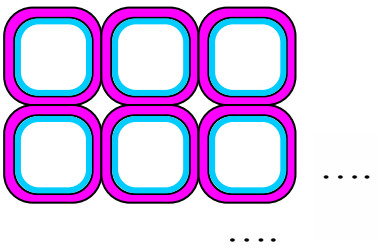

However…, the subroutine TFSTRESS that actually works out the stresses in the horizontal principal axes does not *seem* to be based on the model in the sketch above. It uses a "graded winding pack" consisting of three regions with different values of Young's modulus and current density. For each region radial and tangential stress is calculated. (See diagram below.) There seems to be no distinction between winding pack, case, or insulation, and the number of coils is not used. After the results are returned from TFSTRESS, they are used to calculate the stresses in the conduit walls.

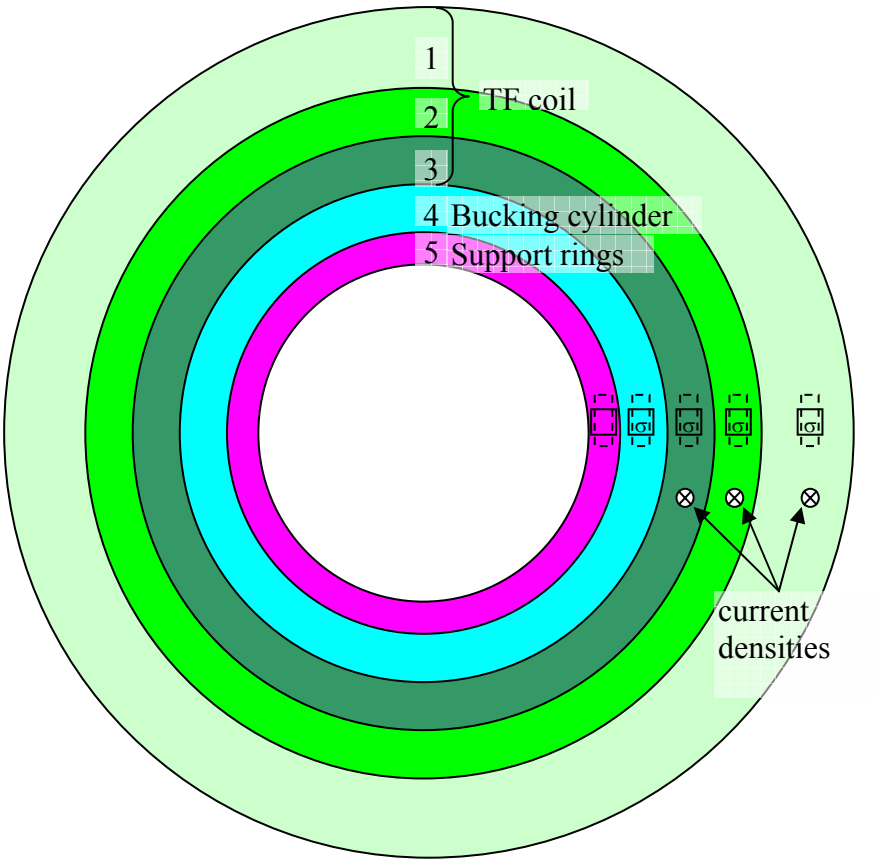

Fig. 9.79: Cross-section of bucking cylinder and inboard legs of the TF coils, as seen by TFSTRESS module in PROCESS. A single current density is assigned to each of the outer three cylinders, and a single value of radial stress and a single value of tangential stress is calculated for each cylinder.

In addition, the "vertical force" is calculated, which seems to be the vertical tension force at the midplane of the inboard leg due to hoop forces. This is used to calculate the tension in the vertical principal axis.

9.5. Power Supply Costs: Tables of Source Data

Table 9.4

Dwell Time	**T1**	**T2**	**V1**	**V2**	**VA PS rating ramp up**	**VA PS rating ramp down**	**MVA Rating**
30	10.71	19.29	93,819	-56,767	3,368,090,133	-3,329,408,444	3368
60	21.43	38.57	46,909	-28,384	1,684,045,067	-1,664,704,222	1684
120	42.86	77.14	23,455	-14,192	842,022,533	-832,352,111	842
300	107.14	192.86	9,382	-5,677	336,809,013	-332,940,844	337
1000	357.14	642.86	2,815	-1,703	101,042,704	-99,882,253	101
2000	714.29	1285.71	1,407	-852	50,521,352	-49,941,127	51

Table 9.5

Cost Scenario 1						
Cost=k*P^0.6		**k= 2000 for 2 quadrant**		**P=power required (kW)**		**1CHF=€0.67**
Dwell Time	Cost (€)	Cost (M€)	MVA Rating			
30	11,054,396	11.05	3368			
60	7,293,182	7.29	1684			
120	4,811,705	4.81	842			
300	2,776,739	2.78	337			
1000	1,348,366	1.35	101			
2000	889,590	0.89	51			

Table 9.6

Cost Scenario 2: 0.5CHF/W for power <1MW				**1CHF=€0.67**
Cost Scenario 3: 0.3CHF/W for power 1MW-100MW				
Cost Scenario 2: 0.25CHF/W for power >100MW				
Dwell Time	Cost (€)	Cost (M€)	MVA Rating	
30	564,155,097	564	3368	
60	282,077,549	282	1684	
120	141,038,774	141	842	
300	56,415,510	56	337	
1000	20,309,584	20	101	
2000	10,154,792	10	51	

Table 9.7

Cost Scenario 5: Neumeyer data $100/kW (=€71/kW)				**1$=€0.71**
Dwell Time	Cost (€)	Cost (M€)	MVA Rating	
30	239,134,399	239.13	3368	
60	119,567,200	119.57	1684	
120	59,783,600	59.78	842	
300	23,913,440	23.91	337	
1000	7,174,032	7.17	101	
2000	3,587,016	3.59	51	

Table 9.8

Cost Scenario 6A: Warder data £54.00/kW (=€62.1/kW)				**1£=€1.15**
Dwell Time	Cost (€)	Cost (M€)	MVA Rating	
30	209,158,397	209.16	3368	
60	104,579,199	104.58	1684	
120	52,289,599	52.29	842	
300	20,915,840	20.92	337	
1000	6,274,752	6.27	101	
2000	3,137,376	3.14	51	

Table 9.9

Cost Scenario 6B: Warder data £70.00/kW (=€80.5/kW)				**1£=€1.15**
Dwell Time	Cost (€)	Cost (M€)	MVA Rating	
30	271,131,256	271.13	3368	
60	135,565,628	135.57	1684	
120	67,782,814	67.78	842	
300	27,113,126	27.11	337	
1000	8,133,938	8.13	101	
2000	4,066,969	4.07	51	

9.6. Energy Storage

9.6.1. Molten Salt Technology Issues

This material comes from the paper by Kelly et al [8.14a].

First generation solar plants used synthetic oil as a heat transfer medium and this limits the maximum operating temperature. Molten nitrate/nitrite mixtures allow a 50-100^{o}C increase which, in turn, raises the Rankine efficiency from about 37% to 41%. Molten salts also offer the potential for low cost energy storage as well. The main liability is that the melting point of these salts lies between 120^{o}C and 220^{o}C. Electric heating is used to keep the plant above the melting point. Molten salts can also be corrosive to ball joints between sections of the thermal plant.

With oils the upper temperature limit in practice is 370oC. Oil-based thermal storage is too expensive as it needs 10bar pressurisation to prevent boiling and at $3/kg it far exceeds the $0.5 target.

The cost of salt thermal storage is estimated to lie between $15-20 per kWh(thermal) or $50 per kWh(electric), as quoted in the Scientific American article. Detailed investment analysis has been used in the calculations.

The best salt of all is a simple nitrate/nitrite binary which can operate up to 600^{o}C. However, the key drawback is its high melting point (190^{o}C).

Direct thermal storage is estimated to be scalable to at least 3.6GWh(t) i.e. 10x Andasol or about 280,000 tonnes.

The main challenges are: field temperature maintenance, freeze-up recovery, loop maintenance and seals.

Impedance heating of salt containing tubes appears to be the most practical method of maintaining molten salt but because of the low resistance of steel tubing this does necessitate high current (100's of amps) and low voltages (3 volts). Sometimes these large currents have to be carried considerable distances.

[reference Kelly B, Price H, Brosseau D, Kearney D, "Adopting nitrate/nitrite salt mixtures as the heat transport fluid in parabolic trough power plants" Proc. ES2007 / Energy Sustainability 2007, June 27-30, 2007, Long Beach CA., paper# 2007-36172]

9.6.2. The Use of FLiBe Salt as a Breeder Blanket Medium

Benefits and drawbacks of (FLiBe) salt as a reactor heat transfer fluid and blanket breeder material

"FLiBe" is a fluoride salt of lithium and beryllium proposed as nuclear reactor coolant and moderator, and was successfully used in the ORNL Molten Salt Reactor Experiment in the 1960's [8.17]. Modified versions of the salt incorporating thorium have been proposed as the fuel and coolant of a thorium breeder reactor that uses an "inherently safe" "freeze plug" safety

concept. Flibe has a high m.p. 459^{o}C but a very high boiling point 1430^{o}C. Its volumetric heat capacity (4540kJ/m^{3}.^{o}C) is similar to that of water, over 4 times that of liquid sodium and *over 200 times that of helium at reactor conditions.*

In the foregoing analysis only the cost and thermal properties of molten salts have been considered. High temperature salts, even the highly stable alkali fluorides are affected by reactor conditions and there have been a number of studies examining the feasibility of FLiBe for use in fusion machines.

The following points are taken from the report produced by Idaho National Engineering and Environmental Laboratory for US DOE in 1999 [8.21]

FLiBe use in Fusion Reactors: an Initial Safety Assessment

FLiBe is typically a 66 mole% fraction LiF – 34 mole% BeF_2 mixture. Safety issues include chemical toxicity, radiological hazards (n-activation) and handling of a high temperature coolant. Beryllium is a known toxic agent and fluorine is also toxic (can cause pulmonary oedema). However, actual experience in the ORNL MSRE experiment suggests that these hazards are at least manageable.

Flibe research is of interest to both the MCF and ICF communities because it offers potential as moderator, a breeder and heat transfer fluid.

A key question requiring research (as of 1999) is to what extent radiolysis and Hall-effects in high fields might cause chemical dissociation. Evidence to date suggests that any such effects lead to rapid re-combination of the alkalis as fluorides.

Another area of interest is whether fluorine released by the neutron bombardment of ^{6}Li to ^{3}H will combine with the tritium or remain volatile. Experiments in which molten FLiBe is deliberately tritiated have been considered but it has to be remembered that the fluorine, tritium or ^{3}HF volatility is only one aspect of a series of complex interactions caused by neutrons. A particular concern would whether highly corrosive ^{3}HF remained active for any appreciable time. One suggestion is that excess beryllium could be added as a sacrificial agent.

In considering leakages, a key benefit is the low pressure needed to circulate FLiBe (0.35 bar was used in MSRE). As already noted the thermal properties can be considered to be at least ‘fair’ and probably ‘good’.

Another area for consideration is the activation of fluorine to ^{18}F in particular ($t_{1/2}$ =1.8h). This may lead to the build-up of oxygen impurity decay products.

The solubility of hydrogen isotopes in FLiBe is very low, so it is probably that if un-combined the tritium may escape into secondary (steam) cooling or power cycles and ultimately into the environment or into worker areas of a normal power plant. The presence of steam / FLiBe interfaces in conventional shell and tube type heat exchangers poses particular concerns. However, heat exchanger designs and integrity has advanced significantly since the 1970-1980s experiences with sodium etc.

9.6.3. The Thermal Model

The five Programs of Table 8.2 were used to create a requirements column in the Excel spreadsheet. The time intervals were subdivided into 6 minute intervals.

An initial temperature of 500^{o}C was imposed on the salt and the aim (by manual iteration) was to adjust the salt mass so that the maximum and minimum temperatures were contained within the limits set in Table 8.1. The fusion power plant margin was also set manually. It represents the extent to which the plant thermal power needs to be increased in order to achieve a 500^{o}C salt temperature at the end of the day.

At the 2nd and subsequent time steps the resulting salt temperature was determined from a global heat balance:

$$T_{i+1} = T_i + \Delta\theta(Q_{th,fusion} - Q_{th,grid} - Q_{pre\text{-}pulse} - Q_{radiative} - Q_{other}) / (1000.M_{salt} \,.\, c_p)$$

where

T_{i+1} = temperature in next time step
T_i = temperature in previous time step
$\Delta\theta$ = time step (360 seconds)
$Q_{th,fusion}$ = thermal contribution to salt by reactor when operating (as per Program)
$Q_{th,grid}$ = thermal equivalent of electricity supplied to grid (i.e. electricity / efficiency)
$Q_{pre\text{-}pulse}$ = thermal equivalent of energy required to switchover inductive CD; this was forward calculated by determining when the reactor would start (IF statements)
$Q_{radiative}$ = radiative loss in reactor from hot components (blankets, divertor etc); this was calculated using actual salt temperatures at time θ
Q_{other} = guestimated static thermal load(s) e.g. salt plant heat loss
M_{salt} = mass of salt (tonnes)
c_p = nominal specific heat of salt (typically 1550J/kg^{o}C for HTS salt)

Salt plant capital costs were calculated using the $50/kWh figure i.e.

$$\text{Capital cost} = \$50.1000 / (3600.1000 / (c_p \,.\, \Delta T))$$

where

ΔT = assumed allowable temperature span (100^{o}C), although as noted for the Andasol-1 solar plant it appears a tighter temperature span of 30^{o}C may be required